A 3D molecular model background featuring several orange, textured cylindrical structures and a large, smooth, light blue spherical structure. The scene is set against a light, hazy background with a grid of thin lines.

# **Illuminating molecular motors at work**

Petra van Bergeijk

---

# illuminating molecular motors at work

Het belichten van moleculaire motoren in functie

(met een samenvatting in het Nederlands)

## Proefschrift

ter verkrijging van de graad van doctor aan de Universiteit Utrecht op gezag van de rector magnificus, prof. dr. G.J. van der Zwaan, ingevolge het besluit van het college voor promoties in het openbaar te verdedigen op woensdag 8 juni 2016 des middags te 4.15 uur

door

**Petra Marian van Bergeijk**

geboren op 25 december 1986  
te Lelystad

---

ISBN: 978-90-393-6527-4

The studies described in this thesis were performed at the division of Cell Biology at the Faculty of Science of Utrecht University in Utrecht, the Netherlands

Printed by: Gildeprint

Cover: Redrum bureau

Design & layout: P& ontwerp

Copyright © by P.M. van Bergeijk

All rights reserved.

Promotor: Prof. dr. C.C. Hoogenraad

Copromotor: Dr. L.C. Kapitein

*I will love the light for it shows me the way,  
yet I will enjoy the darkness for it shows me the stars.*

after Og Mandino

# Table of contents

Chapter 1	General introduction	9
Chapter 2	Right time, right place: Probing the functions of organelle positioning	29
Chapter 3	Myosin-V opposes microtubule-based cargo transport and drives directional motility on cortical actin	55
Chapter 4	Myosin-V opposes kinesin-driven cargo entry into the axon	77
Chapter 5	Optogenetic control of organelle transport and positioning	93
Chapter 6	Light-controlled intracellular transport in <i>Caenorhabditis elegans</i>	125
Chapter 7	KIF19 is required for axon maintenance and neuronal polarity in hippocampal neurons	139
Chapter 8	General discussion	167
Addendum	Summary	184
	Nederlandse samenvatting	187
	Curriculum vitae	190
	List of publications	191
	Acknowledgements	192

---



# 1

## General introduction

Petra van Bergeijk<sup>1</sup>

---

<sup>1</sup> Division of Cell Biology, Faculty of Science, Utrecht University, Utrecht, The Netherlands.

# General introduction

## Cellular compartmentalization

Cells are the basic units of life and constitute all living things on earth. For an organism to survive, cells need to grow, reproduce, respond to stimuli, perform metabolic reactions and adapt to changing environments. In order to do so, eukaryotic cells are compartmentalized into membranous organelles that each contains a specialized set of molecules to perform specific biochemical reactions and functions. Representations of eukaryotic cells often depict organelles such as mitochondria and lysosomes at random positions around the centrally located nucleus and endoplasmic reticulum (ER). However, the proper spatial arrangement of organelles is important for many cellular events such as signaling, polarization and growth. It is therefore not surprising that the localization of most, if not all, organelles is tightly controlled and can be adjusted in case of changing conditions and demands [1-10].

Polarized cells such as neurons have yet another level of compartmentalization since they consist of a somatodendritic domain that comprises the cell body and multiple tapering processes called dendrites, and a single long and thin process called the axon. Whereas the somatodendritic compartment can receive and integrate signals from many other neurons, the axon transmits and delivers signals to target cells [11-13]. The contact site where signal transduction between neurons takes place is called a synapse and involves the presynaptic axon terminal and a postsynaptic region that usually resides on the dendritic shaft or on dendritic protrusions called dendritic spines. Both structures are separated by a synaptic cleft across which chemical signaling molecules are transmitted from the pre- to post synapse [14].

The axon and the somatodendritic domain are functionally very different and need their distinct morphology and customized set of organelles and proteins to perform their particular functions. A specialized structure at the proximal end of the axon, called the axon initial segment (AIS), functions as a physical barrier between the somatodendritic and axonal domain [15-19]. The scaffolding protein Ankyrin-G is restricted to the AIS [20] and is considered the AIS master organizer [21] by binding to cell adhesion molecules, including Neurofascin [22], Na<sup>+</sup> channels [23,24], K<sup>+</sup> channels [25] and the cytoskeletal protein  $\beta$ -IV-Spectrin, which connects Ankyrin-G to the underlying actin meshwork [26,27]. The AIS not only prevents mingling constituents of the distinct compartments, the high density of voltage-gated Na<sup>+</sup> and K<sup>+</sup> channels is also responsible for the initial depolarization that is required for and precedes action potential generation [28]. Thus, the correct spatial cellular organization of organelles

and proteins as well as the organization into distinct compartments such as axons and dendrites is important for cell survival and functioning.

## The cytoskeleton

Cellular morphology is defined by the cytoskeleton, which provides a structural framework to organize the cell. Although this might suggest a static structure, the cytoskeleton is very dynamic and cytoskeletal rearrangements are involved in many cellular processes such as mitosis, axon outgrowth, spine formation and cell migration [29]. Besides structuring the cell, cytoskeletal filaments can serve as tracks for motor proteins and thus define transport routes and directions [1]. Therefore, the cytoskeleton is important for organelle transport and positioning, and for the establishment and maintenance of polarity through providing structure and directing polarized transport.

### Microtubules

The two most-studied filament types that constitute the cytoskeleton are microtubules (MTs) and actin. MTs are hollow cylinders that usually consist of 13 linear protofilaments, each built up by head-to-tail organized  $\alpha/\beta$ -Tubulin heterodimers. During MT growth, tubulin heterodimers are primarily added onto the plus-end of MTs where  $\beta$ -Tubulin is facing the MT tip. Interestingly, this is also the site where tubulin dimers are most frequently being removed. The ability of MTs to rapidly switch between plus-end growth and shrinkage is called dynamic instability. This phenomenon allows the rapid adaptation of the MT cytoskeleton to changing conditions and needs [30].

For most MTs the overall structure is the same, but properties such as polymerization rate, depolymerization rate, catastrophe- and rescue frequencies can substantially differ between MTs. The 'tubulin-code' hypothesis suggests that the incorporation of different tubulin isoforms, or the exposure of tubulin to post-translational modifications (PTMs) results in unique interactions of MTs with MT-associated proteins (MAPs). This can in turn modify MT dynamics, spacing and motor preferences, and eventually influences MT functions [31-35].

How MTs are distributed and organized within cells largely depends on the location where MTs are nucleated. In non-polarized cells, the centrosome is the microtubule-organizing center (MTOC) where the majority of MTs are nucleated. The centrosome consists of two centrioles surrounded by the pericentriolar material (PCM) that includes the MT nucleation factor  $\gamma$ -Tubulin [36,37]. MTs growing from the centrosome form a radial array in which most MTs are pointing with their plus-end towards the cell periphery (Figure 1A), thereby centralizing the centrosome and the associated nucleus [38,39].

In mature neurons, uniformly plus-end-out microtubules can be found in the axon, whereas microtubules with a mixed orientation can be observed in mammalian dendrites [40-43] (Figure 1B) and with a minus-end-out orientation in invertebrate dendrites [44,45]. Previous studies that used the hook decoration technique and the imaging of MT plus-end binding proteins in mammalian neurons, suggested that MTs are initially uniformly oriented with their plus-end distal to the cell body in all neurites [40-43]. However, MT ablation during early stages of neuronal development revealed that minus-end-out microtubules were already present before neuronal polarization. This indicates that the selective reorganization of axonal MTs into a uniformly plus-end-out orientation, rather than the formation of a mixed MT network in the dendrites, is a critical process underlying neuronal polarization [40-43]. Importantly, the MT rearrangements are believed to contribute to differentiated trafficking into these processes since the MT minus-end-directed motor dynein has been shown to drive

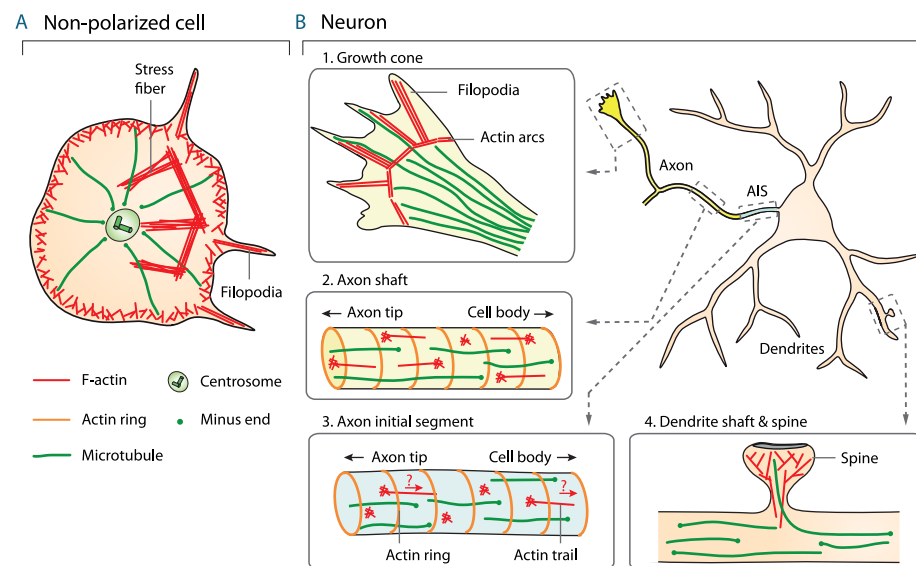


**Figure 1 | Microtubule and actin organization in non-polarized cells and neurons.**

**(A)** Microtubules form a radial array with the minus-ends clustered at the cell center in spherical, non-polarized cells. Highly branched actin is found at the cell cortex, whereas actin fibers constitute stress fibers and filopodia. **(B)** In neurons, microtubules are oriented plus-end out in axons but have a mixed orientation in the dendrites (2,4). The dynamic character of microtubules is exploited to transiently enter dendritic spines (4) or growth cone filopodia (1). Subplasmalemmal actin rings (2,3) and bidirectional actin trails, arising from actin patches, have recently been revealed in the axon (2,3), but the exact actin organization in the AIS is still unsolved (3). Moreover, branched actin structures can be found in dendritic spines (4), whereas actin cables constitute filopodia and actin arcs in the growth cones (1).

transport into the dendrites [46], whereas it is responsible for retrograde transport in the axon [47]. In addition to MT orientations, also PTMs and MAPs that decorate the MT lattice differ between axons and dendrites. Axonal MTs are enriched in acetylated and detyrosinated tubulin [48], which are marks for stable MTs, and decorated by the MAPs Tau and MAP1B, whereas MAP2 positive and tyrosinated MTs can be found in the dendrite [49,50]. Although some studies suggest that the varying MT characteristics play a role in neuronal polarization by affecting motor preferences [48,51,52], the exact role of MT modifications in these compartments is not clear.

Besides MTs in the axonal and dendritic shafts, specialized MTs can be found at particular localizations in the neuron. At the AIS for example, stable MTs positive for the MT bundler Trim46 can permanently be seen [53]. In contrast, the dynamic instability of MTs is employed to transiently enter dendritic spines [54-56], and to enter the outermost area of the growth cone upon growth cone adhesion [57] (Figure 1B). These MTs may facilitate the retrograde transport of endocytosed vesicles or increase surface delivery of intracellular cargoes through exocytosis. Thus, MTs can vary in their exact tubulin composition, PTMs, interacting proteins, and their exact function, but altogether they structure the cell and direct transport.

### Actin filaments

Actin filaments are composed of two intertwined linear F-actin strands that each consists of polymerized actin monomers. Actin monomers are added to the plus (barbed) end and dissociate from the minus (pointed) end. This might lead to actin treadmilling in which the total filament length remains approximately constant [58,59]. Like the MT lattice, the actin lattice can be subjected to PTMs that affect polymerization dynamics [60]. In the groove of the actin helix, tropomyosin dimers can bind along the actin fiber and regulate the interactions between molecular motors and actin [61-63], thereby affecting motor processivity. Interestingly, three types of actin assemblies are known; anti-parallel bundles that can generate contractility, parallel bundles that often form protrusions, and the branched actin meshwork that can push cell membranes forward at the cell cortex [58] (Figure 1A).

In neurons, several distinct actin structures can be distinguished. Most obvious are the actin-rich growth cones [57] and dendritic spines [64,65], in which the actin plus-ends are predominantly pointing into the protrusions. In the axon, subplasmalemmal actin rings have been observed evenly spaced along the axon shaft [66]. In addition, focal actin patches of continuously assembling/disassembling actin were found to colocalize with stationary endosomes along the axon, and to give rise to the formation of intra-axonal actin trails that run bidirectionally inside the axon [67] (Figure 1B). Whereas these dynamic actin filaments are believed to induce spatio-temporal actin enrichment to support axonal and synaptic plasticity, the static actin

rings have been suggested to provide mechanical support [67]. However, the exact functions remain to be determined. The actin structure in the AIS is still controversial, unidirectional actin filaments have been described to point with their plus-end towards the cell body [68], however, more recent EM data failed to detect any systematic actin directionality within the AIS [69] (Figure 1B, panel 3). In summary, actin filaments can be organized into a bundle or meshwork, which often relates to their subcellular localization and function.

## Motor proteins

Besides structuring the cell, most cytoskeletal filaments serve as tracks for motor proteins that use the energy derived from ATP hydrolysis to transport membranes, proteins and mRNA molecules along the cytoskeleton. This motor-driven transport is very important since simple diffusion cannot establish cargo asymmetry and would be too slow to relocate cargo over long distances [1]. Two types of motors run along MTs; kinesins that mostly walk to the plus-end of MTs [70], and dynein that walks to the minus-end [71]. In the actin-based myosin motor family, some motors move towards the minus-end whereas others walk towards the plus-end of F-actin filaments [72]. Although there is a single dynein molecule responsible for cytoplasmic transport [73], 45 mammalian kinesin superfamily (KIF) genes classified into 14 families [74] and 40 human myosin genes classified into 12 myosin families [75] are known up to date.

### Motor structure and properties

A typical kinesin consists of a motor domain that binds to MTs, and is connected via a short flexible neck linker to the stalk domain. The stalk domain contains multiple coiled-coil domains that mediate dimerization and is linked to a globular tail domain that can bind cargo or cargo binding proteins (Figure 2). Kinesins move in a hand-over-hand mechanism where the two heads step alternately and exchange leading and trailing positions. This way, every step results in an 8-nanometer displacement [76,77]. Myosin motors have a very similar organization, except that the neck linker consists of IQ calmodulin-binding motifs and functions as a lever arm (Figure 2). The lever arm varies in length and together with the degree of rotation during stepping, determines the myosin step size [78-80]. For example, the Myosin-V lever arm is three times longer than the lever arm of Myosin-II, accordingly, the step size of myosin II is 7-nanometer whereas Myosin-V takes 36-nanometer steps [81].

Dynein motors have a more complex structure, the MT binding domain is connected via a stalk to a donut shaped ring containing 6 AAA domains that together form the ATP hydrolyzing motor domain. Two tail projections extend from the head and can in turn bind adaptor molecules [82] (Figure 2). Dynein steps are variable in size and

range from 8- to 32-nanometer. Interestingly, it was shown that dynein decreases its step size when moving against a load [83,84]. Moreover, unlike kinesins, individual dyneins rarely show processive movements *in vitro* but need the addition of dynactin and a cargo adaptor such as BICD2, Hook3, Spindly or RAB11-FIP3 for unidirectional movements [85,86].

To prevent unnecessary motor activity and energy consumption, the motility of motor proteins is often regulated according to the presence or absence of cargo. In case of kinesin and myosin motors, the tail is often backfolded onto the motor domain to inhibit processive walking. This autoinhibition is released upon cargo binding when the tail is no longer available for binding to the motor domain [87-89]. For dynein it is believed that intramolecular head-to-head stacking is responsible for autoinhibition. Cargo binding would increase the distance between the motor domains of a dynein dimer and thereby release motor inhibition [90].

Despite structural similarities, each motor protein has different properties such as motor velocity [91], stall force [92,93], cargo binding [70], MT modification preferences [51,94-96], and the capacity to bundle [97,98], slide [99,100] and depolymerize [101] actin or microtubule fibers. The protein domain topology can be indicative for the properties of the motor. In fact, all plus-end-directed kinesins have their motor domain at the N-terminus (kinesin family 1–12), whereas kinesin-14 family members have a C-terminal motor domain and show minus-end-directed motility. In

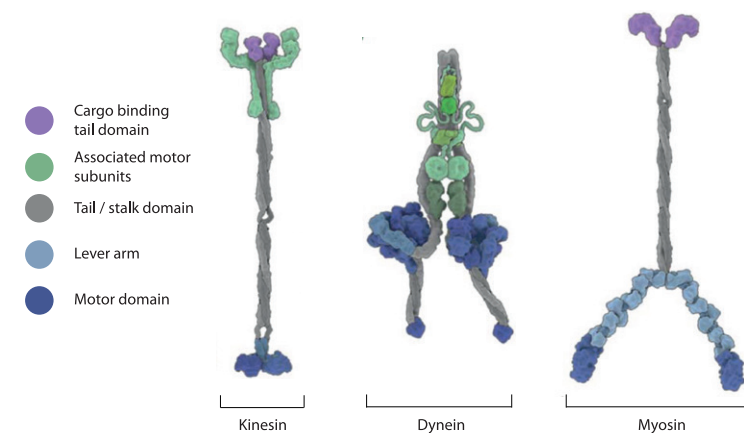


**Figure 2 | Protein domains and structure of the three motor protein families.**

Representations of a kinesin, dynein and myosin motor. Motor domains are shown in dark blue whereas the stalk domains and the dynein tail domain are depicted in grey. The myosin lever arm is displayed in light blue, and the cargo-binding domain in purple. Kinesin and dynein associated subunits are depicted in green. Adapted from Vale 2003 and Carter 2013.

contrast, kinesin-13 proteins, which can be recognized by an internal motor domain, do not walk along the MT lattice but have the ability to depolymerize MTs [70].

**Motor functions**

Motor properties in turn determine motor functions, of which three broad categories can be distinguished; cargo transport, filament sliding, and the regulation of filament (de)polymerization. Motors can accomplish cargo transport by binding their tail domain to specific cargo or cargo adaptor molecules (Figure 3A).

Filament sliding can occur when motors form tetrameric molecules, allowing the two motor pairs at opposite ends of the tetramer to simultaneously walk along a MT [102]. Alternatively, the motor tail can be cross-linked to a second MT or an immobile membrane structure to drive MT sliding [103,104]. At last, each motor domain of a motor dimer can bind a different MT and thereby drive MT sliding, as was shown for dynein-induced MT sliding [99] (Figure 3B). MT sliding plays an important role in mitotic spindle formation [105] and perhaps also during neurite outgrowth [106].

A third function accomplished by motor proteins is the regulation of MT polymerization and depolymerization. The most well known MT depolymerizing motors are the kinesin-13 family members, including MCAK. MCAK is targeted by EB3 to the growing MT plus-end where it promotes catastrophes. The combination of MCAK and EB3 at the MT plus-end promotes rapid switching between MT growth and shortening, which is

important during MT cytoskeleton remodeling [107]. Kinesin-8s, despite having their motor domain at the N-terminus and walking processively towards to MT plus-end, are also potent MT depolymerizers. The exact depolymerization mechanism is not clear but could include protofilament bending similar to kinesin-8s, inhibition of tubulin incorporation at the plus-end, or pushing off the last motor together with the tubulin dimer when new motors arrive at the plus-end [101] (Figure 3C). At last, kinesin-4 KIF21A has been shown to restrict microtubule growth at the cell edge, thereby promoting MT capture at specified patches at the cell cortex [108]. Microtubule dynamics can thus be modulated by motor proteins and is amongst other things important for mitotic spindle formation [105] and axon pruning [109]. So, a plethora of specialized motor proteins can modify the cytoskeleton in several ways, and control the transport and direction of a diverse set of cargoes to maintain cell compartmentalization and polarity.

**Interplay between motors**

Motor proteins run unidirectionally along cytoskeletal tracks and therefore cargo transport has to be coordinated carefully to prevent excessive accumulation at sites where either the plus- or minus-ends of cytoskeletal tracks terminate. It is therefore not surprising that individual cargoes are attached to multiple motors of various classes. The interplay between these motors determines cargo speed, pausing and reversal. In addition, cargoes often travel along both MTs and actin filaments and need to switch tracks to reach their final destination. Therefore, the final cargo distribution depends on the overall MT and actin organization as well as the interplay between the motors attached [110-113].

Whereas both kinesin and myosin motors can walk along filaments, kinesin motors are known to drive fast and long-range transport while the slower myosin motors have been proposed to function predominantly in short-range transport as well as cargo tethering [114-116]. How the integrated activity of kinesin and myosin motors affects cargo motility is unknown. In addition, how myosins and the specialized actin structure at the AIS affect the motility of anterograde moving cargoes remains controversial.

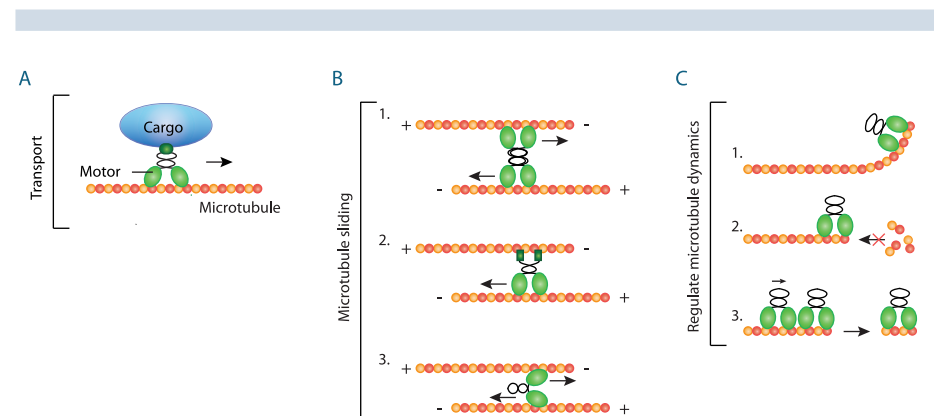


**Figure 3 | Motor functions.**

**(A)** Motors can carry cargo while moving along the microtubule. **(B)** Motors can slide antiparallel microtubules through; (1) forming tetrameric motors that can simultaneously walk on two different microtubules (2) cross-linking the motor tail on a second microtubule, or (3) binding each motor head to a different microtubule. Adapted from Walczak 2013 and Tanenbaum 2013. **(C)** Motors can modulate microtubule polymerization and depolymerization through; (1) bending protofilaments (2) inhibiting tubulin incorporation at the microtubule plus-end, or (3) pushing off the last motor together with the outermost tubulin dimer.

**Light-based strategies for cellular manipulations**

A deeper insight into the role of specific proteins, signaling pathways or other biological processes, is usually obtained by comparing wild type with knock in, knockout or knockdown samples. Alternatively, drugs can be used to inhibit proteins and to induce molecular perturbations. However, these conventional approaches are inevitably linked to significant side effects because they affect the complete cell at all times after

treatment (See chapter 2 for more details). Therefore, the discovery and development of light-controllable proteins some 10 years ago, marked the beginning of a new era in which laser light could be used to control numerous proteins with spatiotemporal precision [117,118].

The technique in which cellular processes can be optically controlled in cells that have been genetically modified to express light-sensitive proteins is referred to as optogenetics. Although optogenetics has initially been used to open Channel-rhodopsin-2 to depolarize neurons and evoke action potentials in cultured neurons [119-121], a myriad of light sensitive proteins is now available to control a broad-spectrum of processes. For example, light-induced protein activation [122], dimerization [123-129], dissociation [128,130], clustering [131,132], inactivation [133] and degradation [134] have been developed to control processes such as protein secretion [135], phosphoinositide metabolism [136], actin polymerization [122,137], synaptic vesicle release [138], signaling activity [117], DNA mutagenesis [139] and endogenous transcription and epigenetic states [140].

One of the most versatile light-sensitive units to build new optogenetic tools are the optically controlled protein heterodimerization systems [123-125]. Using these systems, proteins of interest can be recruited to defined locations within living cells by fusing specified proteins to the light-inducible interaction modules. Currently available heterodimerization systems are based on light-sensitive protein interactions occurring in plants that mediate processes such as flowering, shade avoidance and seed germination. For example, the light-sensitive interaction between Cryptochrome-2 (CRY2) and CIB1 [123], Phytochrome B (PHY) and PIF3/6 [125], and the LOV2 domain of

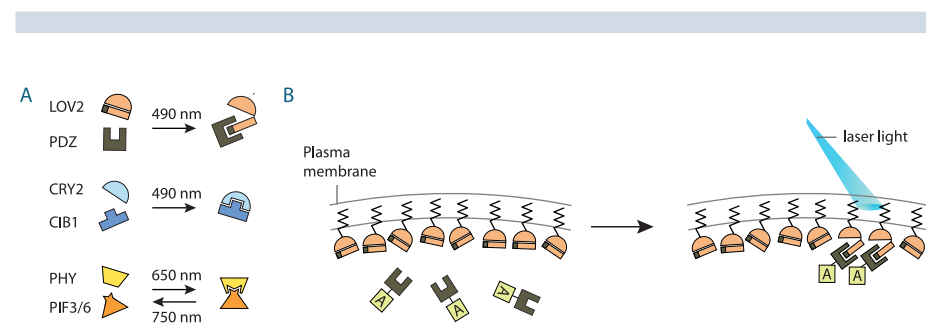


**Figure 4 | Light-induced protein heterodimerization and translocation.**

(A) The three most used light-induced protein heterodimerization systems are shown. LOV2/PDZ and CRY2/CIB1 interactions can be induced by 490 nm light whereas the interaction between PHY/PIF3/6 can be initiated by 650 nm light and reversed by 750 nm light. (B) Light-inducible heterodimerization systems can be used to enrich freely diffuse proteins of interest (protein A) with spatiotemporal precision to defined structures inside the cell.

Phototropin 1 with and engineered PDZ domain [124] are most extensively used (Figure 4A). Each system possesses different on/off kinetics, light sensitivity, co-factor requirements and activation wavelengths, and can be used to manipulate defined processes with varying dynamics (See chapter 2 for more details). Thus, a light-inducible heterodimerization toolbox is now available to recruit many different cytosolic proteins to well-defined locations in the cell (Figure 4B) in order to spatiotemporally control cellular events. In contrast, organelles cannot be relocated using the same strategy because of much lower diffusion rates. It therefore remains largely unknown how the spatial arrangement of organelles affects cellular processes.

### Scope of this thesis

Molecular motors ensure the proper spatial and temporal arrangement of cargoes and organelles. **Chapter 2** discusses how organelle positioning is important for cell survival and functioning and why currently available tools to interfere with endogenous organelle localizations are not sufficient to resolve the precise connection between position and function.

In order to develop a tool that can manipulate cargo localization with spatiotemporal precision, it is essential to understand how the integrated activity of different motor types affects cargo transport and positioning. In fact, a single cargo often travels along both microtubule and actin filaments, but how microtubule and actin-based motors contribute to the final motility and distribution of these cargoes is largely unknown. In **Chapter 3** we show that on cargoes that contain both motor types, Myosin-V is able to stall fast kinesin-driven organelle movements and can drive slow short-range transport towards the plasma membrane. **Chapter 4** describes how Myosin-V stalls, but not reverses, kinesin-driven transport at the AIS to prevent cargo transport into the axon.

The acquired insights on cargo positioning by molecular motors are deployed in **Chapter 5**, where molecular motors are hijacked to control the localization of organelles with spatiotemporal precision using blue light. Using our developed tool, we show that basal cellular processes are dependent on, and can be manipulated by changing organelle localization. To facilitate organelle-positioning studies within individual cells of a multicellular organism, we extended the developed light-induced transport assay to the *in vivo* model *C. elegans*, as described in **Chapter 6**.

A plethora of specialized molecular motors can modify the cytoskeleton and direct transport to maintain cell compartmentalization and polarity. However, it has remained unknown which motor proteins play a role in neuronal axon formation. In **Chapter 7** we find that microtubule-depolymerizing kinesins are involved in axon formation. To allow the direct assessment of the effect of microtubule shrinkage on

axon outgrowth, we developed a tool to induce microtubule depolymerization in living cells. We conclude with an overall summary of the results described in this thesis and discuss remaining questions and future research directions in **Chapter 8**.

## References

1. Vale, R.D. (2003) The molecular motor toolbox for intracellular transport. *Cell* **112**, 467–480
2. Sheng, Z.-H. and Cai, Q. (2012) Mitochondrial transport in neurons: impact on synaptic homeostasis and neurodegeneration. *Nat Rev Neurosci* **13**, 77–93
3. Korolchuk, V.I. et al. (2011) Lysosomal positioning coordinates cellular nutrient responses. *Nat. Cell Biol.* **13**, 453–460
4. Yadav, S. and Linstedt, A.D. (2011) Golgi positioning. *Cold Spring Harb Perspect Biol* **3**,
5. Sadowski, L. et al. (2009) Signaling from endosomes: location makes a difference. *Exp. Cell Res.* **315**, 1601–1609
6. Ori-McKenney, K.M. et al. (2012) Golgi outposts shape dendrite morphology by functioning as sites of acentrosomal microtubule nucleation in neurons. *Neuron* **76**, 921–930
7. Spillane, M. et al. (2013) Mitochondria coordinate sites of axon branching through localized intra-axonal protein synthesis. *Cell Rep* **5**, 1564–1575
8. Courchet, J. et al. (2013) Terminal axon branching is regulated by the LKB1-NUAK1 kinase pathway via presynaptic mitochondrial capture. *Cell* **153**, 1510–1525
9. Luxton, G.W.G. and Gundersen, G.G. (2011) Orientation and function of the nuclear-centrosomal axis during cell migration. *Current Opinion in Cell Biology* **23**, 579–588
10. Wang, Z. et al. (2008) Myosin Vb mobilizes recycling endosomes and AMPA receptors for postsynaptic plasticity. *Cell* **135**, 535–548
11. Dotti, C.G. et al. (1988) The establishment of polarity by hippocampal neurons in culture. *J. Neurosci.* **8**, 1454–1468
12. Barnes, A.P. and Polleux, F. (2009) Establishment of axon-dendrite polarity in developing neurons. *Annual review of neuroscience* **32**, 347–381
13. Bradke, F. and Dotti, C.G. (2000) Establishment of neuronal polarity: lessons from cultured hippocampal neurons. *Curr. Opin. Neurobiol.* **10**, 574–581
14. Jessell, T.M. and Kandel, E.R. (1993) Synaptic transmission: a bidirectional and self-modifiable form of cell-cell communication, 72
15. Winckler, B. et al. (1999) A diffusion barrier maintains distribution of membrane proteins in polarized neurons. *Nature* **397**, 698–701
16. Song, A.-H. et al. (2009) A selective filter for cytoplasmic transport at the axon initial segment. *Cell* **136**, 1148–1160
17. Li, X. et al. (2011) Novel diffusion barrier for axonal retention of Tau in neurons and its failure in neurodegeneration. *The EMBO Journal* **30**, 4825–4837
18. Al-Bassam, S. et al. (2012) Differential trafficking of transport vesicles contributes to the localization of dendritic proteins. *Cell Rep* **2**, 89–100
19. Rasband, M.N. (2010) The axon initial segment and the maintenance of neuronal polarity. *Nat Rev Neurosci* **11**, 552–562
20. Galiano, M.R. et al. (2012) A distal axonal cytoskeleton forms an intra-axonal boundary that controls axon initial segment assembly. *Cell* **149**, 1125–1139
21. Hedstrom, K.L. et al. (2008) AnkyrinG is required for maintenance of the axon initial segment and neuronal polarity. *J. Cell Biol.* **183**, 635–640
22. Hedstrom, K.L. et al. (2007) Neurofascin assembles a specialized extracellular matrix at the axon initial segment. *J. Cell Biol.* **178**, 875–886
23. Srinivasan, Y. et al. (1988) Ankyrin and spectrin associate with voltage-dependent sodium channels in brain. *Nature* **333**, 177–180
24. Zhou, D. et al. (1998) AnkyrinG is required for clustering of voltage-gated Na channels at axon initial segments and for normal action potential firing. *J. Cell Biol.* **143**, 1295–1304

25. Garrido, J.J. et al. (2003) A targeting motif involved in sodium channel clustering at the axonal initial segment. *Science* **300**, 2091–2094
26. Berghs, S. et al. (2000) betaIV spectrin, a new spectrin localized at axon initial segments and nodes of ranvier in the central and peripheral nervous system. *J. Cell Biol.* **151**, 985–1002
27. Jenkins, S.M. and Bennett, V. (2001) Ankyrin-G coordinates assembly of the spectrin-based membrane skeleton, voltage-gated sodium channels, and L1 CAMs at Purkinje neuron initial segments. *J. Cell Biol.* **155**, 739–746
28. Clark, B.D. et al. (2009) Electrogenic tuning of the axon initial segment. *Neuroscientist* **15**, 651–668
29. Fletcher, D.A. and Mullins, R.D. (2010) Cell mechanics and the cytoskeleton. *Nature* **463**, 485–492
30. Akhmanova, A. and Steinmetz, M.O. (2008) Tracking the ends: a dynamic protein network controls the fate of microtubule tips. *Nat. Rev. Mol. Cell Biol.* **9**, 309–322
31. Janke, C. and Bulinski, J.C. (2011) Post-translational regulation of the microtubule cytoskeleton: mechanisms and functions. *Nat. Rev. Mol. Cell Biol.* **12**, 773–786
32. Subramanian, R. and Kapoor, T.M. (2012) Building complexity: insights into self-organized assembly of microtubule-based architectures. *Dev. Cell* **23**, 874–885
33. Sirajuddin, M. et al. (2014) Regulation of microtubule motors by tubulin isotypes and post-translational modifications. *Nat. Cell Biol.* **16**, 335–344
34. Janke, C. (2014) The tubulin code: molecular components, readout mechanisms, and functions. *J. Cell Biol.* **206**, 461–472
35. Song, Y. and Brady, S.T. (2015) Post-translational modifications of tubulin: pathways to functional diversity of microtubules. *Trends Cell Biol.* **25**, 125–136
36. Petry, S. and Vale, R.D. (2015) Microtubule nucleation at the centrosome and beyond. *Nat. Cell Biol.* **17**, 1089–1093
37. Oakley, B.R. et al. (2015)  $\gamma$ -Tubulin complexes in microtubule nucleation and beyond. *Mol. Biol. Cell* **26**, 2957–2962
38. Morgan, J.T. et al. (2011) Nesprin-3 regulates endothelial cell morphology, perinuclear cytoskeletal architecture, and flow-induced polarization. *Mol. Biol. Cell* **22**, 4324–4334
39. Schneider, M. et al. (2011) Molecular mechanisms of centrosome and cytoskeleton anchorage at the nuclear envelope. *Cell. Mol. Life Sci.* **68**, 1593–1610
40. Baas, P.W. et al. (1988) Polarity orientation of microtubules in hippocampal neurons: uniformity in the axon and nonuniformity in the dendrite. *Proc. Natl. Acad. Sci. U.S.A.* **85**, 8335–8339
41. Stepanova, T. et al. (2003) Visualization of microtubule growth in cultured neurons via the use of EB3-GFP (end-binding protein 3-green fluorescent protein). *J. Neurosci.* **23**, 2655–2664
42. Burton, P.R. (1988) Dendrites of mitral cell neurons contain microtubules of opposite polarity. *Brain Res.* **473**, 107–115
43. Yau, K.W. et al. (2016) dendrites in vitro and in vivo contain microtubules of opposite polarity and axon formation correlates with uniform plus-end-out microtubule orientation. *Journal of Neuroscience* **36**, 1071–1085
44. Maniar, T.A. et al. (2012) UNC-33 (CRMP) and ankyrin organize microtubules and localize kinesin to polarize axon-dendrite sorting. *Nat. Neurosci.* **15**, 48–56
45. Hill, S.E. et al. (2012) Development of dendrite polarity in Drosophila neurons. *Neural Dev* **7**, 34
46. Kapitein, L.C. et al. (2010) Mixed microtubules steer dynein-driven cargo transport into dendrites. *Curr. Biol.* **20**, 290–299
47. Schnapp, B.J. and Reese, T.S. (1989) Dynein is the motor for retrograde axonal transport of organelles. *Proc. Natl. Acad. Sci. U.S.A.* **86**, 1548–1552
48. Hammond, J.W. et al. (2010) Posttranslational modifications of tubulin and the polarized transport of kinesin-1 in neurons. *Mol. Biol. Cell* **21**, 572–583
49. Kosik, K.S. and Finch, E.A. (1987) MAP2 and tau segregate into dendritic and axonal domains after the elaboration of morphologically distinct neurites: an immunocytochemical study of cultured rat cerebrum. *J. Neurosci.* **7**, 3142–3153
50. Black, M.M. et al. (1994) Microtubule-associated protein 1b (MAP1b) is concentrated in the distal region of growing axons. *J. Neurosci.* **14**, 857–870
51. Reed, N.A. et al. (2006) Microtubule acetylation promotes kinesin-1 binding and transport. *Current Biology* **16**, 2166–2172
52. Jacobson, C. et al. (2006) A change in the selective translocation of the Kinesin-1 motor domain marks the initial specification of the axon. *Neuron* **49**, 797–804
53. van Beuningen, S.F.B. et al. (2015) TRIM46 Controls Neuronal Polarity and Axon Specification by Driving the Formation of Parallel Microtubule Arrays. *Neuron* **88**, 1208–1226
54. Merriam, E.B. et al. (2013) Synaptic regulation of microtubule dynamics in dendritic spines by calcium, F-actin, and drebrin. *J. Neurosci.* **33**, 16471–16482
55. Jaworski, J. et al. (2009) Dynamic microtubules regulate dendritic spine morphology and synaptic plasticity. *Neuron* **61**, 85–100
56. Hu, X. et al. (2008) Activity-dependent dynamic microtubule invasion of dendritic spines. *J. Neurosci.* **28**, 13094–13105
57. Lowery, L.A. and Vactor, D.V. (2009) The trip of the tip: understanding the growth cone machinery. *Nat. Rev. Mol. Cell Biol.* **10**, 332–343
58. Blanchoin, L. et al. (2014) Actin dynamics, architecture, and mechanics in cell motility. *Physiol. Rev.* **94**, 235–263
59. Pollard, T.D. and Cooper, J.A. (2009) Actin, a central player in cell shape and movement. *Science* **326**, 1208–1212
60. Terman, J.R. and Kashina, A. (2013) Post-translational modification and regulation of actin. *Current Opinion in Cell Biology* **25**, 30–38
61. Gunning, P.W. et al. (2005) Tropomyosin isoforms: divining rods for actin cytoskeleton function. *Trends Cell Biol.* **15**, 333–341
62. Hodges, A.R. et al. (2012) Tropomyosin is essential for processive movement of a class V myosin from budding yeast. *Curr. Biol.* **22**, 1410–1416
63. Gunning, P.W. et al. (2015) Tropomyosin - master regulator of actin filament function in the cytoskeleton. *J. Cell. Sci.* **128**, 2965–2974
64. Hotulainen, P. and Hoogenraad, C.C. (2010) Actin in dendritic spines: connecting dynamics to function. *J. Cell Biol.* **189**, 619–629
65. Korobova, F. and Svitkina, T. (2010) Molecular architecture of synaptic actin cytoskeleton in hippocampal neurons reveals a mechanism of dendritic spine morphogenesis. *Mol. Biol. Cell* **21**, 165–176
66. Xu, K. et al. (2013) Actin, spectrin, and associated proteins form a periodic cytoskeletal structure in axons. *Science* **339**, 452–456
67. Ganguly, A. et al. (2015) A dynamic formin-dependent deep F-actin network in axons. *J. Cell Biol.* **210**, 401–417
68. Watanabe, K. et al. (2012) Networks of polarized actin filaments in the axon initial segment provide a mechanism for sorting axonal and dendritic proteins. *Cell Rep* **2**, 1546–1553
69. Jones, S.L. et al. (2014) Axon initial segment cytoskeleton comprises a multiprotein submembranous coat containing sparse actin filaments. *J. Cell Biol.* **205**, 67–81

70. Hirokawa, N. et al. (2009) Kinesin superfamily motor proteins and intracellular transport. *Nat. Rev. Mol. Cell Biol.* **10**, 682–696
71. Schroer, T.A. et al. (1989) Cytoplasmic dynein is a minus end-directed motor for membranous organelles. *Cell* **56**, 937–946
72. Hartman, M.A. and Spudich, J.A. (2012) The myosin superfamily at a glance. *J. Cell. Sci.* **125**, 1627–1632
73. Hirokawa, N. et al. (2010) Molecular motors in neurons: transport mechanisms and roles in brain function, development, and disease. *Neuron* **68**, 610–638
74. Miki, H. et al. (2001) All kinesin superfamily protein, KIF, genes in mouse and human. *Proc. Natl. Acad. Sci. U.S.A.* **98**, 7004–7011
75. Berg, J.S. et al. (2001) A millennial myosin census. *Mol. Biol. Cell* **12**, 780–794
76. Asbury, C.L. et al. (2003) Kinesin moves by an asymmetric hand-over-hand mechanism. *Science* **302**, 2130–2134
77. Yildiz, A. et al. (2004) Kinesin walks hand-over-hand. *Science* **303**, 676–678
78. Purcell, T.J. et al. (2002) Role of the lever arm in the processive stepping of myosin V. *Proc. Natl. Acad. Sci. U.S.A.* **99**, 14159–14164
79. Sakamoto, T. et al. (2005) Step-size is determined by neck length in myosin V. *Biochemistry* **44**, 16203–16210
80. Köhler, D. et al. (2003) Different degrees of lever arm rotation control myosin step size. *J. Cell Biol.* **161**, 237–241
81. Kneussel, M. and Wagner, W. (2013) Myosin motors at neuronal synapses: drivers of membrane transport and actin dynamics. *Nat Rev Neurosci* **14**, 233–247
82. Asai, D.J. and Koonce, M.P. (2001) The dynein heavy chain: structure, mechanics and evolution. *Trends Cell Biol.* **11**, 196–202
83. Mallik, R. et al. (2004) Cytoplasmic dynein functions as a gear in response to load. *Nature* **427**, 649–652
84. Reck-Peterson, S.L. et al. (2006) Single-molecule analysis of dynein processivity and stepping behavior. *Cell* **126**, 335–348
85. Schlager, M.A. et al. (2014) In vitro reconstitution of a highly processive recombinant human dynein complex. *The EMBO Journal* **33**, 1855–1868
86. McKenney, R.J. et al. (2014) Activation of cytoplasmic dynein motility by dynactin-cargo adapter complexes. *Science* **345**, 337–341
87. Verhey, K.J. and Hammond, J.W. (2009) Traffic control: regulation of kinesin motors. *Nat. Rev. Mol. Cell Biol.* **10**, 765–777
88. Liu, J. et al. (2006) Three-dimensional structure of the myosin V inhibited state by cryoelectron tomography. *Nature* **442**, 208–211
89. Thirumurugan, K. et al. (2006) The cargo-binding domain regulates structure and activity of myosin 5. *Nature* **442**, 212–215
90. Torisawa, T. et al. (2014) Autoinhibition and cooperative activation mechanisms of cytoplasmic dynein. *Nat. Cell Biol.* **16**, 1118–1124
91. Woehlke, G. and Schliwa, M. (2000) Walking on two heads: the many talents of kinesin. *Nat. Rev. Mol. Cell Biol.* **1**, 50–58
92. Derr, N.D. et al. (2012) Tug-of-war in motor protein ensembles revealed with a programmable DNA origami scaffold. *Science* **338**, 662–665
93. Jannasch, A. et al. (2013) Kinesin-8 is a low-force motor protein with a weakly bound slip state. *Biophys. J.* **104**, 2456–2464
94. Cai, D. et al. (2009) Single molecule imaging reveals differences in microtubule track selection between Kinesin motors. *PLoS Biol.* **7**, e1000216
95. Hammond, J.W. et al. (2008) Tubulin modifications and their cellular functions. *Current Opinion in Cell Biology* **20**, 71–76
96. Ikegami, K. et al. (2007) Loss of alpha-tubulin polyglutamylation in ROSA22 mice is associated with abnormal targeting of KIF1A and modulated synaptic function. *Proc. Natl. Acad. Sci. U.S.A.* **104**, 3213–3218
97. Burnette, D.T. et al. (2011) A role for actin arcs in the leading-edge advance of migrating cells. *Nat. Cell Biol.* **13**, 371–381
98. Medeiros, N.A. et al. (2006) Myosin II functions in actin-bundle turnover in neuronal growth cones. *Nat. Cell Biol.* **8**, 215–226
99. Tanenbaum, M.E. et al. (2013) Cytoplasmic dynein crosslinks and slides anti-parallel microtubules using its two motor domains. *Elife* **2**, e00943
100. Lu, W. et al. (2015) Kinesin-1-powered microtubule sliding initiates axonal regeneration in Drosophila cultured neurons. *Mol. Biol. Cell* **26**, 1296–1307
101. Walczak, C.E. et al. (2013) Microtubule-depolymerizing kinesins. *Annu. Rev. Cell Dev. Biol.* **29**, 417–441
102. Kapitein, L.C. et al. (2005) The bipolar mitotic kinesin Eg5 moves on both microtubules that it crosslinks. *Nature* **435**, 114–118
103. Jolly, A.L. et al. (2010) Kinesin-1 heavy chain mediates microtubule sliding to drive changes in cell shape. *Proc. Natl. Acad. Sci. U.S.A.* **107**, 12151–12156
104. van Heesbeen, R.G.H.P. et al. (2013) Nuclear envelope-associated dynein cooperates with Eg5 to drive prophase centrosome separation. *Commun Integr Biol* **6**, e23841
105. Sharp, D.J. et al. (2000) Microtubule motors in mitosis. *Nature* **407**, 41–47
106. Lu, W. et al. (2013) Initial neurite outgrowth in Drosophila neurons is driven by kinesin-powered microtubule sliding. *Curr. Biol.* **23**, 1018–1023
107. Montenegro Gouveia, S. et al. (2010) In vitro reconstitution of the functional interplay between MCAK and EB3 at microtubule plus ends. *Curr. Biol.* **20**, 1717–1722
108. van der Vaart, B. et al. (2013) CFEOM1-associated kinesin KIF21A is a cortical microtubule growth inhibitor. *Dev. Cell* **27**, 145–160
109. Maor-Nof, M. et al. (2013) Axonal pruning is actively regulated by the microtubule-destabilizing protein kinesin superfamily protein 2A. *Cell Rep* **3**, 971–977
110. Barlan, K. et al. (2013) The journey of the organelle: teamwork and regulation in intracellular transport. *Current Opinion in Cell Biology* **25**, 483–488
111. Soppina, V. et al. (2009) Tug-of-war between dissimilar teams of microtubule motors regulates transport and fission of endosomes. *Proc. Natl. Acad. Sci. U.S.A.* **106**, 19381–19386
112. Fu, M.-M. and Holzbaur, E.L.F. (2014) Integrated regulation of motor-driven organelle transport by scaffolding proteins. *Trends Cell Biol.* **24**, 564–574
113. Schroeder, H.W. et al. (2012) Force-dependent detachment of kinesin-2 biases track switching at cytoskeletal filament intersections. *Biophys. J.* **103**, 48–58
114. Woolner, S. and Bement, W.M. (2009) Unconventional myosins acting unconventionally. *Trends Cell Biol.* **19**, 245–252
115. Provance, D.W. et al. (2008) Myosin-Vb functions as a dynamic tether for peripheral endocytic compartments during transferrin trafficking. *BMC Cell Biology* **9**, 44
116. Wu, X. et al. (1998) Visualization of melanosome dynamics within wild-type and dilute melanocytes suggests a paradigm for myosin V function In vivo. *J. Cell Biol.* **143**, 1899–1918
117. Tischer, D. and Weiner, O.D. (2014) Illuminating cell signalling with optogenetic tools. *Nat. Rev. Mol. Cell Biol.* **15**, 551–558

118. Weitzman, M. and Hahn, K.M. (2014) Optogenetic approaches to cell migration and beyond. *Current Opinion in Cell Biology* **30**, 112–120
119. Zemelman, B.V. et al. (2002) Selective photostimulation of genetically chARGed neurons. *Neuron* **33**, 15–22
120. Boyden, E.S. et al. (2005) Millisecond-timescale, genetically targeted optical control of neural activity. *Nat. Neurosci.* **8**, 1263–1268
121. Fenno, L. et al. (2011) The development and application of optogenetics. *Annual review of neuroscience* **34**, 389–412
122. Wu, Y.I. et al. (2009) A genetically encoded photoactivatable Rac controls the motility of living cells. *Nature* **461**, 104–108
123. Kennedy, M.J. et al. (2010) Rapid blue-light-mediated induction of protein interactions in living cells. *Nat. Methods* **7**, 973–975
124. Strickland, D. et al. (2012) TULIPs: tunable, light-controlled interacting protein tags for cell biology. *Nat. Methods* **9**, 379–384
125. Levsikaya, A. et al. (2009) Spatiotemporal control of cell signalling using a light-switchable protein interaction. *Nature* **461**, 997–1001
126. Zoltowski, B.D. and Crane, B.R. (2008) Light activation of the LOV protein vivid generates a rapidly exchanging dimer. *Biochemistry* **47**, 7012–7019
127. Nihongaki, Y. et al. (2014) Genetically engineered photoinducible homodimerization system with improved dimer-forming efficiency. *ACS Chem. Biol.* **9**, 617–621
128. Zhou, X.X. et al. (2012) Optical control of protein activity by fluorescent protein domains. *Science* **338**, 810–814
129. Crefcoeur, R.P. et al. (2013) Ultraviolet-B-mediated induction of protein-protein interactions in mammalian cells. *Nat Commun* **4**, 1779
130. Conrad, K.S. et al. (2013) Light-induced subunit dissociation by a light-oxygen-voltage domain photoreceptor from *Rhodobacter sphaeroides*. *Biochemistry* **52**, 378–391
131. Bugaj, L.J. et al. (2013) Optogenetic protein clustering and signaling activation in mammalian cells. *Nat. Methods* **10**, 249–252
132. Taslimi, A. et al. (2014) An optimized optogenetic clustering tool for probing protein interaction and function. *Nat Commun* **5**, 4925
133. Lee, S. et al. (2014) Reversible protein inactivation by optogenetic trapping in cells. *Nat. Methods* **11**, 633–636
134. Renicke, C. et al. (2013) A LOV2 domain-based optogenetic tool to control protein degradation and cellular function. *Chem. Biol.* **20**, 619–626
135. Chen, D. et al. (2013) A light-triggered protein secretion system. *J. Cell Biol.* **201**, 631–640
136. Idevall-Hagren, O. et al. (2012) Optogenetic control of phosphoinositide metabolism. *Proc. Natl. Acad. Sci. U.S.A.* **109**, E2316–23
137. Leung, D.W. et al. (2008) Genetically encoded photoswitching of actin assembly through the Cdc42-WASP-Arp2/3 complex pathway. *Proc. Natl. Acad. Sci. U.S.A.* **105**, 12797–12802
138. Lin, J.Y. et al. (2013) Optogenetic inhibition of synaptic release with chromophore-assisted light inactivation (CALI). *Neuron* **79**, 241–253
139. Noma, K. and Jin, Y. (2015) Optogenetic mutagenesis in *Caenorhabditis elegans*. *Nat Commun* **6**, 8868
140. Konermann, S. et al. (2013) Optical control of mammalian endogenous transcription and epigenetic states. *Nature* **500**, 472–476





# Right time, right place: Probing the functions of organelle positioning

# 2

Petra van Bergeijk<sup>1</sup>, Casper C. Hoogenraad<sup>1</sup> &  
Lukas C. Kapitein<sup>1</sup>

*Trends in Cell Biology* (2016); **26 (2)**, pp. 121–134

---

<sup>1</sup> Division of Cell Biology, Faculty of Science, Utrecht University, Utrecht, The Netherlands.

## Abstract

The proper spatial arrangement of organelles underlies many cellular processes including signaling, polarization, and growth. Despite the importance of local positioning, the precise connection between subcellular localization and organelle function is often not fully understood. To address this, recent studies have developed and employed different strategies to directly manipulate organelle distributions, such as the use of (light-sensitive) heterodimerization to control the interaction between selected organelles and specific motor proteins, adaptor molecules, or anchoring factors. We review here the importance of subcellular localization as well as tools to control local organelle positioning. Because these approaches allow spatiotemporal control of organelle distribution, they will be invaluable tools to unravel local functioning and the mechanisms that control positioning.

## Review

### Organelle positioning often correlates with function

Organelles are confined compartments within cells and carry a specialized set of molecules to perform specific functions. Distinct organelle positioning and spatially defined activities of organelles occur in many cell types but they are especially apparent in cells that are either polarized, spatially extended, or both, such as epithelial cells, muscle syncytium, or neurons (Figure 1). For example, the nucleus is typically centrally located with the centrosome and Golgi apparatus in close proximity, whereas the endoplasmic reticulum (ER) often spreads throughout the cytoplasm. Elements of the secretory and endosomal systems are more dynamically located because they shuttle between the Golgi apparatus, the plasma membrane (PM), and lysosomes. In recent years evidence has accumulated that cells exploit the subcellular distribution of organelles to locally orchestrate cellular processes including signaling, polarization, and outgrowth. These developments have sparked an interest in exploring non-canonical functions of organelles that depend on proper spatial arrangement.

Local organelle positioning is often a two-step process that involves active transport followed by immobilization. Active transport is driven by cytoskeletal motor proteins that can move directionally along either of two types of cytoskeletal biopolymers: actin filaments or microtubules [1]. Actin facilitates the motility of motor proteins of the myosin superfamily, whereas microtubules serve as tracks for two families of motor proteins, kinesin and dynein, which move towards the microtubule plus-end or minus-end, respectively. Most cytoskeletal motor proteins associate with cargoes through their tail domain, often mediated by specific adaptor molecules that regulate particular motor-cargo interactions [2,3]. These interactions determine cargo loading as well as off-loading in space and time, and, together with the activity of controlled anchoring factors [4], define cargo distribution. Interestingly, motor proteins can also operate as anchoring factors. For example, dynein positions the Golgi apparatus [5], whereas several myosin motors can oppose microtubule-based transport and anchor cargoes [6–8].

Given the important roles of cytoskeletal and motor proteins, many conventional techniques have been aimed at manipulating the activity of these proteins to better understand the roles of organelle position. However, recent technical advances, such as optogenetics, are beginning to provide newer and more accurate ways to manipulate organelle positioning. We review here the importance of organelle localization and highlight several exciting strategies to manipulate organelle positioning that have recently emerged. We briefly discuss existing evidence for the importance of positioning

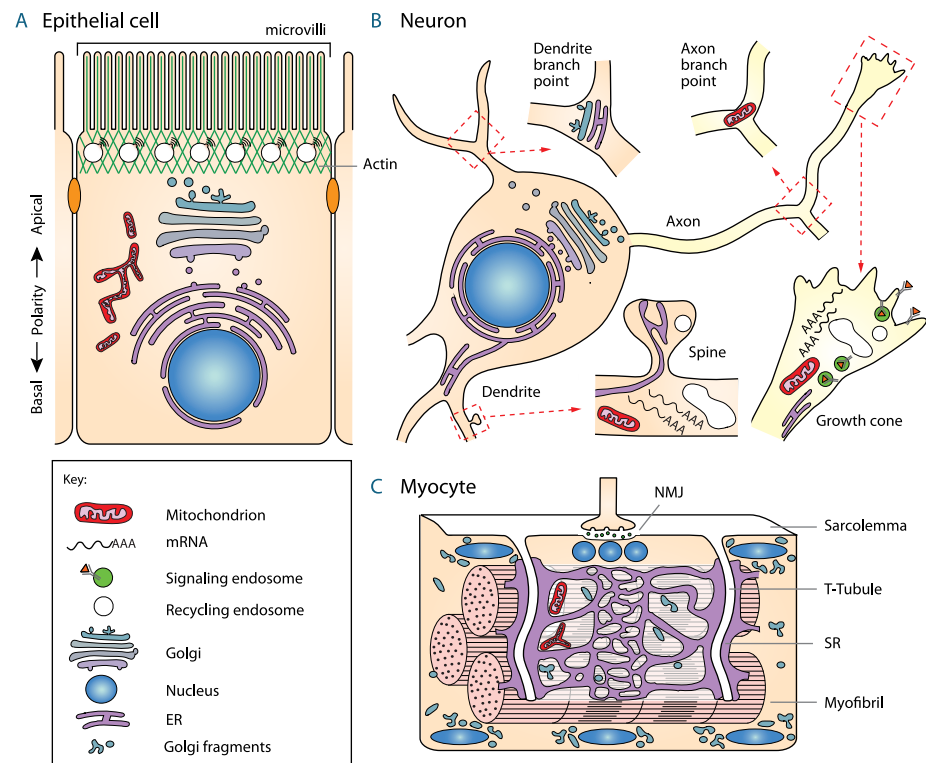


**Figure 1 | Functional subcellular organelle positioning in different cell types.**

**(A)** In epithelial cells the nucleus is located more basally, with the endoplasmic reticulum (ER) and Golgi oriented towards the apical side. In epithelial cells with microvilli, recycling endosomes and their associated kinases are positioned underneath the apical membrane to induce actin polymerization and microvilli formation. The green lines are actin. **(B)** In neurons, the ER can be found in the cell body, near axonal growth cones, in the dendritic shaft, and in dendritic spines. The Golgi resides in the cell body but is oriented towards the biggest dendrite or the emerging axon in developing neurons. Mitochondria localize near dendritic spines, axonal branch points, and growth cones, where they are believed to satisfy local energy demand. mRNA is locally translated in axonal growth cones and dendritic spines to allow LTP induction and growth-cone turning upon encountering extracellular cues. A pool of recycling endosomes is stored at the growth-cone tip and at the base of dendritic spines to allow rapid delivery of membranes and receptors to the surface when needed. In the opposite direction, signaling endosomes travel from the growth cone towards the cell body upon ligand-induced receptor internalization. **(C)** Myocytes have a specific organelle distribution, with the sarcoplasmic reticulum (SR) being aligned between the t-tubule and mitochondria to control calcium homeostasis during muscle excitation and contraction. The typical Golgi ribbon is dispersed into smaller Golgi stacks that concentrate around the nuclei that are evenly spaced along the muscle fiber. In addition, a few nuclei are anchored underneath the neuromuscular junction (NMJ), presumably to aid the local translation of specialized mRNAs.

of larger organelles such as the nucleus, ER, and Golgi apparatus, followed by a more extensive discussion about the distribution of dynamic organelles such as mRNA granules, mitochondria, endosomes and lysosomes, and inter-organelle contact sites.

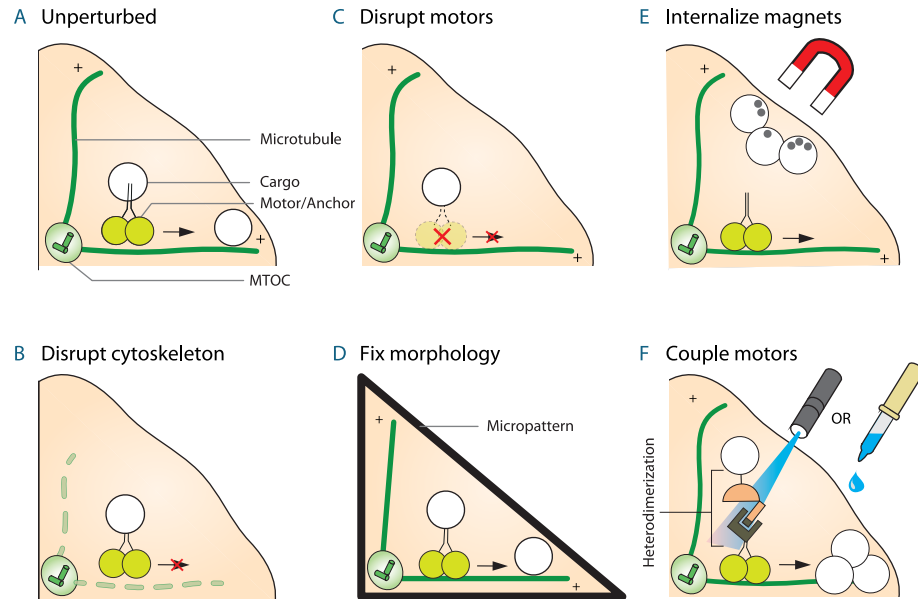
## Conventional methods to interfere with organelle positioning

Because the cytoskeletal network is crucial for proper cellular organization (Figure 2A), disrupting the microtubule network using microtubule-targeting agents has been frequently used to alter organelle positioning [9,10] (Figure 2B). For example, destabilizing microtubules using nocodazole results in the dispersion of lysosomes and the Golgi apparatus [11,12]. Although affecting cytoskeletal build-up or break-down is an effective method to alter cellular organization, manipulating tubulin post-translational modifications (PTMs) [13] or structures might be more subtle. PTMs are believed to affect microtubule stability and motor protein preferences. For example, treatment with the  $\alpha$ -Tubulin-specific deacetylase inhibitor tubacin redirected JIP1 (JNK-interacting protein 1) from a subset to nearly all neurite tips [14]. Similar effects have been observed upon treatment with the microtubule-stabilizing agent taxol [15,16]. Thus, modifying cytoskeletal dynamics or microtubule PTMs are methods to disrupt cargo distributions. Nevertheless, changing the cytoskeleton does not only affect specific organelles of interest but also dramatically changes cell morphology, often leading to many unwanted side effects.

Specific motor–cargo and docking factor–cargo interactions can control organelle localization and their activity can be artificially enhanced or reduced to alter organelle positioning [17,18] (Figure 2C). For example, KIF5 (kinesin family protein 5) over-expression has been used to reduce the perinuclear accumulation of lysosomes [19], whereas the knockout of the mitochondrial anchor syntaphilin was shown to increase mitochondrial motility in mouse hippocampal axons [18]. Small molecule inhibitors can also be used and are effective within minutes. For example, to study the role of RAB11-positive recycling endosomes (Ras-related protein 11) in organizing and orienting the mitotic spindle, a dynein inhibitor was used to deplete the centrosomal RAB11 pool during mitosis [20]. Thus, changing motor protein abundance or activity can relocate a subset of organelles due to specific motor–cargo interactions. Nevertheless, a single class of motor proteins generally binds more than one type of cargo, and will therefore disrupt the positioning of multiple types of organelles.

## Roles of organelle positioning

Below we highlight recent insights into the roles of organelle positioning. Most of these insights have emerged either by observing co-occurrence of organelle movements



Tool	Advantages	Side effects	Disadvantages
Conventional techniques			
Unperturbed	-	No	Only descriptive
Disrupt cytoskeleton	Chemical inhibitors are widely available and inexpensive	Disrupts cell morphology	Typically not acute
Disrupt motors	Drug treatments and knockdowns are relatively straightforward	Affects multiple organelles	Typically not acute
Emerging techniques			
Fix morphology	Unifies the spatial organization of organelles	No	Only descriptive, additional tools needed for perturbations
Internalize magnets	Endocytosed magnetic particles can precisely mobilize targeted organelles	No	Only possible for endocytic compartments Not for <i>in vivo</i> use
Couple motors	Recruitment of specific motors to cargo of interest can drive motility in specified direction	No	Not reversible (drugs) Not for <i>in vivo</i> use (drugs)

with the process of interest or by disrupting organelle distributions through changes in cytoskeletal dynamics or motor protein activity, as described above.

### Large organelles: Nucleus, ER, Golgi apparatus

The nucleus is one of the biggest organelles in eukaryotic cells and is often represented as a centralized and stationary organelle. However, in many cell types the nucleus is neither centrally located nor immotile [21]. Imaging of migrating cells revealed that the nucleus moves away from the leading edge to position the stationary microtubule-organizing center (MTOC) between the nucleus and the leading edge, which is needed for directed migration [22–24]. In epithelial cells nuclei are usually observed closer to the basolateral side [25] (Figure 1A), but can move apically before mitosis. Impairing nuclear migration by interfering with the typical actomyosin distribution showed that migration of the nucleus towards the apical side is necessary for reintegration of daughter cells into the developing epithelium [26]. In the multinucleated muscle syncytium most of the nuclei are evenly spaced along the fiber axis [27], but a few nuclei are anchored underneath acetylcholine receptor clusters at the post-synapse of the neuromuscular junction (NMJ) (Figure 1C), presumably to aid local translation of specialized mRNAs near the NMJ [28–31].

The ER is continuous with the outer membrane of the nuclear envelope and often spreads throughout the whole cytoplasm. In neurons, the ER enriches at dendritic branchpoints (Figure 1B). Changing the ER localization and complexity by altering the activity of an ER–microtubule anchoring protein revealed the involvement of these local ER structures in the formation of new branches [32]. ER can also be found in the axon where it processes locally synthesized proteins. Interestingly, drug-induced disruption of ER–Golgi trafficking prevented repulsive axon guidance, indicating a role for local ER-processed proteins in growth-cone responses [33]. The muscle syncytium features a specialized ER, known as the sarcoplasmic reticulum (SR), that specifically aligns perpendicular to invaginations of the PM (Figure 1C) and is involved in  $Ca^{2+}$  signaling upon muscle excitation [34,35].

**Figure 2 | Different approaches to manipulate subcellular organelle positioning.**

(A) In eukaryotic cells, cytoskeletal motor proteins control the transport and positioning of proteins, RNAs, and organelles. (B) Modifying cytoskeletal dynamics or microtubule post-translational modifications (PTMs) alters how motor proteins distribute organelles. (C) Changing motor protein abundance, activity, speed, or direction can reposition organelles. (D) Plating cells on a micropattern of adhesion molecules unifies organelle distribution and allows systematic analysis of organelle positioning. (E) Organelles loaded with magnetic nanoparticles can accumulate at sites where local magnetic forces are applied. (F) Physically linking motors or anchors to organelles using chemically or light-induced heterodimerization can relocate specific organelles with spatiotemporal precision. (G) Properties of organelle-repositioning tools.

Secreted proteins often travel via the Golgi apparatus, and its location can bias the membrane targeted for secretion and hence influence cellular polarization. For example, Golgi outposts enrich at dendritic branchpoints (Figure 1B). Because blocking both ER-to-Golgi and late secretory trafficking led to reduced dendritic outgrowth and branching, Golgi outposts were proposed to provide membranes necessary for the newly-forming neurite and branch to grow [36]. Interestingly, Golgi outposts at dendritic branchpoints were also found to colocalize with sites of microtubule nucleation. This acentrosomal nucleation was abrogated in the absence of functional  $\gamma$ -Tubulin or the *Drosophila* homolog of AKAP450 (A-Kinase Anchor Protein 9/AKAP9), and resulted in reduced dendritic arborization [37]. In the muscle syncytium, small and fragmented Golgi stacks are associated with ER exit sites throughout the muscle fiber, but concentrate around the nuclei [38,39] (Figure 1C). In summary, the specific positioning of nuclei, the ER, and the Golgi apparatus is important for proper polarization, tissue formation, and muscle development.

#### Centrosomes

Centrosomes are composed of two cylindrical centrioles surrounded by a dense mass of pericentriolar material (PCM). In many cells the centrosome serves as the major MT-organizing center (MTOC) and is thought to determine the orientation of the microtubule network and the direction of post-Golgi trafficking [40]. Because centrosome relocation was observed before initial axon formation [41,42], and centrosome inactivation mediated by the red fluorescent protein KillerRed affected axon formation [43], the centrosome has been suggested to play a role in neuronal axon formation by providing the necessary membranes and proteins. However, because mutant flies lacking centrosomes still have normal axon outgrowth [44], centrosome ablation does not prevent axon outgrowth in rat hippocampal neurons [45], and centrosome localization does not predict the site of axon formation in zebrafish retinal ganglion cells [46], the exact role of the centrosome in neuronal polarization has remained elusive.

#### mRNA granules and ribosomes

The subcellular storage of mRNA molecules and ribosomes allows local protein synthesis when circumstances require and can be used to establish gradients of protein concentration. For example, during the attractive turning of axonal growth cones,  $\beta$ -actin mRNA was shown to relocate towards the side of the growth cone nearest to the attractive cue (Figure 1B). Inhibition of  $\beta$ -actin synthesis by antisense morpholino oligonucleotides prevented the increase in actin polymerization and growth-cone turning, indicating that local mRNA translation is required for attractive growth-cone turning [47,48]. Similarly, repulsive cues induce the accumulation of

mRNAs encoding for proteins involved in actin depolymerization, resulting in local growth-cone withdrawal [49,50]. In addition, it was shown that polyribosomes and a subset of mRNAs specifically localize to dendritic spines [51,52], where local translation is linked with synaptic plasticity [53–55].

#### Mitochondria

Mitochondria are often distributed throughout the cell and fulfill diverse functions, including ATP production, calcium buffering, and signal transduction [56]. Nevertheless, their localization is very specific and precisely regulated. Both adaptor proteins and anchoring factors have been reported to sense  $\text{Ca}^{2+}$  concentrations, resulting in mitochondria enrichment at sites with increased  $\text{Ca}^{2+}$  levels, such as presynaptic boutons [57,58] (Figure 1B). In hippocampal neurons from syntaphilin knockout mice, increased mitochondrial motility correlates with increased pulse-to-pulse variability in presynaptic strength, showing that stable mitochondria facilitate robust presynaptic transmission [59]. In addition, stalled mitochondria at axonal branchpoints have been correlated with branch stabilization. Mito-KillerRed-mediated ablation of these mitochondria impaired branch formation, demonstrating a role for these mitochondria in branch stabilization [60,61].

In muscle cells mitochondria reside at the ER–PM junctions and take up  $\text{Ca}^{2+}$  upon muscle excitation [35] (Figure 1C). In epithelial cells, mitochondria are uniformly distributed under normal conditions [62], but enrich anteriorly in some epithelial cancer cells. Perturbing the asymmetric distribution through overexpression or knock-down of mitochondria fusion, fission, or motor adaptor molecules in these cancer cells resulted in reduced cell migration. This indicates that the apical accumulation of mitochondria is important for cancer cell migration and promotes cancer invasion and metastasis [63]. Mitochondria also enrich at the cleavage furrow during cytokinesis [64], and relocate to distinct subcellular regions upon differentiation of professional secreting cells [65], but the function of mitochondria in these processes and the importance of their positioning have not been resolved.

#### Early endosomes

Endocytosis has traditionally been considered as a pathway for the degradation and deactivation of surface receptors that are internalized in response to ligand binding. However, it has become clear that the tails of internalized receptors can associate with signaling targets on the endosome, resulting in signaling regulation. In addition, multiple endosome-associated adaptors and scaffold proteins on the endosome can function as sites of signaling complex assembly to spatially regulate signaling [66–68].

In zebrafish neural precursor cells, the asymmetric distribution of Sara endosomes has been linked to asymmetric cell division. Sara endosomes are early endosomes

containing Notch receptors, and are labeled by the endosomal adaptor protein Sara. Increasing the level of Sara endosome asymmetry by means of expressing a constitutively-active RAB5 resulted in more asymmetric cell divisions. This shows that directional trafficking of endosomes within the mother cell can determine whether cells divide asymmetrically and subsequently define cell fate [69,70]. In summary, early endosomes are sites of protein-complex assembly that concentrate signaling events, and the motility of these endosomes is used to propagate signals to different cellular compartments. The correct localization of early endosomes is therefore crucial for proper cellular functioning.

### Recycling endosomes

Internalized membranes and receptors can be degraded by the lysosome or recycled back to the PM, either directly or via a recycling compartment. Recycling endosomes (REs) are marked by the RAB11 GTPase, which is the key regulator of RE trafficking. Because REs can be localized close to the cell surface, cells can respond quickly to external stimuli through local exocytosis of REs, resulting in dynamic reorganization of the cell surface [71]. For example, in response to neuronal growth factor (NGF) REs and its cargo NgCAM (neuron-glia cell adhesion molecule) are redirected towards the PM in PC12 cells. Overexpression of the dominant negative form of RAB11 abrogates the relocation of REs and impairs NGF-induced neurite formation [72]. Similarly, the recycling of RE into the distal axon was shown to stimulate axon growth through the increased delivery of tropomyosin-related kinase (TRK) receptors and  $\beta$ 1-integrins [73–75]. Moreover, the membrane protein VAMP2 (vesicle-associated membrane protein 2) is initially delivered to both axons and dendrites, but the preferential recycling of VAMP2 from the dendritic membrane results in the axonal localization of VAMP2 [76]. These results suggest that outgrowth and polarization in developing neurons depends on the selective activity of REs.

During long-term potentiation (LTP), which is the enlargement and strengthening of excitatory synapses upon repeated activation, more AMPA-type glutamate receptors (AMPA) are inserted into the post-synapse. This process co-occurred with membrane trafficking from REs to the spine surface. Disrupting vesicle recycling by interfering with the actin-based motor protein Myosin-Vb, by overexpression of a dominant-negative form of RAB11, or by blocking membrane fusion hampered LTP-induced spine enlargement. This indicates that the relocation of REs is essential for LTP induction [77,78], consistent with recent mathematical modeling showing that positioning REs within spines increases the chance that exocytosed AMPA receptors will be incorporated into the post-synapse [79].

In addition to delivering membranes and other cargoes, REs can also function as

signaling hubs. REs carry kinases and other regulatory factors, such as activators of actin nucleation, and their position within the cell can locally enhance signaling processes or the polymerization of actin. In enterocytes, REs are believed to dictate where microvilli form, and this is closely linked to Myosin-V-dependent positioning of REs at the apical end of the cell (Figure 1A). Patients suffering from microvillus inclusion disease, which is associated with mutations in Myosin-Vb, cannot position REs apically, resulting in microvilli atrophy, nutrient malabsorption, and the appearance of microvilli inclusions near the nucleus, where RAB11<sup>+</sup> REs are enriched [80,81].

### Lysosomes

During autophagy, intracellular proteins and organelles are enclosed by a double membrane, delivered to lysosomes, and subsequently degraded. The induction of autophagy is highly regulated. In the presence of sufficient nutrients, ATP, and oxygen, the master regulator mTORC1 (mammalian target of rapamycin complex 1) is recruited to and activated at lysosomes [82–84] where it inhibits autophagy and facilitates protein synthesis and cell growth.

Nutrient-induced activation of mTORC1 was recently shown to correlate with relocation of lysosomes from the perinuclear area towards the cell periphery. Remarkably, the forced peripheral localization of lysosomes induced by overexpression of KIF2A, KIF1B- $\beta$ , or the ARL8 (ADP-ribosylation factor-like 8) adaptor, enhanced mTORC1 activation upon nutrient recovery, showing that the nutrient response is modulated by the position of lysosomes [11]. Interestingly, in striatal cell lines derived from mutant huntingtin (mHTT) knock-in mice, which models Huntington's disease (HD), a severe perinuclear localization of lysosomes and an increase in mTORC1 activity were observed under basal conditions [19].

The clearance of toxic copper accumulations in hepatocytes is accomplished by the ATP7B ATPase and copper transporter that pumps copper from the cytosol into lysosomes. Upon high copper concentrations, ATP7B repositions from the Golgi to the lysosome, pumps copper, and recruits dynein to induce the relocation of lysosomes to the canalicular surface for lysosomal exocytosis. The ATP7B-mediated dynein-driven delivery of lysosomes to the canalicular surface is thus required for copper detoxification [85].

In addition to affecting autophagy and copper clearance, the centrifugal movement of lysosomes has also been shown to stimulate cell migration and motility, perhaps owing to increased delivery of adhesion molecules, signaling scaffolds, and acid hydrolases via lysosomal exocytosis [86]. Thus, nutrient-induced mTORC1 activation, cell motility, and cell spreading can all depend on the positioning of lysosomes.

### Inter-organelle contact sites

Most organelles are membranous compartments that carry a specialized set of molecules to perform specific biochemical reactions. However, exchange of lipids, metabolites, and  $\text{Ca}^{2+}$  between organelles is often required and can be achieved through membrane contact sites (MCS) [35]. For example, the ER contacts the PM, mitochondria, endosomes, and the Golgi [87–93], whereas contact sites between mitochondria and the same cellular structures have also been described [56], as well as lysosome–peroxisome [94], Golgi–PM [95] and Golgi–lysosome interactions [96].

Many different lipid species constitute the cellular membranes, with each organelle having its own characteristic lipid composition. Most lipids are made in the ER and can be trafficked to other organelles via vesicular transport or via lipid-transport proteins (LTPs), which are often targeted to MCSs and can interchange one lipid molecule at a time. For example, phosphatidylserine (PS), phosphatidylethanolamine (PE), and phosphatidylcholine (PC) are exchanged between the ER and mitochondria at MCSs [35]. In addition, recent studies showed that specific oxysterol-binding protein (OSBP)-related proteins (ORPs) mediated the exchange of PS and phosphatidylinositol 4-phosphate (PI4P) at ER–PM contact sites. Interestingly, artificial recruitment of ER-bound ORP5 to the PM, but not of a truncated and cytosolic form of ORP5, could change PS and PI4P levels [97,98]. These results show that MCSs are required for lipid exchange and the correct lipid distribution among organelles.

The classical example of a  $\text{Ca}^{2+}$  response in which close organelle contacts are absolutely required is excitation-contraction coupling in muscle fibers. The initial  $\text{Ca}^{2+}$  influx triggers a more pronounced  $\text{Ca}^{2+}$  release from the SR, leading to myosin activation and muscle contraction. To restore  $\text{Ca}^{2+}$  levels in the SR, the luminal  $\text{Ca}^{2+}$  sensor STIM1 (stromal interaction molecule 1) relocates to ER–PM junctions (Figure 1C) where it opens  $\text{Ca}^{2+}$  channels in the PM, which allows the SR to restore its  $\text{Ca}^{2+}$  levels [99]. A comparable response has been reported for excitatory neuronal synapses, where synaptic activity induces the relocation of STIM2 to ER–PM junctions (Figure 1B). STIM2 relocation then leads to GLUA1 (AMPA receptor subunit) phosphorylation and delivery of AMPA receptors to the surface, resulting in synapse strengthening [100].

In addition to exchanging materials, ER-marked endosome constriction sites were observed before endosome fission, and to form a diffusion barrier for endosomal cargo. Interestingly, upon overexpression of RTN4 (reticulin 4) to elongate the ER, the number of endosome fissions were significantly reduced [101]. Similarly, ER-mitochondria contact sites were shown to colocalize with sites of mitochondria fission [102] and autophagosome formation [103]. These results indicate that the position and dynamics of the ER spatiotemporally control the fission of endosomes and mitochondria, as well as autophagosome formation. The exact role of ER contact sites in these processes is not known. The ER might function as a scaffolding platform, and

it may provide ER-specific lipid species or supply  $\text{Ca}^{2+}$  to drive  $\text{Ca}^{2+}$ -dependent processes [101]. Moreover, the importance of ER-mediated fission has also remained elusive, but these events might contribute to whole cell rearrangements and sorting during mitosis, cell migration, or polarization. Importantly, altered ER–mitochondria contacts have been associated with Alzheimer’s disease, Parkinson’s disease, and amyotrophic lateral sclerosis [104–106], indicating that organelle contact sites are important for proper cell functioning.

### Emerging tools to study and manipulate organelle positioning

We presented evidence above for the importance of organelle positioning in many basal cellular processes. However, a substantial amount of this evidence is based on the co-occurrence of organelle movements with the process of interest, and this does not prove a causal relationship. Other evidence is based on the effects of organelle redistribution upon disrupting cytoskeletal dynamics or motor protein activity, but these treatments can have many side effects and are often not selective for the organelles of interest. Thus, to better explore the roles of specific organelle localization, more selective tools should be used. We will now highlight different recently established approaches that allow more-controlled and selective perturbation of organelle positioning.

#### Manipulating cell morphology

To systematically study the precise connection between organelle localization and function, the spatial organization of organelles should be well defined. However, strong morphological differences are observed between cells in a population, caused by differences in local cell density and cell position within a cellular islet. The presence and distribution of cell–cell and cell–extracellular matrix (ECM) contacts influence the cytoskeletal organization and consequently organelle positioning [107,108]. To standardize the spatial cellular organization, single cells can be plated on micropatterns of cell adhesion molecules in which subtle perturbations in organelle topology can be observed and quantified [107–109] (Figure 2D). For example, the nucleus–centrosome polarity axis appeared to differ between cells plated on geometrically different fibronectin adhesive patterns [107], showing that the localization of cell–ECM contacts can affect organelle positioning. In addition to standardization, micropatterns could also be used to study how geometrical constraints affect organelle distribution [110].

#### Manipulating motor protein activity, speed, or directionality using light

Overexpression, knockdown, or inhibition of motor proteins has extensively been used to alter organelle positioning. Recently developed approaches now allow motor activation with spatiotemporal precision using light. One strategy is to photocontrol

ATP hydrolysis by incorporating photochromic molecules into the ATPase domain of motor proteins, as was done to control the motility of kinesin-5 and kinesin-1 *in vitro* [111,112]. Alternatively, light-induced uncaging of motor protein activators can be used to control motor protein processivity [113]. In addition, a recent study showed that, upon exposure to blue light, both the speed and directionality of engineered Myosin-VI and kinesin-14 motors could be manipulated *in vitro* [114]. However, these techniques have so far not been applied to reposition organelles and, similarly to conventional methods to alter motor activity, such manipulations would in most cases affect the positioning of multiple types of organelles.

### Manipulating organelles using magnetic nanoparticles (MNPs)

Focally applied magnetic forces allow the spatial accumulation of MNPs inside living cells. MNPs can be coupled to nearly any protein or protein-binding domain, enabling the local concentration of a protein or structure of interest [115–117]. For example, magnetic nanoparticles conjugated with RAN (Ras-related nuclear protein)-GTP [118] could be used to artificially and locally polymerize microtubules. Moreover, to study the role of signaling endosomes in neurite outgrowth, neurons were loaded with MNPs coupled to TrkB-agonist antibodies that were subsequently endocytosed into signaling endosomes. Application of defined magnetic forces could pull the signaling endosomes away from the growth cone, and this resulted in stalled neurite outgrowth [115]. Importantly, the transport of other organelles such as mitochondria and vacuoles remained unchanged (Figure 2E).

The transport of MNP-targeted vesicles can be controlled very precisely; however, only endocytic compartments are suitable for ligand-mediated MNP loading. Alternative methods can deliver smaller MNPs into the cytosol and could potentially be targeted to other organelles for subsequent manipulation.

### Coupling molecular motors or anchors to specific organelles

Most cytoskeletal motor proteins associate with cargoes through their tail domain, often mediated by specific adaptor molecules that mediate specific motor–cargo interactions [2,3]. These interactions determine cargo loading and offloading in space and time, and thus define cargo distribution. Therefore, physically linking a selected motor or adaptor molecule to an organelle of interest can induce organelle displacements. The role of mitochondria in axonal degeneration was studied in *C. elegans* by expressing a fusion construct of full-length kinesin-1 and the outer mitochondrial membrane protein TOM7. This approach forced mitochondria to move from the cell body into the axon [119]. However, as with motor protein overexpression, these manipulations last for the lifetime of an organism and are not suited to achieve temporal control over organelle relocations.

Dimerization system <sup>a</sup>	Exogenous compound	Dimerization speed	Reversibility	Activation light	Refs
<i>Chemical-induced protein heterodimerization</i>					
FKBP – rapalog – FRB	Rapalog	Minutes	No	–	[120]
GID – gibberellin – GAI	Gibberellin	Minutes	No	–	[129]
SNAPtag – CoreM – HaloTag	CoreM	Minutes	No	–	[130]
14-3-3 protein – fusicoccin – PMA	Fusicoccin	Minutes	Minutes	–	[131]
<i>Photocaged-induced protein heterodimerization</i>					
FKBP – photocaged rapamycin – FRB	Photocaged rapamycin	Minutes	Not shown	365–405 nm	[132, 133]
SNAPtag – photocleavable MeNV – HaloTag	Photocleavable MeNV	Minutes	1 round, seconds	365–405 nm	[134]
DHFR – photocaged TMP/ HaloTag – HaloEnzyme	Photocaged TMP/HaloTag	Seconds	Minutes (After addition of free TMP)	365–405 nm	[124]
<i>Photo-induced protein heterodimerization</i>					
Phytochrome – PIF	PCB	Seconds	Seconds (750 nm light) or hours (dark reversion)	650 nm (on) 750 nm (off)	[135, 136]
FKF1 – GIGANTEA	–	Seconds	No / very slow	450 nm	[137]
UVR8 – COP1	–	Seconds	No	280–315 nm	[138]
VIVID A – VIVID B	–	Seconds	Seconds to hours (different variants)	470 nm	[139]
Cryptochrome – CIB	–	Seconds	Minutes	405–488 nm	[135, 126]
LOVpep – ePDZ	–	Seconds	Tens of seconds to minutes for different variants	440–473 nm	[135, 125]

**Table 1 | Properties of protein heterodimerization systems.**

<sup>a</sup>Abbreviations: COP1, constitutively photomorphogenic 1; FKF, flavin binding, kelch repeat, F-box 1; GAI, gibberellin-insensitive; GID, gibberellin-insensitive dwarf1; MeNV, methyl-6-nitroveratryl; PCB, phycocyanobilin; PIF, phytochrome-interacting factor; UVR 8, UV resistance locus 8; TMP, trimethoprim. For further abbreviations see text.

The recruitment of molecular motors to cargoes using chemically induced heterodimerization does allow the controlled initiation of cargo transport. In short, organelle membrane-targeting signals can be fused to FKBP (FK506 binding protein) that, upon the addition of rapalog, can crosslink to FRB-fused motor proteins or adaptors fused to a FRB (FKBP rapamycin binding domain) [120–122] (Figure 2F). By recruiting different types of motor proteins, organelles could be forced to move anterogradely, retrogradely, or become immobilized [7,121]. Because the uptake of rapalog takes several minutes, it is difficult to precisely control the start of cargo movement. A recently developed photocaged linker that connects dihydrofolate reductase (DHFR) to the Halo-tag was recently used to instantly couple DHFR-tagged motor proteins to Halo-tagged organelles upon exposure to 385–405 nm light [123]. However, similarly to rapalog-induced heterodimerization, this interaction could not be reversed [121,124] and resulted in persistent motor–cargo interactions [123].

Light-controlled motor recruitment would be ideal, because this interaction would be reversible and does not require exogenous co-factors. The blue light-induced interaction of a LOV2 (light-oxygen-voltage-sensing) domain with an engineered PDZ domain (PSD95/discs large/zonula occludens 1) [125], and the interaction between Cryptochrome-2 and CIB1 (cryptochrome-interacting basic-helix-loop-helix 1) [126], have recently been exploited to recruit motors to specific organelles with spatiotemporal control [127]. Using these two systems, the motility of peroxisomes, mitochondria, and recycling endosomes could be started or stopped [127]. Targeted laser illumination could specifically deplete selected areas from peroxisomes or mitochondria, whereas recycling endosomes could be forced into specific dendritic spines, or targeted away or towards axonal growth cones. Surprisingly, the addition of recycling endosomes stimulated outgrowth, revealing that growth-cone dynamics are sensitive to endosome positioning [127]. Subsequent work extended this optogenetic approach to lysosomes [128]. Different (optogenetic) heterodimerization systems differ in sensitivity to blue light, dissociation speed, compatibility with N-terminal versus C-terminal fusions, and in their oligomerizing versus homodimerizing properties (summarized in Table 1), and can be used to manipulate organelle positioning with different dynamics.

## Concluding remarks

In recent years it has become increasingly clear that many organelles have functions that depend on proper positioning. However, in many cases the precise local functions and the molecular pathways underlying localization have remained unclear due to a lack of tools to perturb the placement of a selected organelle without off-target effects. Nonetheless, novel approaches are now emerging that use (light-sensitive)

coupling of motor proteins or anchoring factors to selected organelles to spatio-temporally control organelle positioning. These tools will be valuable in addressing many outstanding questions, for example in addressing how stationary mitochondria contribute to axon branching and synapse function, how recycling endosomes contribute to polarization and axon outgrowth, and how lysosomes at the surface stimulate cell migration and motility. In addition, future research might uncover more correlations between aberrant organelle distributions and pathological conditions.

The majority of organelle positioning studies has so far been conducted in simple 2D cell cultures, and the importance of organelle localization in a multicellular context might be underestimated in such models. Therefore, using controlled organelle repositioning in 3D models or *in vivo* might uncover (additional) roles for proper spatial arrangements in processes such as asymmetric cell division, stem cell maintenance, and tissue formation. For all these questions, further development of the optogenetic modules will be necessary to combine on–off control of organelle transport with multi-spectral imaging without the need for exogenous compounds. Despite these challenges, future work using these exciting techniques will undoubtedly illuminate the many local functions of organelles.

## Acknowledgements

This research is supported by the Dutch Technology Foundation STW, which is part of The Netherlands Organisation for Scientific Research (NWO). Additional support came from NWO (NWO-ALW-VICI to C.C.H and NWO-ALW-VIDI to L.C.K.) and the European Research Council (ERC Starting Grant to L.C.K.).

## Author contributions

P.B. designed the outline, wrote the manuscript and made the figures with advice from L.C.K and C.C.H.

## References

- Vale, R.D. (2003) The molecular motor toolbox for intracellular transport. *Cell* **112**, 467–480
- Schlager, M.A. and Hoogenraad, C.C. (2009) Basic mechanisms for recognition and transport of synaptic cargos. *Mol Brain* **2**, 25
- Fu, M.-M. and Holzbauer, E.L.F. (2014) Integrated regulation of motor-driven organelle transport by scaffolding proteins. *Trends Cell Biol.* **24**, 564–574
- Sheng, Z.-H. (2014) Mitochondrial trafficking and anchoring in neurons: New insight and implications. *J. Cell Biol.* **204**, 1087–1098
- Yadav, S. and Linstedt, A.D. (2011) Golgi positioning. *Cold Spring Harb Perspect Biol* **3**, a005322
- Woolner, S. and Bement, W.M. (2009) Unconventional myosins acting unconventionally. *Trends Cell Biol.* **19**, 245–252
- Kapitein, L.C. et al. (2013) Myosin-V opposes microtubule-based cargo transport and drives directional motility on cortical actin. *Curr. Biol.* **23**, 828–834
- McIntosh, B.B. et al. (2015) Control of the initiation and termination of kinesin-1-driven transport by myosin-Ic and nonmuscle tropomyosin. *Curr. Biol.* **25**, 523–529
- De Brabander, M.J. et al. (1976) The effects of methyl (5-(2-thienylcarbonyl)-1H-benzimidazol-2-yl) carbamate, (R 17934; NSC 238159), a new synthetic antitumoral drug interfering with microtubules, on mammalian cells cultured in vitro. *Cancer Res.* **36**, 905–916
- Dumontet, C. and Jordan, M.A. (2010) Microtubule-binding agents: a dynamic field of cancer therapeutics. *Nat Rev Drug Discov* **9**, 790–803
- Korolchuk, V.I. et al. (2011) Lysosomal positioning coordinates cellular nutrient responses. *Nat. Cell Biol.* **13**, 453–460
- Cole, N.B. et al. (1996) Golgi dispersal during microtubule disruption: regeneration of Golgi stacks at peripheral endoplasmic reticulum exit sites. *Mol. Biol. Cell* **7**, 631–650
- Song, Y. and Brady, S.T. (2015) Post-translational modifications of tubulin: pathways to functional diversity of microtubules. *Trends Cell Biol.* **25**, 125–136
- Reed, N.A. et al. (2006) Microtubule acetylation promotes kinesin-1 binding and transport. *Current Biology* **16**, 2166–2172
- Kapitein, L.C. et al. (2010) Mixed microtubules steer dynein-driven cargo transport into dendrites. *Curr. Biol.* **20**, 290–299
- Hammond, J.W. et al. (2010) Posttranslational modifications of tubulin and the polarized transport of kinesin-1 in neurons. *Mol. Biol. Cell* **21**, 572–583
- Hirokawa, N. et al. (2010) Molecular motors in neurons: transport mechanisms and roles in brain function, development, and disease. *Neuron* **68**, 610–638
- Kang, J.-S. et al. (2008) Docking of axonal mitochondria by syntaphilin controls their mobility and affects short-term facilitation. *Cell* **132**, 137–148
- Erie, C. et al. (2015) Altered lysosomal positioning affects lysosomal functions in a cellular model of Huntington's disease. *Eur. J. Neurosci.* **42**, 1941–1951
- Hehnlly, H. and Doxsey, S. (2014) Rab11 endosomes contribute to mitotic spindle organization and orientation. *Dev. Cell* **28**, 497–507
- Gundersen, G.G. and Worman, H.J. (2013) Nuclear positioning. *Cell* **152**, 1376–1389
- Gomes, E.R. et al. (2005) Nuclear movement regulated by Cdc42, MRCK, myosin, and actin flow establishes MTOC polarization in migrating cells. *Cell* **121**, 451–463

23. Luxton, G.W.G. and Gundersen, G.G. (2011) Orientation and function of the nuclear-centrosomal axis during cell migration. *Current Opinion in Cell Biology* **23**, 579–588
24. Etienne-Manneville, S. (2013) Microtubules in cell migration. *Annu. Rev. Cell Dev. Biol.* **29**, 471–499
25. Koeneman, B.A. et al. (2010) Toxicity and cellular responses of intestinal cells exposed to titanium dioxide. *Cell Biol. Toxicol.* **26**, 225–238
26. Strzyz, P.J. et al. (2015) Interkinetic nuclear migration is centrosome independent and ensures apical cell division to maintain tissue integrity. *Dev. Cell* **32**, 203–219
27. Bruusgaard, J.C. et al. (2003) Number and spatial distribution of nuclei in the muscle fibres of normal mice studied in vivo. *J. Physiol. (Lond.)* **551**, 467–478
28. Englander, L.L. and Rubin, L.L. (1987) Acetylcholine receptor clustering and nuclear movement in muscle fibers in culture. *J. Cell Biol.* **104**, 87–95
29. Burke, B. and Roux, K.J. (2009) Nuclei take a position: managing nuclear location. *Dev. Cell* **17**, 587–597
30. Elhanany-Tamir, H. et al. (2012) Organelle positioning in muscles requires cooperation between two KASH proteins and microtubules. *J. Cell Biol.* **198**, 833–846
31. Chakkalakal, J.V. and Jasmin, B.J. (2002) Localizing synaptic mRNAs at the neuromuscular junction: It takes more than transcription. *Bioessays* **25**, 25–31
32. Cui-Wang, T. et al. (2012) Local zones of endoplasmic reticulum complexity confine cargo in neuronal dendrites. *Cell* **148**, 309–321
33. Merianda, T.T. et al. (2009) A functional equivalent of endoplasmic reticulum and Golgi in axons for secretion of locally synthesized proteins. *Mol. Cell. Neurosci.* **40**, 128–142
34. Block, B.A. et al. (1988) Structural evidence for direct interaction between the molecular components of the transverse tubule/sarcoplasmic reticulum junction in skeletal muscle. *J. Cell Biol.* **107**, 2587–2600
35. Helle, S.C.J. et al. (2013) Organization and function of membrane contact sites. *Biochim. Biophys. Acta* **1833**, 2526–2541
36. Horton, A.C. et al. (2005) Polarized secretory trafficking directs cargo for asymmetric dendrite growth and morphogenesis. *Neuron* **48**, 757–771
37. Ori-McKenney, K.M. et al. (2012) Golgi outposts shape dendrite morphology by functioning as sites of centrosomal microtubule nucleation in neurons. *Neuron* **76**, 921–930
38. Ralston, E. (1993) Changes in architecture of the Golgi complex and other subcellular organelles during myogenesis. *J. Cell Biol.* **120**, 399–409
39. Lu, Z. et al. (2001) Golgi complex reorganization during muscle differentiation: visualization in living cells and mechanism. *Mol. Biol. Cell* **12**, 795–808
40. Sütterlin, C. and Colanzi, A. (2010) The Golgi and the centrosome: building a functional partnership. *J. Cell Biol.* **188**, 621–628
41. Zmuda, J.F. and Rivas, R.J. (1998) The Golgi apparatus and the centrosome are localized to the sites of newly emerging axons in cerebellar granule neurons in vitro. *Cell Motil. Cytoskeleton* **41**, 18–38
42. de Anda, F.C. et al. (2005) Centrosome localization determines neuronal polarity. *Nature* **436**, 704–708
43. de Anda, F.C. et al. (2010) Centrosome motility is essential for initial axon formation in the neocortex. *J. Neurosci.* **30**, 10391–10406
44. Basto, R. et al. (2006) Flies without centrioles. *Cell* **125**, 1375–1386
45. Stiess, M. et al. (2010) Axon extension occurs independently of centrosomal microtubule nucleation. *Science* **327**, 704–707
46. Zolessi, F.R. et al. (2006) Polarization and orientation of retinal ganglion cells in vivo. *Neural Dev* **1**, 2
47. Leung, K.-M. et al. (2006) Asymmetrical beta-actin mRNA translation in growth cones mediates attractive turning to netrin-1. *Nat. Neurosci.* **9**, 1247–1256
48. Yao, J. et al. (2006) An essential role for beta-actin mRNA localization and translation in Ca<sup>2+</sup>-dependent growth cone guidance. *Nat. Neurosci.* **9**, 1265–1273
49. Wu, K.Y. et al. (2005) Local translation of RhoA regulates growth cone collapse. *Nature* **436**, 1020–1024
50. Piper, M. et al. (2006) Signaling mechanisms underlying Slit2-induced collapse of *Xenopus* retinal growth cones. *Neuron* **49**, 215–228
51. Steward, O. and Levy, W.B. (1982) Preferential localization of polyribosomes under the base of dendritic spines in granule cells of the dentate gyrus. *J. Neurosci.* **2**, 284–291
52. Steward, O. et al. (1998) Synaptic activation causes the mRNA for the IEG Arc to localize selectively near activated postsynaptic sites on dendrites. *Neuron* **21**, 741–751
53. Kang, H. and Schuman, E.M. (1996) A requirement for local protein synthesis in neurotrophin-induced hippocampal synaptic plasticity. *Science* **273**, 1402–1406
54. Huber, K.M. et al. (2000) Role for rapid dendritic protein synthesis in hippocampal mGluR-dependent long-term depression. *Science* **288**, 1254–1257
55. Holt, C.E. and Schuman, E.M. (2013) The central dogma decentralized: new perspectives on RNA function and local translation in neurons. *Neuron* **80**, 648–657
56. Klecker, T. et al. (2014) Making connections: interorganelle contacts orchestrate mitochondrial behavior. *Trends Cell Biol.* **24**, 537–545
57. Wang, X. and Schwarz, T.L. (2009) The mechanism of Ca<sup>2+</sup>-dependent regulation of kinesin-mediated mitochondrial motility. *Cell* **136**, 163–174
58. MacAskill, A.F. et al. (2009) Miro1 is a calcium sensor for glutamate receptor-dependent localization of mitochondria at synapses. *Neuron* **61**, 541–555
59. Sun, T. et al. (2013) Motile axonal mitochondria contribute to the variability of presynaptic strength. *Cell Rep* **4**, 413–419
60. Spillane, M. et al. (2013) Mitochondria coordinate sites of axon branching through localized intra-axonal protein synthesis. *Cell Rep* **5**, 1564–1575
61. Tao, K. et al. (2014) AMP-activated protein kinase mediates activity-dependent axon branching by recruiting mitochondria to axon. *Dev Neurobiol* **74**, 557–573
62. Fox, R.M. and Andrew, D.J. (2015) Changes in organelle position and epithelial architecture associated with loss of CrebA. *Biol Open* **4**, 317–330
63. Desai, S.P. et al. (2013) Mitochondrial localization and the persistent migration of epithelial cancer cells. *Biophys. J.* **104**, 2077–2088
64. Lawrence, E.J. and Mandato, C.A. (2013) Mitochondria localize to the cleavage furrow in mammalian cytokinesis. *PLoS ONE* **8**, e72886
65. Jin, R.U. and Mills, J.C. (2014) RAB26 coordinates lysosome traffic and mitochondrial localization. *J. Cell. Sci.* **127**, 1018–1032
66. Di Fiore, P.P. and De Camilli, P. (2001) Endocytosis and signaling. an inseparable partnership. *Cell* **106**, 1–4
67. Seto, E.S. et al. (2002) When cell biology meets development: endocytic regulation of signaling pathways. *Genes Dev.* **16**, 1314–1336
68. Sadowski, L. et al. (2009) Signaling from endosomes: location makes a difference. *Exp. Cell Res.* **315**, 1601–1609
69. Bökel, C. et al. (2006) Sara endosomes and the maintenance of Dpp signaling levels across mitosis. *Science* **314**, 1135–1139
70. Kressmann, S. et al. (2015) Directional Notch trafficking in Sara endosomes during asymmetric cell division in the spinal cord. *Nat. Cell Biol.* **17**, 333–339

71. van IJzendoorn, S.C.D. (2006) Recycling endosomes. *J. Cell. Sci.* **119**, 1679–1681
72. Shirane, M. and Nakayama, K.I. (2006) Protrudin induces neurite formation by directional membrane trafficking. *Science* **314**, 818–821
73. Ascaño, M. et al. (2009) Axonal targeting of Trk receptors via transcytosis regulates sensitivity to neurotrophin responses. *J. Neurosci.* **29**, 11674–11685
74. Eva, R. et al. (2010) Rab11 and its effector Rab coupling protein contribute to the trafficking of beta 1 integrins during axon growth in adult dorsal root ganglion neurons and PC12 cells. *J. Neurosci.* **30**, 11654–11669
75. Takano, T. et al. (2012) LMTK1/AATYK1 is a novel regulator of axonal outgrowth that acts via Rab11 in a Cdk5-dependent manner. *J. Neurosci.* **32**, 6587–6599
76. Sampo, B. et al. (2003) Two distinct mechanisms target membrane proteins to the axonal surface. *Neuron* **37**, 611–624
77. Park, M. et al. (2006) Plasticity-induced growth of dendritic spines by exocytic trafficking from recycling endosomes. *Neuron* **52**, 817–830
78. Wang, Z. et al. (2008) Myosin Vb mobilizes recycling endosomes and AMPA receptors for postsynaptic plasticity. *Cell* **135**, 535–548
79. Kusters, R. et al. (2013) Shape-induced asymmetric diffusion in dendritic spines allows efficient synaptic AMPA receptor trapping. *Biophys. J.* **105**, 2743–2750
80. Szperl, A.M. et al. (2011) Functional characterization of mutations in the myosin Vb gene associated with microvillus inclusion disease. *J. Pediatr. Gastroenterol. Nutr.* **52**, 307–313
81. Dhekne, H.S. et al. (2014) Myosin Vb and Rab11a regulate phosphorylation of ezrin in enterocytes. *J. Cell. Sci.* **127**, 1007–1017
82. Sancak, Y. et al. (2010) Ragulator-Rag complex targets mTORC1 to the lysosomal surface and is necessary for its activation by amino acids. *Cell* **141**, 290–303
83. Russell, R.C. et al. (2014) Autophagy regulation by nutrient signaling. *Cell Res.* **24**, 42–57
84. Menon, S. et al. (2014) Spatial control of the TSC complex integrates insulin and nutrient regulation of mTORC1 at the lysosome. *Cell* **156**, 771–785
85. Polishchuk, E.V. et al. (2014) Wilson disease protein ATP7B utilizes lysosomal exocytosis to maintain copper homeostasis. *Dev. Cell* **29**, 686–700
86. Pu, J. et al. (2015) BORC, a multisubunit complex that regulates lysosome positioning. *Dev. Cell* **33**, 176–188
87. de Brito, O.M. and Scorrano, L. (2008) Mitofusin 2 tethers endoplasmic reticulum to mitochondria. *Nature* **456**, 605–610
88. Friedman, J.R. et al. (2010) ER sliding dynamics and ER-mitochondrial contacts occur on acetylated microtubules. *J. Cell Biol.* **190**, 363–375
89. Alpy, F. et al. (2013) STARD3 or STARD3NL and VAP form a novel molecular tether between late endosomes and the ER. *J. Cell. Sci.* **126**, 5500–5512
90. Friedman, J.R. et al. (2013) Endoplasmic reticulum-endosome contact increases as endosomes traffic and mature. *Mol. Biol. Cell* **24**, 1030–1040
91. Ladinsky, M.S. et al. (1999) Golgi structure in three dimensions: functional insights from the normal rat kidney cell. *J. Cell Biol.* **144**, 1135–1149
92. Mogelsvang, S. et al. (2004) Predicting function from structure: 3D structure studies of the mammalian Golgi complex. *Traffic* **5**, 338–345
93. English, A.R. and Voeltz, G.K. (2013) Endoplasmic reticulum structure and interconnections with other organelles. *Cold Spring Harb Perspect Biol* **5**, a013227
94. Chu, B.-B. et al. (2015) Cholesterol transport through lysosome-peroxisome membrane contacts. *Cell* **161**, 291–306
95. Sytnyk, V. et al. (2002) Neural cell adhesion molecule promotes accumulation of TGN organelles at sites of neuron-to-neuron contacts. *J. Cell Biol.* **159**, 649–661
96. Wang, T. and Hong, W. (2002) Interorganellar regulation of lysosome positioning by the Golgi apparatus through Rab34 interaction with Rab-interacting lysosomal protein. *Mol. Biol. Cell* **13**, 4317–4332
97. Moser von Filseck, J. et al. (2015) Phosphatidylserine transport by ORP/Osh proteins is driven by phosphatidylinositol 4-phosphate. *Science* **349**, 432–436
98. Chung, J. et al. (2015) PI4P/phosphatidylserine countertransport at ORP5- and ORP8-mediated ER-plasma membrane contacts. *Science* **349**, 428–432
99. Lam, A.K.M. and Galione, A. (2013) The endoplasmic reticulum and junctional membrane communication during calcium signaling. *Biochim. Biophys. Acta* **1833**, 2542–2559
100. Garcia-Alvarez, G. et al. (2015) STIM2 regulates PKA-dependent phosphorylation and trafficking of AMPARs. *Mol. Biol. Cell* **26**, 1141–1159
101. Rowland, A.A. et al. (2014) ER contact sites define the position and timing of endosome fission. *Cell* **159**, 1027–1041
102. Friedman, J.R. et al. (2011) ER tubules mark sites of mitochondrial division. *Science* **334**, 358–362
103. Hamasaki, M. et al. (2013) Autophagosomes form at ER-mitochondria contact sites. *Nature* **495**, 389–393
104. Area-Gomez, E. et al. (2012) Upregulated function of mitochondria-associated ER membranes in Alzheimer disease. *The EMBO Journal* **31**, 4106–4123
105. Guardia-Laguarta, C. et al. (2014)  $\alpha$ -Synuclein is localized to mitochondria-associated ER membranes. *J. Neurosci.* **34**, 249–259
106. Stoica, R. et al. (2014) ER-mitochondria associations are regulated by the VAPB-PTIP51 interaction and are disrupted by ALS/FTD-associated TDP-43. *Nat Commun* **5**, 3996
107. Thery, M. et al. (2006) Anisotropy of cell adhesive microenvironment governs cell internal organization and orientation of polarity. *Proc. Natl. Acad. Sci. U.S.A.* **103**, 19771–19776
108. Schauer, K. et al. (2010) Probabilistic density maps to study global endomembrane organization. *Nat. Methods* **7**, 560–566
109. Schauer, K. et al. (2014) A novel organelle map framework for high-content cell morphology analysis in high throughput. *J. Biomol. Screen* **19**, 317–324
110. Roth, S. et al. (2012) How morphological constraints affect axonal polarity in mouse neurons. *PLoS ONE* **7**, e33623
111. Ishikawa, K. et al. (2014) Photocontrol of mitotic kinesin Eg5 facilitated by thiol-reactive photochromic molecules incorporated into the loop L5 functional loop. *J. Biochem.* **155**, 195–206
112. Kamei, T. et al. (2012) A photochromic ATP analogue driving a motor protein with reversible light-controlled motility: controlling velocity and binding manner of a kinesin-microtubule system in an in vitro motility assay. *Chem. Commun. (Camb.)* **48**, 7625–7627
113. Goguen, B.N. et al. (2011) Light-triggered myosin activation for probing dynamic cellular processes. *Angew. Chem. Int. Ed. Engl.* **50**, 5667–5670
114. Nakamura, M. et al. (2014) Remote control of myosin and kinesin motors using light-activated gearshifting. *Nat Nanotechnol* **9**, 693–697
115. Steketee, M.B. et al. (2011) Nanoparticle-mediated signaling endosome localization regulates growth cone motility and neurite growth. *Proc. Natl. Acad. Sci. U.S.A.* **108**, 19042–19047
116. Etoc, F. et al. (2013) Subcellular control of Rac-GTPase signalling by magnetogenetic manipulation inside living cells. *Nat Nanotechnol* **8**, 193–198
117. Etoc, F. et al. (2015) Magnetogenetic control of protein gradients inside living cells with high spatial and temporal resolution. *Nano Lett.* **15**, 3487–3494

118. Hoffmann, C. et al. (2013) Spatiotemporal control of microtubule nucleation and assembly using magnetic nanoparticles. *Nat Nanotechnol* **8**, 199–205
119. Rawson, R.L. et al. (2014) Axons degenerate in the absence of mitochondria in *C. elegans*. *Curr. Biol.* **24**, 760–765
120. Clackson, T. et al. (1998) Redesigning an FKBP-ligand interface to generate chemical dimerizers with novel specificity. *Proc. Natl. Acad. Sci. U.S.A.* **95**, 10437–10442
121. Kapitein, L.C. et al. (2010) Probing intracellular motor protein activity using an inducible cargo trafficking assay. *Biophys. J.* **99**, 2143–2152
122. Hoogenraad, C.C. et al. (2003) Bicaudal D induces selective dynein-mediated microtubule minus end-directed transport. *The EMBO Journal* **22**, 6004–6015
123. Ballister, E.R. et al. (2015) Optogenetic control of organelle transport using a photocaged chemical inducer of dimerization. *Curr. Biol.* **25**, R407–8
124. Ballister, E.R. et al. (2014) Localized light-induced protein dimerization in living cells using a photocaged dimerizer. *Nat Commun* **5**, 5475
125. Strickland, D. et al. (2012) TULIPs: tunable, light-controlled interacting protein tags for cell biology. *Nat. Methods* **9**, 379–384
126. Kennedy, M.J. et al. (2010) Rapid blue-light-mediated induction of protein interactions in living cells. *Nat. Methods* **7**, 973–975
127. van Bergeijk, P. et al. (2015) Optogenetic control of organelle transport and positioning. *Nature* **518**, 111–114
128. Duan, L. et al. (2015) Optogenetic control of molecular motors and organelle distributions in cells. *Chem. Biol.* **22**, 671–682
129. Miyamoto, T. et al. (2012) Rapid and orthogonal logic gating with a gibberellin-induced dimerization system. *Nat. Chem. Biol.* **8**, 465–470
130. Erhart, D. et al. (2013) Chemical development of intracellular protein heterodimerizers. *Chem. Biol.* **20**, 549–557
131. Skwarczynska, M. et al. (2013) Activation of NF- $\kappa$ B signalling by fusicoccin-induced dimerization. *Proc. Natl. Acad. Sci. U.S.A.* **110**, E377–86
132. Umeda, N. et al. (2011) A photocleavable rapamycin conjugate for spatiotemporal control of small GTPase activity. *J. Am. Chem. Soc.* **133**, 12–14
133. Karginov, A.V. et al. (2011) Light regulation of protein dimerization and kinase activity in living cells using photocaged rapamycin and engineered FKBP. *J. Am. Chem. Soc.* **133**, 420–423
134. Zimmermann, M. et al. (2014) Cell-permeant and photocleavable chemical inducer of dimerization. *Angew. Chem. Int. Ed. Engl.* **53**, 4717–4720
135. Tischer, D. and Weiner, O.D. (2014) Illuminating cell signalling with optogenetic tools. *Nat. Rev. Mol. Cell Biol.* **15**, 551–558
136. Levskaia, A. et al. (2009) Spatiotemporal control of cell signalling using a light-switchable protein interaction. *Nature* **461**, 997–1001
137. Yazawa, M. et al. (2009) Induction of protein-protein interactions in live cells using light. *Nat. Biotechnol.* **27**, 941–945
138. Crefcoeur, R.P. et al. (2013) Ultraviolet-B-mediated induction of protein-protein interactions in mammalian cells. *Nat Commun* **4**, 1779
139. Kawano, F. et al. (2015) Engineered pairs of distinct photoswitches for optogenetic control of cellular proteins. *Nat Commun* **6**, 6256





## Myosin-V opposes microtubule-based cargo transport and drives directional motility on cortical actin

Lukas C. Kapitein<sup>1,2</sup>, Petra van Bergeijk<sup>1</sup>,  
Joanna Lipka<sup>1,3</sup>, Nanda Keijzer<sup>2</sup>, Phebe S. Wulf<sup>1,2</sup>,  
Eugene A. Katrukha<sup>1</sup>, Anna Akhmanova<sup>1</sup>, &  
Casper C. Hoogenraad<sup>1,2</sup>

*Current Biology* (2013); **23**, pp. 828–834

---

<sup>1</sup> Division of Cell Biology, Faculty of Science, Utrecht University, Utrecht, The Netherlands.

<sup>2</sup> Department of Neuroscience, Erasmus Medical Center, Rotterdam, The Netherlands.

<sup>3</sup> International Institute of Molecular and Cell Biology, 02-109 Warsaw, Poland.

## Abstract

Intracellular transport is driven by motor proteins that either use microtubules or actin filaments as their tracks [1], but the interplay between these transport pathways is poorly understood [2–4]. Whereas many microtubule-based motors are known to drive long-range transport, several actin-based motors have been proposed to function predominantly in cargo tethering [4–6]. How these opposing activities are integrated on cargoes that contain both types of motors is unknown. Here we use inducible intracellular transport assays to show that acute recruitment of Myosin-V to kinesin-propelled cargo reduces their motility near the cell periphery and enhances their localization at the actin-rich cell cortex. Myosin-V arrests rapid microtubule-based transport without the need for regulated auto- or other inhibition of kinesin motors. In addition, Myosin-V, despite being an ineffective long-range transporter, can drive slow, medium-range (1–5  $\mu\text{m}$ ), point-to-point transport in cortical cell regions. Altogether, these data support a model in which Myosin-V establishes local cortical delivery of kinesin-bound cargoes through a combination of tethering and active transport.

## Results & discussion

The unconventional myosin motor Myosin-V has clear transporting roles in yeast and plants [7–11], but direct evidence for Myosin-V-driven point-to-point transport in vertebrate cells is surprisingly limited [2,4]. In these cells, microtubule-based motor proteins mediate most long-range transport, and Myosin-V-dependent vectorial transport has only been directly demonstrated in specialized structures with distinct actin organization, such as dendritic spines [12–14]. In contrast, experiments in which the intracellular motility of quantum dot-labeled Myosin-V was examined showed very short directional runs ( $<1$  s), whereas motility at longer timescales was random [15]. Myosin-V-dependent melanosome movements have also been reported, but the extent to which these movements were dependent on Myosin-V stepping, rather than dynamics of the actin cytoskeleton, has remained unclear [4,6,16]. Thus, it remains uncertain whether Myosin-V motors can drive directional cargo transport over longer distances on the non-uniform, disorganized actin cytoskeleton of mammalian cells [2,4]. Several models instead propose a role for Myosin-V in tethering of cargo transported by microtubule-based motors [2,4,5,17,18], but whether the presence of Myosin-V is sufficient to stall microtubule-based cargo motility is not known.

To directly probe the intracellular activity of Myosin-V in fibroblast cells, we created a fusion construct of GFP and Myosin-V, which was truncated such that it contained the motor domain and dimerization (coiled-coil) region but lacked the known cargo-binding domain [2,19,20] (MyoVb[1–1090]-GFP-FRB, hereafter called “Myosin-V”; Figure 1A). Upon expression in COS-7 cells, Myosin-V was highly enriched in actin-rich protrusions at the cell border (see Figure S1A). This specific distribution could be a consequence of motor activity towards the actin barbed end or represent a specific affinity for the actin present in these protrusions. To discriminate between these possibilities, we constructed a catalytically impaired motor (MyoVb[1–1090;G441A]-GFP-FRB [21], hereafter called “rMyosin-V,” from “rigor”; Figure 1A) and found no enrichment at the cell border (Figure S1B). In addition, because processive motor activity requires two coordinated motor domains, we also created MyoVb(1–893)-GFP-FRB, a construct lacking the dimerization domain. Again, no accumulation at the cell border was observed upon expression of this monomeric myosin construct (mMyosin-V, Figure S1C). In contrast, strong cortical accumulation of the shorter construct could be stimulated by chemically induced mMyosin-V dimer formation using the FKBP-rapalog-FRB system (Figures S1D and S1E), indicating that dimeric Myosin-V can move processively inside live COS-7 cells.

To further examine the intracellular dynamics of non-cargo-bound Myosin-V, we

performed time-lapse microscopy in cells expressing Myosin-V together with CDC42 to enhance formation of filopodia rich in uniformly barbed-end, out-oriented actin [22,23] (Figure S1F). Remarkably, although clear Myosin-V accumulation at the tips could be observed, the most apparent motility was directed inward and was similar to the retrograde flow observed for actin (Figure S1G). We next photobleached intermediate segments of filopodia to test for directional motility into filopodia and observed two modes of motility into the photobleached area, as expected from numerical simulations (Figure S1H). Myosin-V entered the distal part of the bleached area at the expected velocity of ~30 nm/s, whereas motility from the cell body into the

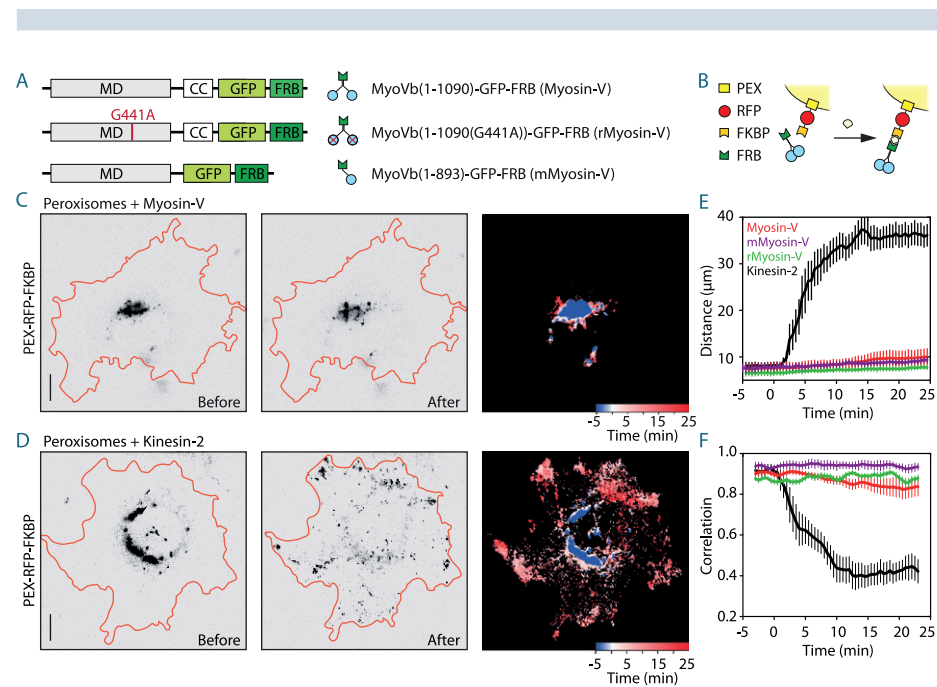


**Figure 1 | Intracellular dynamics of dimeric, monomeric, and catalytically impaired Myosin-V constructs.**

**(A)** Overview of Myosin-V constructs used in this study. **(B)** Assay: a fusion construct of PEX3, RFP and FKBP targets peroxisomes. Fusion of FRB with truncated motor construct (Myosin-V or kinesin-2) is recruited to FKBP and consequently the peroxisomes upon addition of rapalog. **(C and D)** Peroxisome distribution before and after recruitment of Myosin-V (C) or kinesin-2 (D) by rapalog addition (inverted contrast). Red curves indicate cell outline. Each third panel depicts an overlay of sequential binarized images from the respective recordings, color-coded by time as indicated. Blue marks the initial distribution, whereas red marks regions targeted upon addition of rapalog. **(E and F)** Average time traces of the  $R_{90\%}$  (radius of circle enclosing 90% of cellular fluorescence; see supplemental experimental procedures) (E) and the frame-to-frame correlation index (F) for peroxisomes in COS-7 cells expressing Myosin-V (red, see C,  $n = 6$  cells), mMyosin-V (purple,  $n = 4$  cells), rMyosin-V (green,  $n = 7$  cells), or kinesin-2 (black, see D,  $n = 10$ ) to which rapalog is added at time point 0. Error bars depict standard error (SE). Scale bars, 10  $\mu\text{m}$ .

filopodia occurred at the faster rate of ~300 nm/s (Figure S1I). Interestingly, many of the newly entered Myosin-V motors changed behavior in the bleached zone and started drifting back to the cell body at the slow rate (Figure S1I). Similar behaviors were observed for chemically-dimerized mMyosin-V (Figures S1J and S1K). Together, these data demonstrate that individual Myosin-V dimers alternate between active and passive actin-binding modes.

To directly probe the activity of Myosin-V bound to cargo, we employed our recently developed intracellular cargo-trafficking assay [24]. In this assay, we employ the FKBP-rapalog-FRB heterodimerization system to induce specific motor protein recruitment to peroxisomes during live-cell recordings (Figure 1B). Because peroxisomes are largely immobile in the perinuclear region before rapalog addition, their motility after rapalog addition selectively reports the activity of the specific FRB-tagged motor that was recruited. Whereas peroxisomes rapidly redistributed to the cell periphery upon recruitment of the plus-end-directed, microtubule-based motor kinesin-1 (KIF5, data not shown [24,25]) or kinesin-2 (KIF17, Figure 1D), very little peroxisome motility was observed upon chemically induced recruitment of Myosin-V (Figure 1C). To quantify these effects, we calculated for each time point the radius required to include 90% of all fluorescence intensity from the peroxisomes,  $R_{90\%}$  [24], and found a large increase upon recruitment of kinesin-2, whereas  $R_{90\%}$  hardly changed upon recruitment of Myosin-V, rMyosin-V, or mMyosin-V (Figure 1E). These data indicate that Myosin-V, when recruited to cargo in the perinuclear region, is not an effective long-range transporter inside live COS-7 cells.

The lack of robust cargo motility driven by Myosin-V could reflect an alternative role for Myosin-V on cargo, such as opposing microtubule-based motor proteins. Importantly, we observed that most kinesin-propelled peroxisomes never stopped moving after reaching the cell periphery but instead continued to be mobile (Figure 1D). To quantify this observation, we used image correlation analysis [26] to measure the overall frame-to-frame differences in our recordings. The average correlation index  $c_{30}(t)$  was calculated for each 30 s interval within a moving window of six frames to determine how the peroxisome motility changed over time. A correlation of 1 indicates that two images are completely identical, whereas 0 indicates that the intensity is distributed over a completely different set of pixels. Recruitment of kinesin-2 to peroxisomes caused a persistent drop in correlation  $c_{30}$  from  $0.91 \pm 0.02$  to  $0.42 \pm 0.06$  (mean  $\pm$  SD,  $n = 10$  cells), reflecting the rapid displacement of peroxisomes (Figure 1F). Consistent with our primary observations, the correlation index remained low even after arrival in the cell periphery. Only upon depolymerization of microtubules using nocodazole did the correlation index rapidly increase, reflecting that kinesin-driven motility was now prohibited (Figures S2A and S2B). These results demonstrate that kinesin-2 continues to drive rapid motility of cargo near the cell periphery.

To test how Myosin-V affects the motility of cargo driven by microtubule-based motor proteins, we next recruited kinesin-2 to peroxisomes together with Myosin-V or rMyosin-V (Figure 2A). Peroxisomes again rapidly moved outward in most cells (Figures

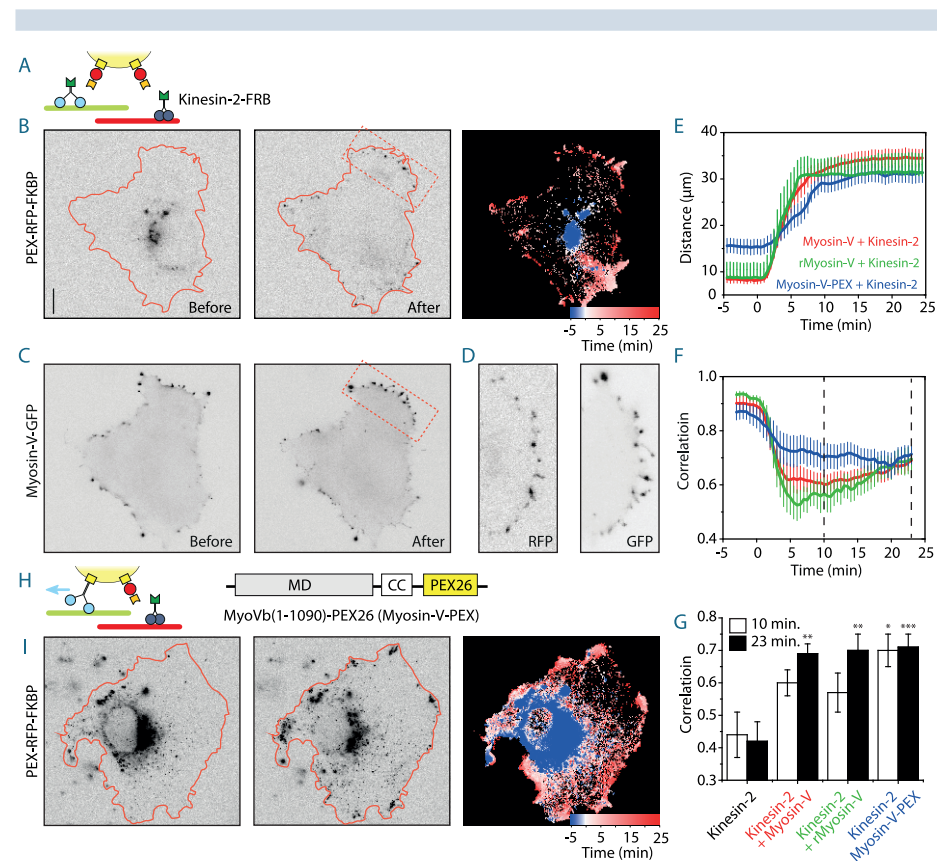


**Figure 2 | Myosin-V anchors kinesin-propelled cargo near the cell periphery.**

(A) Assay: two different motors are recruited to the peroxisomes upon addition of rapalog. (B) Peroxisome distribution before and after recruitment of Myosin-V and kinesin-2 by rapalog addition. Red curves indicate cell outline. Third panel depicts an overlay of sequential binarized images from the respective recordings, color-coded by time as indicated. (C) Distribution of MyoVb(1–1090)-GFP-FRB before and after addition of rapalog. (D) Enlargement of the regions marked in red in B and C. (E and F) Average time traces of the  $R_{90\%}$  (E) and the frame-to-frame correlation index (F) versus time for peroxisomes in COS-7 cells expressing kinesin-2 together with Myosin-V (red,  $n = 17$  cells), rMyosin-V (green,  $n = 7$  cells) or MyoVb(1–1090)-PEX26 (blue,  $n = 16$  cells). Dotted line marks time points used for G. (G) Average correlation at 10 and 23 minutes after rapalog addition for the indicated experiments. Asterisks depict p-values obtained from t-tests of values against control with KIF17 only (\*,  $p < 0.01$ ; \*\*,  $p < 0.005$ ; \*\*\*,  $p < 0.001$ ). (H) Assay: kinesin-2 is recruited to peroxisomes preloaded with Myosin-V using the fusion construct MyoVb(1–1090)-PEX26 (PEX26 to allow a fusion at the C-terminus of Myosin-V). (I) Peroxisome distribution before and after rapalog addition to recruit kinesin-2 to Myosin-V-coated peroxisomes. Red curves indicate cell outline. Third panel depicts an overlay of sequential binarized images from the respective recordings, color-coded by time as indicated. Contrast is inverted for all fluorescence images. Error bars depict SE. Scale bars, 10  $\mu\text{m}$ .

2B and 2E), but now most peroxisomes stopped at the cell border, where they became strongly colocalized with Myosin-V (Figures 2B–2D). Calculation of the correlation index over time revealed that, for both Myosin-V and rMyosin-V, the initial rapid drop upon addition of rapalog was now followed by an increase when peroxisomes reached the cell periphery, reflecting the reduced motility (Figures 2F and 2G). This selective peripheral anchoring by Myosin-V could reflect that Myosin-V recruitment to peroxisomes is inefficient in regions where it is not enriched. To test whether Myosin-V could oppose kinesin-based motility throughout the whole cell if recruited at sufficiently high levels, we recruited kinesin-2 to peroxisomes that were preloaded with Myosin-V through a direct fusion with the peroxisomal protein PEX26 (Figures 2H and 2I). Kinesin-2-driven displacement to the cell periphery was now decelerated (Figure 2E), and the correlation index was high throughout the cell and not only when peroxisomes reached the cell periphery (Figures 2F and 2G). These results demonstrate that Myosin-V can oppose kinesin-driven motility throughout the cell.

To specifically probe how acute Myosin-V recruitment affects the motility of kinesin-propelled cargo, we next used a fusion construct of kinesin-2 and PEX26 that, upon expression, induced the radial redistribution of peroxisomes (Figures 3A and 3B). Similar to the experiment where kinesin-2 was recruited by rapalog addition, these peroxisomes were not immobile near the cell periphery but kept changing positions, as reflected in the low correlation index of  $0.43 \pm 0.05$  (Figure 3F). When myosin was recruited to these motile peroxisomes, their dynamics slowed down dramatically (Figures 3B–3F). The observed increase in the correlation index from  $0.42 \pm 0.07$  (at 0:00) to  $0.65 \pm 0.07$  (at 23 minutes after rapalog addition) was only slightly less than the effect of complete microtubule depolymerization (from  $0.5 \pm 0.15$  to  $0.8 \pm 0.04$ ; see Figure S2B). However, in addition to the attenuation of microtubule-based motility, two effects could be distinguished. A subset of peroxisomes now appeared at the cell edge, where they co-localized with Myosin-V, whereas the other peroxisomes slowly moved away from the cell edge (Figures 3B–3E). Similar results were obtained when Myosin-V was recruited to peroxisomes propelled by the kinesin-1 family member KIF5B (Figure 3F). In contrast, although recruitment of rMyosin-V was sufficient to arrest kinesin-driven motility, it did not result in cargo accumulation at the cell edge, suggesting that peripheral accumulation requires active motility of Myosin-V (Figure 3F).

To directly test for directional Myosin-V-driven transport at the cell periphery of vertebrate cells, we repeated the dual-motor assay but now incubated cells with the microtubule-depolymerizing agent nocodazole before the start of the experiment to stop kinesin-2-driven peroxisomal motility (Figures 4A, S2A, and S2B). Recruitment of dimeric Myosin-V, but not rMyosin-V, resulted in the persistent directional motility of many peroxisomes toward the cell edge (Figures 4B–4N). Furthermore, recruitment of

(multiple) monomeric Myosin-V motors was also sufficient to induce directional motility of peroxisomes to the cell edge (Figures S2C–S2H). Finally, to maintain cytoskeletal integrity and stop kinesin-driven motility without microtubule depolymerization, we used specific chemical inhibition of kinesin-5-PEX26 using S-trityl-L-cysteine (STLC) [27,28] before addition of rapalog and again observed directional motility driven upon recruitment of Myosin-V (Figures S2J–S2P). These results directly demonstrate that, in contrast to the metabolically impaired rMyosin-V, Myosin-V can drive medium-range point-to-point transport ( $>1 \mu\text{m}$ ) toward the cell edge in mammalian cells.

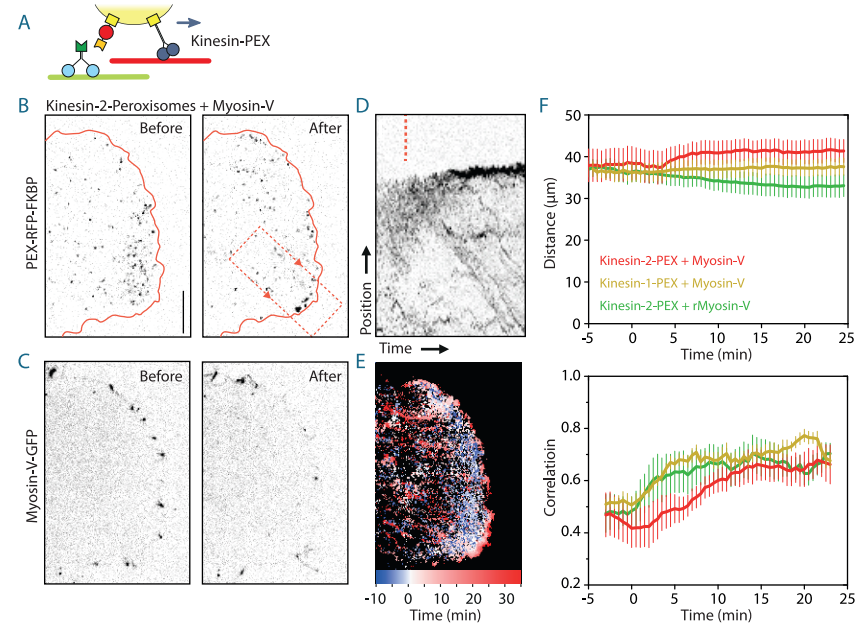


**Figure 3 | Acute recruitment of Myosin-V to kinesin-propelled cargo at the cell periphery.**

**(A)** Assay: a fusion construct of PEX26 with either kinesin-1 or kinesin-2 targets peroxisomes and redistributes them throughout the cell. PEX-RFP-FKBP also targets these peroxisomes and recruits Myosin-V upon addition of rapalog. **(B and C)** Peroxisome (B) and Myosin-V (C) distributions before and after recruitment of Myosin-V to kinesin-2 propelled peroxisomes by rapalog addition. Box indicates region used for kymograph in D. **(D)** Kymograph of the recordings shown in B. Dotted line marks rapalog addition. **(E)** Overlay of sequential binarized images from the recording in B, color-coded by time as indicated. **(F)** Time traces of the  $R_{90\%}$  (distance, top) and the frame-to-frame correlation index (bottom) versus time for peroxisomes in COS-7 cells expressing kinesin-2-PEX together with Myosin-V (red,  $n = 6$  cells) or rMyosin-V (green,  $n = 4$  cells), or kinesin-1-PEX together with Myosin-V (yellow,  $n = 5$  cells). Rapalog is added at time point 0. For this analysis, only peroxisomes located in the outer 10–20  $\mu\text{m}$  of the cell were included. Contrast is inverted for all fluorescence images. Error bars depict SE. Scale bars, 10  $\mu\text{m}$ .

To quantify these results, we traced individual peroxisomes linked to either Myosin-V or rMyosin-V, averaged their mean-squared displacements (MSD) for different time intervals  $\tau$ , and found that Myosin-V induced more motility than rMyosin-V (Figures 4N and 4O). The power dependence  $\alpha$  of the MSD with increasing time intervals  $\tau$ ,  $\text{MSD} \propto \tau^\alpha$ , is the anomalous diffusion exponent [15,29] and indicates whether motility is completely random ( $\alpha \approx 1$ , diffusive), directed ( $1 < \alpha \leq 2$ , superdiffusive), or confined ( $0 < \alpha < 1$ , subdiffusive). The overall Myosin-V-driven peroxisome motility was superdiffusive (slope in log-log plot  $> 1$ , Figure 4O), whereas motility in the presence of rMyosin-V was subdiffusive at short time scales ( $\tau < 100$  s) and superdiffusive at longer time scales as a result of slow movement away from the cell edge (Figure 4N). However, directed motility of Myosin-V was also often interspersed with long pauses or more random movements (Figures 4N and 4P). We therefore further analyzed peroxisome trajectories by calculating the MSD( $\tau$ ) and  $\alpha$  for a sliding window of 28 s to examine how  $\alpha(t)$  varied over time (Figures 4P and 4Q). This analysis revealed that peroxisome motility was often subdiffusive for many minutes ( $< \alpha > = 1.0 \pm 0.5$ , mean  $\pm$  SD, Figures 4P and 4Q). Nevertheless, many intervals were classified as superdiffusive episodes ( $\alpha > 1$ ), whereas for rMyosin-V most intervals were subdiffusive ( $< \alpha > = 0.6 \pm 0.4$ , mean  $\pm$  SD, Figure 4Q). Thus, Myosin-V can drive directional transport.

In this study, we have provided direct evidence for Myosin-V-driven directional cargo transport at the cell periphery, demonstrating that the dynamic and irregular peripheral actin organization still supports robust actin-based directional motility. Despite the overall directionality toward the cell edge, Myosin-V-mediated motility was highly irregular and frequently halted for long periods, consistent with earlier work showing that most Myosin-V-based motility is effectively random at 1–5 s time scales [15]. In addition, we have shown that acute recruitment of Myosin-V to kinesin-propelled cargo is sufficient to attenuate their motility. These results are consistent with the pioneering study of melanosome dynamics in mouse melanocytes, where Myosin-Va was shown to dampen both speed and length of microtubule-based runs [6]. Similar results have also been reported for mitochondria and secretory granules in neurons [17, 30] and recycling endosomes in HeLa cells [5]. The immediate stalling of kinesin-driven cargo observed upon stochastic coupling of Myosin-V demonstrates a kinesin inactivation scheme alternative to regulated unbinding or auto- or other inhibition.

Our model system provides a well-controlled method to examine the interplay between different types of motors inside cells but (intentionally) does not incorporate all aspects known to regulate motor activity. For example, the use of constitutively active and permanently attached Myosin-V and kinesin bypasses the regulatory layer in which specific adaptor molecules, such as melanophilin, and specific post-

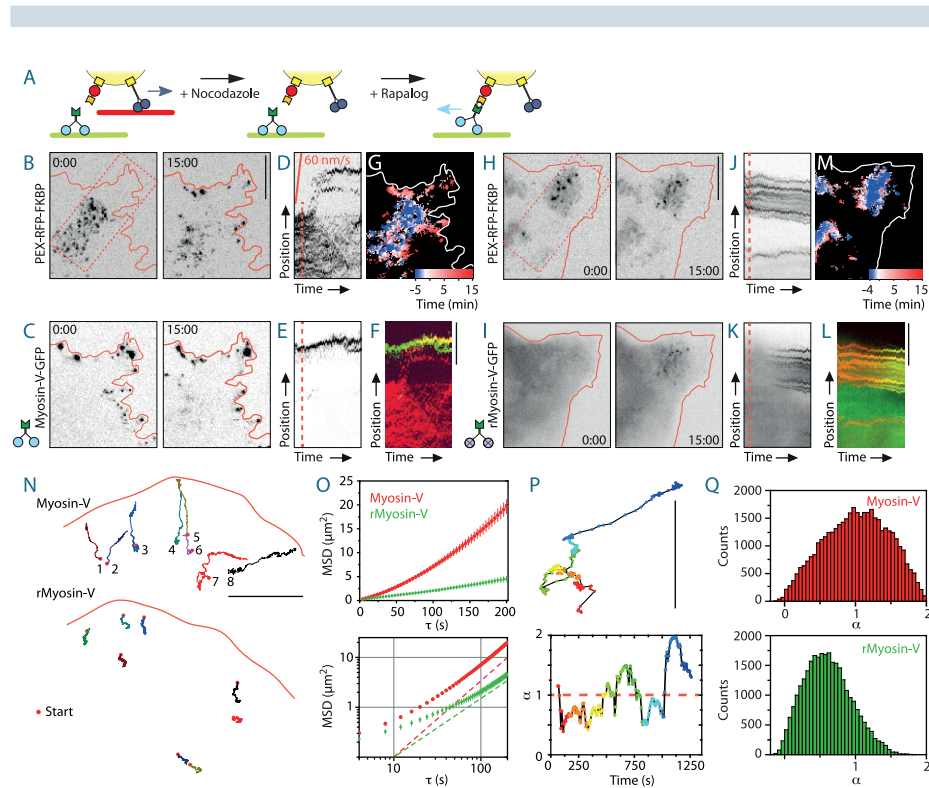


**Figure 4 | Myosin-V can autonomously drive directional cargo motility near the cell periphery.**

**(A)** Assay: peroxisomes are preloaded with kinesin-2 to induce peripheral distribution. After microtubule depolymerization by nocodazole addition, rapalog is added to recruit Myosin-V. **(B and C)** Frames from a time-lapse recording of peroxisomes (B) and Myosin-V (C) for the assay depicted in A. Time point 0:00 marks the addition of rapalog. Box indicates region used for kymograph in D-E. **(D and E)** Kymograph of the recordings shown in B and C, respectively. Dotted line marks rapalog addition. **(F)** Pseudocolored merge of D and E. **(G)** Overlay of sequential binarized images from the recording in B, color-coded by time as indicated. **(H and I)** Frames from a time-lapse recording of peroxisomes (H) and rMyosin-V (I) for the assay depicted in A. Time point 0:00 marks the addition of rapalog. Box indicates region used for kymograph in J-K. **(J and K)** Kymograph of the recordings shown in H and I, respectively. Dotted line marks rapalog addition. **(L)** Pseudocolored merge of J and K. **(M)** Overlay of sequential binarized images from the recording in B, color-coded by time as indicated. **(N)** Example trajectories of peroxisomes linked to Myosin-V (top) or rMyosin-V (bottom) near the cell edge (marked in red). Red dot marks start of the trajectory. Data acquired with 4 second intervals. Total time of trajectory: 1, 7:04; 2, 7:48; 3, 24:36; 4, 17:16; 5, 6:00; 6, 9:40; 7, 30:00; 8, 30:00. 16:44 for all trajectories of rMyosin-V. **(O)** Average mean squared displacement calculated from trajectories of peripherally located peroxisomes linked to either Myosin-V or rMyosin-V, plotted with linear (top) or logarithmic axes (bottom).  $n = 285$  and  $168$  trajectories for Myosin-V and rMyosin-V, respectively. **(P)** Example trajectory, color-coded for time from red to blue as indicated in the windowed  $\alpha_{0-28\text{ s}}(t)$  trace shown at bottom. **(Q)** Histograms of  $\alpha_{0-28\text{ s}}$  obtained from 38,426 and 29,937 28 s intervals from 285 and 168 different trajectories of Myosin-V and rMyosin-V. Contrast is inverted for all fluorescence images. Scale bars, 10  $\mu\text{m}$ , except N and P: 5  $\mu\text{m}$ .

translational modifications, such as phosphorylation, regulate motor attachment and conformation [2,31,32]. Future work will be needed to better understand how Myosin-V activity is controlled [13] and how the outcome of motor antagonism depends on the precise numbers of motors involved [33]. The approach introduced here will be an important starting point for such developments.

## Experimental procedures

### DNA constructs

The DNA constructs used in this study are cloned in pGW1-CMV or p $\beta$ actin-16-pl. Myosin-V(1-1090)-GFP-FRB (Myosin-V), Myosin-V(1-1090;G441A)-GFP-FRB (rMyosin-V), and Myosin-V(1-893)-GFP-FRB (mMyosin-V) were made by PCR from mouse Myosin-Vb cDNA (NM\_201600), purchased from Geneservice (IMAGE 40099275). PEX3 and PEX26 constructs were described previously [24]. For details, see supplemental experimental procedures.

### Cell cultures, live-cell image acquisition, and image processing and analysis

COS-7 were cultured in DMEM/Ham's F10 (1:1) medium containing 10% FCS and 1% penicillin/streptomycin. Cells were plated on 24-mm diameter coverslips and 2-3 days later transfected with FuGENE6 transfection reagent (Roche). Time-lapse live-cell imaging was performed on an Eclipse TE2000E (Nikon) equipped with a CoolSNAP HQ (Photometrics) camera and an incubation chamber (Tokai Hit; INUG2-ZILCS-H2) mounted on a motorized stage (Prior). COS-7 cells were imaged in Ringer's solution at 37  $^{\circ}\text{C}$ . During image acquisition, rapalog was added to establish a final rapalog concentration of 100 nM. Images of live cells were processed and analyzed using MetaMorph (Molecular Devices) and LabVIEW (National Instruments) software. For details, see supplemental experimental procedures.

## Acknowledgements

We are grateful to N. Hussain for Cdc42-myc cDNA, to Y. Hayashi for GFP-actin cDNA, and to Ariad Pharmaceuticals for FKBP/FRB cDNAs and rapalog (AP21967). J.L. is supported by the International Ph.D. Projects Program of Foundation for Polish Science (Studies of Nucleic Acids and Proteins—from Basic to Applied Research), co-financed by the European Union, Regional Development Fund, and co-supervised by J. Jaworski. This work was supported by the Erasmus Medical Center (EMC fellowship to L.C.K.) and the Netherlands Organisation for Scientific Research (NWO- ALW-VENI to L.C.K., NWO-ALW-VICI to A.A. and C.C.H., and NWO-nano to L.C.K. and C.C.H.), the Netherlands Organisation for Health Research and Development (ZonMW-TOP to A.A. and C.C.H.), and EMBO Young Investigators Program (YIP to C.C.H.). This research is also supported by the Dutch Technology Foundation STW, which is part of the Netherlands Organisation for Scientific Research (NWO), and which is partly funded by the Ministry of Economic Affairs.

## Author contributions

P.B., J.L., N.K. and P.S.W. cloned the DNA constructs. P.B. cloned all rigor myosin related constructs and the construct shown in Figure 2H, and validated the motor properties. L.C.K. designed the study, conducted the imaging experiments, analyzed the data with help from E.K., and wrote the paper with input from A.A. C.C.H. and P.B. A.A. and C.C.H. helped with the study design. C.C.H. supervised the project.

## References

- Vale, R.D. (2003) The molecular motor toolbox for intracellular transport. *Cell* **112**, 467-480
- Hammer, J.A., 3rd, and Sellers, J.R. (2011) Walking to work: roles for class V myosins as cargo transporters. *Nat Rev Mol Cell Biol*. **13**, 13-26
- Ross, J.L. et al. (2008) Cargo transport: molecular motors navigate a complex cytoskeleton. *Curr Opin Cell Biol* **20**, 41-47
- Woolner, S. and Bement, W.M. (2009) Unconventional myosins acting unconventionally. *Trends Cell Biol* **19**, 245-252
- Provance, D.W. et al. (2008) Myosin-Vb functions as a dynamic tether for peripheral endocytic compartments during transferrin trafficking. *BMC cell biology* **9**, 44
- Wu, X. et al. (1998) Visualization of melanosome dynamics within wild-type and dilute melanocytes suggests a paradigm for myosin V function In vivo. *J Cell Biol* **143**, 1899-1918
- Schott, D.H. et al. (2002) Secretory vesicle transport velocity in living cells depends on the Myosin-V lever arm length. *J Cell Biol* **156**, 35-39
- Pruyne, D. et al. (2004) Mechanisms of polarized growth and organelle segregation in yeast. *Annu Rev Cell Dev Biol* **20**, 559-591
- Verchot-Lubicz, J. and Goldstein, R.E. (2010) Cytoplasmic streaming enables the distribution of molecules and vesicles in large plant cells. *Protoplasma* **240**, 99-107
- Peremyslov, V.V. et al. (2010) Class XI myosins are required for development, cell expansion, and F-Actin organization in Arabidopsis. *The Plant cell* **22**, 1883-1897
- Zhang, J. et al. (2011) Aspergillus Myosin-V supports polarized growth in the absence of microtubule-based transport. *PLoS One* **6**, e28575
- Wagner, W. et al. (2011) Myosin-Va transports the endoplasmic reticulum into the dendritic spines of Purkinje neurons. *Nat Cell Biol* **13**, 40-48
- Wang, Z. et al. (2008) Myosin Vb mobilizes recycling endosomes and AMPA receptors for postsynaptic plasticity. *Cell* **135**, 535-548
- Schuh, M. (2012) An actin-dependent mechanism for long-range vesicle transport. *Nat Cell Biol* **13**, 6
- Nelson, S.R. et al. (2009) Random walk of processive, quantum dot-labeled myosin Va molecules within the actin cortex of COS-7 cells. *Biophys J* **97**, 509-518
- Gross, S.P. et al. (2002) Interactions and regulation of molecular motors in *Xenopus* melanophores. *J Cell Biol* **156**, 855-865
- Pathak, D. et al. (2010) Evidence that myosin activity opposes microtubule-based axonal transport of mitochondria. *J Neurosci* **30**, 8984-8992
- Desnos, C. et al. (2007) 'Should I stay or should I go?': myosin V function in organelle trafficking. *Biology of the cell / under the auspices of the European Cell Biology Organization* **99**, 411-423
- Liu, J. et al. (2006) Three-dimensional structure of the myosin V inhibited state by cryoelectron tomography. *Nature* **442**, 208-211
- Thirumurugan, K. et al. (2006) The cargo-binding domain regulates structure and activity of myosin 5. *Nature* **442**, 212-215
- Yengo, C.M. et al. (2002) Kinetic characterization of the weak binding states of myosin V. *Biochemistry* **41**, 8508-8517
- Hussain, N.K. et al. (2001) Endocytic protein intersectin-1 regulates actin assembly via Cdc42 and N-WASP. *Nat Cell Biol* **3**, 927-932

23. Nobes, C.D. and Hall, A. (1995) Rho, rac, and cdc42 GTPases regulate the assembly of multimolecular focal complexes associated with actin stress fibers, lamellipodia, and filopodia. *Cell* **81**, 53-62
24. Kapitein, L.C. et al. (2010) Probing intracellular motor protein activity using an inducible cargo trafficking assay. *Biophys J* **99**, 2143-2152
25. Kapitein, L.C. et al. (2010) Mixed microtubules steer dynein-driven cargo transport into dendrites. *Curr Biol* **20**, 290-299
26. Kolin, D.L. and Wiseman, P.W. (2007) Advances in image correlation spectroscopy: measuring number densities, aggregation states, and dynamics of fluorescently labeled macromolecules in cells. *Cell biochemistry and biophysics* **49**, 141-164
27. Skoufias, D.A. et al. (2006) S-trityl-L-cysteine is a reversible, tight binding inhibitor of the human kinesin Eg5 that specifically blocks mitotic progression. *J Biol Chem* **281**, 17559-17569
28. Ally, S. et al. (2009) Opposite-polarity motors activate one another to trigger cargo transport in live cells. *J Cell Biol* **187**, 1071-1082
29. Saxton, M.J. and Jacobson, K. (1997) Single-particle tracking: applications to membrane dynamics. *Annu Rev Biophys Biomol Struct* **26**, 373-399
30. Desnos, C. et al. (2007) Myosin va mediates docking of secretory granules at the plasma membrane. *J Neurosci* **27**, 10636-10645
31. Akhmanova, A. and Hammer, J.A., 3rd (2010) Linking molecular motors to membrane cargo. *Curr Opin Cell Biol* **22**, 479-487
32. Karcher, R.L. et al. (2002) Motor-cargo interactions: the key to transport specificity. *Trends Cell Biol* **12**, 21-27
33. Derr, N.D. et al. (2012) Tug-of-war in motor protein ensembles revealed with a programmable DNA origami scaffold. *Science* **338**, 662-665

## Supplemental figures

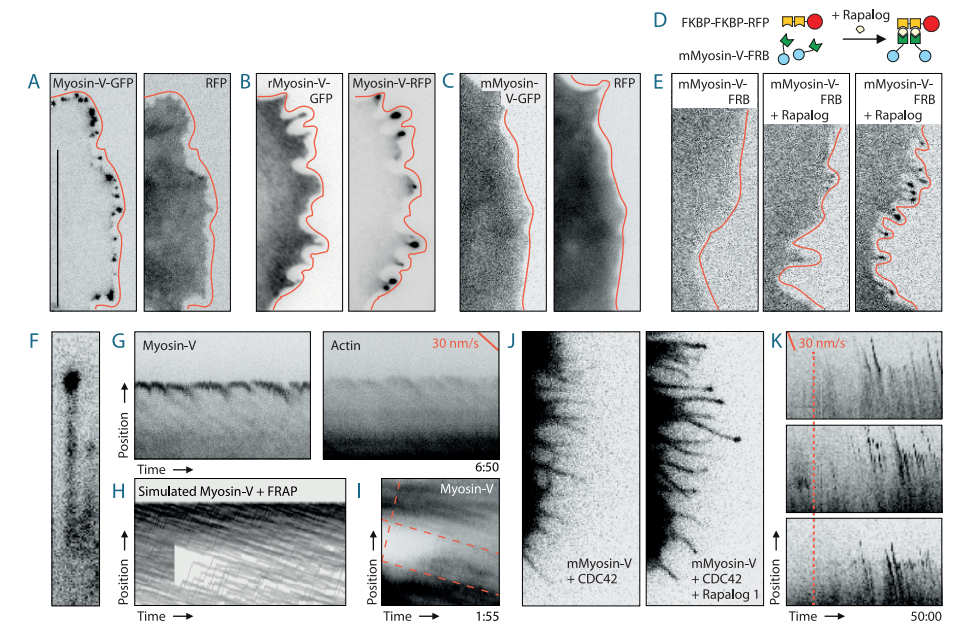


**Figure S1 | Related to Figure 1.**

**(A)** Distribution of MyoVb(1–1090)-GFP-FRB (left) and mRFP (right) in a COS-7 cell. **(B)** Distribution of MyoVb(1–1090(G441A))-GFP-FRB (left) and MyoVb(1–1090)-mRFP-FRB (right) in a COS-7 cell. **(C)** Distribution of MyoVb(1–893)-GFP-FRB (left) and RFP (right) in a COS-7 cell. **(D)** Schematic of FRB-MyoV-FRB based dimerization of MyoVb(1–893)-GFP-FRB. **(E)** Distribution of MyoVb(1–893)-GFP-FRB before and after addition of rapalog. **(F)** Distribution of MyoVb(1–1090)-GFP-FRB in a filopodium of a CDC42 overexpressing COS-7 cell. **(G)** Kymograph showing the dynamics of MyoVb(1–1090)-mRFP-FRB and GFP-actin in a filopodium. **(H)** Simulated FRAP experiment on Myosin-V in a filopodium, assuming that motors stochastically switch between active motility at 300 nm/s and passive binding to actin treadmilling at 30 nm/s. Fast fluorescence recovery in the bleached zone depends on active motility from the filopodium base, followed by switching to passive binding. **(I)** FRAP experiment on MyoVb(1–1090)-GFP-FRB in a filopodium, revealing fast motility to the filopodium tip at 300 nm/s. Yellow lines indicate the average speeds of slow (20 nm/s) and fast (300 nm/s) motility observed for Myosin-Vb. **(J)** Distribution of MyoVb(1–893)-GFP-FRB before and after addition of rapalog in COS-7 cells overexpressing CDC42. **(K)** Kymographs showing the dynamics of MyoVb(1–893)-mRFP-FRB in filopodia of COS-7 cells overexpressing CDC42 before and after addition of rapalog, marked by the dotted line.

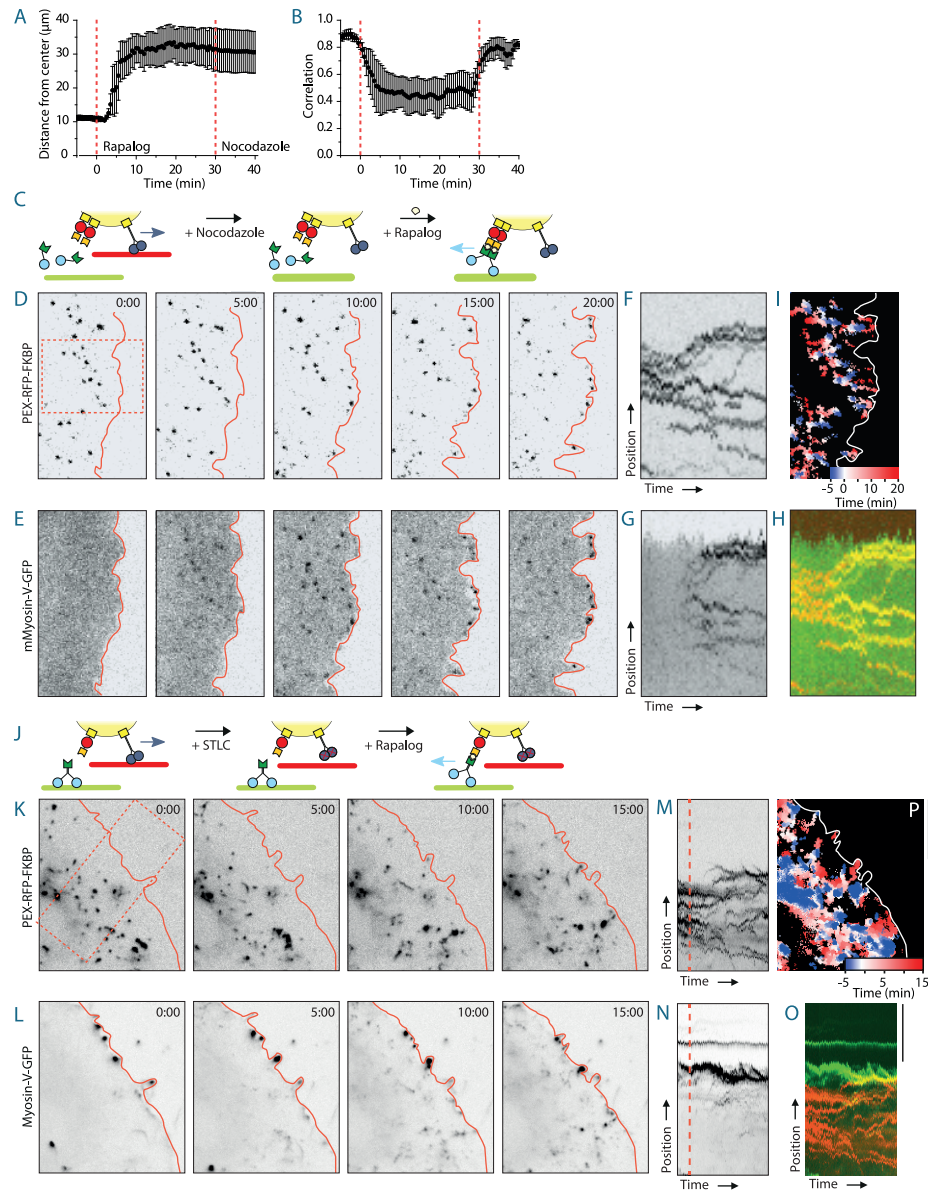


**Figure S2 | Related to Figure 4.**

**(A and B)** Time traces of the  $R_{90\%}$  (distance, A) and the frame-to-frame correlation index (B) versus time for peroxisomes in COS-7 cells expressing kinesin-2. Rapalog is added at time point 0 and nocodazole is added at time point 30. Onset of effect before time point 30 is the result of the windowed analysis (see supplemental experimental procedures). **(C)** Assay: peroxisomes are preloaded with kinesin-2 to induce peripheral distribution. After kinesin-5 inhibition by  $50 \mu\text{M}$  S-trityl-L-cysteine, rapalog is added to recruit mMyosin-V (MyoVb(1–893)-GFP-FRB). **(D and E)** Frames from a time-lapse recording of peroxisomes (D) and Myosin-V (E) for the assay depicted in C. Time point 0:00 marks the addition of rapalog. Box indicates region used for kymograph in F–G. **(F and G)** Kymograph of the recordings shown in D and E, respectively. Dotted line marks rapalog addition. **(H)** Pseudocolored merge of F and G. **(I)** Overlay of sequential binarized images from the recording in D, color-coded by time as indicated. **(J)** Assay: Peroxisomes are preloaded with kinesin-5 to induce peripheral distribution. After kinesin-5 inhibition by  $50 \mu\text{M}$  S-trityl-L-cysteine, rapalog is added to recruit Myosin-V. **(K and L)** Frames from a time-lapse recording of peroxisomes (K) and Myosin-V (L) for the assay depicted in J. Time point 0:00 marks the addition of rapalog. Box indicates region used for kymograph in M–N. **(M and N)** Kymograph of the recordings shown in K and L, respectively. Dotted line marks rapalog addition. **(O)** Pseudocolored merge of M and N. **(P)** Overlay of sequential binarized images from the recording in K, color-coded by time as indicated. Contrast is inverted for all fluorescence images. Error bars depict standard error. Scale bars,  $10 \mu\text{m}$ .

# Supplemental experimental procedures

## DNA constructs

The constructs used in this study are cloned in the following mammalian expression vectors; pGW1-CMV (British Biotechnology) or pβactin-16-pl (chicken β-actin promoter) [34]. The original pGW1-CMV vector was modified by inserting a multiple cloning site (HindIII-Ascl-EcoRI-BamHI-Sall-NotI-XbaI) in order to generate pGW2. The original pβactin-16-pl vector was modified by inserting a multiple cloning site (NheI-HindIII-Ascl-EcoRI-BamHI-Sall-SpeI-NotI-XbaI). Cloning of pβactin-PEX3-mRFP-FKBP (PEX-RFP-FKBP), pβactin-KIF17(1-547)-FRB (kinesin-2-FRB) and pGW2-KIF17(1-547)-GFP-PEX26 (kinesin-2-PEX) was described previously [24]. GW1-mRFP-FKBP was generated by taking out the PEX3 targeting sequence from GW1-PEX-mRFP-FKBP [24]. pβactin-MyosinVb-(amino acid 1-1090)-GFP-FRB (Myosin-V), pβactin-MyosinVb-(amino acid 1-1090((G441A))-GFP-FRB (rMyosin-V) and pβactin-MyosinVb-(amino acid 1-893)-GFP-FRB (mMyosin-V) were made by PCR from mouse Myosin-Vb cDNA (NM\_201600), purchased from Geneservice (IMAGE 40099275) and inserted in pβactin-GFP-FRB [34]. The mutation G441A is similar to G440A in chicken Myosin-Va, which traps the motor in an ATP-bound form with high affinity for F-actin [21]. Cdc42-myc was a gift of Dr. N. Hussain [22] and GFP-actin was a gift of Dr. Y. Hayashi [35]. pGW2-PEX26 was made by PCR using pGW2-GFP-PEX26 as a template [23]. Subsequently, MyosinVb-(amino acid 1-1090) and KIF5bMD [23] were ligated in the Ascl and EcoRI sites of pGW2-PEX26 to generate pGW2-MyosinVb-(amino acid 1-1090)-PEX26 and pGW2-KIF5bMD-PEX26. pGW2-Kinesin-5(amino acid 1-526)-PEX26 was made by PCR from human kinesin-5 cDNA (NM\_004523.3), purchased from Imagene (IMAGE 9020463) and inserted in EcoRI and Sall sites of pGW2-PEX26.

## Cell cultures and transfection

COS-7 were cultured in DMEM/Ham's F10 (1:1) medium containing 10% FCS and 1% penicillin/streptomycin. 2–3 days before transfection, cells were plated on 24-mm diameter coverslips. Cells were transfected with Fugene6 transfection reagent (Roche) according to the manufacturers protocol and grown for 16 hours, respectively.

## Live-cell image acquisition

Time-lapse live-cell imaging was performed on a Nikon Eclipse TE2000E (Nikon) equipped with an incubation chamber (Tokai Hit; INUG2-ZILCS-H2) mounted on a motorized stage (Prior). Coverslips (24 mm) were mounted in metal rings, immersed in 0.6 ml Ringer's solution (10 mM Hepes, 155 mM NaCl, 1 mM CaCl<sub>2</sub>, 1 mM MgCl<sub>2</sub>, 2 mM NaH<sub>2</sub>PO<sub>4</sub>, 10 mM glucose, pH 7.2) and maintained at 37°C. For most acquisitions 4–6 cells were selected and imaged every 30 seconds for 30–60 minutes using a 40x objective (Plan Fluor, NA=1.3, Nikon) and a Coolsnap HQ camera (Photometrics). A mercury lamp (Osram) was used for excitation. For some of the recordings in Figure S1, TIRFM was performed using a 100x objective (Apo TIRF, NA=1.49, Nikon), 2.5x Optovar, and EMCDD camera (QuantEM, Roper Scientific) as described previously [36].

Rapalog (AP21967) was dissolved to 1 mM in ethanol and further diluted to 0.1 mM in ethanol. During image acquisition, 0.2 ml of Ringer's solution with rapalog (400 nM) was added to establish a final rapalog concentration of 100 nM. To block motility of kinesin-2-PEX or KIF11-PEX before recruitment of Myosin-V, nocodazole or S-Trityl-L-Cysteine was added to a final concentration of 20 μM or 50 μM, respectively.

## Image processing and analysis

Images of live cells were processed and analyzed using MetaMorph (Molecular Devices) and LabVIEW (National Instruments) software. Before analysis, cells were masked to exclude contributions from neighboring

cells to the analysis. For the color-coded redistribution plots, all images of a time-lapse recording were thresholded to yield binary images that were subsequently overlaid non-transparently, starting with the final frame (first frame on top). Each frame was colored using a time-coded gradient that ran from blue to white before and from white to red after rapalog addition at 0:00 [25]. Before calculation of  $R_{90\%}(t)$  and  $c_{30}(t)$  curves (see below), background subtracted recordings were thresholded to include only intensities exceeding 3–5 times the standard deviation of the background, limiting analysis to peroxisomes and eliminating potential contributions from weak background objects.

To quantify the radial redistribution of peroxisomes upon recruitment of (additional) motor proteins, the radius required to include 90% of the total intensity of the cell,  $R_{90\%}(t)$ , was calculated for each frame as described previously [24]. To quantify the overall dynamics of peroxisomes for a given cell, we defined a correlation index  $c(\tau)$  that measures the similarity between images in a time series as a function of the time gap  $\tau$  between these images [26]. The average integrated intensity of all images obtained by multiplying all possible pairs of  $\tau$ -spaced images in a time series was calculated for each  $\tau$  and normalized by the average integrated intensity obtained for  $\tau=0$ . For a time series of N images with an image size of X by Y pixels with intensities  $i(x,y,t)$ , this can be expressed as

$$c(\tau) = c(n\Delta t) = \frac{N}{N-n} \frac{\sum_{a=1}^{N-n} \sum_{x=1}^X \sum_{y=1}^Y i(x,y,a) i(x,y,a+n)}{\sum_{a=1}^N \sum_{x=1}^X \sum_{y=1}^Y i(x,y,a)^2}$$

in which  $\tau$  is discretized as  $n\Delta t$ , with n denoting frame number (starting at 0) and  $\Delta t$  the interval between frames.  $c(\tau)$  will be 1 if the particles are completely anchored and their positions unchanged after a time  $\tau$ , whereas  $c(\tau)$  will be 0 if all particles moved to previously unoccupied locations. In practice,  $c(\tau)$  will remain finite even in very dynamic samples, because a subset of particles will move to locations that were occupied by different particles in the first image.

$c(\tau)$  measures the average similarity between images for increasing time intervals  $\tau$ , assuming that no sudden changes in overall dynamics occur during acquisition of the time series. To quantify changes in the dynamics of peroxisomes upon recruitment of (additional) motor proteins (i.e. Figure 3L), we measured the average  $c(\tau)$  for  $\tau=30$  seconds in a moving window of 6 frames to obtain a correlation time trace  $c_{30}(t)$  for the whole time lapse recording. Averaging over a small window of frames reduced the fluctuations that emerged from small repositioning errors in multi-position recordings.

To analyze individual peroxisome trajectories in the presence of nocodazole (Fig. 4N–Q), peroxisomes located within ~10–20 μm of the cell edge were traced using the u-track Matlab program [37]. Default parameters were used for detection and tracking, apart from the size of point spread function that was equal to experimental. For each trajectory the mean squared displacement,  $MSD(\tau)$ , was calculated by internal averaging for a sliding time window of 30 frames, and the first 7 points (excluding zero) were used to fit  $MSD = a \cdot \tau^\alpha$ , with  $\alpha$  termed the diffusive exponent [15]. For purely random motion,  $\alpha = 1$ , for unidirectional motility at constant speed,  $\alpha = 2$ , whereas  $1 < \alpha < 2$  is indicative of directed, but irregular motility. In addition  $0 < \alpha < 1$  suggests subdiffusive behavior, where motility is confined within a certain zone. This analysis yielded a time traces of a for each particle (Fig. 4P). In addition to this windowed analysis, non-windowed  $MSD(\tau)$  traces were calculated for each trajectory and averaged (Fig. 4O).

## Simulation of Myosin-V dynamics in filopodia

Simulations of Myosin-V dynamics in filopodia were performed as described previously for bidirectional dynein-driven motility on the mixed microtubule array of neuronal dendrites, but now with different velocity and run length for anterograde (300 nm/s and 3 s) and retrograde motility (30 nm/s and 28 s). Simulations start with an empty filopodium and require some time to reach steady state. The segment shown is cutout of a simulation of 50.000 frames, with entry rate  $0.2 \text{ s}^{-1}$  and filopodium length 20 μm.

## Supplemental references

34. Kapitein, L.C. et al. (2010) Microtubule dynamics in dendritic spines. *Methods Cell Biol* **97**, 111-132
35. Okamoto, K. et al. (2004) Rapid and persistent modulation of actin dynamics regulates postsynaptic reorganization underlying bidirectional plasticity. *Nat Neurosci* **7**, 1104-1112
36. Kapitein, L.C. et al. (2008) Microtubule-driven multimerization recruits ase1p onto overlapping microtubules. *Curr Biol* **18**, 1713-1717
37. Jaqaman, K. et al. (2008) Robust single-particle tracking in live-cell time-lapse sequences. *Nat Methods* **5**, 695-702





## Myosin-V opposes kinesin-driven cargo entry into the axon

# 4

Anne F.J. Janssen<sup>1</sup>, Roderick P. Tas<sup>1</sup>,  
Petra van Bergeijk<sup>1</sup>, Rosalie Oost<sup>1</sup>,  
Casper C. Hoogenraad<sup>1</sup> & Lukas C. Kapitein<sup>1</sup>

---

<sup>1</sup> Division of Cell Biology, Faculty of Science, Utrecht University, Utrecht, The Netherlands.

• These authors contributed equally to this work.

## Abstract

The selective transport of different cargoes into axons and dendrites underlies the polarized organization of the neuron. Although it has become clear that the combined activity of different motors determines the destination and selectivity of transport, little is known about the mechanistic details of motor cooperation. For example, the exact role of Myosin-V in opposing microtubule-based axon entries has remained unclear. Here we use two orthogonal chemically-induced heterodimerization systems to independently recruit different motors to cargoes at known stoichiometries. We find that recruiting Myosin-V to kinesin-propelled cargoes at equal numbers is sufficient to stall motility. Kinesin-driven cargoes entering the axon were arrested in the axon initial segment (AIS) upon Myosin-V recruitment and accumulated in distinct actin-rich hotspots. Importantly, unlike proposed previously, Myosin-V did not return these cargoes to the cell body, suggesting that additional mechanisms are required to establish cargo retrieval from the AIS.

## Introduction

The selective transport of different cargoes into axons and dendrites underlies the polarized organization of the neuron. Recent work has revealed that different motor proteins have different selectivity for axons and dendrites. For example, some kinesins selectively target axons, while others target both axons and dendrites [1,2]. In addition, Myosin-V has been implicated in selective targeting to dendrites [3]. Expression of a dominant negative form of Myosin-Va caused the non-specific localization of cargo otherwise enriched in the somatodendritic compartment. Furthermore, coupling a protein to a Myosin-Va binding domain was sufficient to cause its somatodendritic localization. More recent work has reported that vesicles with dendritic cargoes often enter the axon, but stop and reverse in the axon initial segment (AIS) in a process that depends on Myosin-Va and an intact actin cytoskeleton [4]. Nevertheless, the exact contribution of actin and Myosin-V to axonal exclusion has remained controversial, given that actin disruption also distorted the sorting of cargoes into the proper carriers [5]. In addition, whether recruitment or activation of Myosin-V is sufficient to cause the reversal of dendritic cargo has remained unclear.

Although it has become clear that the combined activity of different motors determines transport destination and selectivity, little is known about the mechanistic details of motor cooperation. For example, it is not known whether acute activation or recruitment of Myosin-V is sufficient to oppose kinesin-based axon entries. More generally, how the outcome of multiple motors depends on the relative amounts of motor proteins recruited to cellular cargoes has remained unexplored. Elegant *in vitro* assays have used DNA origami to assemble well-defined combinations of different motor proteins [6], but similar control has not yet been achieved inside cells. Previously, acute recruitment of different motor proteins using chemically-induced heterodimerization has been used to probe combinatorial motor activity in non-neuronal cells [7,8]. These experiments revealed that, in non-neuronal COS-7 cells, recruitment of Myosin-V is sufficient to attenuate kinesin-propelled cargo [8]. However, in these assays, the ratio between myosin and kinesin motors could not be tuned nor assessed.

Here we introduce a new assay that allows the independent recruitment of different motor proteins at defined ratios. We find that recruiting Myosin-V to kinesin-propelled cargoes at equal numbers is sufficient to stall motility. Kinesin-driven cargoes entering the axon were arrested in the AIS upon Myosin-V recruitment and accumulated in distinct actin-rich hotspots. Importantly, unlike proposed previously, Myosin-V did not return these cargoes to the cell body, suggesting that additional mechanism are required to establish cargo retrieval from the AIS.

# Results

To establish an assay for the independent recruitment of different motors, the FKBP-*rapalog*-FRB heterodimerization system was combined with a recently introduced chemically-induced heterodimerization system in which the cell-permeable, AM-modified plant hormone gibberellin triggers the interaction between a GID1 and a GAI domain [9]. We chose this dimerization system over light-induced systems, because, similar to the FKBP-*rapalog*-FRB system, the induced complex formation has been reported to be essentially irreversible. As a result, the available sites on the cargoes will be quickly saturated as long as the number of GAI-labeled motors in the cell is higher than the total number of GID1-sites on the cargoes, irrespective of the exact concentrations. Therefore, if both heterodimerization systems are combined in one peroxisome-targeting construct, PEX3-mRFP-FKBP-linker-GID1, the FRB and GAI domains will be recruited with equal probabilities. Since FKBP was shown to be functional irrespective of N- or C-terminal fusions, it was decided to place GID1 rather than FKBP at the C-terminus.

To test the independent recruitment of different motors, COS-7 cells were transfected with PEX3-mRFP-FKBP-linker-GID1, KIF17-GFP-GAI and MyoVb-iRFP-FRB (Figures 1A and 1B). Upon addition of gibberellin, KIF17-GFP-GAI was recruited to PEX3-mRFP-FKBP-linker-GID1 and peroxisomes were rapidly redistributed to the cell periphery (Figure 1C). Similar to previous observations, peroxisomes in the cell periphery remained mobile even after reaching the periphery of the cell [8]. In addition, contrary to FKBP-based heterodimerization, we noted that a subset of peroxisomes was already mobile at the periphery before addition of gibberellin, indication some degree of background heterodimerization. To still ensure independent recruitment of different motors, gibberelin-based motor recruitment was always performed prior to *rapalog*-based recruitment.

25 minutes after addition of gibberellin to recruit kinesin, *rapalog* was added to recruit Myosin-V (Figure 1A), resulting in an arrest of the kinesin-driven motility and the accumulation of peroxisomes near the cell cortex (Figure 1C). These effects were quantified using two previously introduced metrics [10]. First, we calculated for all frames the radius required to include 90% of the fluorescence intensity of the peroxisomes ( $R_{90\%}$ ), which revealed that peroxisomes moved rapidly to the periphery upon recruitment of kinesin, but did not move much further upon recruitment of Myosin-V (Figures 1D and 1E). Second, we used image correlation analysis to measure the overall frame-to-frame similarity during the experiment. In the absence of transport, two subsequent images are largely identical and the correlation index will

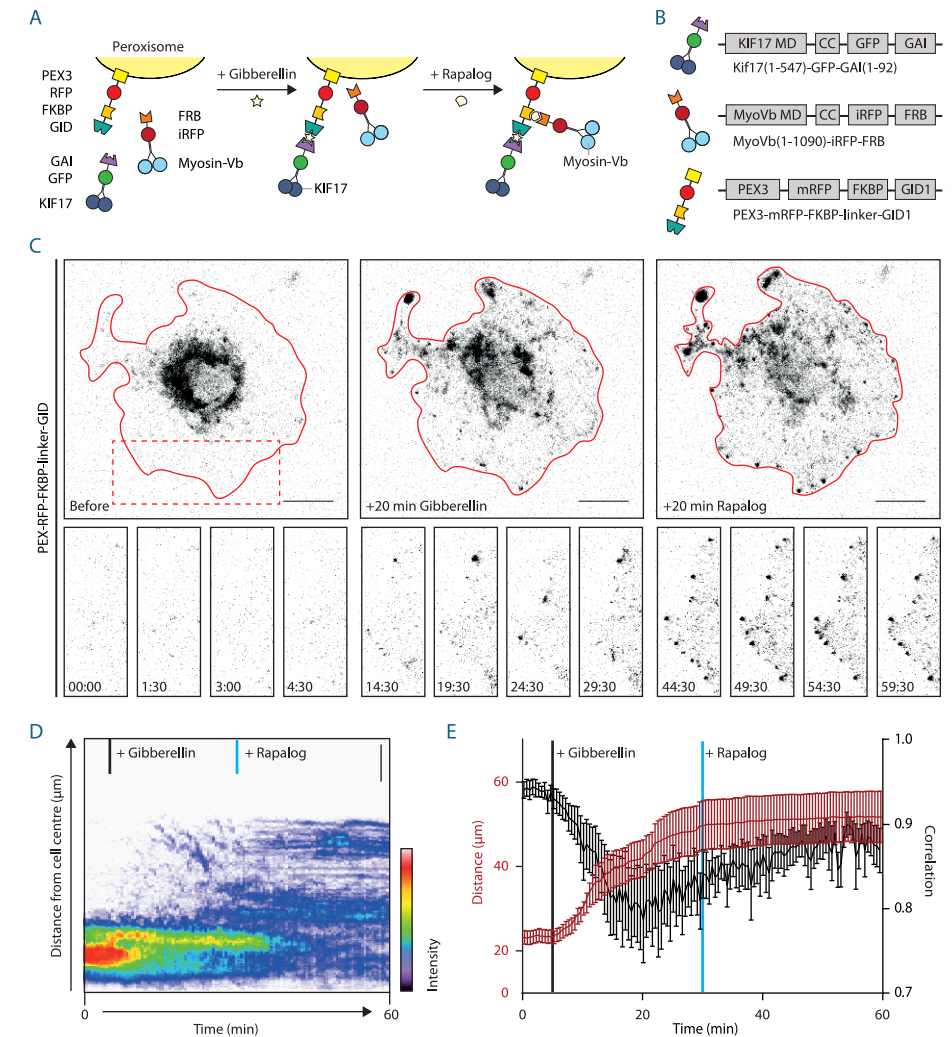
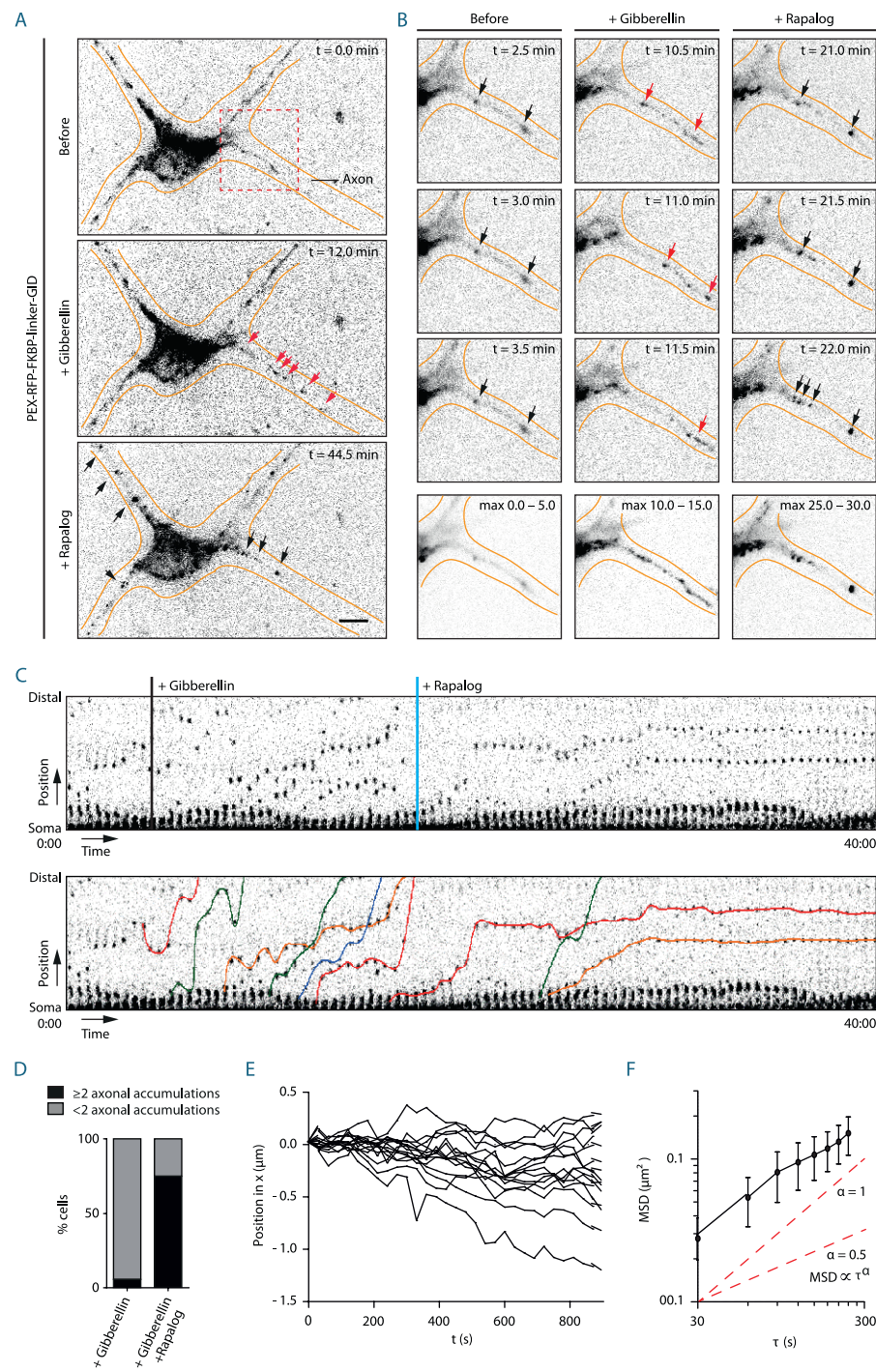


**Figure 1 | Myosin-V anchors kinesin propelled cargo in COS-7 cells.**

**(A)** Assay: sequential recruitment of kinesin and Myosin-V by the addition of gibberellin and *rapalog*, respectively. **(B)** Overview of constructs. MD, motor domain; CC, coiled-coil; NC, neck coil; GAI, gibberellin insensitive; GID1, gibberellin insensitive dwarf1. **(C)** Peroxisome distribution before the recruitment of motors and after sequential recruitment of kinesin and Myosin-V. Red curves indicate cell outline. Panels show individual frames of a cut out. Scale bar, 20  $\mu\text{m}$ . **(D)** Radial kymograph indicating the redistribution of fluorescent peroxisomes relative to the cell axis. Vertical lines indicate addition of gibberellin (black) and *rapalog* (blue). Scale bar, 10  $\mu\text{m}$ . **(E)** Displacement (expressed in  $R_{90\%}$ , red) and correlation (frame-to-frame similarity from 0 to 1, black) versus time.  $n = 8$  cells from two independent experiments, mean  $\pm$  SEM. Vertical lines indicate time of gibberellin (black) and *rapalog* (blue) addition.



be close to 1, whereas a value of 0 indicates that all organelles have moved to previously unoccupied positions. The correlation index decreased upon kinesin recruitment, reflecting the increased peroxisome motility, whereas it increased after recruitment of Myosin-V, indicating that peroxisomes became less motile (Figure 1E). Thus, different heterodimerization systems can be combined to independently recruit different motor proteins at fixed stoichiometry, and the recruitment of Myosin-V to kinesin motors at a 1:1 ratio is sufficient to arrest kinesin-driven motility.

We next switched to neurons to examine how recruitment of Myosin-V alters the kinesin-driven transport of peroxisomes into the axon. We used the kinesin-1 KIF5B, because this motor has been reported to efficiently target cargoes selectively into the axon [5,11,12]. Indeed, the addition of gibberellin to dissociated hippocampal neurons expressing PEX3-mRFP-FKBP-linker-GID1, KIF5-GFP-GAI and MyoVb-iRFP-FRB induced a burst of peroxisome motility selectively into the axon (Figures 2A, 2B second column, 2C). Remarkably, the subsequent addition of rapalog to recruit Myosin-V resulted in the appearance of several spots in the proximal axon where axon-entering peroxisomes would cluster together, whereas the motility of peroxisomes further down the axon continued as before (Figures 2A, 2B third column, 2C). Quantification revealed that the percentage of cells that had more than two proximal axonal accumulations increased from 6.25 to 75% during the first 40 minutes after addition of gibberellin (Figure 2D). Thus, the acute, close-to-equimolar recruitment of Myosin-V to kinesin-1 driven, axon-entering cargoes will cluster these cargoes in the proximal axon.

Previous work has suggested that Myosin-V can drive retrograde axonal transport, thereby returning to the cell body cargoes that have erroneously entered the axon [13]. In contrast, we observed that Myosin-V induced the appearance of cargo clusters that were largely immobile. To analyze the motility of the Myosin-V induced peroxisome clusters in more detail and test for retrograde motility, we traced individual

**Figure 2 | Myosin-V anchors kinesin-1 propelled peroxisomes in the proximal axon.**

**(A)** Dissociated hippocampal neuron showing the distribution of PEX3-mRFP-FKBP-linker-GID1 before (top), after the recruitment of KIF5-GFP-GAI through addition of gibberellin (middle), and after the addition of rapalog to recruit MyoVb-iRFP-FRB (bottom). Red arrows indicate motile peroxisomes, black arrows indicate non-motile peroxisome accumulations. Scale bar, 10  $\mu\text{m}$ . **(B)** Zoom of the proximal axon of neuron shown in A before (left), plus gibberellin (middle), and plus rapalog (right). Bottom row shows a maximum projection of a 5-minute interval before (left) or after (middle, right) the addition of dimerizers. **(C)** Sequential frames of the proximal axon of a dissociated hippocampal neuron treated and imaged as in A. Manually annotated tracks are displayed superimposed on the bottom panel. **(D)** Number of stalled peroxisome accumulations in the axon before and after anchoring with Myosin-V.  $n = 16/24$  for control/ + Rapalog. **(E)** Relative displacements of Myosin-V anchored clusters 10 minutes after the addition of rapalog ( $t = 0$ ). Negative and positive displacement indicates retrograde and anterograde movement, respectively. **(F)** Mean square displacement analysis on Myosin-V anchored peroxisome clusters tracked for at least 25 intervals of 30 seconds ( $n = 26$ ).

peroxisome clusters and averaged their mean-squared displacements (MSD) for different time intervals (Figures 2E and 2F). The power dependence  $\alpha$  of the MSD with increasing time intervals  $\tau$ ,  $\text{MSD} \propto \tau^\alpha$ , is the anomalous diffusion exponent [14] and indicates whether motility is completely random ( $\alpha \approx 1$ , diffusive), directed ( $1 < \alpha \leq 2$ , superdiffusive), or confined ( $0 < \alpha < 1$ , subdiffusive). Our analysis revealed that the clusters were confined and that the average displacement over >13 minutes was less

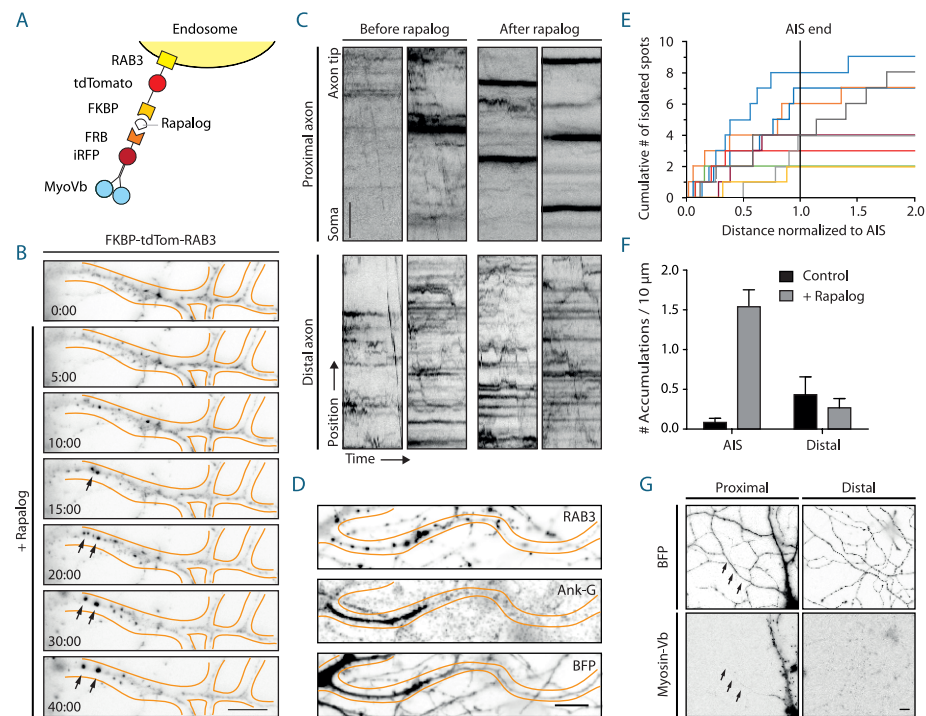


**Figure 3 | Myosin-V anchors RAB3 vesicles in the AIS of hippocampal neurons.**

**(A)** Assay: the addition of rapalog will recruit Myosin-Vb to RAB3 vesicles. **(B)** RAB3 positive vesicle distribution in the proximal axon. Upon coupling of Myosin-Vb to vesicles by the addition of rapalog, RAB3 vesicles start accumulating in big puncta. Scale bar, 10  $\mu\text{m}$ . **(C)** Kymographs of RAB3 vesicles in the proximal (upper panel) and distal axon (bottom panel). Short time lapses were acquired with 500 ms intervals before and after the addition of rapalog. For imaging of distal axons after rapalog treatment, neurons that showed clear RAB3 anchoring in their proximal axon 1 hr after rapalog addition were chosen. Scale bar, 5  $\mu\text{m}$ . **(D)** RAB3 distribution after Myosin-Vb recruitment, together with a staining for Ankyrin-G to indicate the AIS. BFP was used as a fill to show the overall morphology. Scale bar, 10  $\mu\text{m}$ . **(E)** Plot of the cumulative number of RAB3 accumulations in the axon after the addition of rapalog to recruit Myosin-Vb, normalized to the end of the AIS. **(F)** Number of accumulations found in the AIS and the distal axon as determined by Ankyrin-G staining. The number of accumulations was determined in fixed cells after treatment with rapalog or control vehicle.

than 500 nm. Thus, Myosin-V does not drive retrograde transport, but anchors cargo at specific locations in the proximal axon.

To explore how Myosin-V affects the motility of cargoes that autonomously travel into the axon, we next turned to RAB3-positive vesicles. When Myosin-Vb was recruited to RAB3 vesicles using the FKBP-*rapalog*-FRB system (Figure 3A), we observed the emergence of immobile clusters of RAB3-positive vesicles exclusively in the part of the axon that was positive for the axon initial segment (AIS) marker Ankyrin-G (Figures 3B–F). In addition, motility arrest and clustering was observed in the somatodendritic compartment. It is important to note that the selective clustering in the AIS could be a trivial consequence of the very low levels of Myosin-V in the remainder of the axon (Figure 3G). Nevertheless, these results demonstrate that Myosin-V induces cargo clustering, rather than retrograde transport.

Recent work has suggested a role for specialized actin structures in the AIS in Myosin-V based cargo retrieval [13]. To examine the relation between Myosin-V induced cargo clustering and the actin cytoskeleton, we next used superresolution microscopy in control cells (Figure 4A) and rapalog-treated cells that expressed MyoVb-GFP-FRB and FKBP-*tdTomato*-RAB3c (Figure 4B). In control cells, we observed both regularly spaced actin stripes, as described previously [15], and distinct actin patches with concentrated staining. In cells treated with rapalog, a clear colocalization between RAB3 accumulations and these actin-rich regions was observed (Figure 4B zooms), suggesting that these actin patches are the site of myosin-mediated anchoring.

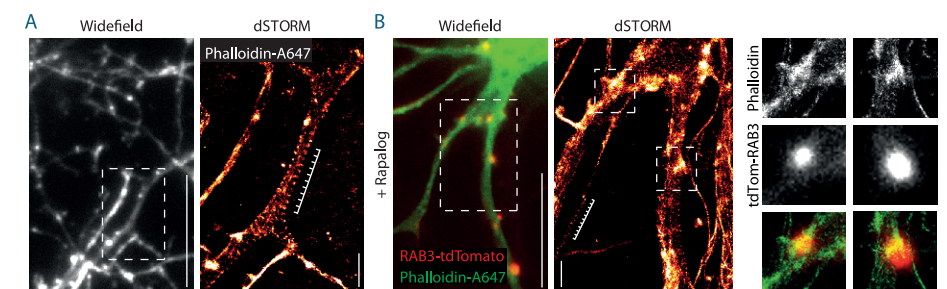


**Figure 4 | Myosin-V-anchored RAB3 vesicles accumulate on axonal actin patches.**

**(A)** Axonal actin labelled by phalloidin-A647. Left is a widefield overview, right is the dSTORM superresolution image of the zoom shown in the left panel. Regularly spaced actin rings are marked using the white combs. **(B)** dSTORM imaging of phalloidin-A647 labelled actin in the proximal axon co-expressed with FKBP-*tdTomato*-RAB3 and MyoVb-GFP-FRB after addition of rapalog. An overview of phalloidin (green) and RAB3 is depicted in the widefield image (left), the middle panel shows the dSTORM image of the phalloidin-A647 of the zoom shown in the left panel. The right panel shows individual RAB3 clusters in widefield together with superresolved actin. Scale bars, 10  $\mu\text{m}$  in widefield image and 1  $\mu\text{m}$  in dSTORM image.

## Discussion

We have developed an assay for sequential motor protein recruitment at a controlled ratio. Using this assay, we were able to show that recruiting Myosin-V to kinesin-1-driven cargo at an equal ratio is sufficient for myosin to attenuate kinesin-driven motility of peroxisomes in COS-7 cells. Future work will be directed towards exploring the myosin-kinesin ratio at which stalling still occurs. In addition, the outcome of other motor combinations could also be explored, for example kinesins and dyneins or combinations of different kinesin motors. In all these cases, it will be important to determine whether the actual ratio of the different motors that are being recruited corresponds to the stoichiometry of GID1 and FKBP in the cargo-targeted construct.

We were able to show a similar anchoring behavior in neurons where peroxisomes coupled to kinesin entered the axon, but were subsequently anchored at the AIS by Myosin-V recruitment. Similar results were obtained upon recruitment of Myosin-V to RAB3-positive vesicles. No reversals of Myosin-V anchored peroxisomes back into the cell soma were observed. These results support a model in which Myosin-V stalls the motility of dendritic vesicles that erroneously entered the axon, but also demonstrate that recruitment of Myosin-V is not sufficient to bring these cargoes back into the soma to facilitate delivery to their proper destination. These findings are consistent with earlier work demonstrating that the coupling of a Myosin-Va binding domain of Melanophilin to vesicles with no specific localization increases their halting frequency in the AIS but not the frequency of reversals [4].

Myosin-V-induced anchoring was also observed in the dendrites and soma, suggesting that anchoring does not depend on specific features of the AIS, but will occur whenever cargoes with active Myosin-V enter actin-rich regions. Indeed, actin hotspots in the distal axon were also described by others [16]. Although Myosin-V based anchoring is not restricted to the axon, the actin in the AIS still establishes an important vesicle filter, because it enables the halting of cargoes that are not supposed to enter the axon. This suggests that the cargo recruitment and/or activation state of Myosin-V determines whether a cargo is allowed to pass the AIS. Upon anchoring, the subsequent recruitment of dynein could return cargoes to the cell body. This is consistent with recent work on the dynein regulator NDEL, which was shown to localize to the AIS via an interaction with the scaffolding protein Ankyrin-G, and to facilitate cargo reversal [17].

## Acknowledgements

We are grateful to Dr. T. Inoue for the gift of AM-modified gibberellin. This work was supported by the Netherlands Organisation for Scientific Research (NWO) (NWO-ALW-VICI to C.C.H., NWO-ALW-VIDI to L.C.K.), the Dutch Technology Foundation STW, which is part of the NWO (to C.C.H and L.C.K), and the European Research Council (ERC Starting Grant to L.C.K., ERC Consolidator Grant to C.C.H).

## Author contributions

P.B. created reagents and supervised the experiments shown in Figure 1 and Figure 2.

## References

- Lipka, J. et al. (2016) Microtubule-binding protein doublecortin-like kinase 1 (DCLK1) guides kinesin-3-mediated cargo transport to dendrites. *The EMBO Journal* DOI: 10.15252/embj.201592929
- Huang, C.-F. and Banker, G. (2012) The translocation selectivity of the kinesins that mediate neuronal organelle transport. *Traffic* **13**, 549–564
- Lewis, T.L. et al. (2009) Myosin-dependent targeting of transmembrane proteins to neuronal dendrites. *Nat. Neurosci.* **12**, 568–576
- Al-Bassam, S. et al. (2012) Differential trafficking of transport vesicles contributes to the localization of dendritic proteins. *Cell Rep* **2**, 89–100
- Petersen, J.D. et al. (2014) Selective microtubule-based transport of dendritic membrane proteins arises in concert with axon specification. *Journal of Neuroscience* **34**, 4135–4147
- Derr, N.D. et al. (2012) Tug-of-war in motor protein ensembles revealed with a programmable DNA origami scaffold. *Science* **338**, 662–665
- Kapitein, L.C. et al. (2010) Probing intracellular motor protein activity using an inducible cargo trafficking assay. *Biophys. J.* **99**, 2143–2152
- Kapitein, L.C. et al. (2013) Myosin-V opposes microtubule-based cargo transport and drives directional motility on cortical actin. *Curr. Biol.* **23**, 828–834
- Miyamoto, T. et al. (2012) Rapid and orthogonal logic gating with a gibberellin-induced dimerization system. *Nat. Chem. Biol.* **8**, 465–470
- van Bergeijk, P. et al. (2015) Optogenetic control of organelle transport and positioning. *Nature* **518**, 111–114
- Kapitein, L.C. et al. (2010) Mixed microtubules steer dynein-driven cargo transport into dendrites. *Curr. Biol.* **20**, 290–299
- Song, A.-H. et al. (2009) A selective filter for cytoplasmic transport at the axon initial segment. *Cell* **136**, 1148–1160
- Watanabe, K. et al. (2012) Networks of polarized actin filaments in the axon initial segment provide a mechanism for sorting axonal and dendritic proteins. *Cell Rep* **2**, 1546–1553
- Saxton, M.J. and Jacobson, K. (1997) Single-particle tracking: applications to membrane dynamics. *Annu Rev Biophys Biomol Struct* **26**, 373–399
- Xu, K. et al. (2013) Actin, spectrin, and associated proteins form a periodic cytoskeletal structure in axons. *Science* **339**, 452–456
- Ganguly, A. et al. (2015) A dynamic formin-dependent deep F-actin network in axons. *J. Cell Biol.* **210**, 401–417
- Kuijpers, M. et al. (2016) Dynein Regulator NDEL1 controls polarized cargo transport at the axon initial segment. *Neuron* **89**, 461–471
- Kapitein, L.C. et al. (2010) Microtubule dynamics in dendritic spines. *Methods Cell Biol.* **97**, 111–132
- Thévenaz, P. et al. (1998) A pyramid approach to subpixel registration based on intensity. *IEEE Trans Image Process* **7**, 27–41
- Tarantino, N. et al. (2014) TNF and IL-1 exhibit distinct ubiquitin requirements for inducing NEMO-IKK supramolecular structures. *J. Cell Biol.* **204**, 231–245
- Yau, K.W. et al. (2014) Microtubule minus-end binding protein CAMSAP2 controls axon specification and dendrite development. *Neuron* **82**, 1058–1073

## Supplemental experimental procedures

4

### DNA constructs

DNA constructs used in this study were cloned in pGW1-CMV and pβactin-16-pl vectors. The pβactin-PEX3-mRFP-FKBP-linker-GID1 construct was made by PCR amplification of the GID1 domain with addition of a linker (SAGGSAGGSAGG), then ligated into the SpeI and NotI sites of the pβactin-PEX3-mRFP vector described previously [7], followed by PCR amplification of FKBP(1x) and insertion into the EcoRI and Sall sites of the construct. The FKBP-encoding fragments were described previously [7]. pβactin-MyoVb-(amino acid 1–1090)-GFP-FRB was described before [8]. MyoVb-(1–1090)-iRFP-FRB (Myosin-Vb) was generated by replacing the GFP by iRFP using the EcoRI and SpeI sites. KIF17md-GFP-GAI was generated by insertion of KIF17MD (aa 1–547 of human KIF17) in AscI and Sall sites, GFP in Sall and SpeI sites, and GAI(1–92) in SpeI and NotI sites of pβactin. FKBP-tdTomato-RAB3c was generated by insertion of PCR-amplified tdTomato in Sal and SpeI site, mouse RAB3c in SpeI and NotI sites and FKBP(1x) in BamHI and Sall sites of the pβactin-16-pl vector.

### Cell cultures and transfection

COS-7 cells were cultured in DMEM/Ham's F10 (1:1) medium containing 10% FCS and 1% penicillin/streptomycin. Cells were plated on 18-mm diameter coverslips 2–4 days before transfection. Cells were transfected with Fugene6 transfection reagent (Roche) according to the manufacturer's protocol and imaged one day after transfection.

Primary hippocampal cultures were prepared from embryonic day 18 (E18) rat brains [18]. Cells were plated on coverslips coated with poly-L-lysine (30 μg ml<sup>-1</sup>) and laminin (2 μg ml<sup>-1</sup>). Hippocampal cultures were grown in neurobasal medium (NB) supplemented with B27 (Invitrogen), 0.5 mM glutamine, 12.5 μM glutamate, and penicillin plus streptomycin. Transfections of hippocampal neurons were performed 48 h before imaging with lipofectamine 2000 (Invitrogen). DNA (1.8 μg per well) was mixed with 3.3 μl lipofectamine 2000 in 200 μl NB, incubated for 30 minutes, and added to the neurons in NB supplemented with 0.5 mM glutamine at 37 °C in 5% CO<sub>2</sub>. After 60–90 minutes neurons were washed with NB and transferred to the original medium at 37 °C in 5% CO<sub>2</sub> for 2 days. Transport assays in neurons were imaged at day-*in-vitro* (DIV) 12–16.

### Live-cell imaging

Time-lapse live-cell imaging of peroxisomes in hippocampal neurons was performed on a Nikon Eclipse TE2000E (Nikon) equipped with an incubation chamber (Tokai Hit; INUG2-ZILCS-H2) mounted on a motorized stage (Prior) [8]. Coverslips (18 mm) were mounted in metal rings covered with conditioned medium. Cells were imaged every 30 s for 60 minutes using a 40× objective (Plan Fluor, numerical aperture (NA) 1.3, Nikon) and a Coolsnap HQ2 CCD camera (Photometrics).

Peroxisomes in COS-7 cells and neurons were imaged using a 40× objective (Plan Fluor, numerical aperture (NA) 1.3, Nikon) in Ringer's solution (10 mM HEPES, 155 mM NaCl, 5 mM KCl, 1 mM CaCl<sub>2</sub>, 1 mM MgCl<sub>2</sub>, 2 mM NaH<sub>2</sub>PO<sub>4</sub> and 10 mM glucose, pH 7.4) or conditioned culture medium respectively. RAB3 vesicles in neurons were imaged in conditioned medium using a 100× objective (Apo TIRF, 1.49 NA, Nikon). A mercury lamp (Osram) and filter wheel containing ET-GFP (49002), ET-dsRed (49005), ET-mCherry (49008) and ET-GFPmCherry (59022) emission filters (all Chroma) were used for excitation. Peroxisomes in COS-7 cells and RAB3 in neurons were imaged on a CoolSNAP MYO CCD camera (Photometrics) and peroxisomes in neurons with a Coolsnap HQ camera (Photometrics, Tucson, AZ). During imaging, all cells were maintained at 37 °C and 5% CO<sub>2</sub> in conditioned medium.

Cell-permeable gibberellin (GA<sub>3</sub>-AM, a gift from Dr. T. Inoue [9] and rapalog (AP21967 from Ariad Pharmaceuticals) were added during image acquisition to reach a final concentration of 150–300 nM and 100 nM respectively at the indicated time points. In hippocampal neurons, the axon was identified based on

morphology and RAB3 vesicle enrichment. The proximal axon was defined as the first part of the axon before branching, whereas distal axon refers to axonal segments after at least two branch points.

## Image processing and analysis

Images of live cells were processed and analyzed using MetaMorph (Molecular Devices), LabVIEW (National Instruments) software and ImageJ (NIH). Drift correction was applied using the StackReg plugin for Image [19] for time series during which multiple positions were recorded using a motorized stage.

For analysis of redistribution dynamics in COS-7 cells, cells were masked to exclude contributions from neighboring cells to the analysis. A threshold was set for all images of a time-lapse recording at ~5–28 times the standard deviation of the background above the background to yield binary images. A threshold of 5–15 times the standard deviation was set for analysis of the  $R_{90\%}$ , while a threshold of 8–28 was used before calculating the correlation index.

To quantify peroxisome redistribution upon recruitment of motor proteins in COS-7 cells, the radius required to include 90% of the total intensity of the cell,  $R_{90\%}(t)$ , was calculated for each frame as described previously [7]. To quantify changes in the dynamics of peroxisomes upon recruitment of (additional) motor proteins, we calculated the time-dependent frame-to-frame correlation index  $c_t(t)$  as described before [10]. A value of 1 for  $c_t(t)$  indicates that particles are completely anchored and thus their position is unchanged after a time  $\tau$ , whereas a value of 0 means that all particles moved to locations that were previously unoccupied.

To generate the radial kymograph, pixels that were above the set threshold were inserted into a histogram representing the intensity versus the distance from the center of the cell. This was done for each video frame using the camera pixel size as bin size [7].

To quantify the movement of the peroxisome accumulations formed after recruiting Myosin-V in the proximal axon (Figure 2E), peroxisome positions were analyzed between 10 and 25 minutes after the addition of rapalog with 30 seconds interval acquisition. The spots were tracked using the trackmate plugin for ImageJ. For every time point the x-position relative to the initial position was plotted. For these trajectories, mean square displacement analysis was performed using the MSDanalyzer [20] class for MATLAB, including tracks that were at least 25 ( $n = 26$ ).

To analyze RAB3 clustering (Figures 3E–F), the number of bright isolated spots as shown in Figure 3D were compared between the proximal axon (colocalizing with the AIS marker Ankyrin-G) and more distal segments (after the second branch), both in the presence and absence of rapalog. For the quantification of the RAB3 accumulations relative to the AIS, the AIS length was measured based on the Ankyrin-G staining. Subsequently, the location of the RAB3 accumulations was divided by the measured-length of the AIS.

## Cell fixation and dSTORM imaging

For fixation of transfected cells (Figures 3 and 4A–B), cells were fixed with 4% PFA in PBS for 10 minutes at 37 °C. Subsequently, cells were washed two times with PBS, permeabilized with 0.25% Triton-X-100 in PBS for 10 minutes and washed 3 times in PBS. After washing, cells were blocked for 45 minutes in blocking solution (2% w/v BSA, 0.2% w/v gelatin, 10 mM glycine, 50 mM  $\text{NH}_4\text{Cl}$  in PBS, pH 7.4) and incubated overnight with phalloidin-Alexa647 (diluted: 1:50, Life technologies) or anti-Ankyrin-G (1:200, mouse, Life technologies). Cells were then quickly washed three times in PBS and imaged in case of phalloidin. For Ankyrin-G stainings, cells were further incubated with anti-mouse Alexa647 (1:400, Life technologies) and mounted for imaging in mowiol. For optimal visualization of actin structures in the absence of transfection (Figure 4A) cells were briefly pre-extracted, fixed and stained with phalloidin Alexa647 as described in [15]. This pre-extraction, reducing background and improving actin structure visualization could not be performed when co-visualization of RAB3-vesicles was required because of non-optimal vesicle preservation due to detergents in the pre-extraction buffer.

To determine the localization of the RAB3 accumulations (Figure 3) samples were imaged on a Nikon eclipse TI upright microscope with a 40x objective (UPLFLN, NA 1.3). Myosin-Vb localization was imaged on an Olympus BX53 upright microscope with a 60x objective (oil, UPLSAPO, NA1.35).

dSTORM imaging of phalloidin-A647 was performed on the setup in buffer optimal for Alexa 647 as described before [21].





## Optogenetic control of organelle transport and positioning

Petra van Bergeijk<sup>1</sup>✉, Max Adrian<sup>1</sup>✉,  
Casper C. Hoogenraad<sup>1</sup> & Lukas C. Kapitein<sup>1</sup>

*Nature* (2015); **518**, pp. 111–114

---

<sup>1</sup> Division of Cell Biology, Faculty of Science, Utrecht University, Utrecht, The Netherlands.

• These authors contributed equally to this work.

## Abstract

Proper positioning of organelles by cytoskeleton-based motor proteins underlies cellular events such as signaling, polarization, and growth [1–8]. For many organelles, however, the precise connection between position and function has remained unclear, because strategies to control intracellular organelle positioning with spatiotemporal precision are lacking. Here, we establish optical control of intracellular transport by using light-sensitive heterodimerization to recruit specific cytoskeletal motor proteins (kinesin, dynein or myosin) to selected cargoes. We demonstrate that the motility of peroxisomes, recycling endosomes and mitochondria can be locally and repeatedly induced or stopped, allowing rapid organelle repositioning. We applied this approach in primary rat hippocampal neurons to test how local positioning of recycling endosomes contributes to axon outgrowth and found that dynein-driven removal of endosomes from axonal growth cones reversibly suppressed axon growth, whereas kinesin-driven endosome enrichment enhanced growth. Our strategy for optogenetic control of organelle positioning will be widely applicable to explore site-specific organelle functions in different model systems.

## Results & discussion

Eukaryotic cells use cytoskeletal motor proteins to control the transport and positioning of proteins, RNAs and organelles [1]. In neurons, mitochondria positioning contributes to synapse functioning and axon branching [2,7,8], whereas positioning of Golgi outposts is thought to control dendrite development. Likewise, specific positioning of endosomes has been proposed to contribute to polarization and local outgrowth, either through selective delivery of building blocks or through localized signaling [5,9–12]. In many cases, however, directly resolving the role of specific organelle positioning has remained challenging. Disruption of cytoskeletal elements and inhibition of motor proteins or adaptor molecules have been frequently used to alter organelle positioning, but these approaches often lack target selectivity as well as spatial specificity. Therefore, a tool to modulate locally the distribution of specific organelles with spatiotemporal accuracy is required.

Using light-induced heterodimerization to recruit specific motors to selected cargoes might enable spatiotemporal control of intracellular transport, but whether such light-induced interactions can withstand motor-induced forces has remained unclear [13,14]. To test this, we first used light-induced binding to couple microtubule-based motors to peroxisomes in monkey COS-7 cells, because these vesicular organelles are largely immobile in the perinuclear region and any movement induced by light-targeted motor proteins could easily be observed [15]. Peroxisomes were labelled using PEX-LOV, a fusion between the peroxisomal targeting signal of PEX3 and a photosensitive LOV domain from *Avena sativa* phototropin 1, which cages a small peptide that binds the engineered PDZ domain ePDZb1 after exposure to blue light [14] (Figures 1A and 1B). In addition, ePDZb1 was fused to the plus-end-directed kinesin-3 KIF1A to create KIF-PDZ. After co-expression of these two constructs and illumination with blue light, we observed the rapid redistribution of peroxisomes from the center to the periphery of the cell where most microtubule plus-ends are located (Figures 1C and 1D). Similarly, light-induced recruitment of minus-end-directed dynein using the amino terminus of BICD2 (BICDN) fused to ePDZb1 (BICDN-PDZ) triggered the accumulation of peroxisomes at the center of the cells (Figures S1A–S1C). Importantly, peroxisome redistribution did not alter the spatial organization of mitochondria, the endoplasmic reticulum, or the actin and microtubule cytoskeleton (Figures S2A and S2B).

To quantify peroxisome motility, we first used image correlation analysis to measure the overall frame-to-frame similarity before and after exposure to blue light [16]. In the absence of transport, two subsequent images are largely identical and the

correlation index will be close to 1, whereas a value of 0 indicates that all organelles have moved to previously unoccupied positions. After light-induced recruitment of KIF1A, the correlation index rapidly decreased from  $0.97 \pm 0.01$  (mean  $\pm$  SEM) to  $0.76 \pm 0.04$ , reflecting the induction of continuous peroxisome motility (Figure 1E). By

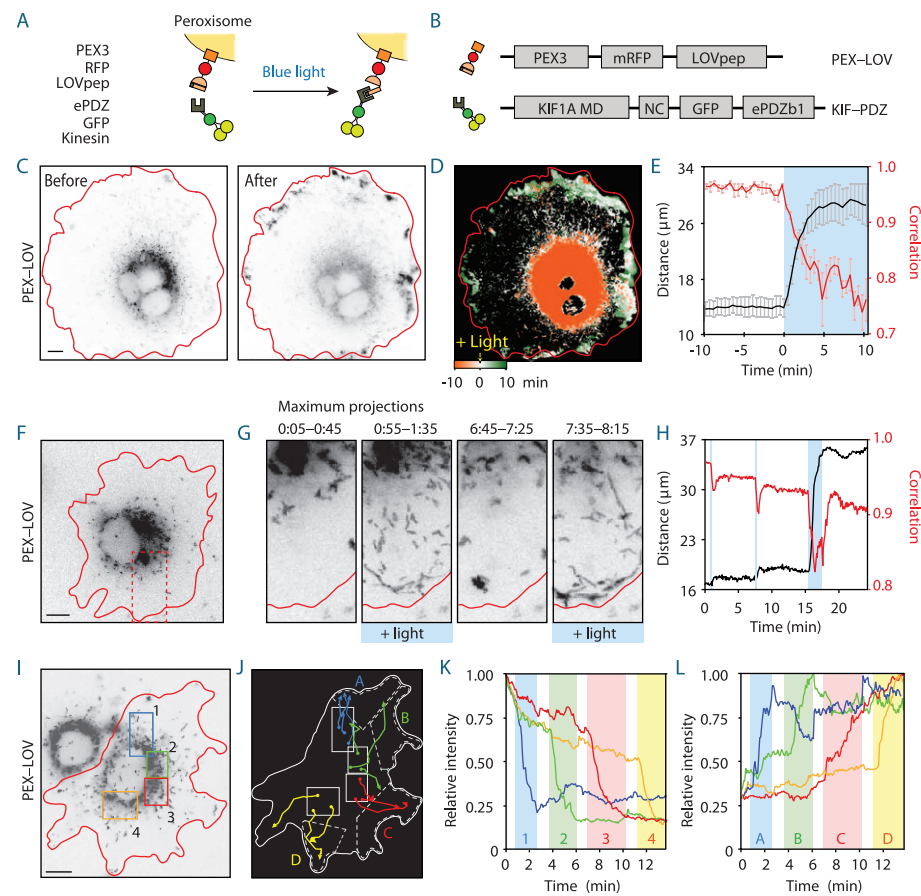


**Figure 1 | Local and reversible activation of microtubule-based transport with light.**

**(A and B)** Assay and constructs. MD, motor domain; NC, neck coil. **(C)** Peroxisome distribution before and after light-induced recruitment of KIF-PDZ. **(D)** Color-coded overlay of time series. **(E)** Displacement (black, expressed in  $R_{90\%}$ ) and correlation (frame-to-frame similarity from 0 to 1, red) versus time ( $n = 6$  cells, mean  $\pm$  SEM). Blue marks illumination. **(F and G)** Reversible activation using pulsed light. **(G)** Maximum intensity projections during periods of 40 seconds. **(H)** Displacement (black,  $R_{90\%}$ ) and correlation (red) versus time. **(I–L)** Local activation using sequential illumination of four regions shown in I, resulting in outward targeting to adjacent regions (J, showing example trajectories), quantified using normalized fluorescence intensity (K, L, colored boxes mark blue-light illumination). Scale bars, 10  $\mu\text{m}$ .

contrast, dynein recruitment eventually increased the correlation index, because most peroxisomes accumulated at the same position in the center of the cell (Figures S1C and S1D). To quantify this overall peroxisome repositioning, we calculated for each time point the radius of the circle required to enclose 90% of the fluorescence intensity of the peroxisomes,  $R_{90\%}$ , and found a large increase from  $14 \pm 2 \mu\text{m}$  to  $29 \pm 3 \mu\text{m}$  on recruitment of KIF1A (Figure 1E). By contrast,  $R_{90\%}$  decreased from  $15.4 \pm 0.3 \mu\text{m}$  to  $12.8 \pm 0.6 \mu\text{m}$  on recruitment of dynein (Figure S1D). Thus, rapid organelle redistribution can be induced by using light to recruit microtubule motors.

To achieve spatiotemporal control, recruitment of motors should be both reversible and locally restricted. To test the reversibility of motility induction, we exposed cells expressing KIF-PDZ and PEX-LOV to three consecutive periods of blue light, interspersed with  $\sim 7$  minutes without blue-light exposure. Whereas peroxisomes moved outwards during blue-light illumination, movement was arrested within seconds without blue light (Figures 1F and 1G). By contrast,  $R_{90\%}$  remained stable without stimulation (Figure 1H), indicating that peroxisomes do not spontaneously return to their original position after motor dissociation (Figure S3A). To test whether transport could be induced locally, we sequentially illuminated four different regions within a cell (Figures 1I and 1J). Peroxisomes in the activated region rapidly redistributed to non-exposed areas, whereas non-exposed peroxisomes remained stationary (Figure 1J). The fluorescence intensity in the illuminated boxes 1–4 decreased by 60–75%, coinciding with a 180–280% increase in the adjacent peripheral boxes A–D (Figures 1J–L). These results demonstrate that transport of intracellular cargo can be induced with spatiotemporal precision.

We have previously shown that Myosin-V can oppose kinesin-driven transport in actin-dense regions [16], suggesting that light-induced recruitment of Myosin-V can be used to anchor organelles at specific sites. To test this, Myosin-Vb was recruited to peroxisomes preloaded with the kinesin-2 KIF17 (refs 15, 16) (Figures 2A and 2B). Whereas the attached kinesin motor ensured continuous motility of many peroxisomes near the cell periphery (Figure 2C), this motility was arrested after recruitment of Myosin-Vb, resulting in a 30% increase of the correlation index (Figure 2D). Local illumination increased the correlation index to similar levels, but only in the exposed region (Figures 2C and 2D). Moreover, individual peroxisome trajectories showed on average four times smaller frame-to-frame displacements during illumination compared to before and after stimulation (Figures 2E and 2F). These data demonstrate that organelle motility can be stalled with spatiotemporal precision through light-induced recruitment of Myosin-Vb.

We next used RAB11-positive recycling endosomes to test our method on organelles whose proper physiological functioning depends on selective transport and positioning. Because C-terminal tagging of both LOVpep and RAB11 is incompatible

with their function, we developed two alternative strategies to enable light-induced coupling of motor proteins to recycling endosomes. First, Rab11 was cloned behind the photolyase homology region of Cryptochrome-2 [13] (CRY–RAB11). Upon photo-excitation, Cryptochrome-2 binds CIBN, resulting in recruitment of CIBN-tagged motor proteins to RAB11 recycling endosomes (Figures S4A and S4B). Using these constructs, light-induced binding of KIF1A or BICDN induced an increased flow of recycling endosomes to the cell periphery or center, respectively (Figures S4C–S4G). As an alternative approach, we first used chemically-induced heterodimerization to connect the N-termini of LOVpep and RAB11, followed by light-dependent recruitment of ePDZb1-tagged motor proteins (Figures S4I, S4J and S5). Using this approach, we observed that upon kinesin recruitment recycling endosomes became enriched near

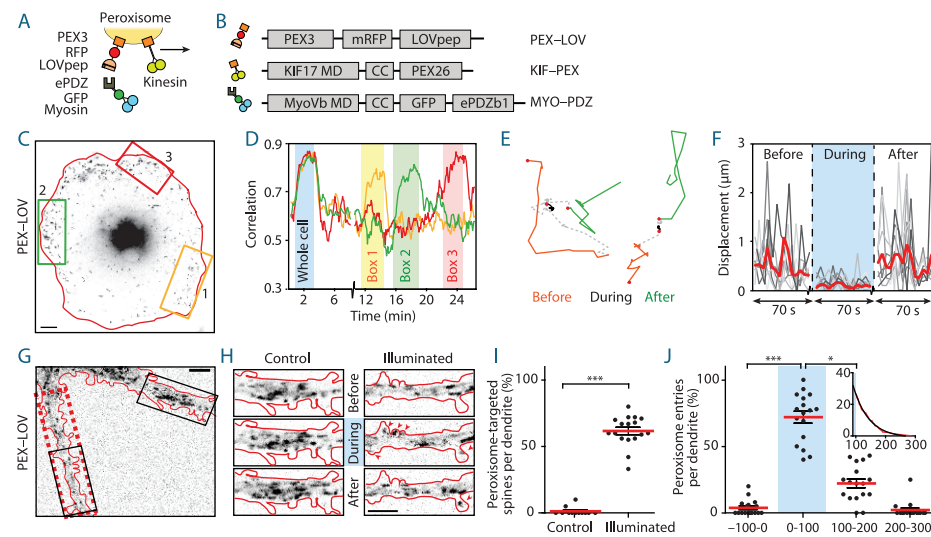


**Figure 2 | Light-induced Myosin-Vb recruitment anchors organelles or targets them into dendritic spines.**

**(A and B)** Assay and constructs. CC, coiled-coil. **(C)** Peroxisome distribution in cell expressing PEX–LOV, KIF–PEX and MYO–PDZ. **(D)** Correlation time trace for areas shown in C. **(E)** Peroxisome trajectories with 70-second episodes before, during and after Myosin-Vb recruitment. **(F)** Frame-to-frame displacements of peroxisomes (5 s interval). Red denotes the average of nine individual peroxisome trajectories. **(G)** Peroxisome distribution in primary hippocampal neuron expressing PEX–LOV and MYO–PDZ. Dashed red rectangle was illuminated. **(H)** Thirty-second maximum projections of regions from G. Arrowheads mark peroxisomes in spines. **(I)** Spine targeting in control ( $n = 12$ ) and illuminated ( $n = 17$ ) dendrites, in three independent experiments. Mean  $\pm$  SEM, \*\*\*  $p < 0.0001$ . Mann-Whitney test. **(J)** Spine entries over time. Mean  $\pm$  SEM, \*  $p < 0.05$ , \*\*\*  $p < 0.0001$ . Kruskal-Wallis analysis of variance (ANOVA), Dunn's post-hoc,  $n = 17$  dendrites. Inset: entry probability after illumination (red) fitted with exponential decay  $\exp(-t/\lambda)$  (black,  $\lambda = 36.36$  s). Scale bars, 5  $\mu$ m, except C, 10  $\mu$ m.

the cell periphery during the illumination interval (Figure S3B), without affecting the distribution of lysosomes or early endosomes (Figure S2C). In addition, recruitment of Myosin-Vb was sufficient to stall recycling endosomes both globally and locally (Figures S4K–S4N). Both CRY–RAB11 and FKBP–RAB11 showed similar distributions as endogenous RAB11, transported transferrin receptors and interacted with the known RAB11 effector, RAB11 family-interacting protein 1 (RAB11FIP1) (Figure S6). We chose FKBP–RAB11 for all subsequent experiments, because the greater sensitivity of CRY–PEX to blue light (Figure S4H) easily led to activation during sample handling. It should be noted that, because of the weak interaction between TagBFP and TagRFP, some light-dependent activation could be observed without addition of rapalog (Figure S5A). Moreover, whereas peroxisomes remained largely immobile at their new location after light-dependent repositioning, the original distribution of recycling endosomes was quickly restored after the light-induced kinesin recruitment was stopped (Figure S3). Thus, kinesin- and dynein-based redistribution and Myosin-Vb-based anchoring of recycling endosomes could be transiently induced with light (Figures S2–S4, Figures S5 and S6), demonstrating that the movement of intrinsically dynamic cargoes can be temporarily amplified or overruled by coupling these cargoes to a specific motor using light.

To test our approach in a more complex and delicate model system, we switched to primary cultures of rat hippocampal neurons. Their polarized morphology and specialized cytoskeletal organization in different compartments, such as axons, dendrites and dendritic spines, should allow transporting cargoes into and out of these compartments by recruiting the appropriate motor proteins. We first examined whether light-induced recruitment of Myosin-Vb was sufficient to drive transport into dendritic spines, as proposed previously [17–20]. Indeed, in cells co-expressing PEX–LOV and a fusion of Myosin-Vb with ePDZb1 (MYO–PDZ),  $62 \pm 3\%$  of the illuminated spines were targeted with peroxisomes compared to  $1 \pm 1\%$  of spines in non-illuminated dendrites (Figures 2G–2J). After the illumination period, the number of peroxisome entries decreased with a half-time of  $\sim 36$  s (Figure 2J). Similarly, RAB11 recycling endosomes could be enriched in specific spines by local illumination (Figures S4O–S4Q), demonstrating that light-controlled transport can be used to manipulate individual dendritic spines.

RAB11 vesicles have been implicated in the control of axon growth, but their local role in the growth cone could not be assessed previously [11,12,21]. We therefore used local light-induced recruitment of motor proteins to RAB11 recycling endosomes to test how local dynein-driven removal or kinesin-driven addition of endosomes affects growth cone dynamics (Figures 3A and 3D). Importantly, neither illumination nor addition of the heterodimerizer rapalog (used to link the LOV domain to the N terminus of RAB11) altered growth cone structure or behavior in cells expressing FRB–

LOV and PDZ only (Figures S5 and S7). Likewise, in control neurons expressing FKBP-RAB11 together with BICDN-PDZ or KIF-PDZ, but lacking the FRB-LOV protein, exposure to blue light did not affect the rapid filopodial and lamellipodial dynamics or the overall growth of most growth cones (Figures 3B and 3E). When dynein was coupled to RAB11, a clear decrease in growth cone dynamics and growth was observed (Figures 3C, 3G and S8). By contrast, coupling of kinesin resulted in rapid axon extension in  $39 \pm 7\%$  of the growth cones (Figures 3F and 3H). Importantly, when growth cones were not completely collapsed upon dynein-dependent RAB11 depletion, this depletion and the reduced growth cone dynamics could be reversed when cells were no longer

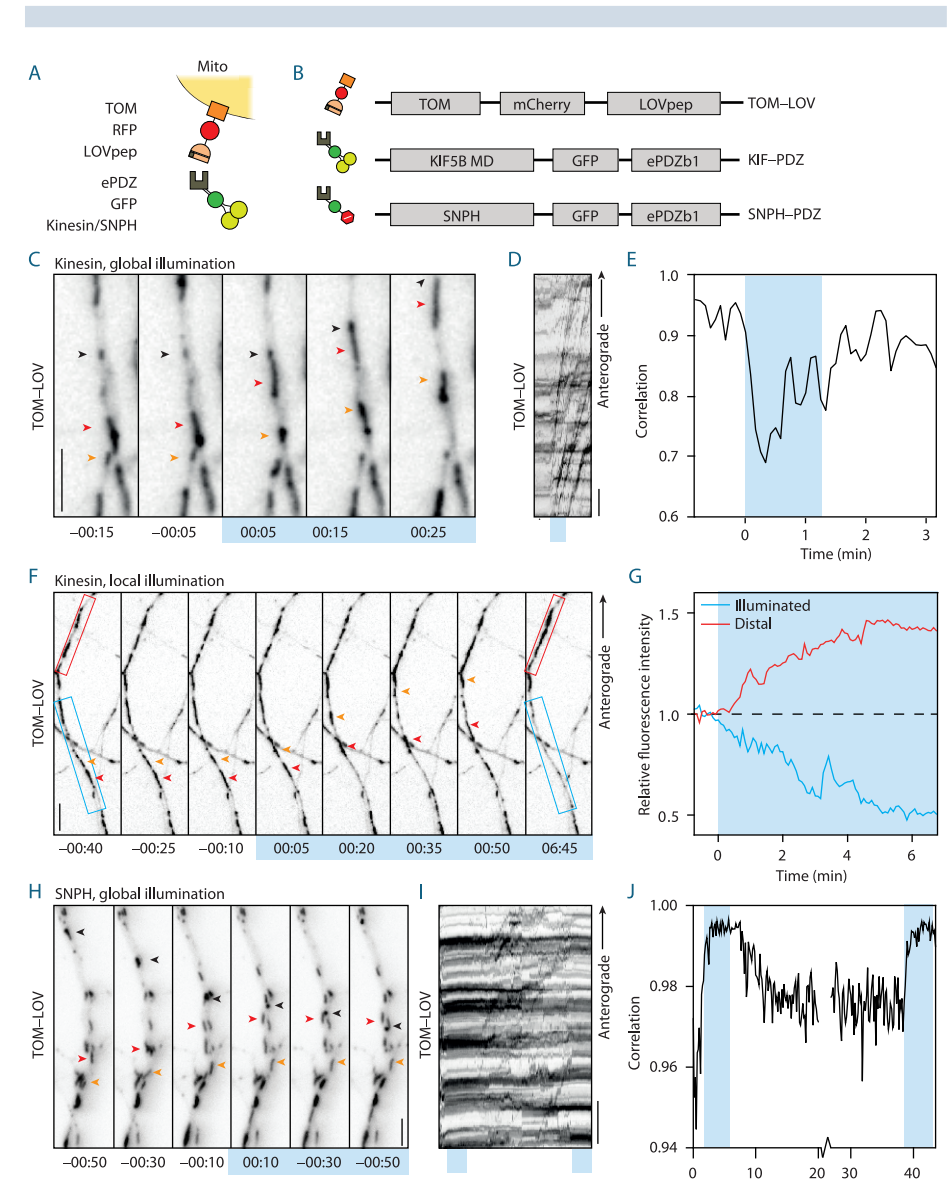
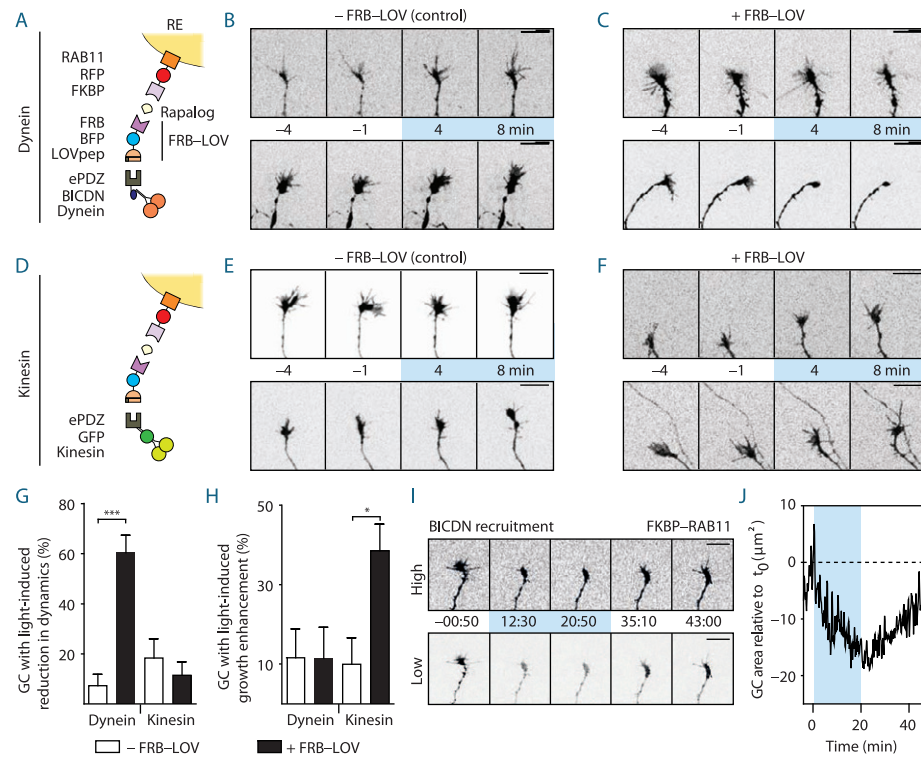


**Figure 4 | Altering mitochondrial dynamics through recruitment of motors and anchors.**

**(A and B)** Assay and constructs. **(C)** Axonal mitochondria before and during KIF-PDZ recruitment. Arrowheads track individual mitochondria. **(D)** Kymograph for axon shown in C, representative for n = 6 axons. Blue box marks activation (1 minute : 15 s). **(E)** Correlation over time for region shown in C. **(F)** Axonal mitochondria before and during local illumination (blue box). **(G)** Relative fluorescence intensity versus time in the illuminated (blue box in F) and the adjacent, distal region (red box in F). **(H)** Axonal mitochondria before and during SNPH recruitment. Arrowheads track individual mitochondria. **(I)** Kymograph for axon shown in H, representative for n = 5 axons. Blue boxes mark activation (4 minutes : 50 s). **(J)** Correlation versus time for region in Video S9. Scale bars, 5  $\mu$ m, except D and I, 10  $\mu$ m.

exposed to blue light (Figures 3I and 3J). These data demonstrate that growth cone dynamics and axon growth directly depend on RAB11 vesicle functioning near the growth cone, rather than on general RAB11 functions elsewhere in the cell.

Recently, the controlled anchoring and mobilization of mitochondria have emerged as key regulatory events in neurons [8,22–24]. Mitochondrial positioning depends on both motor-dependent transport and controlled immobilization by specific docking factors, but the molecular and mechanical interplay between motors and docking factors has remained unclear [22,24]. For example, syntaphilin (SNPH) has been proposed to induce anchoring by crosslinking mitochondria to microtubules and through a direct inactivating interaction with kinesin [25,26], but whether remobilization requires the regulated release of both interactions is not known [23]. To test whether recruitment of more motors can overcome anchoring, we used light to recruit KIF–PDZ to axonal mitochondria labelled with TOM–LOV (Figures 4A and 4B) and found that this was sufficient to mobilize most mitochondria in the illuminated region (Figures 4C–4G). Conversely, light-induced recruitment of the N-terminal part of SNPH was sufficient to acutely anchor motile mitochondria, independent of their directionality (Figures 4H–4J). These results demonstrate that regulation of mitochondrial motility and anchoring does not require all-or-nothing switching between the activation and inactivation of specific motors, but instead depends on the balance of forces between active motors and passive anchors.

We have established optically-controlled intracellular transport by using light-sensitive heterodimerization to recruit specific cytoskeletal motor proteins to selected cargoes. Our ability to control organelle positioning complements recent work that established optogenetic control over nucleocytoplasmic distribution of proteins [27]. We anticipate that this approach will be widely applicable to study how organelle positioning controls cellular functioning, as demonstrated here for the role of recycling endosomes in growth cone dynamics. In addition, it could be used to control cellular processes such as polarization, signaling and outgrowth by depleting or accumulating cargo at specific sites. For example, increased axonal targeting of certain cargoes might promote axon regeneration after injury and provide novel insights into the mechanisms contributing to regeneration failure or success, both in culture and in different animal models [28].

## Acknowledgements

We are grateful to C. Tucker, T. Inoue, Z.-H. Sheng, G. Banker, R. Prekeris, P. Schätzle and M. Esteves da Silva for sharing reagents and to C. Wierenga and A. Akhmanova for discussions. This research is supported by the Dutch Technology Foundation STW and the Foundation for Fundamental Research on Matter (FOM), which are part of the Netherlands Organisation for Scientific Research (NWO). Additional support came from NWO (NWO-ALW-VICI to C.C.H and NWO-ALW-VIDI to L.C.K.) and the European Research Council (ERC starting grant to L.C.K.).

## Author contributions

L.C.K. and C.C.H. initiated research. P.B. created reagents. P.B., M.A., C.C.H. and L.C.K. designed experiments. P.B. and M.A. performed experiments. P.B., M.A. and L.C.K. analyzed data. P.B., M.A., C.C.H. and L.C.K. wrote the manuscript.

# References

1. Vale, R. D. (2003) The molecular motor toolbox for intracellular transport. *Cell* **112**, 467-480
2. Sheng, Z. H. and Cai, Q. (2012) Mitochondrial transport in neurons: impact on synaptic homeostasis and neurodegeneration. *Nat Rev Neurosci* **13**, 77-93
3. Korolchuk, V. I. et al. (2011) Lysosomal positioning coordinates cellular nutrient responses. *Nat Cell Biol* **13**, 453-460
4. Yadav, S. and Linstedt, A. D. (2011) Golgi positioning. *Cold Spring Harbor perspectives in biology* **3**
5. Sadowski, L. et al. (2009) Signaling from endosomes: location makes a difference. *Exp Cell Res* **315**, 1601-1609
6. Ori-McKenney, K. M. et al. (2012) Golgi outposts shape dendrite morphology by functioning as sites of centrosomal microtubule nucleation in neurons. *Neuron* **76**, 921-930.
7. Spillane, M. et al. (2013) Mitochondria coordinate sites of axon branching through localized intra-axonal protein synthesis. *Cell reports* **5**, 1564-1575
8. Courchet, J. et al. (2013) Terminal axon branching is regulated by the LKB1-NUAK1 kinase pathway via presynaptic mitochondrial capture. *Cell* **153**, 1510-1525
9. Golachowska, M. R. et al. (2010) Recycling endosomes in apical plasma membrane domain formation and epithelial cell polarity. *Trends Cell Biol* **20**, 618-626.
10. Higuchi, Y. et al. (2014) Early endosome motility spatially organizes polysome distribution. *J Cell Biol* **204**, 343-357
11. Eva, R. et al. (2012) ARF6 directs axon transport and traffic of integrins and regulates axon growth in adult DRG neurons. *J Neurosci* **32**, 10352-10364
12. Eva, R. et al. (2010) Rab11 and its effector Rab coupling protein contribute to the trafficking of beta 1 integrins during axon growth in adult dorsal root ganglion neurons and PC12 cells. *J Neurosci* **30**, 11654-11669
13. Kennedy, M. J. et al. (2010) Rapid blue-light-mediated induction of protein interactions in living cells. *Nat Methods* **7**, 973-975
14. Strickland, D. et al. (2012) TULIPs: tunable, light-controlled interacting protein tags for cell biology. *Nat Methods* **9**, 379-384
15. Kapitein, L. C. et al. (2010) Probing intracellular motor protein activity using an inducible cargo trafficking assay. *Biophys J* **99**, 2143-2152
16. Kapitein, L. C. et al. (2013) Myosin-V opposes microtubule-based cargo transport and drives directional motility on cortical actin. *Curr Biol* **23**, 828-834
17. Correia, S. S. et al. (2008) Motor protein-dependent transport of AMPA receptors into spines during long-term potentiation. *Nat Neurosci* **11**, 457-466
18. Wagner, W. et al. (2011) Myosin-Va transports the endoplasmic reticulum into the dendritic spines of Purkinje neurons. *Nat Cell Biol* **13**, 40-48
19. Wang, Z. et al. (2008) Myosin Vb mobilizes recycling endosomes and AMPA receptors for postsynaptic plasticity. *Cell* **135**, 535-548
20. Hammer, J. A., 3rd and Wagner, W. (2013) Functions of class V myosins in neurons. *J Biol Chem* **288**, 28428-28434
21. Bhuin, T. and Roy, J. K. (2009) Rab11 is required for embryonic nervous system development in *Drosophila*. *Cell and tissue research* **335**, 349-356
22. Encalada, S. E. and Goldstein, L. S. (2014) Biophysical challenges to axonal transport: motor-cargo deficiencies and neurodegeneration. *Annual review of biophysics* **43**, 141-169
23. Sheng, Z. H. (2014) Mitochondrial trafficking and anchoring in neurons: New insight and implications. *J Cell Biol* **204**, 1087-1098
24. Sun, T. et al. (2013) Motile axonal mitochondria contribute to the variability of presynaptic strength. *Cell reports* **4**, 413-419
25. Chen, Y. and Sheng, Z. H. (2013) Kinesin-1-syntaphilin coupling mediates activity-dependent regulation of axonal mitochondrial transport. *J Cell Biol* **202**, 351-364
26. Kang, J. S. et al. (2008) Docking of axonal mitochondria by syntaphilin controls their mobility and affects short-term facilitation. *Cell* **132**, 137-148
27. Niopek, D. et al. (2014) Engineering light-inducible nuclear localization signals for precise spatiotemporal control of protein dynamics in living cells. *Nature communications* **5**, 4404
28. Bradke, F. et al. (2012) Assembly of a new growth cone after axotomy: the precursor to axon regeneration. *Nat Rev Neurosci* **13**, 183-193

## Supplemental figures

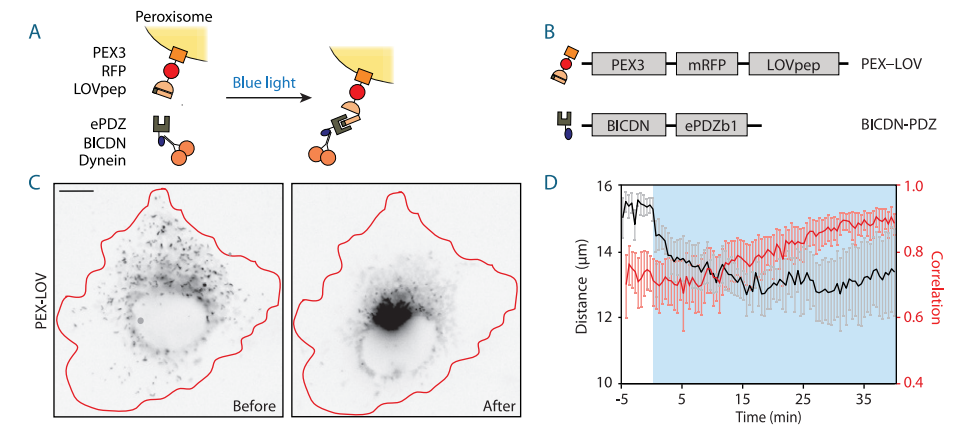


**Figure S1 | Optical control of dynein-based cargo motility.**

**(A and B)** Assay and constructs. A fusion construct of PEX3, monomeric red fluorescent protein (mRFP) and LOVpep (PEX-LOV) targets peroxisomes. After blue-light illumination, a fusion of the N-terminus of the dynein adaptor BICD2 and ePDZb1 (BICDN-PDZ) is recruited to peroxisomes. **(C)** Peroxisome distribution in a COS-7 cell expressing PEX-LOV and BICDN-PDZ before and during light-induced recruitment of dynein (inverted contrast). Red lines indicate cell outline. Scale bar, 10  $\mu\text{m}$ . **(D)** Black: time trace of the  $R_{90\%}$  (radius of circle enclosing 90% of cellular fluorescence; see Experimental Procedures) in cells expressing PEX-LOV and BICDN-PDZ ( $n = 5$  cells). Red: correlation index (frame-to-frame differences in the peroxisome recordings; see supplemental experimental procedures) of the same cells. Blue-light illumination is indicated in blue; mean  $\pm$  SEM.

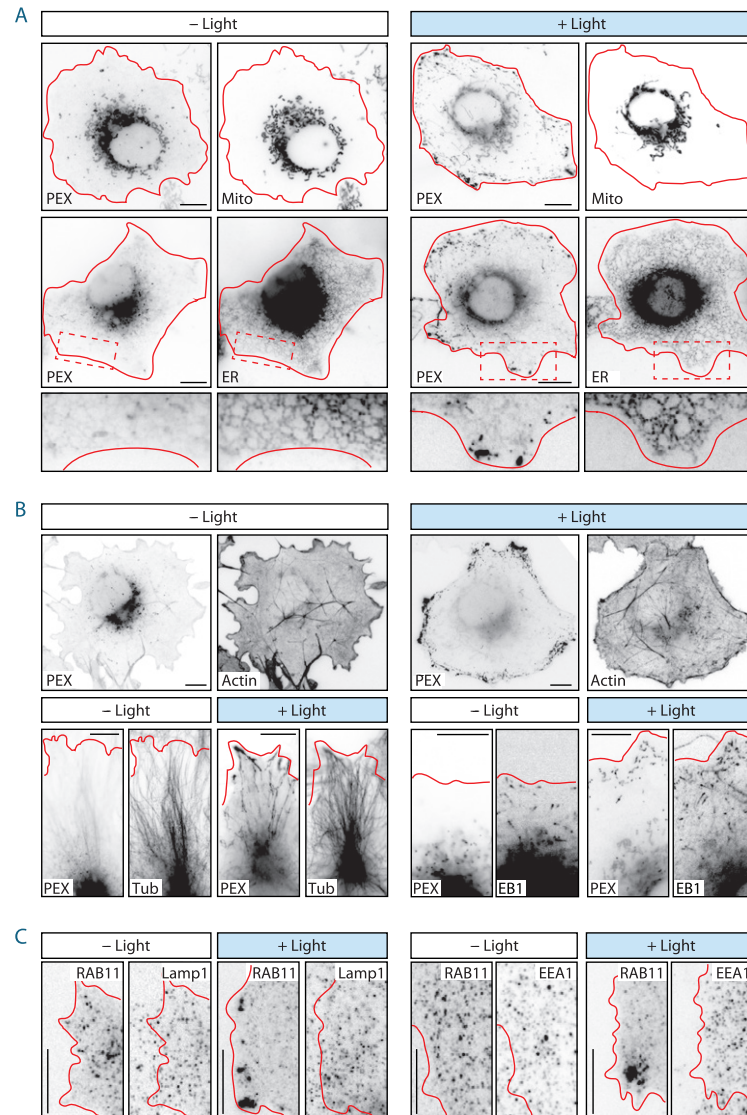


**Figure S2 | Light-induced organelle redistribution is organelle-specific and does not affect the cytoskeleton.**

(A) Images of fixed cells expressing PEX-LOV and KIF-PDZ, showing the distribution of peroxisomes and mitochondria (anti-cytochrome-c), or peroxisomes and the endoplasmic reticulum (anti-protein disulfide isomerase (PDI)) in the absence (left) or presence (right) of blue light. (B) Images of fixed cells expressing PEX-LOV and KIF-PDZ, showing the distribution of peroxisomes and phalloidin,  $\alpha$ -Tubulin or EB1 staining in the absence or presence of blue light. (C) Images of fixed cells expressing FKBP-RAB11, FRB-LOV and KIF-PDZ, showing the distribution of RAB11 recycling endosomes together with lysosomes (anti-Lamp1) or early endosomes (anti-EEA1) in the absence or presence of blue light. Red lines indicate cell outline. Scale bars, 10  $\mu$ m.

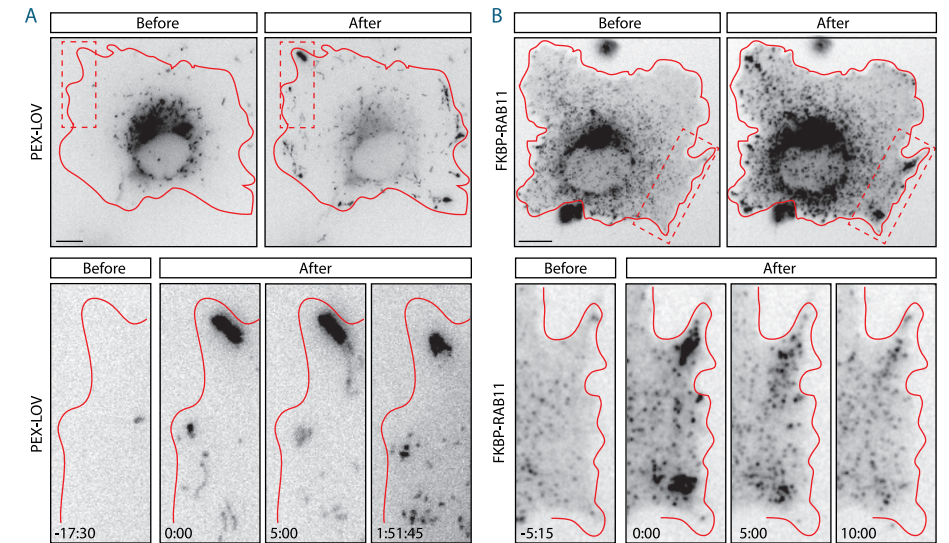


**Figure S3 | After light-induced organelle displacement, peroxisomes remain at their newly obtained position whereas the distribution of recycling endosomes quickly reverses back to normal.**

(A) Peroxisome distribution before and after exposure to blue light in cells expressing PEX-LOV and KIF-PDZ. Blue-light illumination was terminated at  $t_{0:00}$ . (B) Distribution of RAB11 recycling endosomes before and after exposure to blue light in cells expressing FKBP-RAB11, FRB-LOV and KIF-PDZ. Blue light was turned off at  $t_{0:00}$ . Red lines indicate cell outline. Scale bars, 10  $\mu$ m.

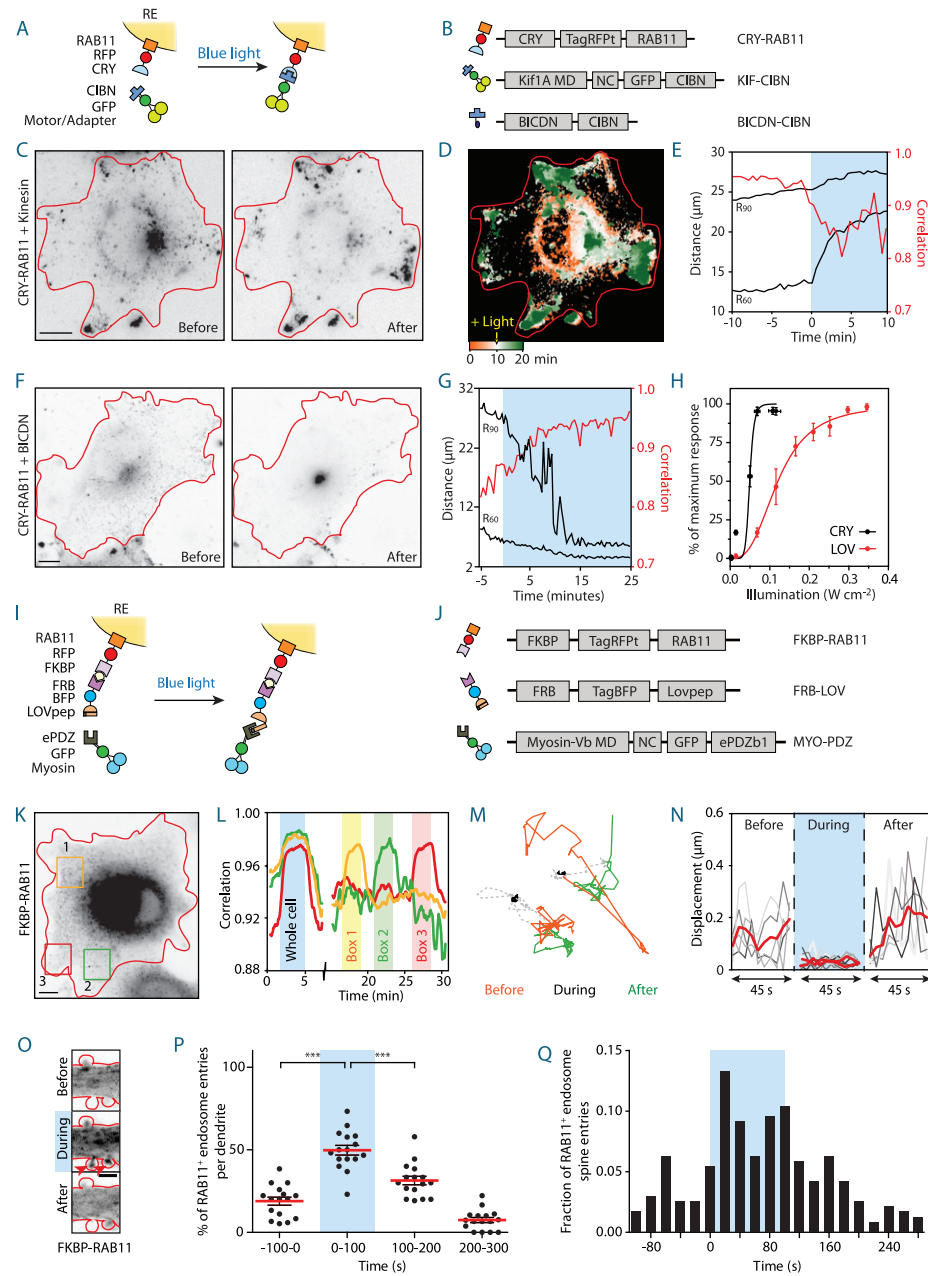


**Figure S4 | Spatiotemporal control of recycling endosome distribution and dynamics.**

**(A and B)** Assay and constructs: a fusion construct of CRY2PHR, tagRFPT and RAB11, (CRY-RAB11) targets RAB11 recycling endosomes. After blue-light illumination, a fusion of truncated KIF1A, GFP and CIBN (KIF-CIBN) or a fusion of truncated BICDN, GFP and CIBN (BICDN-CIBN) is recruited to RAB11 recycling endosomes. **(C)** RAB11 vesicle distribution before and after light-induced recruitment of KIF1A (inverted contrast). Red lines indicate cell outline. Scale bar, 10  $\mu\text{m}$ . **(D)** Overlay of sequential binarized images from the recording in C, color-coded by time as indicated. Orange marks the initial distribution of RAB11 vesicles, whereas green marks regions targeted after exposure to blue light. **(E)** Time trace of the  $R_{60\%}$  and  $R_{90\%}$  (black) and the correlation index (red) of the cell shown in C and D. Blue box marks blue-light illumination. **(F)** RAB11 distribution in a cell expressing CRY-RAB11, and BICDN-CIBN before and after blue-light illumination (inverted contrast). Red lines indicate cell outline. Scale bar, 10  $\mu\text{m}$ . **(G)** Time trace of the  $R_{60\%}$  and  $R_{90\%}$  (black) and correlation index for the cell shown in F. **(H)** Irradiance response curve for cells transfected with CRY-PEX and KIF-CIBN (red), or PEX-LOV plus KIF-PDZ (black). To exclude activation failure due to poorly expressed motors, the number of cells reacting at each concentration was divided by the number of cells responding to subsequent high irradiance ( $\sim 1.3 \text{ W cm}^{-2}$ ). Three biological replicates. Cells per intensity (for increasing intensities): 28, 21, 22, 20, 24, 22 and 20 for CRY, 30, 28, 33, 31, 28, 33, 33, 32 and 26 for LOV. Error bars depict SEM; three biological replicates. Solid line shows fit to  $R=100I^n/(I_0^n+I^n)$  with  $R$  the response,  $I$  the illumination intensity,  $I_0$  the intensity at which the response is 50%, and  $n$  the Hill coefficient. For CRY-PEX and PEX-LOV,  $I_0$  is 0.05 and 0.12  $\text{W cm}^{-2}$ , respectively. **(I and J)** Assay and constructs: a fusion construct of FKBP, tagRFPT and RAB11 (FKBP-RAB11) targets RAB11 recycling endosomes. Rapalog addition couples FKBP to FRB, leading to recruitment of the FRB, tagBFP and LOVpep fusion protein (FRB-LOV). Upon blue-light illumination a fusion of truncated Myosin-Vb, GFP and ePDZb1 (MYO-PDZ) is recruited to RAB11 vesicles. **(K)** RAB11 distribution in a cell expressing FKBP-RAB11, FRB-LOV, and MYO-PDZ before sequential blue-light illumination of the regions marked with numbered boxes (inverted contrast). Scale bar is 10  $\mu\text{m}$ . **(L)** Time traces of the correlation index in the areas shown in K. Blue box marks whole-cell exposure to blue light, whereas colored boxes indicate local illumination. **(M)** Example trajectories of two RAB11 recycling endosomes before, during and after recruitment of Myosin-Vb, as indicated. Data was acquired with 1 s intervals. For each period 40 seconds are shown. **(N)** Frame-to-frame displacements of RAB11 recycling endosomes before, during and after light-induced recruitment of Myosin-Vb (5 s interval). Thick lines show the average of five tracks in shades of gray. **(O)** FKBP-RAB11 distribution (inverted contrast) in a dendrite and dendritic spines before, during and after blue-light illumination. Images are maximum projections spanning 60 s. Red lines indicate cell outline, arrowheads mark spines targeted with recycling endosomes during blue-light illumination. Scale bar, 2  $\mu\text{m}$ . **(P)** Percentage of recycling endosome spine entry events per dendrite before, during and after illumination in bins of 100 s. Blue box indicates blue-light illuminated interval,  $n = 16$  dendrites in three independent experiments. Red bar denotes mean  $\pm$  SEM, \*\*\*  $p < 0.0001$ , one-way ANOVA, Bonferroni's post-hoc test. **(Q)** Histogram of fraction of all ( $n = 237$ ) recycling endosome spine entries in bins of 20 s. Blue box indicate blue-light illuminated interval.

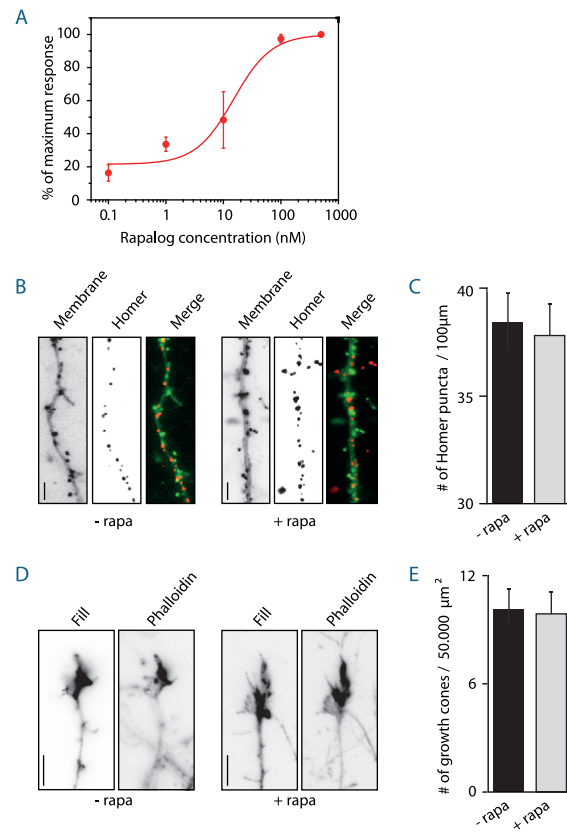


**Figure S5 | Rapalog in the nanomolar range is sufficient to recruit FRB-LOV to FKBP-RAB11 and does not affect the number of spines or growth cones in hippocampal neurons.**

**(A)** Response curve of RAB11 recycling endosome relocalization in cells expressing FKBP-RAB11, FRB-LOV, and KIF-PDZ exposed to blue light in relation to rapalog concentration. To exclude activation failure due to poorly expressed motors, the number of cells reacting at each concentration was divided by the number of cells responding to subsequent high rapalog concentration (1 µM). Solid line shows fit to  $R = (R_{min}I_0^n + 100I^n) / (I_0^n + I^n)$ , with  $R$  the response,  $c$  the rapalog concentration,  $c_0$  the concentration at which the response is 50%,  $n$  the Hill coefficient, and  $R_{min}$  the response at 0 mM rapalog.  $R_{min}$  is 22% and  $c_0$  is 15 nM.  $n = 30$  (0.1 nM), 37 (1 nM), 30 (10 nM), 28 (100 nM) and 28 (500 nM) responsive cells from three independent experiments. Error bars depict SEM. **(B)** Hippocampal neurons transfected with membrane-GFP incubated for 2.5 h in the presence or absence of 100 nM rapalog, co-stained with the post-synaptic marker Homer. **(C)** Quantification of the number of Homer puncta per 100 µm dendrite length in the presence or absence of 100 nM rapalog. ( $n = 13$  neurons per condition). Error bars depict SEM. **(D)** Hippocampal neurons transfected with GFP incubated for 2.5 h in the presence or absence of 100 nM rapalog, co-stained with phalloidin. **(E)** Quantification of the number of growth cones per 50,000 µm<sup>2</sup> in the presence or absence of 100 nM rapalog, co-stained with phalloidin.  $n = 19$ . Scale bars, 5 µm. Error bars depict SEM.

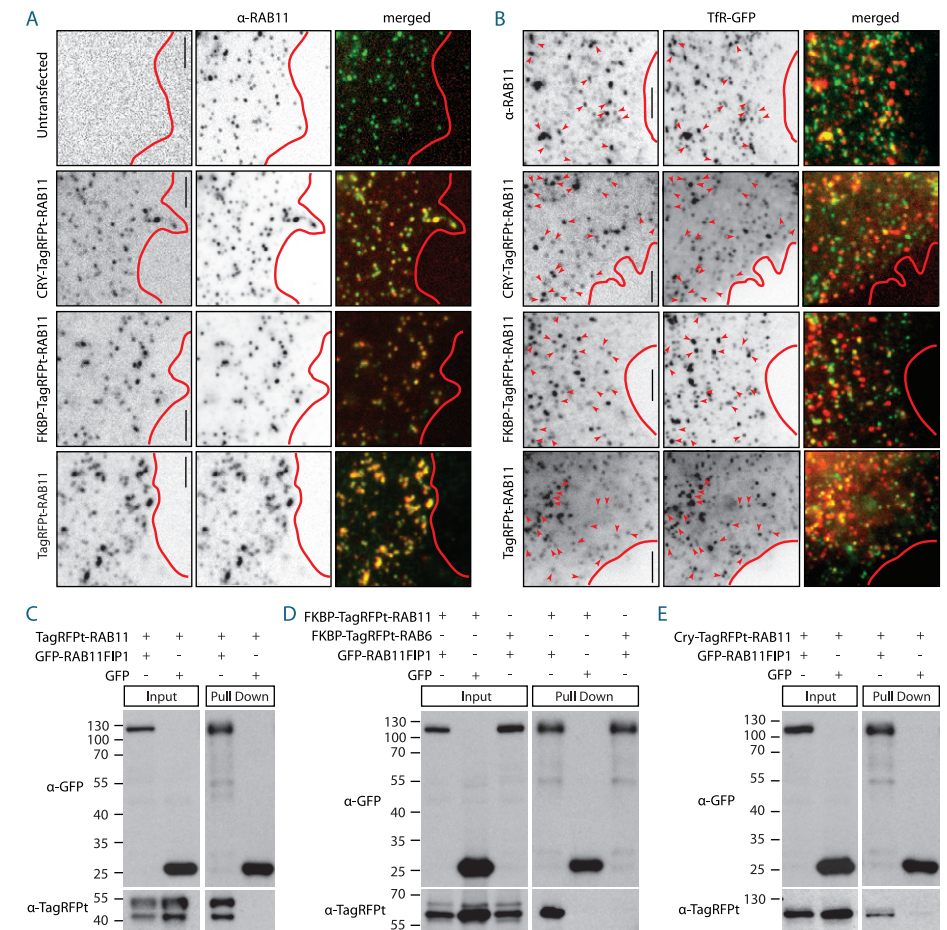


**Figure S6 | RAB11 fusion constructs are recognized by the RAB11 antibody, partially co-localize with transferrin receptors and interact with RAB11FIP1.**

**(A)** Images of untransfected cells or cells transfected with CRY-RAB11, FKBP-RAB11 or TagRFPT-RAB11, co-stained with anti-RAB11 antibody (Inverted contrast). Red lines indicate cell outline. Scale bar, 2.5 µm. **(B)** Images of cells transfected with TfR-GFP only, or co-transfected with CRY-RAB11, FKBP-RAB11 or TagRFPT-RAB11 (Inverted contrast). Red lines indicate cell outline. Scale bar, 2.5 µm. **(C-E)** GFP pull-down assays with lysates of HEK cells expressing GFP or GFP-RAB11FIP1 together with TagRFPT-RAB11 **(C)**, FKBP-RAB11 or FKBP-TagRFPT-RAB6 **(D)** or CRY-RAB11 **(E)** were analyzed by Western blotting using antibodies against TagRFPT and GFP.

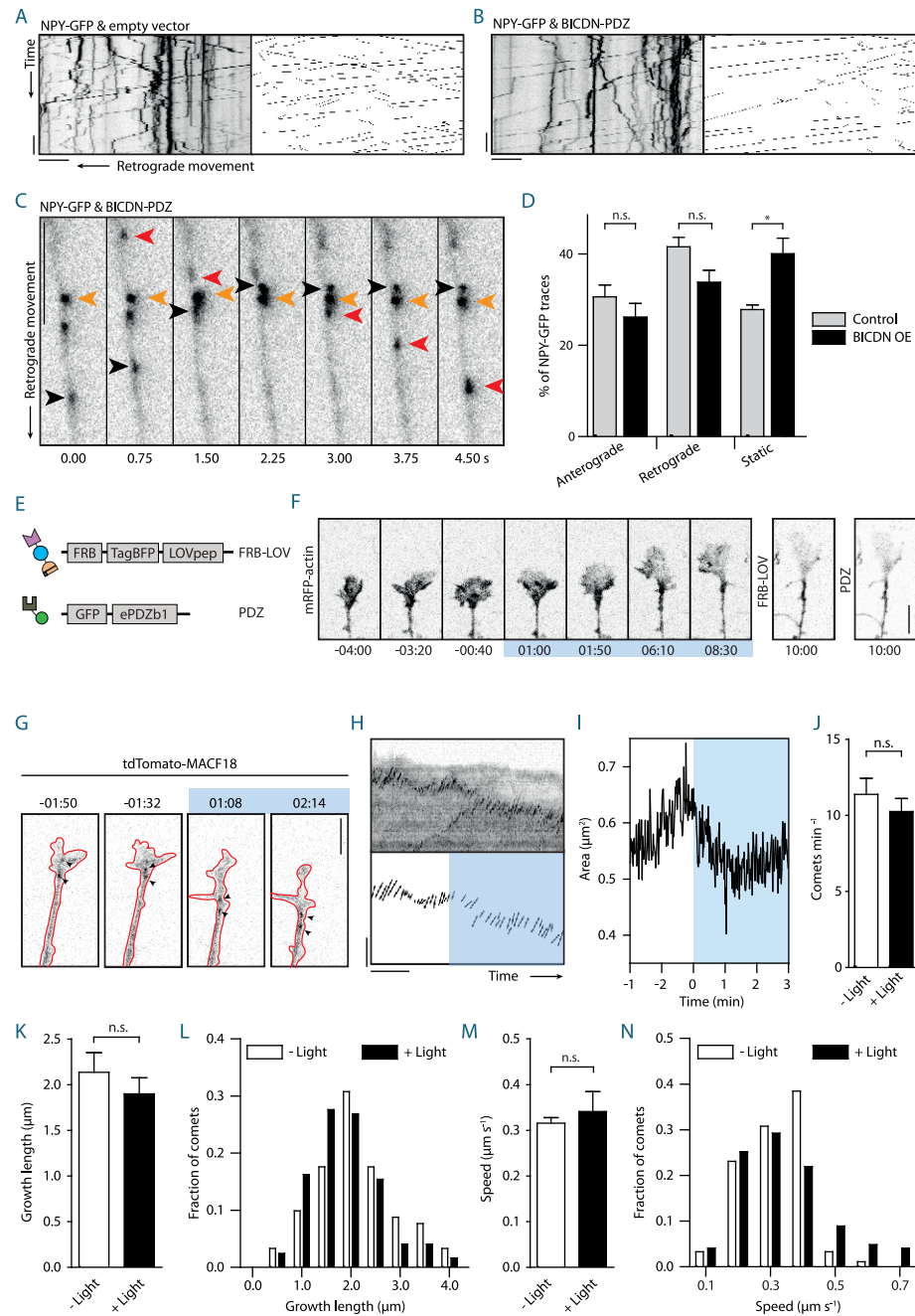


**Figure S7 | BICDN overexpression does not significantly inhibit dynein-based transport and the growth cone cytoskeleton is not affected by light-induced recruitment of BICDN to recycling endosomes.**

**(A and B)** Left: kymograph of dense-core vesicles motility in an axon expressing neuropeptide Y (NPY) fused to GFP (NPY-GFP) and empty vector (A) or BICDN-PDZ (B) (inverted contrast), representative of n = 5 and n = 10 axons, respectively. Right: corresponding binary image of traces used for further analysis of anterograde and retrograde movements. Scale bars, 5  $\mu\text{m}$  and 10 s. **(C)** Position of dense-core vesicles along an axon expressing NPY-GFP and BICDN-PDZ. Single colored arrowheads point to the same vesicle, highlighting retrograde (red), anterograde (black) and non-moving (orange) vesicles. Scale bar, 5  $\mu\text{m}$ . **(D)** Quantification of the percentage of static, anterograde and retrograde moving vesicles from kymographs shown in A and B in axons with (n = 10) or without (n = 5) BICDN-PDZ overexpression. Graph shows mean  $\pm$  SEM, \*  $p > 0.05$ , one-way ANOVA and Bonferroni's multiple comparison test. **(E)** A fusion of FRB, tagBFP and LOVpep (FRB-LOV) and a fusion of GFP and ePDZb1 (PDZ) were expressed in neurons. After blue-light illumination, LOVpep undergoes a conformational change, allowing binding of PDZ to FRB-LOV. **(F)** Actin dynamics in growth cones co-expressing mRFP-actin along with the constructs shown in E, in response to light-induced heterodimerization of FRB-LOV and PDZ, representative of n = 5 growth cones. The blue box indicates the interval of blue-light illumination. Scale bar, 5  $\mu\text{m}$ . **(G)** Imaging of microtubule (MT) plus-ends using tdTomato-MACF18 shows the dynamics of microtubule plus-ends in growth cones before and during blue-light illumination in neurons co-expressing FKBP-RAB11, FRB-LOV and BICDN-PDZ. Red line indicates cell outline, arrowheads point at plus-ends. Scale bar, 5  $\mu\text{m}$ . **(H)** Kymograph of MACF18 comets of the growth cone shown in G and binarized traces used for analysis, representative of n = 4 growth cones. Blue box indicates blue-light illumination interval. Scale bars, 5  $\mu\text{m}$  and 1 minute. **(I)** Area measurement of growth cone shown in G before and during blue-light illumination. Graph shows mean  $\pm$  SEM. Paired two-tailed t-test, n = 4 cells. **(J)** Quantification of the number of MACF18 comets per minute in growth cones before and during blue-light illumination (n = 4 neurons). Graph shows mean  $\pm$  SEM. Paired two-tailed t-test, n = 4 cells. **(L)** Distribution of fraction of MACF18 comets per growth length in bins of 0.5  $\mu\text{m}$  (n = 214 traces). **(M)** Quantification of the growth speed of MACF18 comets in growth cones before and during blue-light illumination (n = 4 neurons). Graph shows mean  $\pm$  SEM. Paired two-tailed t-test, n = 4 cells. **(N)** Distribution of fraction of MACF18 comets per growth speed in bins of 0.1  $\mu\text{m s}^{-1}$  (n = 214 traces).

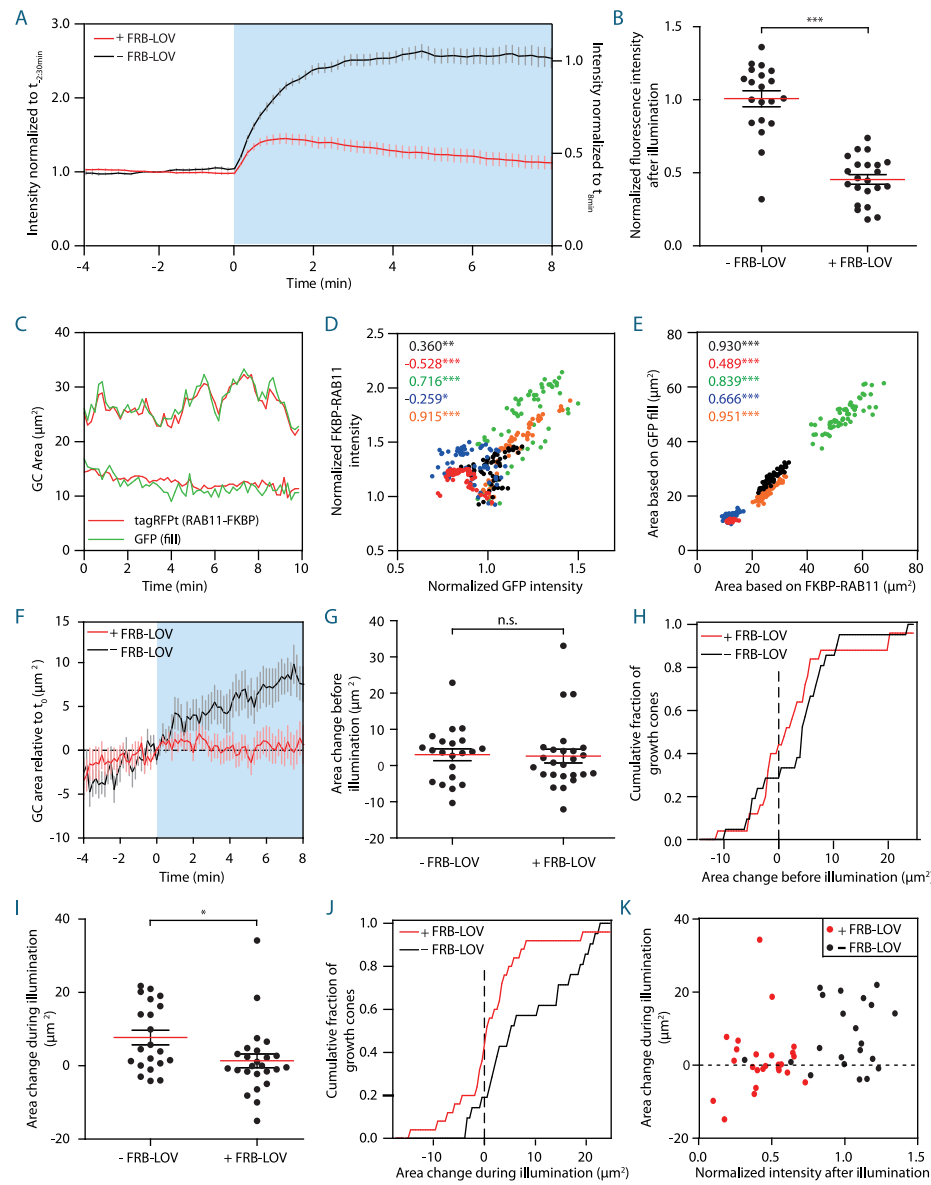


**Figure S8 | Intensity rescaling and accurate growth cone area measurements based on RAB11 fluorescence.**

**(A)** Mean intensity of growth cone FKBP–RAB11 fluorescence from neurons expressing BICDN–PDZ in the absence (black, n = 21) or in the presence (red, n = 25) of FRB–LOV normalized to the intensity before ( $t_{2:30min}$ ) (left axis) and rescaled relatively to the intensity of –LOV growth cones at  $t_{8min}$  (right axis). Blue box indicates blue-light illuminated interval. Graph shows mean  $\pm$  SEM. **(B)** Quantification of FKBP–RAB11 fluorescence intensity in the same neurons as shown in A after 8 minutes of blue-light illumination, normalized to the average fluorescence at  $t_{8min}$  in control neurons. Graph shows mean  $\pm$  SEM, \*\*\* p < 0.0001, Mann-Whitney test. **(C)** Area measurements of two representative growth cones from neurons expressing FKBP–RAB11, FRB–LOV, BICDN–PDZ and soluble GFP over time. Representative of five growth cones (shown in D and E). **(D)** Normalized tagRFPt–RAB11 intensity of five growth cones as in C, plotted against their normalized GFP intensity. Intensity values are averaged over the first five frames per growth cone. Pearson correlation coefficient (r) for each growth cone is indicated in top left corner. Same color indicates measurements of the same growth cone. **(E)** FKBP–RAB11-based area measurements plotted against GFP-based area measurements of the same growth cones as in D. Pearson correlation coefficient (r) for each growth cone is indicated in top left corner. Same color indicates measurements of the same growth cone. **(F)** Traces of growth cone area measurements based on FKBP–RAB11 signal in the absence (n = 25, red trace) and presence (n = 21, black trace) of FRB–LOV in growth cones before and during blue-light illumination (see supplemental experimental procedures). Graph shows mean  $\pm$  SEM. Blue box indicates blue light-exposed interval. **(G)** Quantification of the area increase in the absence and presence of FRB–LOV in growth cones during blue-light illumination (–4 to 0 minutes). Values per growth cone are averaged over three frames. Graph shows mean  $\pm$  SEM. p = 0.4145 (n.s. not significant), Mann-Whitney test. **(H)** Cumulative histogram showing the fraction of growth cones with area shrinkage or growth (left or right of dashed line, respectively) before blue-light illumination (–4 to 0 min). Values per growth cone are averaged over three frames. **(I)** Quantification of the area change of –FRB–LOV and +FRB–LOV growth cones during blue-light illumination (0 to 8 minutes). Values per growth cone are averaged over three frames. Graph shows mean  $\pm$  SEM, \* p = 0.0206, Mann-Whitney test. **(J)** Cumulative histogram showing the fraction of growth cones with area shrinkage or growth (left or right of dashed line, respectively) during blue-light illumination (0–8 min). Values per growth cone are averaged over three frames. **(K)** Scatter plot showing net growth during blue-light illumination and normalized fluorescence intensity after blue-light illumination per +FRB–LOV (red) or –FRB–LOV (black) growth cone.

# Supplemental experimental procedures

## DNA constructs

The following constructs have been described: TagRFpT [29] (Gift from R. Tsien), pCIBN(deltaNLS)-pmGFP and pCry2PHR-mCherryN1 [13] (addgene, plasmids #26867 and #26866), Mid(SS/TM)-GFP-LOVpep and ePDZb1-mCherry [14] (addgene, plasmids #34972 and #34981), TOM20-mCherry-GAI [30] (Gift from T. Inoue), HA-Rab11a [31], Kif1a(1-489)-GFP-FRB, Kif5b(1-807)-GFP-FRB, MyoVb(1-1090)-GFP-FRB, HA-BicD2(1-594)-FRB and Pex3(1-42)-mRFP [15], pGW2-Pex26 and pGW2-Kif17-GFP-Pex26 [16], GFP-SNPH [26] (Gift from Z. Sheng), GFP-RCP [32] (Rab11FIP1, gift from R. Prekeris), NPY-GFP [33] and GFP-MACF18 [34].

**Cloning vectors and fluorescent tags.** The constructs used in this study were cloned in the mammalian expression vectors pGW1-CMV, pGW2-CMV or pβactin [15]. pβactin-GFP, pβactin-TagRFpT, pβactin-TagBFP and pβactin-iRFP were generated by ligating the fluorescent proteins in the Sall and SpeI site of pβactin.

**Tagging motor proteins, adaptors and anchors with CIBN and ePDZb1.** To generate MyoVb(1-1090)-GFP-CIBN and MyoVb(1-1090)-GFP-ePDZb1, amino acids 1-1090 of MyosinVb were cloned in the Ascl and EcoRI sites of pβactin-GFP, and either CIBN or ePDZb1 was inserted downstream of GFP using a PCR-based strategy. Similarly, MyoVb-iRFP-CIBN was made using the pβactin-iRFP vector backbone. Kif1a(1-383)-GFP-CIBN and Kif1a(1-383)-GFP-ePDZb1 were generated by ligating amino acids 1-383 of mouse KIF1A in the Ascl and Sall sites of pβactin-GFP. Subsequently, PCR amplified CIBN or ePDZb1 was inserted downstream of GFP. Haemagglutinin (HA)-tagged-BicD2(1-500)-CIBN and BicD2(1-500)-ePDZ were cloned by inserting PCR amplified BicD2(1-500) (referred to as BICDN in the main text) into the pβactin vector backbone. Subsequently, CIBN and ePDZb1 were ligated downstream of BicDN. Kif5b(1-807)-GFP-ePDZb1 was made by inserting PCR amplified Kif5b(1-807) into the Ascl and BamHI sites of a GFP-ePDZb1 backbone. To create SNPH(45-748)-GFP-ePDZb1, PCR amplified SNPH (forward primer: 5'-agcgctaacgttgccaccatggccatgctccctg-cagggaaag-3' and reverse primer: 5'-gcccttgctcaccatagtcgacccactaccacagccagcatccac-3') was inserted into a GFP-ePDZb1 backbone using Cold Fusion cloning (System Biosciences).

**Tagging peroxisomes, RAB11 vesicles and mitochondria with LOVpep and CRY2PHR.** To generate Pex3-mRFP-LOVpep (PEX-LOV), LOVpep, including a 9-amino-acid linker (GGSGGSGGS), was ligated in the Ascl and Sall sites of pGW1-Pex3-mRFP. To make TOM20-mCherry-LOVpep, Pex3-mRFP was replaced by TOM20(1-34)-mCherry using the HindIII and Ascl sites. To create Cry2PHR-tagRFpT-Rab11 and FKBP-tagRFpT-Rab11, Rab11a was introduced in the SpeI and NotI sites of pβactin-tagRFpT. Subsequently, PCR amplified FKBP or Cry2PHR was ligated upstream of tagRFpT. FRB-TagBFP-LOVpep was made by inserting LOVpep, including a 9-amino-acid linker, in the SpeI and NotI sites of pβactin-TagBFP. Subsequently, PCR-amplified FRB was cloned upstream of tagBFP.

**Other constructs.** pJPA5-TFR-GFP (a gift from Gary Banker) was cloned into a β-actin vector. Membrane targeting of GFP was achieved by inserting the 40 most N-terminal residues of the MARCKS protein with an additional palmitoylation site at residue 3 [35] into GW2-TagRFpT. To generate mRFP-actin, human cytoplasmic β-actin was cloned from pEGFP-actin (Clontech) in the β-actin-mRFP vector.

## Cell cultures and transfection

COS-7 cells were cultured in DMEM/Ham's F10 (1:1) medium containing 10% FCS and 1% penicillin/streptomycin. Then, 2-4 days before transfection, cells were plated on 24-mm diameter coverslips. Cells were transfected with Fugene6 transfection reagent (Roche) according to the manufacturers protocol and imaged one day after transfection.

Primary hippocampal cultures were prepared from embryonic day 18 (E18) rat brains [36]. Cells were plated on coverslips coated with poly-L-lysine (30 μg ml<sup>-1</sup>) and laminin (2 μg ml<sup>-1</sup>) at a density of 75,000 per well. Hippocampal cultures were grown in Neurobasal medium (NB) supplemented with B27, 0.5 mM glutamine, 12.5 μM glutamate, and penicillin plus streptomycin. Hippocampal neurons were transfected 48 h before imaging with Lipofectamine 2000 (Invitrogen). DNA (3.6 μg per well) was mixed with 6.6 μl

Lipofectamine 2000 in 400 μl NB, incubated for 30 minutes, and then added to the neurons in NB supplemented with 0.5 mM glutamine at 37 °C in 5% CO<sub>2</sub> for 1 hour. Next, neurons were washed with NB and transferred to the original medium at 37 °C in 5% CO<sub>2</sub> for 2 days. Transport assays targeting dendritic spines were imaged at day-*in-vitro* (DIV) 20-22 and growth cone or mitochondria assays were imaged at DIV 3-7.

## Live-cell image acquisition

Time-lapse live-cell imaging of COS-7 cells and hippocampal neurons was performed on a Nikon Eclipse TE2000E (Nikon) equipped with an incubation chamber (Tokai Hit; INUG2-ZILCS-H2) mounted on a motorized stage (Prior) [16]. Coverslips (24 mm) were mounted in metal rings, immersed in 0.6 ml Ringer's solution (10 mM Hepes, 155 mM NaCl, 5 mM KCl, 1 mM CaCl<sub>2</sub>, 1 mM MgCl<sub>2</sub>, 2 mM NaH<sub>2</sub>PO<sub>4</sub> and 10 mM glucose, pH 7.4) or full medium (RAB11 imaging in COS-7 cells) or conditioned medium (Neuron imaging), and maintained at 37 °C and 5% CO<sub>2</sub>. Cells were imaged every 5, 10 or 30 seconds for 5-50 minutes using a 40x objective (Plan Fluor, numerical aperture (NA) 1.3, Nikon) and a Coolsnap HQ2 CCD camera (Photometrics). Dense-core vesicles were imaged using a 100x objective (Apo TIRF, 1.49 NA, Nikon) on a Evolve 512 EMCCD camera (Photometrics). A mercury lamp (Osram) and filter wheel containing ET-GFP (49002), ET-DSRed (49005), ET-mCherry (49008) and ET-GFPmCherry (59022) emission filters (all Chroma) were used for excitation and for global activation. For global activation, the GFP excitation filter was used to illuminate the sample for 100-150 ms with every image acquisition during the periods of blue-light exposure. In most experiments, the activation intensity was around 10 W cm<sup>-2</sup> and the total irradiance was about 30 times higher than the minimum irradiance required for full activation (Figure S4H). These settings allowed us to monitor the dynamics of GFP-labeled proteins or growth cones during activation. For local illumination of specific areas using a 488-nm laser line, a FRAP scanning head was used (FRAP L5 D-CURIE, Curie Institute). Compared to standard FRAP experiments the laser was used at much lower intensities.

Live-cell spinning disk confocal microscopy of growth cones and spines of hippocampal neurons was performed on a Nikon Eclipse-Ti (Nikon) microscope with a Plan Apo VC, 60x, 1.40 NA oil objective (Nikon). The microscope is equipped with a motorized stage (ASI; PZ-2000), a Perfect Focus System (Nikon), an incubation chamber (Tokai Hit; INUG2-ZILCS-H2) and uses MetaMorph 7.7.11 software (Molecular Devices) to control the camera and all motorized parts. Confocal excitation and detection is achieved using 100 mW Vortran Stradus 405 nm, 100 mW Cobolt Calypso 491 nm and 100 mW Cobolt Jive 561 nm lasers and a Yokogawa spinning disk confocal scanning unit (CSU-X1-A1N-E; Roper Scientific) equipped with a triple-band dichroic mirror (z405/488/568trans-pc; Chroma) and a filter wheel (CSUX1-FW-06P-01; Roper Scientific) containing 4',6-diamidino-2-phenylindole (DAPI; ET-DAPI (49000)), GFP (ET-GFP (49002)) and mCherry (ET-mCherry (49008)) emission filter (all Chroma). Confocal images were acquired with a QuantEM:512 SC EMCCD camera (Photometrics) at a final magnification of 110 nm per pixel, including the additional 2.5x magnification introduced by an additional lens mounted between scanning unit and camera (VM Lens C-2.5X; Nikon). Local activation of photo-heterodimerization was achieved with an ILas FRAP system (Roper Scientific France/ PICT-IBiSA, Institut Curie) and 491 nm laser line at low power. To couple FRB-LOV to FKBP-RAB11, rapalog (AP21967) was dissolved to 0.1 mM in ethanol. Then, 20 minutes prior imaging, 0.2 ml of culture medium with rapalog (400 nM) was added to establish a final rapalog concentration of 100 nM.

## Image processing and analysis

Images of live cells were processed and analyzed using MetaMorph (Molecular Devices), LabVIEW (National Instruments) software and ImageJ (NIH). If not followed by a quantification in a subsequent panel, representative images are representative of 60-90% of the cells studied in the same conditions, with at least five responding cells per condition (except for Figure S4F with three responding cells, because we used the system in Figures S4I and S4J for all subsequent experiments). The exact organelle distributions and dynamics mostly depended on the levels of protein overexpression, which could not be examined before the experiment without triggering heterodimerization. For example, if the motor were poorly expressed, less redistribution was observed. This was most apparent in experiments where three or more constructs were co-expressed, some of which without fluorescent marker that could be used to confirm expression of the motor.

## Quantification of redistribution dynamics

Before analysis, cells were masked to exclude contributions from neighboring cells to the analysis. For the color-coded redistribution plots, all images of a time-lapse recording were thresholded at ~5-20 times the

standard deviation of the background above the background to yield binary images that were subsequently overlaid non-transparently starting with the final frame (first frame on top) in Figure 1D, and starting with the first frame (last frame on top) in Figure S4D. Each frame was colored using a time-coded gradient that ran from orange to white before and from white to green after blue-light illumination. To quantify the radial redistribution of peroxisomes upon recruitment of (additional) motor proteins, the radius required to include 90% of the total intensity of the cell,  $R_{90\%}(t)$ , was calculated for each frame as described previously [15].

To quantify changes in the dynamics of peroxisomes or RAB11 vesicles upon recruitment of (additional) motor proteins, we calculated the time-dependent frame-to-frame correlation index  $c_\tau(t)$  [16] by first calculating the integrated intensity of the image obtained by multiplying the frames acquired at  $t$  and  $t + \Delta t$ ,

that is,  $\sum_{x=1}^X \sum_{y=1}^Y i(x, y, t) i(x, y, t + \Delta t)$ , in which  $i(x, y, t)$  is the intensity at pixel  $(x, y)$  of the frame acquired at time  $t$ .

These values can then be normalized using either the integrated intensity of the image acquired at  $t$  or  $t + \Delta t$ ,

that is,  $\sum_{x=1}^X \sum_{y=1}^Y i^2(x, y, t)$  or  $\sum_{x=1}^X \sum_{y=1}^Y i^2(x, y, t + \Delta t)$ . For our analysis, we used the average result of these two normalizations as our readout, that is,

$$c_\tau(t) = \frac{1}{2} \left( \frac{\sum_{x=1}^X \sum_{y=1}^Y i(x, y, t) i(x, y, t + \tau)}{\sum_{x=1}^X \sum_{y=1}^Y i^2(x, y, t)} + \frac{\sum_{x=1}^X \sum_{y=1}^Y i(x, y, t) i(x, y, t + \tau)}{\sum_{x=1}^X \sum_{y=1}^Y i^2(x, y, t + \tau)} \right).$$

$c_\tau(t)$  will be 1 if the particles are completely anchored and their positions unchanged after a time  $\tau$ , whereas  $c_\tau(t)$  will be 0 if all particles moved to previously unoccupied locations. In practice,  $c_\tau(t)$  will remain finite even in very dynamic samples, because a subset of particles will move to locations that were occupied by different particles in the first image. In all our analyses, we used frame-to-frame differences. For analyzing the correlation index in small regions (Figures 2D and S4L), measurements were averaged over six adjacent time points.

To determine local changes in fluorescence intensities over time (Figures 1I-L), the mean gray value of the first-frame-subtracted recording (Figure 1L), or last-frame-subtracted recording (Figure 1K) was measured, and the maximum was set to 1. Individual peroxisomes or RAB11 vesicle trajectories were obtained using the MTrackJ plugin in ImageJ [37].

## Analysis of spine entries

Peroxisomes and RAB11 vesicles were imaged at 1-s intervals, preferably in two dendrites of the same neuron, of which one was illuminated with pulses of 491 nm light directly before the frames indicated. Spine entries during periods of 100 s before, 100 s during and 200 s after illumination were detected manually using the Cell Counter plugin in ImageJ to determine the fraction of cargo-targeted spines and the frame of spine entry. The mean percentage of spines targeted with peroxisomes was compared with a Mann-Whitney test (Figure 2I) and the mean percentages of peroxisome and endosome entries were subjected to a Kruskal-Wallis ANOVA with Dunn's post-hoc test (Figure 2J) or a one-way ANOVA with Bonferroni's post-hoc test (Figure S4P), respectively. The half-time of peroxisome entries into dendritic spines after illumination was estimated by fitting a single exponential function ( $R^2 = 0.9942$ ) through the inverted cumulative histogram of the observed entry events after 491 nm illumination was stopped.

## Analysis of axon growth and growth cone area

Axonal growth was manually tracked using the MTrackJ plugin in ImageJ [37]. The percentages of growth cones exhibiting light-induced reduction in dynamics or growth enhancements were compared using unpaired two-tailed  $t$ -tests (Figures 3G and 3H). In all our experiments, only the RFP channel was available for imaging without triggering photo-heterodimerization before, during and after exposure to blue light. We used this channel to image FKBP-tagRFPt-RAB11 to verify that light-controlled recruitment of BICDN induced the removal of RAB11 endosomes (Figures S8A and S8B). FKBP-RAB11 was enriched at vesicles-like structures, whose dynamics altered upon light-dependent recruitment of BICDN to recruit dynein. In addition, FKBP-RAB11 diffusely filled the axon, which could be used to determine axon morphology and size with precision comparable to a cytoplasmic GFP fill (Figure S8C). We counted the positive pixels in a binarized image obtained by thresholding the median-filtered tagRFPt image, followed by two erosions and closure [38]. Because tagRFPt fluorescence of this construct showed a threefold increase in intensity upon 491 nm

excitation (Figure S8A), we established a dynamic threshold  $T$  that scaled with the maximum intensity of the object, that is,  $T = I_{bg} + \sigma_{bg} + 0.02 (I_{max})$ , in which  $I_{bg}$  and  $\sigma_{bg}$  are the average and standard deviation of the intensity in an area outside the axon, respectively, and  $I_{max}$  is the average of the top 2% intensity values above  $I_{bg} + \sigma_{bg}$ . Using these parameters, changes in area are independent of the changes in intensity upon exposure to blue light or due to dynein-mediated removal of RAB11 vesicles (Figures S8D and S8E).

Relative decreases in growth cone RAB11-FKBP signal were calculated by rescaling all intensity values normalized initially to  $t_{-2.30min}$  to the average intensity value of -FRB-LOV control growth cones at  $t_{8min}$  (Figure S8A). To calculate changes in growth cone area before blue-light illumination, we compared single growth cone area values averaged over three frames at  $t_{0min}$  and  $t_{4min}$  relative to illumination onset (Figures S8G and S8H). Analogously, comparing values at  $t_{8min}$  and  $t_{0min}$  shows net growth during blue-light illumination (Figures S8I and S8J). All of these results were compared using Mann-Whitney tests (Figures S8B, S8G and S8I). All statistical testing was performed in GraphPad Prism 5 software. No statistical method was used to predetermine sample size.

## Immunofluorescence cell stainings, imaging and antibodies used

COS-7 cells (1 day after transfection) or primary hippocampal neurons (2 days after transfection) were either kept in the dark or illuminated for 10 minutes using a blue light-emitting diode mounted in the incubator. Afterwards, cells were fixed at room temperature for 10 minutes with 4% Paraformaldehyde (PFA), 4% sucrose. For detection of EB1, cells were fixed for 5 minutes at -20 °C in 100% ice-cold methanol supplemented with 1 mM EGTA, followed by 5 minutes post-fixation at room temperature in 4% PFA, 4% sucrose. After fixation, cells were washed three times in PBS and incubated overnight at 4 °C in GDB buffer (0.1% BSA, 450 mM NaCl, 0.3% Triton X-100, 16.7 mM phosphate buffer, pH 7.4) containing the primary antibody. The next day, cells were washed three times for 10 minutes in PBS, followed by an 1 hour incubation at room temperature with the secondary antibody in GDB buffer. After washing cells three times 10 minutes in PBS, slides were mounted in Vectashield mounting medium (Vector Laboratories). Images were taken with a Nikon eclipse 80i upright fluorescence microscope and a coolsnap HQ2 CCD camera (Photometrics), using a 40x oil objective (Plan Fluor, NA 1.3), 60x oil objective (Plan Apo VC, NA 1.4) or 100x oil objective (Plan Apo VC, NA 1.4).

Antibodies and reagents used: mouse anti-Cytochrome c (6H2.B4, 556432, BD Biosciences), mouse anti-PDI (RL90, MA3-019, affinity BioReagents), phalloidin-Alexa647 (A22287, Invitrogen), mouse anti-alpha Tubulin (B-5-1-2, T-5168, Sigma), mouse anti-EB1 (610535, BD transduction), mouse anti-Lamp1 (This antibody developed by J.T. August and J.E.K Hildreth, was obtained from the hybridoma bank, created by the NICHD of the NIH and maintained at The University of Iowa, Department of Biology, Iowa City, IA52242), mouse anti-EEA1 (BD transduction), rabbit anti-RAB11 (71-5300, Invitrogen), rabbit anti-Homer-1 (160-002, SySy), Alexa 488-, Alexa 568-, Alexa 647-conjugated secondary antibodies (Invitrogen).

## GFP pull-down and Western blotting

HEK cells were cultured in DMEM/Ham's F10 (1:1) medium containing 10% FCS and 1% penicillin/streptomycin. Then 1 day after plating, HEK293T cells were transfected using Polyethylenimine (PEI; Polysciences). After 24 hours, GFP beads (GFP-Trap\_M, Chromotek) were washed in washing buffer (TBS, 0.5% Triton-X-100 and protease Inhibitor) and incubated for 1 hour in blocking buffer (TBS, 0.5% Triton-X-100, 2% glycerol, 2% chicken egg white). Meanwhile, cells were collected in ice-cold TBS, pelleted and lysed in extraction buffer (TBS 0.5% Triton-X-100, 1x protease inhibitor, phosphatase inhibitor (Roche), 100  $\mu$ M GTP $\gamma$ S, 5 mM MgCl<sub>2</sub>, pH 8.0). Cell lysates were centrifuged for 15 minutes at 4 °C at 12.000g, followed by a 1.5-hour incubation of the supernatants with the washed GFP beads, while rotating at 4 °C. Beads were collected using a magnetic separator and washed four times. Samples were eluted in SDS sample buffer, boiled for 5 minutes and loaded onto SDS-PAGE gels and blotted on PVDF membranes (Millipore). Blots were blocked in 5% milk in PBST (0.1% Tween in PBS) and incubated overnight at 4 °C (primary antibody) or for 1 hour at room temperature (secondary antibody conjugated to horseradish peroxidase) in PBST. Finally, blots were developed using enhanced chemiluminescent Western blotting substrate (Pierce).

Antibodies used: rabbit anti-TagRFPt (ab234, Evrogen), rabbit anti-GFP (ab290, abcam) and anti-rabbit IgG antibody conjugated to horseradish peroxidase (DAKO).

## Supplemental references

29. Shaner, N. C. et al. (2008) Improving the photostability of bright monomeric orange and red fluorescent proteins. *Nat Methods* **5**, 545-551
30. Miyamoto, T. et al. (2012) Rapid and orthogonal logic gating with a gibberellin-induced dimerization system. *Nat Chem Biol* **8**, 465-470
31. Hoogenraad, C. C. et al. (2010) Neuron specific Rab4 effector GRASP-1 coordinates membrane specialization and maturation of recycling endosomes. *PLoS Biol* **8**, e1000283
32. Peden, A. A. et al. (2004) The RCP-Rab11 complex regulates endocytic protein sorting. *Mol Biol Cell* **15**, 3530-3541
33. Schlager, M. A. et al. (2010) Pericentrosomal targeting of Rab6 secretory vesicles by Bicaudal-D-related protein 1 (BICDR-1) regulates neuriteogenesis. *EMBO J* **29**, 1637-1651
34. Honnappa, S. et al. (2009) An EB1-binding motif acts as a microtubule tip localization signal. *Cell* **138**, 366-376
35. De Paola, V. et al. (2003) AMPA receptors regulate dynamic equilibrium of presynaptic terminals in mature hippocampal networks. *Nat Neurosci* **6**, 491-500
36. Kapitein, L. C. et al. (2010) Microtubule dynamics in dendritic spines. *Methods Cell Biol* **97**, 111-132
37. Meijering, E. et al. (2012) Methods for cell and particle tracking. *Methods in enzymology* **504**, 183-200
38. Russ, J. C. (2007) The image processing handbook. 5th edn, (CRC/Taylor and Francis)





# Light-controlled intracellular transport in *Caenorhabditis elegans*

# 6

Martin Harterink<sup>1</sup>, Petra van Bergeijk<sup>1</sup>, Calixte Allier<sup>1</sup>, Bart de Haan<sup>1</sup>, Sander van den Heuvel<sup>2</sup>, Casper C. Hoogenraad<sup>1</sup> & Lukas C. Kapitein<sup>1</sup>

*Current Biology* (2016); **4**, pp. 153-154

---

<sup>1</sup> Division of Cell Biology, Faculty of Science, Utrecht University, Utrecht, The Netherlands.

<sup>2</sup> Division of Developmental Biology, Faculty of Science, Utrecht University, Utrecht, The Netherlands.

• These authors contributed equally to this work.

## Abstract

To establish and maintain their complex morphology and function, neurons and other polarized cells exploit cytoskeletal motor proteins to distribute cargoes to specific compartments [1]. Recent studies in cultured cells have used inducible motor protein recruitment to explore how different motors contribute to polarized transport and to control the subcellular positioning of organelles [2,3]. Such approaches also seem promising avenues for studying motor activity and organelle positioning within more complex cellular assemblies, but their applicability to multicellular *in vivo* systems has so far remained unexplored. Here we report the development of an optogenetic organelle transport strategy in the *in vivo* model system *Caenorhabditis elegans*. We demonstrate that movement and pausing of various organelles can be achieved by recruiting the proper cytoskeletal motor protein with light. In neurons, we find that kinesin and dynein exclusively target the axon and dendrite, respectively, revealing the basic principles for polarized transport. *In vivo* control of motor attachment and organelle distributions will be widely useful in exploring the mechanisms that govern the dynamic morphogenesis of cells and tissue, within the context of a developing animal.

## Results & discussion

The nematode *C. elegans* is an important model system for the study of developmental and cell biological questions. A relative weakness is its impermeable exoskeleton, which precludes acute and specific perturbations with small molecules that have been extensively used in cultured cells, for instance with rapamycin-based heterodimerization systems [4,5]. Recently introduced light-sensitive heterodimerization systems that do not require exogenous compounds provide an alternative [6–8]. To test whether light-induced heterodimerization can be used in *C. elegans*, we focused on the LOVpep–ePDZ system, in which a photosensitive LOV domain cages a small peptide that binds an engineered PDZ domain (ePDZ) after exposure to blue light [6]. Codon-optimized LOVpep was fused to the lipid-binding pleckstrin homology (PH) domain for targeting to the plasma membrane, and co-expressed with codon-optimized ePDZ fused to the red fluorescent protein mKate2, under the control of the seam-cell-specific *wrt-2* promoter. Multiple rounds of (subcellular) exposure to blue light resulted in a rapid relocalization of cytosolic mKate2–ePDZ to the illuminated plasma membrane, which was reversed within minutes after stopping the illumination (Figures 1A–C and S1A–C). Similarly, we successfully recruited mKate2–ePDZ to a subset of histone-bound LOVpep by illuminating one half of the nucleus (Figures S1D–F). Thus, light-induced protein dimerization can be locally and reversibly induced in *C. elegans*.

To address whether organelle transport could be triggered with light, LOVpep was targeted to the mitochondrial membrane in seam cells and co-expressed with a fusion construct of ePDZ and a truncated form of the microtubule plus-end-directed motor kinesin-1/UNC-116. Upon exposure to blue light, kinesin-1 motors were recruited to mitochondria, which then began to move and became scattered throughout the cell. The increased mitochondria dynamics upon illumination resulted in a drop in the frame-to-frame correlation index, which measures the similarity between subsequent frames (Figures 1D–F). Conversely, we were able to slow down rapidly moving peroxisomes by coupling them to a Myosin-V/HUM-2 fragment, resulting in an increased correlation index (Figures 1G–I). Together, these data show that organelles can be repositioned within individual cells of a living animal using light.

We next switched to neurons to test how different motors behaved in highly polarized cells. We chose the tail-localized PQR neuron, which possesses one axon and one small ciliated dendrite (Figure 1J). We first tested several fragments and full-length kinesin-1, as well as a motor fragment of kinesin-3/UNC-104 (Figures S1G and S1H), which are both microtubule plus-end-directed motor proteins. Exposure to blue

light triggered rapid motor recruitment to LOVpep-labeled mitochondria (Figure S1I), followed by efficient anterograde motility of axonal mitochondria for all kinesin-1 fusion proteins, except the shortest one (Figures 1K, 1L and S1G–M). Kinesin-3-ePDZ was also able to move mitochondria, but to a lesser extent than kinesin-1 (Figure S1H). The induced transport was more efficient halfway along the axon compared with proximal to the soma, because active motor constructs depleted themselves from the proximal axon by walking towards the axon tip (Figure S1J). Nonetheless, even in *ric-7* mutants, in which mitochondria accumulate in the soma and are largely absent from the axon [9], light-induced kinesin recruitment successfully redistributed mitochondria

to the axon tip (Figure S1K–M).

To induce microtubule minus-end-directed transport we used the dynein-binding and -activating N-terminus of BICD-1 [2]. Exposure to blue light triggered the unidirectional transport of mitochondria towards the dendrite tip (Figure 1K). Despite this acute induction, mitochondria were already accumulating at the tip prior to illumination (Figure 1K), which was largely caused by premature heterodimerization, since accumulation was less pronounced when overexpressing the BICD-1 N-terminus without ePDZ (Figure S1L). Importantly, in all 10 worms where the beginning of the axon and dendrite could be imaged simultaneously, BICD-1 exclusively targeted mitochondria to the dendrite upon exposure to blue light. In contrast, coupling of kinesin-1 resulted in selective transport to the axon in 21 of the 22 worms tested in the same way (Figure 1M). The unidirectionality of dendritic dynein-driven transport is consistent with a dendritic microtubule organization in which all minus-ends are pointing outwards, which also explains why the kinesins selectively targeted the axon, where plus-ends point outwards [10]. These findings highlight the traffic rules that govern polarized sorting in neurons and can be further exploited to alter organelle distributions in a controlled manner. In summary, our optogenetic strategy to control organelle transport and positioning within a multicellular organism should be widely applicable in further unravelling the mechanisms that govern cellular processes such as division, polarization and migration.

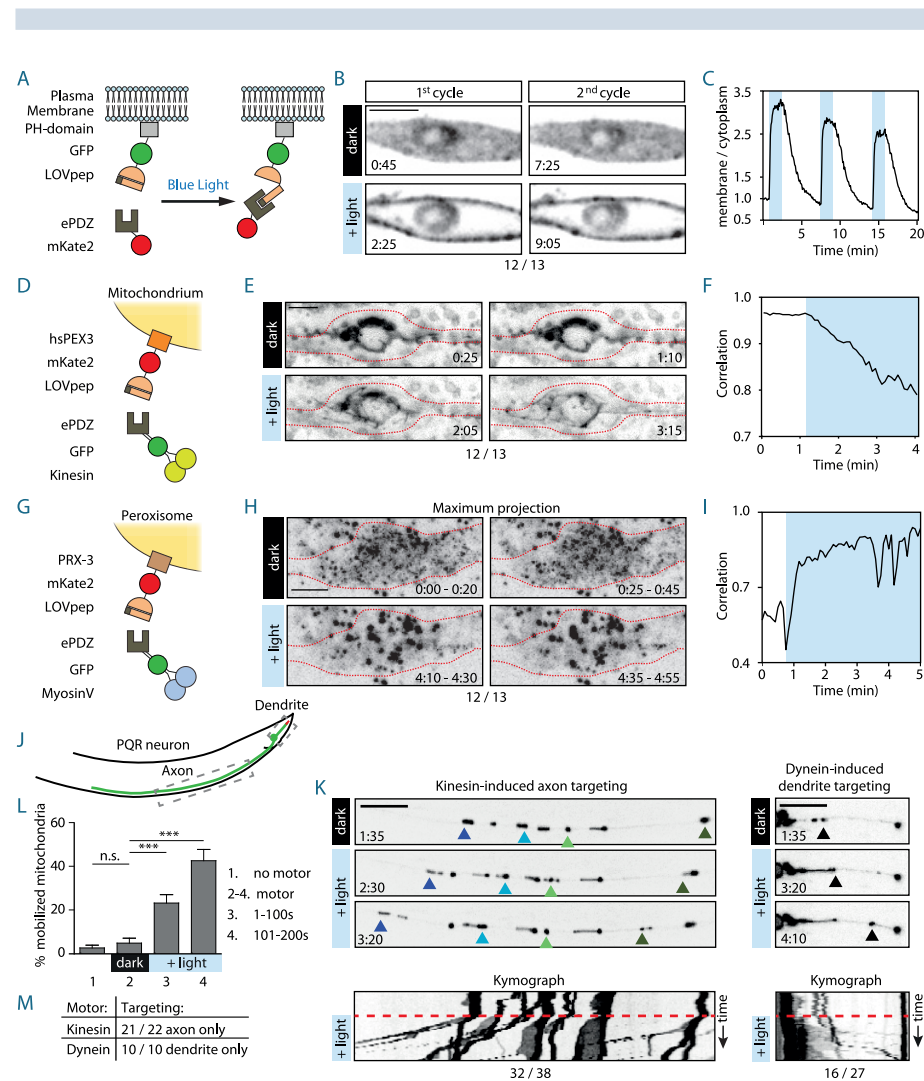


**Figure 1 | Light-controlled organelle transport in *C. elegans*.**

**(A)** Assay: LOVpep binds to ePDZ upon exposure to blue light. **(B)** mKate2–ePDZ distribution in the absence of blue light (upper panels) or during exposure to blue light in a *C. elegans* seam cell. **(C)** Membrane-to-cytoplasm ratio of mKate2–ePDZ fluorescence for the cell shown in B, normalized to the start. Blue boxes mark blue light exposure. **(D)** Assay: hsPEX-3 targets mitochondria. **(E)** Mitochondria before (upper panels) or during (lower panels) exposure to blue light in a *C. elegans* seam cell. Red lines indicate cell outline. **(F)** Time-trace of the correlation index (frame-to-frame differences in mitochondria recordings) of the cell shown in E. Blue box: blue-light illumination. **(G)** Assay: PRX-3 targets peroxisomes. **(H)** Maximum intensity projections of five subsequent frames of peroxisomes (5 seconds intervals) in the absence of blue light (upper panels) or during blue-light exposure (lower panels) in a *C. elegans* seam cell. Red line: cell outline. **(I)** Correlation time-trace of the cell shown in H. Blue box: blue-light illumination. **(J)** PQR neuron with anterior axonal process and posterior dendritic process with sensory cilium (red). Gray dashed boxes are the imaged areas in K. **(K)** Stills and kymograph depicting the distribution of mitochondria (labeled by TOMM-20(aa1–41)-mKate2-LOVpep), before and after light-induced coupling of UNC-116(aa1–381)::GFP::ePDZ (left) or BICD-1(aa1–513)::GFP::ePDZ (right). The cell body is to the right/left for the kinesin/dynein panels, respectively. Arrowheads track individual mitochondria. **(L)** Percentage of mobilized mitochondria (labeled by TOMM-20(aa1–41)-mKate2-LOVpep) without (#1) or with (#2–4) the kinesin construct(UNC-116(aa1–381)::GFP::ePDZ), before (#2) and during the first (#3) or second (#4) 100 s interval of blue light exposure. Mitochondria were counted in the first frame and scored positive if they would displace or undergo fission during the following 100s (n = 10/13 for control/motor). **(M)** Quantification of axon/dendrite targeting of mitochondria by kinesin-1 (UNC-116(aa1–381)) and BICD-1(aa1–513). Only movies with induced transport from the cell body where axon and dendrite could both be seen were analyzed. Numbers below images indicate the number of successful/total light-induced experiments. All images have inverted contrast and scale bars represent 5  $\mu$ m.

## Acknowledgements

We are grateful to Rik Korswagen for the gift of the wrt-2 promoter gateway entry clone, to Henrik Bringmann for the gift of codon-optimized mKate2, and to WormBase. Several strains were provided by the CGC, which is funded by the NIH Office of Research Infrastructure Programs (P40 OD010440). This work is supported by the Netherlands Organisation for Scientific Research (NWO) (NWO-ALW-VENI to M.H., NWO-ALW-VICI to C.C.H., NWO-ALW-VIDI to L.C.K.), the Dutch Technology Foundation STW, which is part of the NWO (to C.C.H and L.C.K), and the European Research Council (ERC Starting Grant to L.C.K., ERC Consolidator Grant to C.C.H).

## Author contributions

M.H., P.B., C.C.H. and L.C.K. designed the study. M.H., P.B., C.A. and B.H. created reagents. M.H. and P.B. performed experiments and analyzed data. M.H., P.B., S.H., C.C.H. and L.C.K. interpreted data and wrote the manuscript. L.C.K. supervised the project.

## References

- Vale, R.D. (2003). The molecular motor toolbox for intracellular transport. *Cell* **112**, 467-480.
- Kapitein, L.C., Schlager, M.A., Kuijpers, M., Wulf, P.S., van Spronsen, M., MacKintosh, F.C., and Hoogenraad, C.C. (2010). Mixed microtubules steer dynein-driven cargo transport into dendrites. *Curr Biol* **20**, 290-299.
- van Bergeijk, P., Adrian, M., Hoogenraad, C.C., and Kapitein, L.C. (2015). Optogenetic control of organelle transport and positioning. *Nature* **518**, 111-114.
- DeRose, R., Miyamoto, T., and Inoue, T. (2013). Manipulating signaling at will: chemically-inducible dimerization (CID) techniques resolve problems in cell biology. *Pflugers Archiv: European journal of physiology* **465**, 409-417.
- Kapitein, L.C., Schlager, M.A., van der Zwan, W.A., Wulf, P.S., Keijzer, N., and Hoogenraad, C.C. (2010). Probing intracellular motor protein activity using an inducible cargo trafficking assay. *Biophys J* **99**, 2143-2152.
- Strickland, D., Lin, Y., Wagner, E., Hope, C.M., Zayner, J., Antoniou, C., Sosnick, T.R., Weiss, E.L., and Glotzer, M. (2012). TULIPs: tunable, light-controlled interacting protein tags for cell biology. *Nat Methods* **9**, 379-384.
- Kennedy, M.J., Hughes, R.M., Peteya, L.A., Schwartz, J.W., Ehlers, M.D., and Tucker, C.L. (2010). Rapid blue-light-mediated induction of protein interactions in living cells. *Nat Methods* **7**, 973-975.
- Yumerefendi, H., Dickinson, D.J., Wang, H., Zimmerman, S.P., Bear, J.E., Goldstein, B., Hahn, K., and Kuhlman, B. (2015). Control of protein activity and cell fate specification via light-mediated nuclear translocation. *PLoS one* **10**, e0128443.
- Rawson, R.L., Yam, L., Weimer, R.M., Bend, E.G., Hartweg, E., Horvitz, H.R., Clark, S.G., and Jorgensen, E.M. (2014). Axons degenerate in the absence of mitochondria in *C. elegans*. *Curr Biol* **24**, 760-765.
- Maniar, T.A., Kaplan, M., Wang, G.J., Shen, K., Wei, L., Shaw, J.E., Koushika, S.P., and Bargmann, C.I. (2012). UNC-33 (CRMP) and ankyrin organize microtubules and localize kinesin to polarize axon-dendrite sorting. *Nat Neurosci* **15**, 48-56.

# Supplemental figures

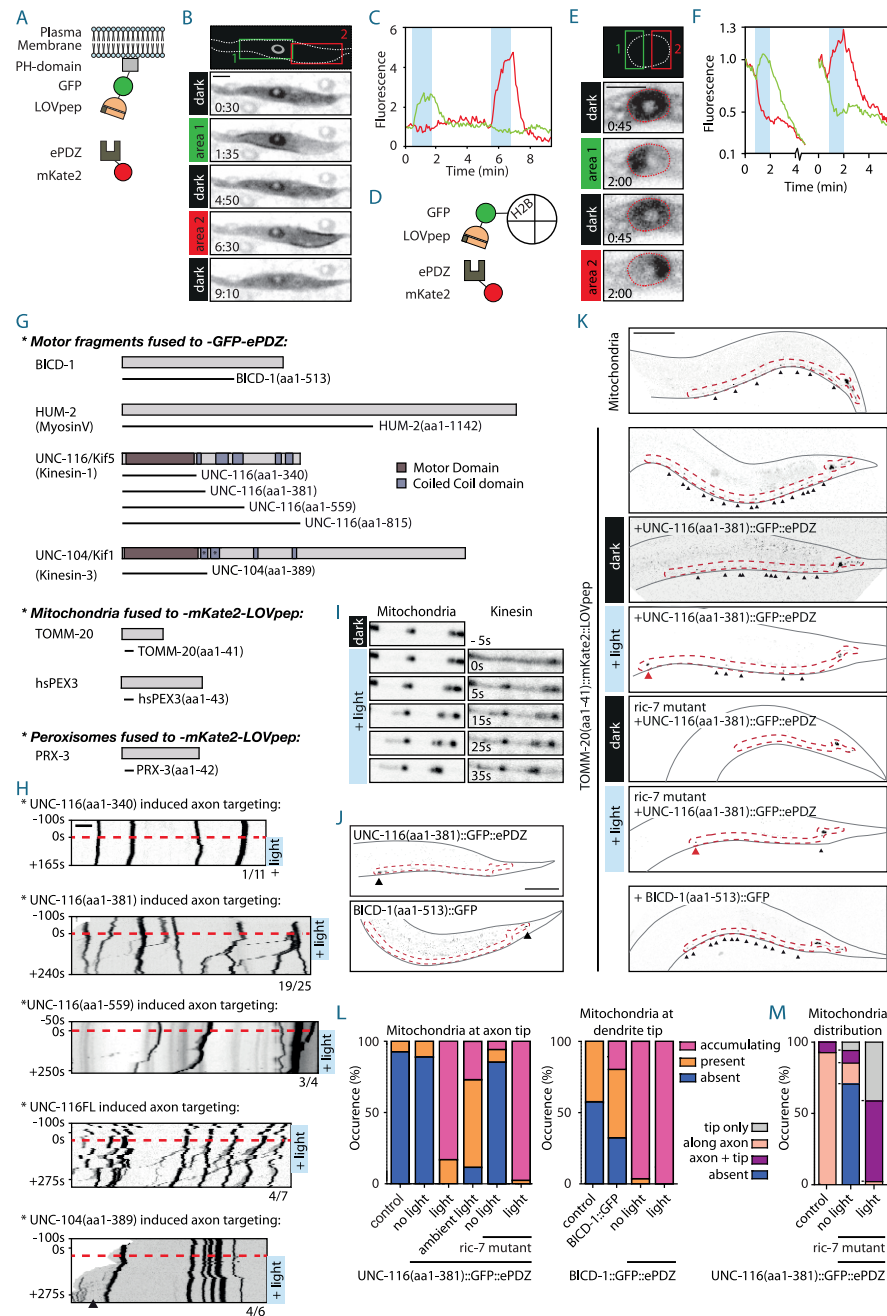


**Figure S1 | Additional data for light-controlled organelle transport.**

**(A)** Assay: a fusion construct of LOVpep, GFP and the lipid-binding pleckstrin homology (PH) domain targets the plasma membrane. Upon exposure to blue light, a fusion of mKate2 and ePDZ is recruited to the plasma membrane. **(B)** mKate2-ePDZ distribution in a seam cell before and after sequential blue-light illumination of the regions indicated in the top picture. **(C)** Time-trace of the mKate2-ePDZ fluorescence of a membrane area in box 1 (green) and box 2 (red) of the cell shown in B, normalized to the start. Blue boxes mark the sequential blue-light illumination of area 1 and 2. **(D)** Assay: a fusion construct of LOVpep, GFP and HIS-58 (H2B) targets the histones in the nucleus. Upon exposure to blue light a fusion of mKate2 and ePDZ is recruited to the histones in the nucleus. **(E)** mKate2-ePDZ distribution in the nucleus of a seam cell before and after sequential blue light illumination of the regions indicated in the top picture. **(F)** Time-trace of the mKate2-ePDZ fluorescence in area 1 (green) and area 2 (red) of the cell shown in (E), normalized to the start of the successive illuminations. Blue boxes mark the sequential blue-light illumination of area 1 and 2. **(G)** Overview of the constructs used for the light-induced transport assays. For the kinesins (UNC-104 and UNC-116) the motor and coiled-coil domains are indicated based on pFam [11] predictions (supplemented by COILS predictions marked by \*) [12]. **(H)** Representative kymographs showing mitochondria movements in the PQR neuron before and after illumination in the presence of the tested motor constructs. Mitochondria coupled to kinesins were imaged in the axon whereas BICD-1-coupled mitochondria were imaged in the dendrite. Numbers below kymographs represent the number of successful/total light-induced transport experiments. Note that for kinesin-3, UNC-104(aa1-389), most experiments did show light-induced mitochondria transport, but much weaker (arrowhead) than for the kinesin-1 (UNC-116) protein fusions. **(I)** Zoom of the left mitochondria of Figure 1K before and after illumination (left panel) and the corresponding kinesin images (right panel). Note that the kinesin is diffusely localized at 0 s (the first frame of blue light exposure) and rapidly accumulates on mitochondria as well as on tubule tips being pulled from mitochondria in subsequent frames. **(J)** UNC-116(aa1-381)::GFP::ePDZ and BICD-1(aa1-513)::GFP localization in the PQR neuron. **(K)** Representative images of mitochondria distribution in the PQR neuron, with either mitochondrial matrix expressing GFP (top) or with the membrane-targeted LOVpep-expressing line used in this study, combined with the indicated constructs and the *ric-7* mutation. Overnight blue-light exposure of kinesin-1-expressing worms resulted in efficient mitochondrial accumulation at the axon tip (large red arrowhead) also in the *ric-7* mutant, which largely lacks axonal mitochondria. BICD-1(aa1-513)::GFP expression (without ePDZ) does not cause severe mitochondrial accumulation at the dendrite tip. Black arrowheads mark the mitochondria along the axon. **(L)** Quantification of mitochondrial presence at the axon or dendrite tip in the TOMM-20(aa1-41)::mKate2::LOVpep line, expressing either GFP (control) or the indicated constructs in wild-type or *ric-7* mutant background, grown in the dark or exposed overnight to blue light or ambient light. The presence was scored as either similar intensity to the axonal/dendritic mitochondria (present) or much stronger (accumulated).  $n > 50$ , except for *ric-7* experiments ( $n > 30$ ) and for the BICD-1::GFP::ePDZ experiment with light exposure ( $n = 18$ ). **(M)** Quantification of mitochondrial distribution in the axon using the mitochondrial-membrane-targeted LOVpep in wild-type and in the *ric-7* mutant expressing the kinesin-1 transport construct UNC-116(aa1-381)::GFP::ePDZ with or without overnight blue-light exposure ( $n > 30$ ). All images have inverted contrast and scale bars represent 5  $\mu\text{m}$  (except in J and K scale bar represents 50  $\mu\text{m}$ ).

# Supplemental experimental procedures

## C. elegans strains and culturing

General methods for culture, manipulation and genetics of *C. elegans* were as described [13]. Strains were cultured at 15 °C and imaged at room temperature. To prevent premature heterodimerization, worm plates were grown wrapped in aluminium foil and an orange optical filter was used while preparing slides. Imaging was performed at L4 or young adult stage animals, except for myosin-induced peroxisome stalling, which was performed in gravid adults. Blue light exposure for Figures S1L–M was performed overnight at room temperature using a Philips Livingcolors lamp.

### Strains used:

- STR222** *unc-119(ed3); hrtEx66[Pwrt-2::mKate2::ePDZ; Pwrt-2::PH::gfp::LOVpep]*  
**STR233** *unc-119(ed3); hrtSi22[Pwrt-2::hsPex3(aa1-43)::mKate2::LOVpep]; hrtEx69[Pwrt2::unc116(aa1-559)::gfp::ePDZ; Pmyo-2::tdTomato]*  
**STR241** *unc-119(ed3); hrtEx74[Pwrt-2::his-58::gfp::LOVpep; Pwrt-2::mKate2::ePDZ; Pmyo-2::tdTomato]*  
**STR254** *unc-119(ed3); hrtSi24[Pgcy-36::tomm-20(aa1-41)::mKate2::LOVpep]; hrtEx78[Pgcy-36::unc-116(aa1-381)::gfp::ePDZ; Pmyo-2::tdTomato]*  
**STR262** *unc-119(ed3); hrtSi24; hrtEx81[Pgcy-36::unc-116(aa1-559)::gfp::ePDZ; Pmyo-2::tdTomato]*  
**STR264** *unc-119(ed3); hrtSi24; hrtEx83[Pgcy-36::bicd-1(aa1-513)::gfp::ePDZ; Pmyo-2::tdTomato]*  
**STR266** *unc-119(ed3); hrtSi24; hrtEx85[Pgcy-36::unc-116(aa1-340)::gfp::ePDZ; Pmyo-2::tdTomato]*  
**STR270** *unc-119(ed3); hrtSi24; hrtEx88[Pgcy-36::unc-104(aa1-389)::gfp::ePDZ; Pmyo-2::tdTomato]*  
**STR271** *unc-119(ed3); hrtSi24; hrtEx89[Pgcy-36::unc-116FL(aa1-815)::gfp::ePDZ; Pmyo-2::tdTomato]*  
**STR287** *unc-119(ed3); hrtSi25[Pwrt-2::prx-3(1-42)::mKate2::LOVpep]; hrtEx94 [Pwrt-2::hum-2(aa1-1142)::gfp::ePDZ; Pmyo-2::tdTomato]*  
**STR305** *unc-119(ed3); hrtEx102[Pgcy-36::bicd-1(aa1-513)::gfp; Pgcy-36::mKate2; Pmyo-2::tdTomato]*  
**STR307** *unc-119(ed3); hrtEx104[Pgcy-36::unc-116(aa1-381)::gfp::ePDZ; Pgcy-36::mKate2; Pmyo-2::tdTomato]*  
**STR309** *unc-119(ed3); hrtEx106[Pgcy-36::mito-gfp; Pgcy-36::mKate2]*  
**STR310** *unc-119(ed3); hrtSi24; hrtEx107[Pgcy-36::bicd-1(aa1-513)::gfp; Pmyo-2::gfp]*  
**STR311** *unc-119(ed3); hrtSi24; hrtEx108[Pgcy-36::gfp; Pmyo-2::tdTomato]*  
**STR315** *ric-7(n2657); hrtEx109[Pgcy-36::tomm-20(aa1-41)::mKate2::LOVpep; Pgcy-36::unc-116(aa1-381)::gfp::ePDZ; Pmyo-2::tdTomato]*

The human Pex3 (hsPex3) construct localizes to mitochondria in seam cells, based on complete overlap with a GFP-labeled mitochondrial marker adapted from Fire lab plasmid pPD96.32 (results not shown), and was used as a mitochondrial adaptor for Figures 1D–F.

## Cloning

Constructs were generated using multisite Gateway cloning (Invitrogen) or with Cold Fusion cloning (System Biosciences). The LOVpep (T406/7A, I532A) and ePDZb1 sequences [14] were codon optimized for *C. elegans* (except the first 39 bps of ePDZ, because of size restrictions when ordering synthetic DNA) [15].

**Gateway 5' entry clones:** We used a plasmid containing 1.6 kb promoter sequence of *wrt-2* (gift of Rik Korswagen) [16] and we generated a plasmid containing 1.2 kb of the *gcy-36* promoter [17].

**Middle entry clone:** The amino-terminal fragment of *C. elegans bicd-1(aa1-513)*, *hum-2(aa1-1142)*, *prx-3(aa1-42)* and *tomm-20(aa1-41)* were cloned from cDNA into the middle entry clone, based on homology to the fragments used in previous cell culture experiments [18–20]. Note that for *hum-2* we were unable to amplify the cDNA fragment based on the predicted ATG in WB250. However based on homology to other *Caenorhabditis* species we successfully cloned the fragment from the ATG (ATGgacggaggcgccactct) which excludes the 2nd exon (8 bps). Design of *unc-104* and *unc-116* fragments was based on the position of coiled-coils as indicated in Figure S1G. The PH domain was PCR amplified from *Pwrt-2::gfp::PH* [16], *his-58* (histone

H2B) was PCR amplified from pCM1.35 [21], mitochondrial matrix *gfp* (mito-*gfp*) was amplified from pPD96.32 (a gift from Andrew Fire; Addgene plasmid #1504), human Pex3 (hsPex3) was used as before [18] and codon optimized mKate2 (gift of H. Bringmann [22]) was used as template to clone it into the middle entry clone.

**3' entry clones:** For the membrane and histone recruitment, *ePDZ::unc-54UTR* and *gfp::LOVpep::unc-54UTR* were cloned into the entry clones (with a 12 aa linker between *gfp* and LOVpep: SGM followed by 3xGGS). For the transport assays *mKate2::LOVpep::unc-54UTR* (9-aa-linker: 3xGGS) and *gfp::ePDZ::unc-54UTR* (5-aa-linker: SAGGS) were cloned into the entry clones.

**Assembly reactions:** All mKate2 containing constructs were cloned into pCFJ150 and all *gfp* containing constructs were cloned into pCFJ210 [23]. For the two constructs for which the gateway reaction did not work, we used a cold fusion approach to generate the identical construct.

## Live image acquisition

All imaging (except Figures 1D–F) was performed on a Nikon Eclipse-Ti microscope with a Plan Apo 20x 0.75 NA (Nikon), a Plan Fluor 40x 1.3 NA oil objective (Nikon) or a Plan Apo VC, 60x, 1.40 NA oil objective (Nikon). The microscope is equipped with a motorized stage (ASI; PZ-2000), a Perfect Focus System (Nikon) and uses MetaMorph 7.8.0.0 software (Molecular Devices) to control the camera and all motorized parts. Confocal excitation and detection is achieved using 100 mW Cobolt Calypso 491 nm and 100 mW Cobolt Jive 561 nm lasers and a Yokogawa spinning disk confocal scanning unit (CSU-X1-A1N-E; Roper Scientific) equipped with a triple-band dichroic mirror (z405/488/568trans-pc; Chroma) and a filter wheel (CSUX1-FW-06P-01; Roper Scientific) containing GFP (ET-GFP (49002)) and mCherry (ET-mCherry (49008)) emission filters (all Chroma). Confocal images were acquired with a QuantEM:512 SC EMCCD camera (Photometrics) at a final magnification of 110 nm (60x objective), 164 nm (40x objective) or 328 nm (20x objective) per pixel, including the additional 2.0x magnification introduced by an additional lens mounted between scanning unit and camera (Edmund Optics). Global activation of photo-heterodimerization was achieved by acquiring GFP images, whereas local activation was achieved using an iLas FRAP system (Roper Scientific France/ PICT-IBISA, Institut Curie) and the 491 nm laser line. Mitochondria imaging in the seam cells (Figures 1D–F) was performed on a Nikon EclipseTE2000E (Nikon) using a 100x objective (Apo TIRF, 1.49 NA, Nikon) equipped with Coolsnap HQ2CCD camera (Photometrics) [20].

For the light-induced transport assays, optimal results were obtained using low expression of the cargo bound LOVpep and slightly higher expression of the motor bound ePDZ. Especially in seam cells, high expression of kinesin-1 affected mitochondrial morphology. For these reasons, strains carrying organelle-targeting construct were in most cases generated using MosSCI [24], followed by injection of the motor constructs and selection for low motor expression.

## Image processing and analysis

Images were processed and analyzed using MetaMorph (Molecular Devices), LabVIEW (National Instruments), ImageJ (NIH) and Photoshop (Adobe). Images were rotated and if necessary flipped to have the anterior to the left and ventral side down. To determine the membrane to cytosol ratio (Figure 1C), the mean gray value of a membrane area (background subtracted) was divided by the mean gray value of a cytoplasm area (background subtracted) and normalized to 1 at *t* = 0 s. The correlation index was calculated as described before [20,25].

## Supplemental references

11. Finn, R.D. et al. (2014) Pfam: the protein families database. *Nucleic Acids Res.* **42**, D222-D230
12. Lupas, A. et al. (1991) Predicting coiled coils from protein sequences. *Science* **252**, 1162-1164
13. Brenner, S. (1974) The genetics of *Caenorhabditis elegans*. *Genetics* **77**, 71-94
14. Strickland, D. et al. (2012) TULIPs: tunable, light-controlled interacting protein tags for cell biology. *Nature Methods* **9**, 379-384
15. Redemann, S. et al. (2011) Codon adaptation-based control of protein expression in *C. elegans*. *Nature Methods* **8**, 250-252
16. Wildwater, M. et al. (2011) Cell shape and Wnt signaling redundantly control the division axis of *C. elegans* epithelial stem cells. *Development* **138**, 4375-4385
17. Kirszenblat, L. et al. (2011) LIN-44/Wnt directs dendrite outgrowth through LIN-17/Frizzled in *C. elegans* Neurons. *PLoS Biol.* **9**, e1001157
18. Kapitein, L.C. et al. (2010) Mixed microtubules steer dynein-driven cargo transport into dendrites. *Curr. Biol.* **20**, 290-299
19. Kapitein, L.C. et al. (2010) Probing intracellular motor protein activity using an inducible cargo trafficking assay. *Biophys. J.* **99**, 2143-2152
20. van Bergeijk, P. et al. (2015) Optogenetic control of organelle transport and positioning. *Nature* **518**, 111-114
21. Merritt, C. et al. (2008) 3' UTRs are the primary regulators of gene expression in the *C. elegans* germline. *Curr. Biol.* **18**, 1476-1482
22. Turek, M. et al. (2013) An AP2 transcription factor is required for a sleep-active neuron to induce sleep-like quiescence in *C. elegans*. *Curr. Biol.* **23**, 2215-2223
23. Frokjaer-Jensen, C. et al. (2012) Improved Mos1-mediated transgenesis in *C. elegans*. *Nature Methods* **9**, 117-118
24. Frokjaer-Jensen, C. et al. (2008) Single-copy insertion of transgenes in *Caenorhabditis elegans*. *Nature Genet.* **40**, 1375-1383
25. Kolin, D.L., and Wiseman, P.W. (2007) Advances in image correlation spectroscopy: measuring number densities, aggregation states, and dynamics of fluorescently labeled macromolecules in cells. *Cell Biochem. Biophys.* **49**, 141-164



# KIF19 is required for axon maintenance and neuronal polarity in hippocampal neurons

Petra van Bergeijk<sup>1</sup>, Cátia P. Frias<sup>1</sup>, Joanna Lipka<sup>1,2</sup>,  
Loek Sanders<sup>1</sup>, Stephan Loenen<sup>1</sup>, Anna Malik<sup>2</sup>,  
Jacek Jaworski<sup>2</sup>, Lukas C. Kapitein<sup>1</sup> &  
Casper C. Hoogenraad<sup>1</sup>

---

<sup>1</sup> Division of Cell Biology, Faculty of Science, Utrecht University, Utrecht, The Netherlands.

<sup>2</sup> International Institute of Molecular and Cell Biology, 02-109 Warsaw, Poland.

## Abstract

Neuronal polarization has extensively been studied but the exact sequence of events leading to the formation of a single axon and multiple dendrites is still unknown. Motor proteins can modify the cytoskeleton and are able to carry polarity factors and building blocks specifically into the axon. Although both processes are important for neuronal polarization, the involvement of motor protein family members has not systematically been tested. For this reason, we used the axon initial segment (AIS) as a marker for polarity and performed a motor protein knockdown screen. We found that the microtubule depolymerizing kinesin motor proteins kinesin-8 KIF19, kinesin-2 KIF3C and kinesin-13 KIF2A are required for AIS preservation. We focused our study on KIF19 and demonstrate it is localized to axon and dendrite tips and is required for the conservation of the AIS as well as neuronal polarization. To be able to directly study the effect of microtubule depolymerization on axon formation, we developed an inducible microtubule depolymerization assay.

## Introduction

Hippocampal neurons are polarized into a single axon and multiple dendrites. Both compartments have a very distinct function; whereas dendrites receive signals the axon transmits signals. It is therefore not surprising that their morphology, which is mainly defined by the cytoskeleton, substantially differs between axons and dendrites. Microtubules (MTs) in the axon are oriented uniformly plus-end out and are enriched in acetylated- and detyrosinated tubulin [1–3], which are markers for stable MTs [4–6]. In contrast, MTs in the dendrites have a mixed orientation [7,8] and are less stable compared to axonal MTs [9]. Differences in MT organization and post-translational modifications (PTMs) between axons and dendrites are believed to contribute to motor-mediated polarized transport [10]. For example, the MT minus-end-directed motor dynein has been shown to drive transport into the dendrites [11], whereas it is responsible for retrograde transport in the axon [12]. Moreover, kinesin-1 has been suggested to preferentially walk on acetylated and detyrosinated MTs [13,14], and therefore to accumulate in the axon [2,15].

Differences in MT organization and properties thus contribute to polarized transport, and shape the dendrites and axon in mature neurons. In addition, there is extensive evidence that changes in MT organization and dynamics drive symmetry breaking and can initiate axon formation in developing neurons. During neuronal development, spherical cells grow minor processes, and the rapid outgrowth of one of these short neurites marks the formation of the future axon [16]. This is followed by a change in MT orientation from a uniformly plus and out to a mixed orientation in all other neurites that will later become the dendrites [7,8,17]. Moreover, treatment with the MT stabilizing drug Taxol resulted in the formation of multiple axons [9], showing that MT dynamics can determine axon formation.

Although neuronal polarization has extensively been studied, it remains elusive what drives the MT network rearrangements during axon formation, and what the downstream consequences would be. The involvement of motor proteins is likely, since they could act both upstream and downstream of MTs during axon formation. For example, a changed MT network could alter motor-mediated transport, leading to the local accumulation of polarity factors in the future axon and thereby enhancing axon formation [18,19]. This idea would be consistent with the observed selective translocation of the kinesin-1 KIF5C transporter prior to axon formation [20]. Alternatively, motor proteins could also act upstream of MTs during axon outgrowth by locally depolymerizing or sliding MTs [21], which in turn could stimulate axon formation. Consistent with this idea, addition or uncaging of taxol and nocodazole at the growth

cone resulted in growth cone attraction and repulsion, respectively [22], indicating that changes in MT dynamics can affect axon outgrowth.

To test for a role of motor proteins in axon formation and maintenance, we here performed a motor protein knockdown screen. Our data shows the involvement of the MT depolymerizing motors KIF2A, KIF3C and KIF19 in AIS preservation. Moreover, depletion of these motors mislocalized axon and AIS markers. To directly investigate the effect of MT depolymerization on axon formation, we developed a tool to induce MT depolymerization using a chemically-induced heterodimerization system. We propose a model in which MT depolymerization in the growth cone contributes to axon outgrowth and maintenance in hippocampal neurons.

## Results & conclusions

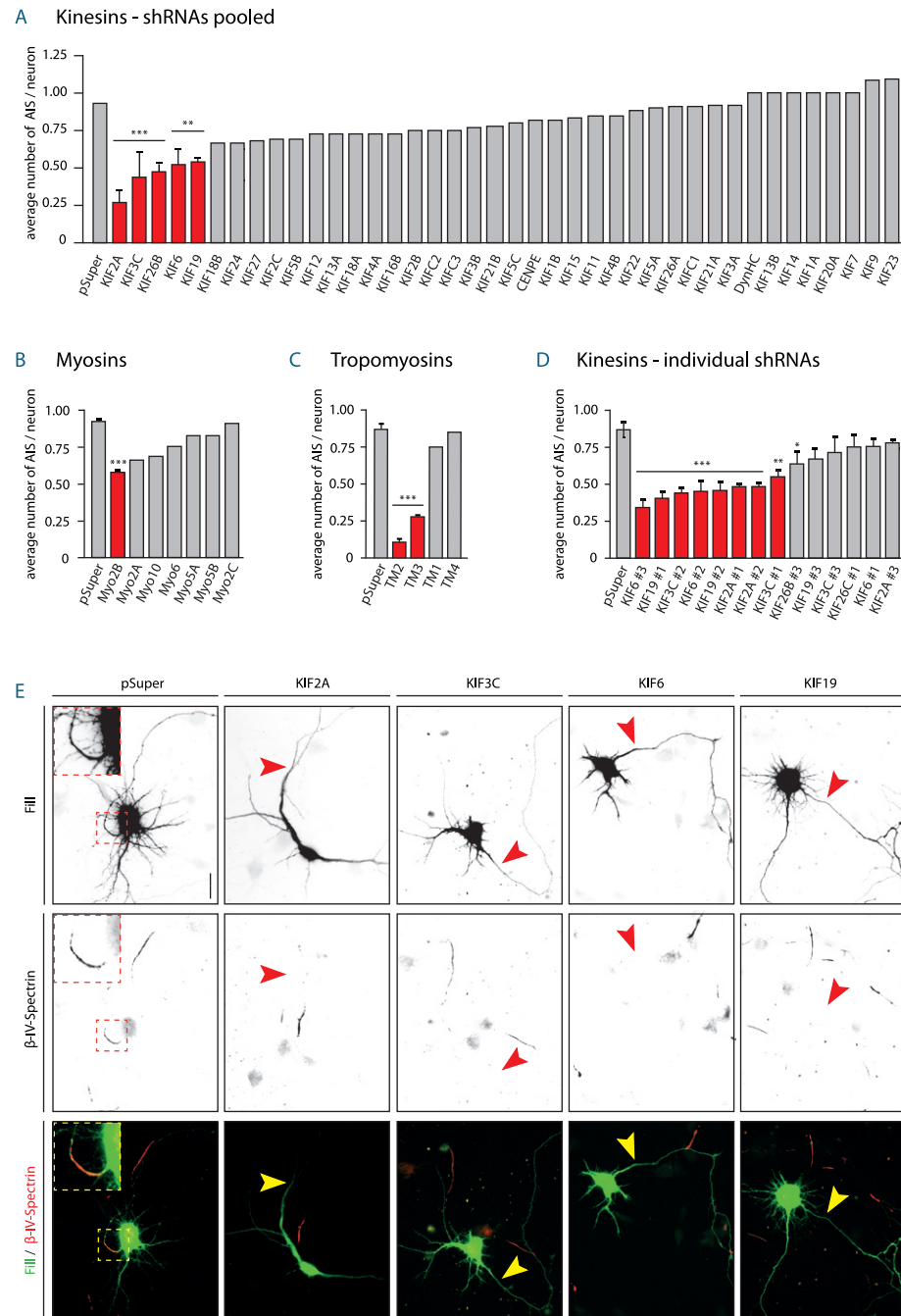
### Depolymerizing kinesins are involved in AIS maintenance and neuronal polarization

To investigate which motor and motor-related proteins are involved in axon formation in hippocampal neurons *in vitro*, we performed a targeted knockdown screen of almost all kinesin, myosin and tropomyosin (TM) family members and of the dynein heavy chain, and examined the localization of the axon specific AIS marker  $\beta$ -IV-Spectrin [23,24]. When pooling three shRNAs targeted to the same protein, depletion of KIF2A, KIF3C, kinesin-11 KIF26B, kinesin-9 KIF6 and KIF19 showed more than 40% decrease in the average number of  $\beta$ -IV-Spectrin positive processes per neuron (Figure 1A). When testing individual shRNA constructs, we found that depletion of MYO2B, TM2, TM3, KIF2A, KIF3C, KIF6 and KIF19 reduced the number of  $\beta$ -IV-Spectrin positive processes per neuron by at least 37% (Figures 1 B–E). Remarkably, although not much is known about the motor properties of KIF6, the three other identified kinesins all appeared to be MT depolymerizing motors [4,25-30]. Therefore, subsequent experiments were focused on the kinesins KIF2A, KIF3C, KIF6 and KIF19.

First, the efficiency of the shRNA-induced depletions was tested. Western blot or immunohistochemistry analysis revealed that the KIF2A- and KIF3C-shRNAs reduced the corresponding protein levels (Figures S1A–C). Unfortunately, endogenous KIF19 could not be detected (Figure S1D) and no proper antibody was available for KIF6 detection. Therefore, Kif6 and Kif19 mRNA levels were determined using Q-RT-PCR, and showed a significant reduction of 40-60% in Kif6 and Kif19 depleted neurons (Figure S1E). These results indicate that the shRNAs directed against the candidate kinesins do lower mRNA and/or protein levels of the corresponding kinesins.

To study if depletion of the four identified kinesins would lead to the complete dismantling of the AIS, we examined the localization of other AIS markers including Neurofascin [31] and the AIS master organizer Ankyrin-G [32] by using two working shRNAs targeted to each kinesin. Whereas KIF6, KIF3C and KIF19 depletion affected the localization of Ankyrin-G, Neurofascin and  $\beta$ -IV-Spectrin, depletion of KIF2A only affected the appearance of  $\beta$ -IV-Spectrin at the AIS (Figures 2A–F). We also noticed that in 29% of the KIF3C depleted and 67% of the KIF6 depleted neurons,  $\beta$ -IV-Spectrin appeared fragmented, compared to 2% in control neurons (Figures 2C and 2F). Together, these data indicate that the depletion of KIF6, KIF3C and KIF19, but not KIF2A leads to the disintegration of the complete AIS.

It has been shown that silencing of Ankyrin-G or the irreversible and preferential degradation of Ankyrin-G and  $\beta$ -IV-Spectrin upon neuronal injury, can



cause a loss of neuronal polarity manifested by the appearance of dendritic characteristics in the axon [33,34]. To determine if silencing of the identified kinesins would interfere with neuronal polarization, we analyzed the distribution of MAP2 and Tau, which are markers for the somatodendritic and axonal compartment, respectively [35]. Interestingly, knockdown of KIF6, KIF3C and KIF2A resulted in the appearance of MAP2 in the axon, 4–5 times more often than in control neurons. Axonal Tau could be observed in the dendrites of 17% of KIF19 silenced neurons whereas this was never observed in pSuper-transfected cells (Figures 3A–D). Furthermore, the recently identified MT bundler Trim46 that normally localizes to the proximal axon and controls neuronal polarity and axon specification [36], appeared in multiple dendrites in KIF19-shRNA transfected cells. These neurons still had a single most clear Trim46 patch at the proximal axon, yet additional Trim46 decorated MTs could be seen in other neurites, 5 times more often than in pSuper-transfected cells (Figures 3B, 3E and 3F). Thus, although three out of four identified kinesins are known to exhibit MT depolymerizing activities, their depletion showed different outcomes on the organization of the AIS and neuronal polarization. Here, further experiments will be focused on KIF19A, of which silencing resulted in the mislocalization of both Trim46 and Tau, indicating that KIF19 is required for axon maintenance and neuronal polarization.

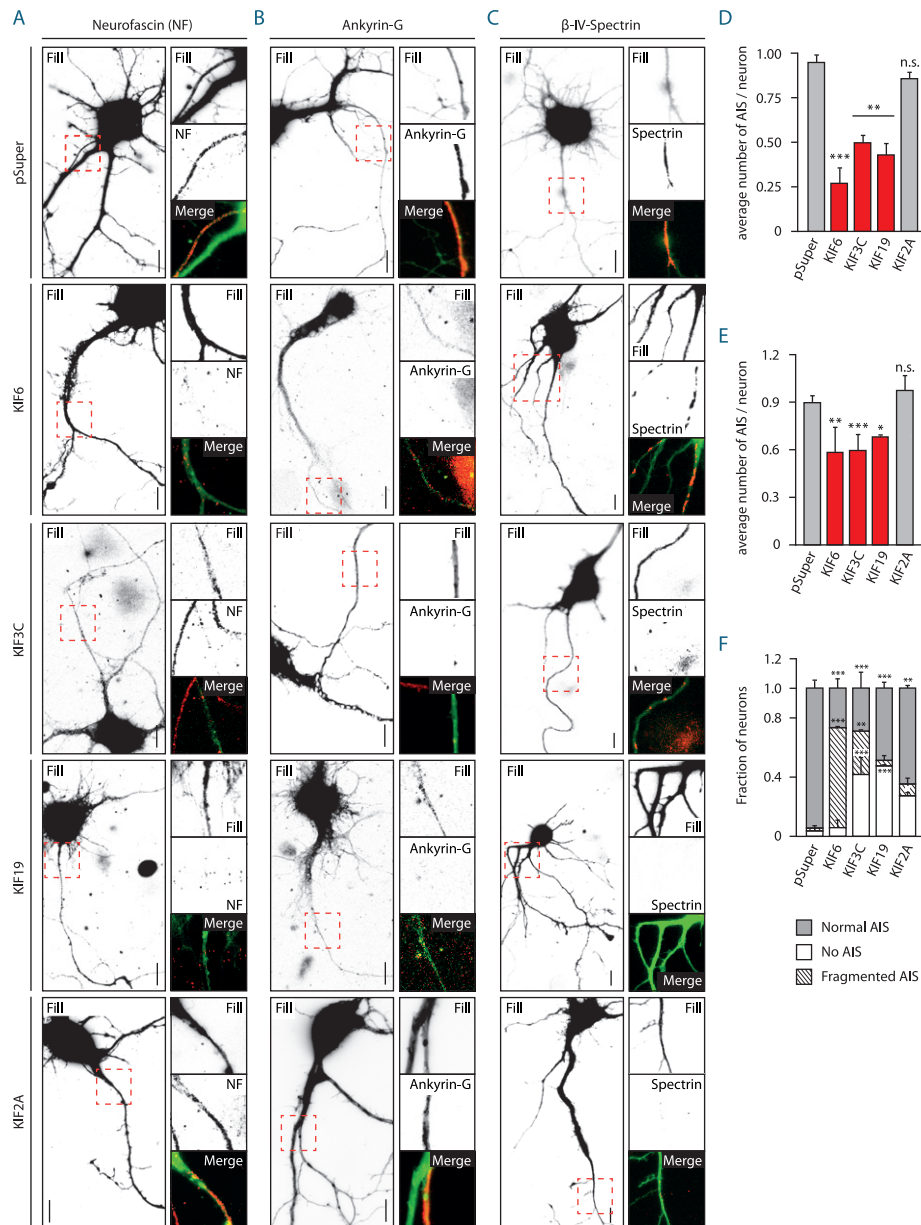
### KIF19 is a microtubule depolymerizer, localizes to neurite tips and is required for axon formation

KIF19 is a kinesin-8 family member and proposed to be involved in the control of cilia length by depolymerizing MT plus-ends at the cilia tip. KIF19 knock out mice have longer epithelial cilia that cannot generate proper fluid flows. Consequently, these mice have an abnormal accumulation of cerebrospinal fluid in the brain and female mice are infertile [30]. Moreover, in a screen for changes in focal adhesion (FA) morphology in HeLa cells, KIF19 knock down cells showed larger FA, more prominent stress fibers and Golgi organization defects. It was hypothesized that defects in vesicle recycling hampered the delivery and removal of FA constituents, FA disassembly

#### Figure 1 | Depolymerizing motor proteins are involved in AIS maintenance.

(A–C) Average number of β-IV-Spectrin positive neurites in control and kinesin/dynein (A), myosin (B) or tropomyosin (C) depleted neurons at DIV 4,5. (D) Average number of β-IV-Spectrin positive neurites in control and kinesin depleted neurons at DIV 4,5 (single shRNAs). (E) Representative images showing a BFP-fill and β-IV-Spectrin staining in control and KIF2A, KIF3C, KIF6 or KIF19 depleted neurons at DIV 4,5. Scale bars represent 20 μm. Error bars indicate mean + SEM. Red bars indicate p < 0.01. A two-tailed Fisher's exact test was performed and at least two experiments and 20 neurons were analyzed per condition.

factors and FA regulators to FA, which in turn resulted in impaired FA turnover and cell migration [37,38]. However, the mechanism by which KIF19 affects FA dynamics remains unknown, as well as the function of KIF19 in neurons and neuronal polarization.



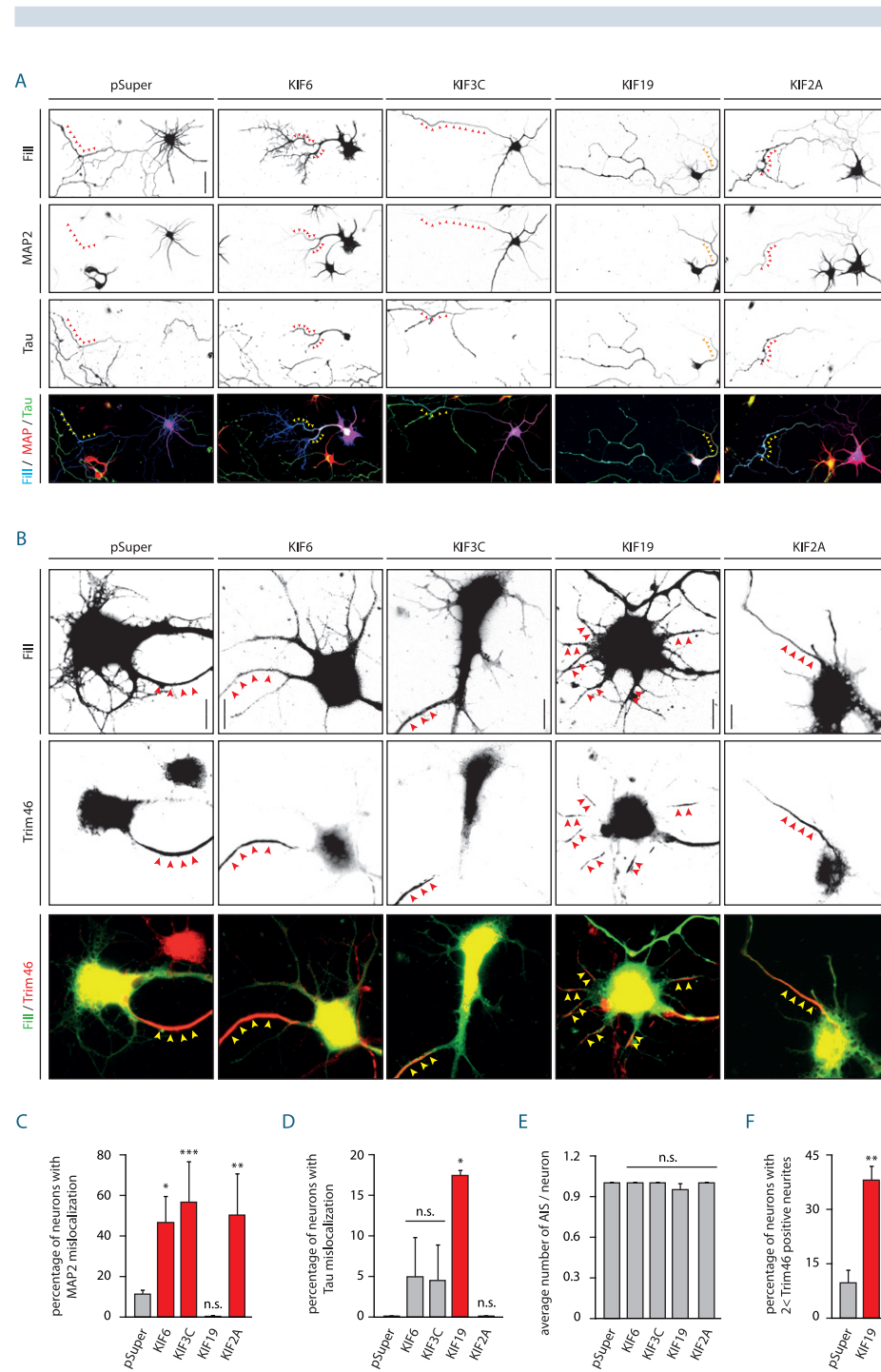
To gain more insight into the role of KIF19, we generated a KIF19-GFP construct to determine the localization of overexpressed KIF19 in COS-7 cells and cortical neurons. In COS-7 cells, full-length KIF19 overlapped with  $\alpha$ -Tubulin staining, showing that KIF19 binds to MTs (Figure 4A). Interestingly, in 33% of the KIF19-GFP transfected cells the MT network was disrupted, compared to 4% in pSuper-transfected cells and 78% in GFP-MCAK transfected cells (Figures 4B and 4C). This indicates that KIF19 depolymerizes MTs but does so less efficient compared to MCAK. In days-*in-vitro* 2 (DIV 2) cortical neurons, KIF19-GFP accumulated in axonal and dendritic tips (Figure 4D). The observed polarization defects in KIF19 depleted cells could thus be a consequence of defects initiated in the axon, dendrites or both. However, the fact that the total axonal length decreased by 50% but the total dendritic length remained unaffected in KIF19 depleted cells (Figures 5A–C) suggests that the observed polarization defects at DIV 4,5 are related to axonal defects. A more detailed analysis revealed that KIF19 depleted neurons have a 35% shorter primary axon, as well as a reduced number of axonal branches from 22 in control to 12 branches in KIF19 depleted neurons (Figures 5D and 5E). *In vitro* axon determination occurs within 24 hours after plating and this is before the knockdown of KIF19 takes full effect. To test if KIF19 plays a role in axon initiation, we treated KIF19 depleted cells with the MT-stabilizing drug taxol that normally induces the formation of multiple axons [9]. In KIF19 depleted cells, new axons were still formed upon taxol treatment (Figures 5F and 5G), indicating that KIF19 is needed for axon outgrowth and/or maintenance rather than the initiation of axon formation.

## KIF19 is required for proper Golgi but not microtubule organization

KIF19 is proposed to depolymerize MTs at cilia tips. Therefore we investigated the MT morphology in axonal growth cones where KIF19-GFP was shown to localize (Figure 4D). When looking at the percentage of growth cones containing visible MTs or buckled

**Figure 2 | Neurofascin, Ankyrin-G and  $\beta$ -IV-Spectrin localization at the AIS depends on KIF6, KIF3C and KIF19.**

(A–C) Representative images showing a BFP-fill and Neurofascin (A), Ankyrin-G (B) or  $\beta$ -IV-Spectrin (C) staining in control and KIF6, KIF3C, KIF19 or KIF2A depleted neurons at DIV 4.5. (D and E) Average number of Neurofascin (D) or Ankyrin-G (E) positive neurites in control and KIF6, KIF3C, KIF19 or KIF2A depleted hippocampal neurons at DIV 4.5. (F) Fraction of neurons showing a normal, fragmented or no  $\beta$ -IV-Spectrin staining in neurons transfected with empty pSuper or KIF6, KIF3C, KIF19 or KIF2A shRNAs. Error bars indicate mean + SEM. Scale bars represent 10  $\mu$ m. Red bars indicate  $p < 0.05$ . A two-tailed Fisher exact test was performed and at least two experiments and 22 neurons were analyzed per condition.



MTs, we could not observe any difference (Figures S2A-C), and also the enrichment of tyrosinated MTs at the axon tip appeared normal in KIF19-shRNA transfected neurons (Figures S2D and S2E). Although these preliminary results suggest no major differences in the MT organization at the axon growth cone, more detailed analyses such as live EB-comet tracking should be performed. Silencing of KIF19 has also been reported to affect Golgi organization in HeLa cells [37], therefore, Golgi morphology was determined in KIF19 depleted hippocampal neurons at DIV 4. Whereas Golgi in control neurons often showed a series of interconnected cisternae that occupied a substantial part of the cell body, the Golgi apparatus in KIF19-silenced neurons happened to be more condensed and packed (Figures S2F and S2G). Whether Golgi disorganization is consequent to polarization defects or a direct effect of KIF19 depletion remains to be tested.

### An inducible microtubule-depolymerization assay

Because three out of the four kinesins that were identified as required for axon maintenance appeared to be MT depolymerizing motors, we set out to develop an inducible MT-depolymerization assay to allow the direct assessment of MT depolymerization on axon growth, formation and maintenance. Preferably this assay would use the depolymerizing activity of KIF19. Full-length KIF19 consists of an N-terminal motor domain, followed by several coiled-coils that are responsible for motor dimerization and thereby the increased affinity for MTs (Figure 6A, left panel). We hypothesized that the dimerization of a truncated KIF19 monomer, consisting of the motor domain and a large part of the first neck coil, would be sufficient to induce MT depolymerization. Therefore, a truncated KIF19 lacking the dimerizing coils was fused to GFP and a modified FK506 Binding Protein (FKBP\*) that homodimerizes upon the addition of AP20187 (ARIAD) (Figure 6A, right panel). In cells transfected with

**Figure 3 | Depletion of KIF6, KIF3C, KIF19 and KIF2A mislocalizes either axonal or dendritic markers.**

**(A and B)** Representative images showing a BFP-fill and MAP2 and Tau staining (A) or a BFP-fill and Trim46 staining (B) in control and KIF6, KIF3C, KIF19 or KIF2A depleted cells. Scale bars represent 40  $\mu$ m (A) or 10  $\mu$ m (B). **(C and D)** Percentage of neurons showing MAP2 (C) or Tau (D) mislocalization in DIV 4,5 neurons transfected with empty pSuper or KIF6, KIF3C, KIF19 and KIF2A shRNAs. A one-tailed Fisher's exact test was performed and at least two experiments and 19 neurons were analyzed per condition. **(E)** Average number of Trim46 positive neurites in control and KIF6, KIF3C, KIF19 or KIF2A depleted neurons at DIV 4,5. A two-tailed Fisher's exact test was performed and at least two experiments and 22 neurons were analyzed per condition. **(F)** Percentage of neurons showing more than two Trim46 positive neurites at DIV 4,5 in control and KIF19 depleted neurons. A two-tailed Fisher's exact test was performed and at least two experiments and 29 neurons were analyzed per condition. Error bars indicate mean + SEM. Red bars indicate  $p < 0.05$ .

KIF19-FKBP\*-GFP, 40% of the cells showed MT depolymerization upon the addition of AP20187, whereas no MT depolymerization was observed in the absence of AP20187 (Figures 6B and 6C). These preliminary results show that MT depolymerization can be induced by means of KIF19 dimerization, however, optimized systems with a higher response rate are desirable.

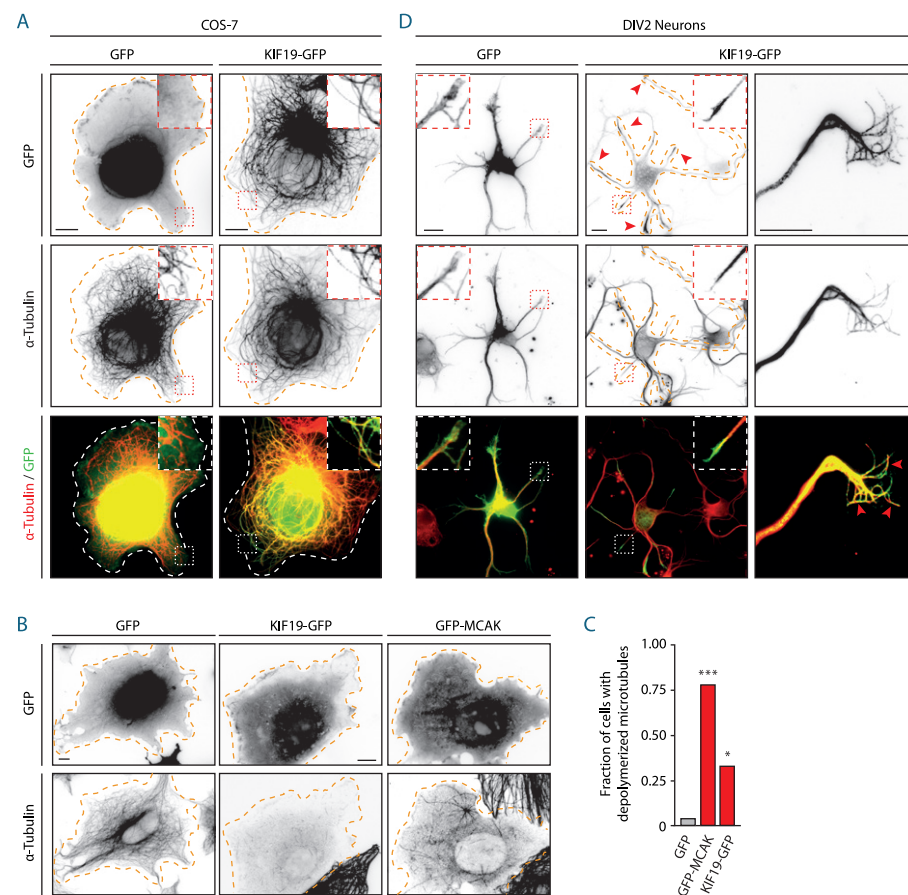


**Figure 4 | KIF19 localizes to microtubules and axonal and dendritic growth cones and depolymerizes microtubules.**

(A) Representative images showing GFP and  $\alpha$ -Tubulin in COS-7 cells transfected with GFP (left) or KIF19-GFP (right). (B and C) Images of COS-7 cells transfected with GFP, KIF19-GFP or GFP-MCAK and stained for  $\alpha$ -Tubulin (B). The fraction of cells showing depolymerized microtubules is quantified in C. A two-tailed Fisher's exact test was performed and at least 9 cells were analyzed per condition. Scale bars represent 10  $\mu$ m and dashed brown lines indicate cell outlines. (D) Representative images showing GFP and  $\alpha$ -Tubulin in cortical neurons at DIV 2 transfected with GFP (left) or KIF19-GFP (right). Note that KIF19-GFP accumulates on microtubules in the growth cones of both short (dendritic) and long (axonal) processes.

## Discussion

Here we showed that the depolymerizing motors KIF19, KIF3C and KIF2A are required for AIS maintenance. We focused our study on KIF19 and demonstrate that KIF19-GFP is enriched at axon and dendrite tips and that KIF19 is required for AIS maintenance, neuronal polarity and axon outgrowth, but not axon initiation. To be able to directly study the effect of MT depolymerization on axon formation, we developed an inducible MT-depolymerization assay.

### Inducible microtubule-depolymerization assay

When screening for motor proteins required for proper AIS marker localization, we identified three MT depolymerizing kinesins that all appeared to accumulate at the axon tip. This raises the question whether MT depolymerization at the axon tip is a general mechanism needed for axon formation. Our developed drug-based MT depolymerization assay could be used to study this question. Nevertheless, limiting MT depolymerization to the growth cone only would be challenging. The recently developed photoactivatable MT depolymerizing drug photostatin would allow MT depolymerization with a higher spatial precision. However, diffusion of the active drug away from the illuminated area would limit the spatial resolution in this system as well, since the reverse time is on a minute scale [39]. For this reason, replacing the homodimerizing FKBP in our MT depolymerization assay with the light inducible-homodimerizing protein VIVID [40] would be a good alternative to control MT depolymerization with a higher spatiotemporal precision, to limit MT depolymerization to the axonal growth cone.

### Confirmation of KIF19 knockdown

In cortical neuron cultures, silencing of KIF19 resulted in reduced Kif19 mRNA levels. Unfortunately, endogenous KIF19 levels were too low to be detected by Western blot. To better examine KIF19 protein levels upon knock down, it would be useful to enrich for KIF19 prior to Western blot analysis. Moreover, a rescue of the observed phenotypes by co-expression of HA-KIF19 would be a good indicator for KIF19 depletion as well.

### Tau mislocalization in KIF19 depleted neurons

Upon knockdown of KIF2A, KIF6 and KIF3C, the dendritic marker MAP2 could be

observed in the axon. This is consistent with the loss of the AIS that is normally responsible for the exclusion of MAP2 from the axon [33]. Remarkably, the depletion of KIF19 had an opposite effect since the axonal marker Tau was now observed in the dendrites, similar to Tau distribution observed in neurological disorders such as Alzheimer's disease [41–43]. Under healthy conditions, only phosphorylated Tau is located in dendrites since unphosphorylated Tau binds with a higher affinity to MTs in the axon [44]. The localization of unphosphorylated Tau in KIF19 depleted neurons might be due to passive leakage of unphosphorylated Tau from the axon into the dendrites, or because the neuron is actively trying to form a new axon. The double positive neurites perhaps display a dendrite that is converting into an axon. This model would also be consistent with the presence of Trim46 in multiple neurites. For this

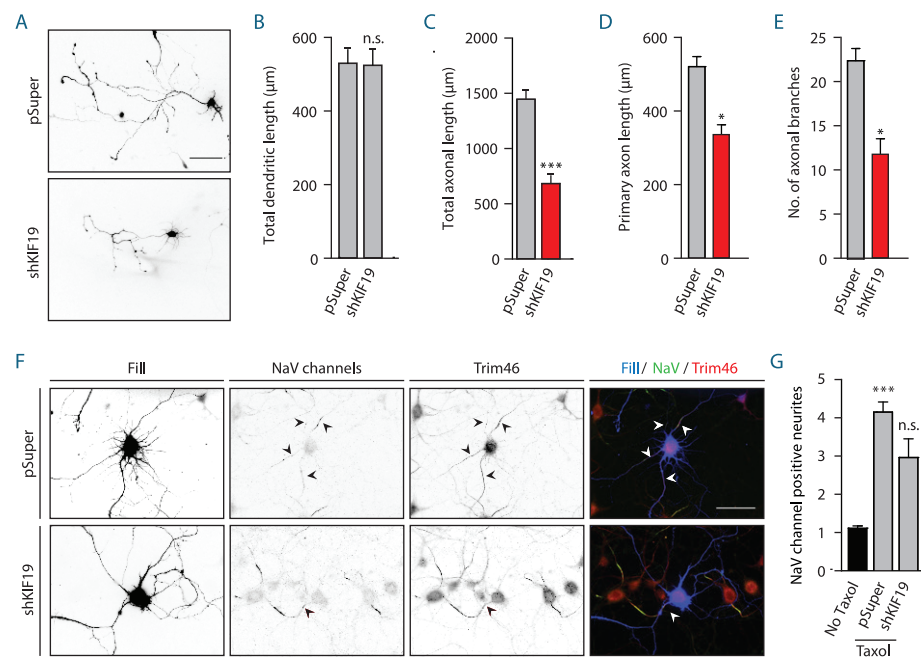


**Figure 5 | KIF19 is required for axon formation and axon outgrowth.**

**(A–E)** Representative images of DIV 4 hippocampal neurons transfected at DIV 0 with empty pSuper or KIF19-shRNAs, showing a GFP-fill (A). Total dendritic length (B), total axonal length (C), primary axon length (D) and the number of axonal branches (E) were quantified. Scale bar represents 100 µm. A two-tailed Kruskal-Wallis test was performed and at least two experiments and 27 neurons were analyzed per condition.

**(F and G)** Representative images of DIV 6 hippocampal neurons transfected at DIV 1 with empty pSuper or KIF19-shRNA, treated at DIV 4 for 48 hours with 10 nM Taxol (or DMSO in control neurons), showing a BFP-fill, NaV and Trim46 staining (F). The number of NaV channel positive neurites is quantified in G. Scale bar represents 50 µm. A two-tailed Kruskal-Wallis test was performed and at least two experiments and 16 neurons were analyzed per condition. Error bars indicate mean + SEM. Red bars indicate  $p < 0.05$

reason, it would be interesting to follow-up KIF19 knockdown neurons for a few more days to determine if the Trim46 positive neurites would ultimately transform into axons.

### Possible models: KIF19 as a transporter of axon identity factors

There are several possible models to explain how KIF19 could affect axon outgrowth and neuronal polarization. First, although KIF19 is observed in both axons and dendrites, KIF19 could mediate the transport of axonal identity factors and polarization factors specifically into the axon. Although KIF19 was shown to be a plus-end-directed motor [30], truncated KIF19 lacking the tail domain did not show any processive transport [45], but this could be due to the lack of the C-terminus, which facilitates MT-binding in other kinesin-8 family members [21]. To see if KIF19 is an active cargo transporter, it would be good to determine the cargo displacement properties of full-length instead of truncated KIF19.

### Possible models: KIF19 as a microtubule slider

Because KIF19 is localized at neurite tips, we believe KIF19 depletion affects axon outgrowth first, leading to AIS impairment as a secondary effect. One way KIF19 at the axon tip could affect axon outgrowth is via MT sliding, since motor proteins have been shown to contribute to axon outgrowth via MT sliding before. For example, dynein was shown to push the MT mass forward during axonal elongation [46] whereas kinesin-driven MT sliding was shown to be essential for neurite outgrowth and axon regeneration in *Drosophila* neurons [47–49]. KIF19 might be responsible for MT sliding in the axonal growth cone, leading to axon growth. To investigate if MT sliding occurs in axonal growth cones and whether this is dependent on KIF19, tubulin tagged with photoactivatable fluorescent proteins could be used. By activating a small area, MT movements could be analyzed in control and KIF19 depleted neurons.

### Possible models: KIF19 as a microtubule depolymerizer

Recent studies have suggested that proper MT dynamics are needed for tension-mediated axon formation. In fact, by plating neurons on top of a geometrically constrained micropattern, it was shown that neurons cannot polarize if the extension of all neurites is restricted. If extension of a single neurite is permitted, this neurite is predetermined to become the future axon [50,51]. Interestingly, this type of axon specification could be inhibited by allowing the extension of a single neurite along a curved instead of a straight line [51], indicating that neurite length in itself does not

determine axon specification. It has been proposed that a larger intrinsic mechanical tension in the longest neurite is responsible for axon specification when grown along a straight line [51]. Consistent with this idea, experimental tension applied by pulling on a minor process with a glass needle could convert a minor neurite into an axon. These data indicate that tension, normally occurring in the longest neurite, is required for axon outgrowth and specification [52]. The mechanism by which mechanical tension could promote axon formation is not known. Interestingly, there is evidence that MTs act as curvature sensors and thereby mediate tension-mediated axonal formation since treatment with low doses of both taxol and nocodazole, to affect MT dynamics, decreased the artificial axon formation [51]. Therefore, KIF19-mediated alterations in MT stability might affect tension-induced axon extension. To test this, it would be critical to test the effects of KIF19 depletion on MT dynamics in the axon by

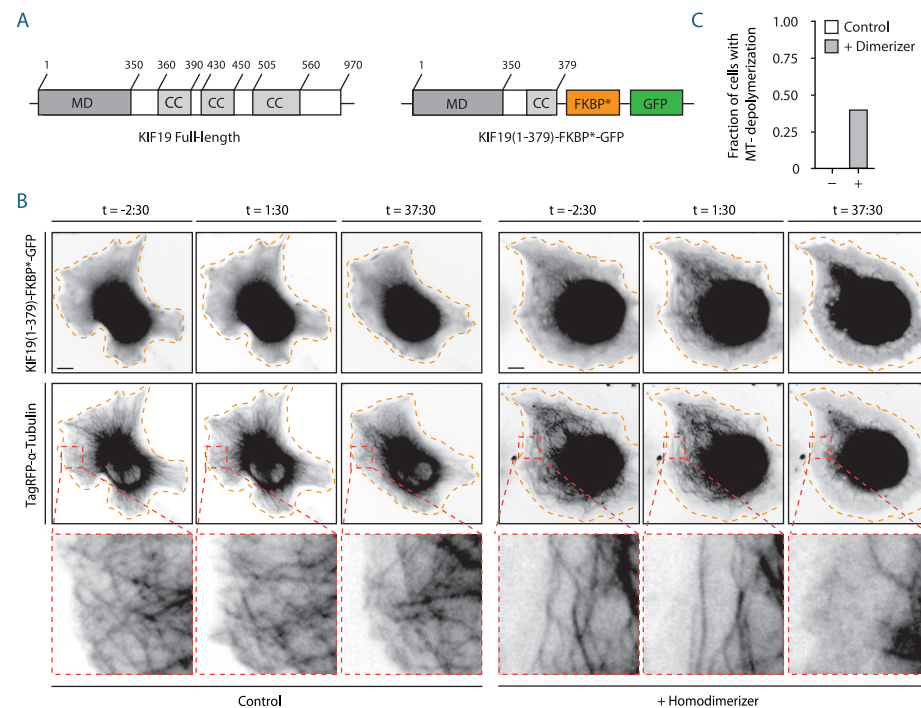


**Figure 6 | Inducible microtubule-depolymerization assay.**

**(A)** KIF19 Full-length (left) and the KIF19 construct used for the microtubule depolymerization assay (right). MD = Motor Domain, CC = coiled-coil, numbers indicate amino acids. **(B and C)** Stills of COS-7 cells transfected with KIF19(1-379)-FKBP\*-GFP and TagRFP-α-Tubulin upon addition at t = 0:00 of control vehicle (left panel) or 100 μM homodimerizer (right panel). The fraction of COS-7 cells that showed microtubule depolymerization is quantified in C. At least 9 cells were analyzed per condition. Orange dashed lines indicate cell outline and scale bar represents 10 μm

means of live EB-comet tracking. Furthermore, it would be interesting to see if the one neurite of which the extension is permitted, would still transform into an axon in KIF19 depleted neurons.

MT polymerization and stabilization in the neurite shaft is critical for axon formation [9]. However, live imaging of fluorescently labeled MTs revealed that a few MTs can invade and explore the actin dense growth cone periphery [53,54] where the fragmentation of looped MTs was associated with the start of growth in previously stalled growth cones [53]. Moreover, growth cone attraction and repulsion was completely blocked by low concentrations of drugs that inhibit MT dynamics, and the addition of guidance cues such as Sema3A, Netrin and Wnt3A was shown to alter MT dynamics [22]. These data suggest that changes in MT dynamics are associated with growth cone dynamics and axon outgrowth. KIF19 might contribute to axon outgrowth by depolymerizing MTs in the axon growth cone at places where they are not needed, to allow MT polymerization at other places to drive directed axon outgrowth.

### Possible models: KIF19 as a microtubule-actin interactor

Alternatively, KIF19 might affect the interaction between the pioneering MTs and the actin network in the axon growth cone. Growth cones are actin rich structures and actin polymerization near the plasma membrane together with myosin-stimulated actin retrograde flow, and the engagement of actin to focal adhesions that withstand the retrograde flow, are believed to drive the growth cone forward. The pioneering MTs were shown to track along F-actin bundles in the filopodia and therefore, actin fibers can guide MT growth to the growth cone surface where they can push the membrane forward or deliver cargo and signals needed for outgrowth. However, physical coupling of MTs to F-actin bundles can also inhibit MT growth because the MTs will be pushed back by the actin retrograde flow. It is therefore not surprising that MT-actin coupling is tightly regulated and KIF19 at the growth cone is perhaps involved in MT-actin coupling, MT guidance and consequently axon outgrowth. To investigate if KIF19 binds to actin related proteins, it would be useful to perform mass spectrometry to determine the interaction partners of KIF19 in neurons. Because MTs can in turn affect actin structures, it would also be useful to determine the actin morphology and structure in the growth cone, for example by performing a phalloidin staining.

### Possible models: KIF19 as a modulator of focal adhesions

Silencing of KIF19 in HeLa cells has been associated with increased FA size, the formation of stress fibers and Golgi morphology defects [37]. Especially the FA phenotype is interesting because FA in the growth cone, besides halting the actin

retrograde flow, are required for the regulation of the actin nucleator N-WASP that is known to be involved in neurite extension [55]. Moreover, in the presence of beads coated with the adhesion molecule apCAM, MTs in the *Aplysia* growth cone first explore the peripheral domain of the growth cone before changes in actin dynamics and growth cone morphology occur. Remarkably, these pioneering MTs have unchanged polymerization rates but progress more forwardly due to uncoupling from the actin retrograde flow, indicating that focal adhesions guide neuronal growth. Besides a role for actin coupling as discussed above, KIF19 might be required for the formation and deformation of FA in axonal growth cones, which is essential for neurite extension. In fact, MT regrowth and FA targeting after nocodazole washout was shown to induce the disassembly of FA via targeting of dynamin, a GTPase responsible for endocytosis [56]. Therefore it would be interesting to see if the organization of focal adhesion proteins such as integrins, focal adhesion kinase and Paxillin are changed in the growth cone upon KIF19 depletion, which is known to affect MT growth.

Above we have discussed several models for the role of KIF19 in axon outgrowth and maintenance. Up to date there is no evidence that KIF19 can perform cargo transport. Moreover, actin binding has not been shown and there are no known actin binding domains in the KIF19 protein sequence. Therefore, we favor a model in which changes in MT depolymerization at the growth cone affect the dynamics of the MTs that explore the growth cone periphery. Consequently, the delivery of FA disassembly factors such as dynamin is impaired, leading to larger FA with a decreased turnover rate (Figure 7). Although FAs are required for neurite extension [55], stabilized FAs

have been reported to impair cell migration [38]. We hypothesize that axon outgrowth is hampered in KIF19 depleted growth cones and that this leads to the disruption of the axon initial segment (AIS), as has been described to occur after neuronal injury [34]. However, future experiments along the lines described above are needed to unravel the exact mechanism by which KIF19 affects AIS maintenance, axon outgrowth and neuronal polarization.

## Author contributions

P.B. L.C.K and C.C.H designed the study. P.B wrote the manuscript and composed all the figures with advice from L.C.K and C.C.H. The experiments described in Figure 5 were performed by C.P.F. All the shRNAs were cloned by J.L. The experiments described in Figure 1D and S1A were completed by L.S. The experiments as described in Figure 6 were performed by S.L. The experiments described in Figure S1E were performed by A.M under supervision of J.J. All other experiments were performed by P.B.

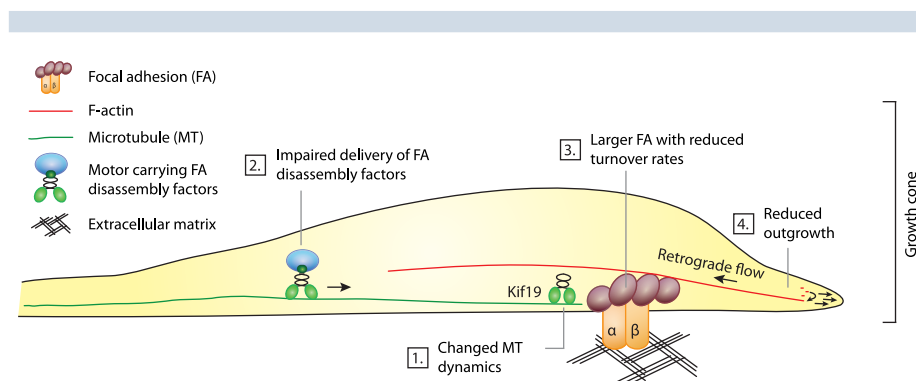


**Figure 7 | Hypothetical model of how KIF19 affects axon outgrowth.**

As proposed by the “clutch hypothesis”, the binding of growth cone receptors to adhesive substrates leads to the mechanical coupling of the receptors to F-actin. The anchoring of F-actin stalls the retrograde flow, and actin polymerization at the plus tip now drives forward growth cone protrusions. In KIF19 depleted cells, MT dynamics are changed and this leads to an impaired delivery of FA disassembly factors to existing FA. FAs get bigger and their turnover rates reduce, presumably leading to decreased rates of FA formation at more distal sites, the capability to anchor F-actin and to push the membranes further forward.

## Acknowledgements

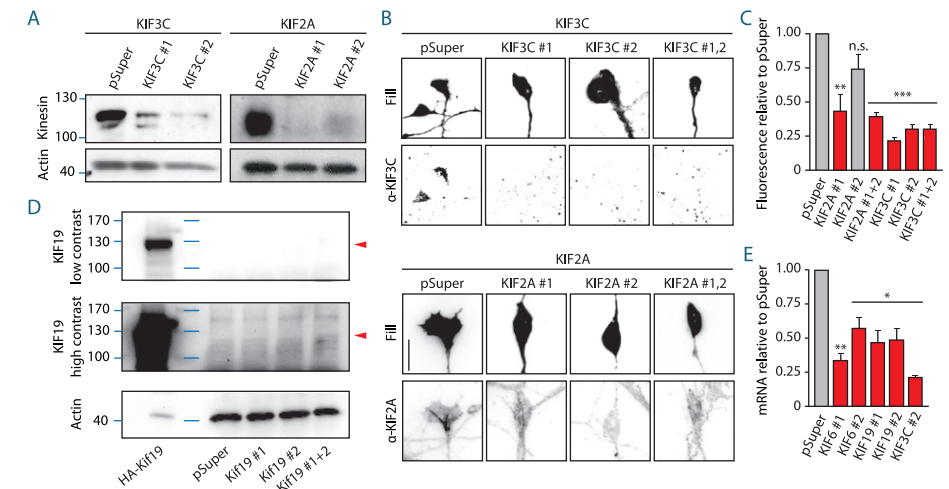
This work is supported by the Netherlands Organisation for Scientific Research (NWO) (NWO-ALW-VICI to C.C.H., NWO-ALW-VIDI to L.C.K.), the Dutch Technology Foundation STW, which is part of the NWO (to C.C.H and L.C.K), and the European Research Council (ERC Starting Grant to L.C.K., ERC Consolidator Grant to C.C.H). J.L. is supported by International PhD Projects Programme of Foundation of Polish Science (Studies of nucleic acids and proteins – from basic to applied research) co-financed by the European Union - Regional Development Fund. C.P.F is supported by the People Programme (Marie Curie Actions) of the European Union’s Seventh Framework Programme FP7/2007-2013/ under REA grant agreement n° 289581. J.J. is supported by Polish National Science Centre Sonata Bis grant (2012/07/E/NZ3/00503) and the Foundation for Polish Science “Mistrz” Professorial Subsidy.

# References

1. Ems-McClung, S.C. et al. (2007) The interplay of the N- and C-terminal domains of MCAK control microtubule depolymerization activity and spindle assembly. *Mol. Biol. Cell* **18**, 282–294
2. Hammond, J.W. et al. (2010) Posttranslational modifications of tubulin and the polarized transport of kinesin-1 in neurons. *Mol. Biol. Cell* **21**, 572–583
3. Cooper, J.R. et al. (2010) Catalysis of the microtubule on-rate is the major parameter regulating the depolymerase activity of MCAK. *Nat. Struct. Mol. Biol.* **17**, 77–82
4. Ogawa, T. and Hirokawa, N. (2015) Microtubule destabilizer KIF2A undergoes distinct site-specific phosphorylation cascades that differentially affect neuronal morphogenesis. *Cell Rep* **12**, 1774–1788
5. Hammond, J.W. et al. (2008) Tubulin modifications and their cellular functions. *Current Opinion in Cell Biology* **20**, 71–76
6. Watanabe, T. et al. (2015) TTBK2 with EB1/3 regulates microtubule dynamics in migrating cells through KIF2A phosphorylation. *J. Cell Biol.* **210**, 737–751
7. Baas, P.W. et al. (1988) Polarity orientation of microtubules in hippocampal neurons: uniformity in the axon and nonuniformity in the dendrite. *Proc. Natl. Acad. Sci. U.S.A.* **85**, 8335–8339
8. Burton, P.R. (1988) Dendrites of mitral cell neurons contain microtubules of opposite polarity. *Brain Res.* **473**, 107–115
9. Witte, H. et al. (2008) Microtubule stabilization specifies initial neuronal polarization. *J. Cell Biol.* **180**, 619–632
10. Hoogenraad, C.C. and Bradke, F. (2009) Control of neuronal polarity and plasticity – a renaissance for microtubules? *Trends Cell Biol.* **19**, 669–676
11. Kapitein, L.C. et al. (2010) Mixed microtubules steer dynein-driven cargo transport into dendrites. *Curr. Biol.* **20**, 290–299
12. Schnapp, B.J. and Reese, T.S. (1989) Dynein is the motor for retrograde axonal transport of organelles. *Proc. Natl. Acad. Sci. U.S.A.* **86**, 1548–1552
13. Reed, N.A. et al. (2006) Microtubule acetylation promotes kinesin-1 binding and transport. *Current Biology* **16**, 2166–2172
14. Konishi, Y. and Setou, M. (2009) Tubulin tyrosination navigates the kinesin-1 motor domain to axons. *Nat. Neurosci.* **12**, 559–567
15. Huang, C.-F. and Banker, G. (2011) The translocation selectivity of the kinesins that mediate neuronal organelle transport. *Traffic DOI: 10.1111/j.1600-0854.2011.01325.x*
16. Dotti, C.G. et al. (1988) The establishment of polarity by hippocampal neurons in culture. *J. Neurosci.* **8**, 1454–1468
17. Baas, P.W. et al. (1989) Changes in microtubule polarity orientation during the development of hippocampal neurons in culture. *J. Cell Biol.* **109**, 3085–3094
18. Nakata, T. (2003) Microtubules provide directional cues for polarized axonal transport through interaction with kinesin motor head. *J. Cell Biol.* **162**, 1045–1055
19. Nakata, T. et al. (2011) Preferential binding of a kinesin-1 motor to GTP-tubulin-rich microtubules underlies polarized vesicle transport. *J. Cell Biol.* **194**, 245–255
20. Jacobson, C. et al. (2006) A change in the selective translocation of the Kinesin-1 motor domain marks the initial specification of the axon. *Neuron* **49**, 797–804
21. Walczak, C.E. et al. (2013) Microtubule-depolymerizing kinesins. *Annu. Rev. Cell Dev. Biol.* **29**, 417–441
22. Buck, K.B. and Zheng, J.Q. (2002) Growth cone turning induced by direct local modification of microtubule dynamics. *J. Neurosci.* **22**, 9358–9367
23. Berghs, S. et al. (2000) betaIV spectrin, a new spectrin localized at axon initial segments and nodes of ranvier in the central and peripheral nervous system. *J. Cell Biol.* **151**, 985–1002
24. Yang, Y. et al. (2007) betaIV spectrin is recruited to axon initial segments and nodes of Ranvier by ankyrinG. *J. Cell Biol.* **176**, 509–519
25. Homma, N. et al. (2003) Kinesin superfamily protein 2A (KIF2A) functions in suppression of collateral branch extension. *Cell* **114**, 229–239
26. Maor-Nof, M. et al. (2013) Axonal pruning is actively regulated by the microtubule-destabilizing protein kinesin superfamily protein 2A. *Cell Rep* **3**, 971–977
27. Niwa, S. (2014) Kinesin superfamily proteins and the regulation of microtubule dynamics in morphogenesis. *Anat Sci Int* **90**, 1–6
28. Noda, Y. et al. (2012) Phosphatidylinositol 4-phosphate 5-kinase alpha (PIP5K) regulates neuronal microtubule depolymerase kinesin, KIF2A and suppresses elongation of axon branches. *Proc. Natl. Acad. Sci. U.S.A.* **109**, 1725–1730
29. Gumy, L.F. et al. (2013) The Kinesin-2 family member KIF3C regulates microtubule dynamics and is required for axon growth and regeneration. *J. Neurosci.* **33**, 11329–11345
30. Niwa, S. et al. (2012) KIF19A is a microtubule-depolymerizing kinesin for ciliary length control. *Dev. Cell DOI: 10.1016/j.devcel.2012.10.016*
31. Hedstrom, K.L. et al. (2007) Neurofascin assembles a specialized extracellular matrix at the axon initial segment. *J. Cell Biol.* **178**, 875–886
32. Rasband, M.N. (2010) The axon initial segment and the maintenance of neuronal polarity. *Nat Rev Neurosci* **11**, 552–562
33. Hedstrom, K.L. et al. (2008) AnkyrinG is required for maintenance of the axon initial segment and neuronal polarity. *J. Cell Biol.* **183**, 635–640
34. Schafer, D.P. et al. (2009) Disruption of the axon initial segment cytoskeleton is a new mechanism for neuronal injury. *Journal of Neuroscience* **29**, 13242–13254
35. Kosik, K.S. and Finch, E.A. (1987) MAP2 and tau segregate into dendritic and axonal domains after the elaboration of morphologically distinct neurites: an immunocytochemical study of cultured rat cerebrum. *J. Neurosci.* **7**, 3142–3153
36. van Beuningen, S.F.B. et al. (2015) TRIM46 controls neuronal polarity and axon specification by driving the formation of parallel microtubule arrays. *Neuron* **88**, 1208–1226
37. Andreyeva, N. (2008) Dissertation: Role of vesicular trafficking in focal adhesion turnover.
38. Yue, J. et al. (2014) Microtubules regulate focal adhesion dynamics through MAP4K4. *Dev. Cell* **31**, 572–585
39. Borowiak, M. et al. (2015) Photoswitchable inhibitors of microtubule dynamics optically control mitosis and cell death. *Cell* **162**, 403–411
40. Nihongaki, Y. et al. (2014) Genetically engineered photoinducible homodimerization system with improved dimer-forming efficiency. *ACS Chem. Biol.* **9**, 617–621
41. Buée, L. et al. (2000) Tau protein isoforms, phosphorylation and role in neurodegenerative disorders. *Brain Res. Brain Res. Rev.* **33**, 95–130
42. Brandt, R. et al. (2005) Tau alteration and neuronal degeneration in tauopathies: mechanisms and models. *Biochim. Biophys. Acta* **1739**, 331–354
43. Gendron, T.F. and Petrucelli, L. (2009) The role of tau in neurodegeneration. *Mol Neurodegener* **4**, 13

44. Kanai, Y. and Hirokawa, N. (1995) Sorting mechanisms of tau and MAP2 in neurons: suppressed axonal transit of MAP2 and locally regulated microtubule binding. *Neuron* **14**, 421–432
45. Lipka, J. et al. (2016) Microtubule-binding protein doublecortin-like kinase 1 (DCLK1) guides kinesin-3-mediated cargo transport to dendrites. *The EMBO Journal* DOI: 10.15252/embj.201592929
46. Roossien, D.H. et al. (2014) Cytoplasmic dynein pushes the cytoskeletal meshwork forward during axonal elongation. *J. Cell. Sci.* **127**, 3593–3602
47. Lu, W. et al. (2013) Initial neurite outgrowth in Drosophila neurons is driven by kinesin-powered microtubule sliding. *Curr. Biol.* **23**, 1018–1023
48. Lu, W. et al. (2015) Kinesin-1-powered microtubule sliding initiates axonal regeneration in Drosophila cultured neurons. *Mol. Biol. Cell* **26**, 1296–1307
49. del Castillo, U. et al. (2015) Pavarotti/MKLP1 regulates microtubule sliding and neurite outgrowth in drosophila neurons. *Current Biology* **25**, 200–205
50. Yamamoto, H. et al. (2012) Differential neurite outgrowth is required for axon specification by cultured hippocampal neurons. *J. Neurochem.* DOI: 10.1111/jnc.12001
51. Roth, S. et al. (2012) How morphological constraints affect axonal polarity in mouse neurons. *PLoS ONE* **7**, e33623
52. Lamoureux, P. et al. (2002) Mechanical tension can specify axonal fate in hippocampal neurons. *J. Cell Biol.* **159**, 499–508
53. Dent, E.W. et al. (1999) Reorganization and movement of microtubules in axonal growth cones and developing interstitial branches. *J. Neurosci.* **19**, 8894–8908
54. Schaefer, A.W. et al. (2002) Filopodia and actin arcs guide the assembly and transport of two populations of microtubules with unique dynamic parameters in neuronal growth cones. *J. Cell Biol.* **158**, 139–152
55. Chacón, M.R. et al. (2012) Focal adhesion kinase regulates actin nucleation and neuronal filopodia formation during axonal growth. *Development* **139**, 3200–3210
56. Ezratty, E.J. et al. (2005) Microtubule-induced focal adhesion disassembly is mediated by dynamin and focal adhesion kinase. *Nat. Cell Biol.* **7**, 581–590
57. Kapitein, L.C. et al. (2010) Probing intracellular motor protein activity using an inducible cargo trafficking assay. *Biophys. J.* **99**, 2143–2152
58. Brummelkamp, T.R. et al. (2002) A system for stable expression of short interfering RNAs in mammalian cells. *Science*
59. Honnappa, S. et al. (2009) An EB1-binding motif acts as a microtubule tip localization signal. *Cell* **138**, 366–376
60. Kapitein, L.C. et al. (2010) Microtubule dynamics in dendritic spines. *Methods Cell Biol.* **97**, 111–132
61. Kapitein, L.C. et al. (2013) Myosin-V opposes microtubule-based cargo transport and drives directional motility on cortical actin. *Curr. Biol.* **23**, 828–834
62. Ganem, N.J. and Compton, D.A. (2004) The KinI kinesin Kif2a is required for bipolar spindle assembly through a functional relationship with MCAK. *J. Cell Biol.* **166**, 473–478
63. Ogawa, Y. et al. (2006) Spectrins and ankyrinB constitute a specialized paranodal cytoskeleton. *J. Neurosci.* **26**, 5230–5239
64. Malik, A.R. et al. (2013) Cyr61, a matricellular protein, is needed for dendritic arborization of hippocampal neurons. *Journal of Biological Chemistry* **288**, 8544–8559

## Supplemental figures



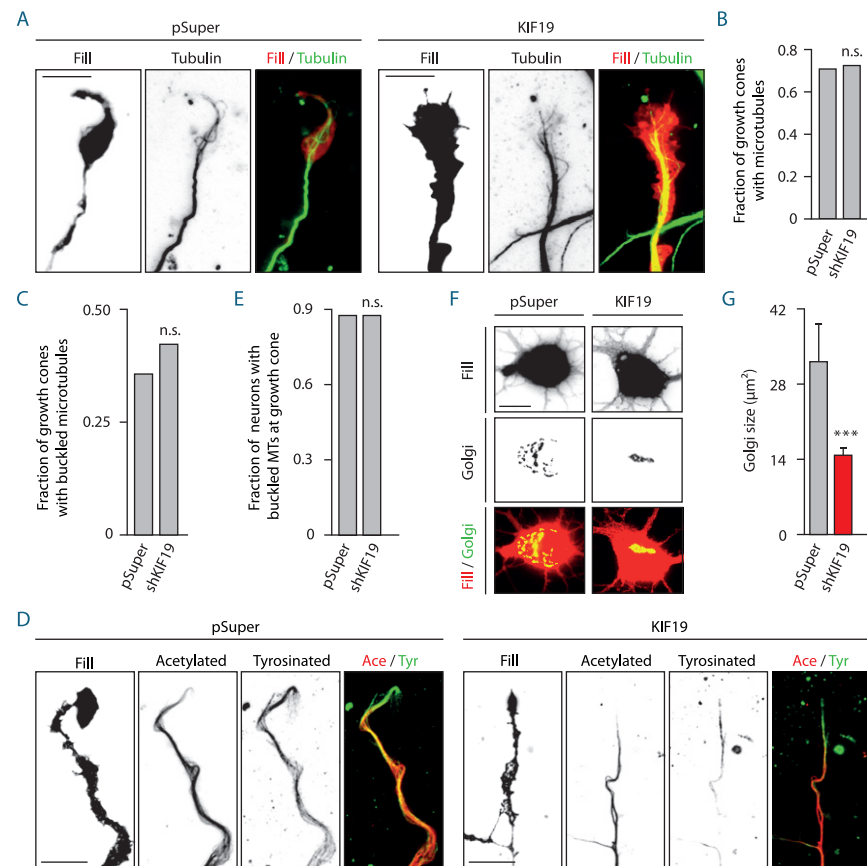


**Figure S2 | KIF19 is required for proper Golgi but not microtubule organization.**

(A–C) Representative images show a BFP-fill and  $\alpha$ -Tubulin staining of DIV 5 control and KIF19 depleted hippocampal neurons (A). The fractions of growth cones in which microtubules (B) or buckled microtubules (C) could be observed are shown. At least 13 neurons were analyzed per condition. (D and E) Representative images show a BFP-fill and acetylated- and tyrosinated-tubulin stainings at DIV 5, in control and KIF19 depleted neurons (D). The fraction of neurons with an enrichment of tyrosinated microtubules in axonal growth cones is quantified in (E). At least 8 neurons were analyzed per condition. (F and G) Representative images show a BFP-fill and a GM130-staining in DIV 5 hippocampal neurons transfected at DIV 1 with empty pSuper or KIF19-shRNA (F). The area covered by the Golgi is quantified in G. Two-tailed Mann-Whitney test was performed and at least 18 neurons were analyzed per condition. Scale bars represent 10  $\mu$ m. Error bars indicate mean + SEM. Red bars indicate  $p < 0.05$

## Supplemental experimental procedures

### DNA and shRNA constructs

The constructs used in this study were cloned in the mammalian expression vectors pGW2-CMV, p $\beta$ actin [57] or pSuper [58]. pGW2-CMV-tagBFP was generated by ligating tagBFP in the HindIII and Ascl sites of pGW2 whereas p $\beta$ actin-GFP and p $\beta$ actin-mGFP were generated by inserting GFP in the Sall and NotI sites of p $\beta$ actin. To make Kif19-GFP, PCR amplified Kif19 (Template: cDNA clone MGC:183958 IMAGE:9087958) was cloned in the Ascl and Sall sites of p $\beta$ actin-GFP. To generate Kif19(1–379)-FKBP\*-mGFP, FKBP\* was PCR amplified from pC4M-Fv2E (Ariad Pharmaceuticals) and ligated into the BamI and Sall sites of p $\beta$ actin-mGFP, followed by the upstream insertion of Kif19(1–379). p $\beta$ actin-TagRFP-TC- $\alpha$ -Tubulin was made by inserting both TagRFP-T (Evrogen) with the linker GMDELYKSGLRSSR and the N-terminus of  $\alpha$ -Tubulin into the NheI and BamHI site of p $\beta$ actin. The shRNA sequences (See Table 1) were ligated into the pSuper vector using the BglII and HindIII sites. GFP-MCAK was a gift from Dr. M. Steinmetz [59].

### Primary hippocampal neuron cultures and transfection

Primary hippocampal cultures were prepared from embryonic day 18 (E18) rat brains [60]. Cells were plated on 18-mm coverslips coated with poly-L-lysine (37.7  $\mu$ g/ml) and laminin (5  $\mu$ g/ml) at a density of 100,000 per well (High Density) or 50,000 per well (Low Density). Hippocampal cultures were grown in Neurobasal medium (NB) supplemented with 2% B27, 0.5 mM glutamine, 15.6  $\mu$ M glutamate, and 1% penicillin/streptomycin. Hippocampal neurons were transfected at 0 or 1 day-*in-vitro* (DIV) with lipofectamine 2000 (Invitrogen). DNA (1.8  $\mu$ g per well) was mixed with 3.3  $\mu$ l lipofectamine 2000 in 200  $\mu$ l NB, incubated for 30 minutes, and then added to the neurons in NB supplemented with 0.5 mM glutamine at 37  $^{\circ}$ C in 5% CO<sub>2</sub> for 1 hour. Next, neurons were washed with NB and transferred to the original medium at 37  $^{\circ}$ C in 5% CO<sub>2</sub> for 4 days.

### Primary cortical neuron culture and transfection

Primary cortical cultures were prepared from embryonic day 18 (E18) rat brains [60] and transfected using the Amaxa Nucleofection kit (Lonza).  $1.2 \times 10^6$  cells were pelleted for 5 minutes at 200g, resuspended in 80  $\mu$ l Nucleofector® solution supplemented with 20  $\mu$ l FCS per sample, and added to 3  $\mu$ g DNA. This mixture was transferred to a cuvette, neurons were electroporated and 800  $\mu$ l DMEM/10%FCS was added. Cells were then divided over 2 wells (35 mm) for Western blotting, or plated on 18-mm coverslip for immunofluorescence. Wells were pre-filled with DMEM/10% FCS and coated with poly-L-lysine (37.7  $\mu$ g/ml) and laminin (5  $\mu$ g/ml). After an incubation of 3 hours at 37  $^{\circ}$ C in 5% CO<sub>2</sub>, medium was replaced for NB supplemented with 2% B27, 0.5 mM glutamine, 15.6  $\mu$ M glutamate and 1% penicillin/streptomycin.

### Live-cell image acquisition

Time-lapse live-cell imaging of COS-7 cells was performed on a Nikon Eclipse TE2000E (Nikon) equipped with an incubation chamber (Tokai Hit; INUG2-ZILCS-H2) mounted on a motorized stage (Prior) [61]. Coverslips (24 mm) were mounted in metal rings, immersed in 0.6 ml Ringer's solution (10 mM HEPES, 155 mM NaCl, 5 mM KCl, 1 mM CaCl<sub>2</sub>, 1 mM MgCl<sub>2</sub>, 2 mM NaH<sub>2</sub>PO<sub>4</sub> and 10 mM glucose, pH 7.4) and maintained at 37  $^{\circ}$ C and 5% CO<sub>2</sub>. Cells were imaged every 30 s for 45 minutes using a 40 $\times$  objective (Plan Fluor, numerical aperture (NA) 1.3, Nikon) and a Coolsnap HQ2 CCD camera (Photometrics). A mercury lamp (Osram) and filter wheel containing ET-GFP (49002), ET-dsRed (49005), ET-mCherry (49008) and ET-GFPmCherry (59022) emission filters (all Chroma) were used for excitation. To homodimerize KIF19-FKBP\*-GFP, rapalog (AP20187) (ARIAD Pharmaceuticals) was dissolved to 1 mM in ethanol. During imaging, 0.2 ml of culture medium with rapalog (4  $\mu$ M) was added to establish a final rapalog concentration of 1  $\mu$ M.

### Image processing and analysis

Images were processed and analyzed using MetaMorph (Molecular Devices) and ImageJ (NIH). To calculate the Golgi area, images were first binarized.

### Immunofluorescence cell staining, imaging and antibodies

COS-7 cells (1 day after transfection), primary hippocampal neurons (4 days after transfection) or cortical neurons (2 days after transfection) were fixed at room temperature for 10 minutes with 4% paraformaldehyde (PFA), 4% sucrose. After fixation, cells were washed three times in PBS and permeabilized for 15 minutes in PBS 0.1% Triton-X-100, followed by an overnight incubation at 4 °C in GDB buffer (0.1% BSA, 450 mM NaCl, 0.3% Triton-X-100 and 16.7 mM phosphate buffer, pH 7.4) containing the primary antibody. The next day, cells were washed three times for 10 minutes with PBS, followed by a 1-h incubation at room temperature with the secondary antibody in GDB buffer. After washing cells three times for 10 minutes in PBS, slides were mounted in Mowiol. Images were taken with a Nikon eclipse 80i upright fluorescence microscope and a Coolsnap HQ2 CCD camera (Photometrics), using a 40× oil objective (Plan Fluor, NA 1.3), 60× oil objective (Plan Apo VC, NA 1.4) or 100× oil objective (Plan Apo VC, NA 1.4). Antibodies used: rabbit anti-KIF3C (O27AKINO9-A, Cytoskeleton), rabbit anti-KIF2A [62] (gift from D. Compton), mouse anti-alpha Tubulin (B-5-1-2, T-5168, Sigma), mouse anti-Ankyrin-G (33-8800, 4G3F8, Zymed), mouse anti-Neurofascin (L11A/41, 75-027, NeuroMab), chicken anti-MAP2 (ab5392, Abcam), mouse anti-Tau (MAB3420, chemicon), mouse anti-acetylated tubulin (6-11B-1, T7451, Sigma), rat anti-tyrosinated tubulin (YL1/2, ab6160, Abcam), rabbit anti-β-IV-Spectrin [63] (gift from M. Rasband), mouse anti-GM130 (BD Bioscience, 610823), rabbit anti-GFP (MBL Sanbio, 598), rabbit anti-Trim46 was described before [36], Alexa 488- and Alexa 568-conjugated secondary antibodies (Invitrogen).

### Western blotting

4 or 7 days after transfection, medium was aspirated and cells were collected in SDS sample buffer, boiled for 10 minutes and loaded onto SDS-PAGE gels and blotted on PVDF membranes (Millipore). Blots were blocked in 3% BSA in PBST (0.1% Tween in PBS) and incubated overnight at 4 °C (primary antibody) or for 1 h at room temperature (secondary antibody conjugated to horseradish peroxidase) in PBST. Finally, blots were developed using enhanced chemiluminescent Western blotting substrate (Pierce). Antibodies used: rabbit anti-KIF3C (O27AKINO9-A, Tebu Bio), rabbit anti-KIF2A [62] (gift from Duane Compton), rabbit anti-KIF19 (HPA043638 Sigma-Aldrich), mouse anti-actin (MAB1501R, Merck Millipore) and anti-rabbit/mouse IgG antibody conjugated to horseradish peroxidase (DAKO).

### Q-RT-PCR

Freshly isolated rat cortical neurons were transfected with use of the AMAXA-kit (Lonza, VPG-1003) and G-013 program according to the manufacturer's protocol and seeded on PDL-precoated plates (BD). 48 hours later neurons were lysed and RNA was isolated using the RNA mini kit (Qiagen). Reverse transcription was performed with use of the High Capacity Reverse Transcription Kit (Applied Biosystems, #4368813). qPCR was performed as described before [64]. For gene expression analysis the following TaqMan rat probes (applied Biosystems) were used: GAPDH Rn99999916\_s1, Kif19 Rn01470721\_m1 and Kif6 Rn0175185\_m1. SDS 2.4 and RQ Manager 1.2.1 programs were used for data acquisition and preliminary analysis. The data were analyzed by comparative Ct method for relative quantification.

### Statistical Analysis

Data and statistical analysis were performed with SPSS software or GraphPad Prism. \* p<0.05, \*\* p<0.01, \*\*\* <0.001.

Gene	shRNA Sequence 5' to 3'	Gene	shRNA Sequence 5' to 3'	Gene	shRNA Sequence 5' to 3'
CENPE	GGAAGGATCTAGCGATGAA	KIF22	GAGAGCGAATGGTACTCAT	KIF5C	GGATCGCACACGATATTT
CENPE	GCTGTACATAAATCGGAA	KIF22	GCTTAAGATGAAGCAAAA	KIF5C	CAATGCCTGTGCGAAGCAG
CENPE	CTGAAGGTATGCGATTGAA	KIF22	GGAATTCGGCTAAAAGAGA	KIF5C	GCTGCAATTACGACCAGA
DYNC1H1	GTTGATGCATGTAGCGTAT	KIF23	GGAGAAACGACATCGCTTA	KIF6	CAGACGGATTCGTAACAA
DYNC1H1	GTGGAACACATACGAACTA	KIF23	GAAGTGGTCAATGATACAA	KIF6	CCGACATGCTAAGCTTCAT
DYNC1H1	GCCACACTATATCTAATCA	KIF23	CCTTTGAGAACGGCAGAA	KIF6	CGTACACATATCCCTTACA
KIF11	GCTGGTATAATCCACGTA	KIF24	GGATAGAGCTGGTTATGCT	KIF7	GGTCGACACATGTGGATA
KIF11	CCACGTACTCTTCATCAGA	KIF24	GTGCTTAGAATCAGACTCT	KIF7	GAGCAAGGTATATCCCAA
KIF11	GCAGAGTATTATACGGATA	KIF24	CAGTCGGAATCAGACATCT	KIF7	GGATAACCAGGAGCTCAA
KIF12	GCCAAAGCATTAAACCGCA	KIF26A	GCGGTTTCGATAACTCAGA	KIF9	GCAATGACATGGAATATGA
KIF12	CTTACCTGGCTATTAGAT	KIF26A	GGAGTGATGATAGGCGAGT	KIF9	GTTAGACGAACGCTATCT
KIF12	GAAGCTTTGATGGAACTAT	KIF26A	AGATCAAGGTGTATGAGAT	KIF9	CGGGAAGTCATACCTCT
KIF13A	CGTACCTTATCGAGATTCA	KIF26B	GCTCAACCGTTACAATGCT	KIFC1	CCAGTTACGTAGAGATCTA
KIF13A	GAACCAGTTAGACGTGCT	KIF26B	GTGACCGACACATTAGGA	KIFC1	CTGTCAACATGCACGATA
KIF13A	GCTCATAAACGACGGGAA	KIF26B	CCTACACCATGATCGGAAG	KIFC1	CACGTGCCCTACCGAAATA
KIF13B	GAAGCCGACAAACGTTGAA	KIF27	GGTGATAATTCGAGAA	KIFC2	CACACTGGGACGTACTTAA
KIF13B	GACGAGAAATGACTTACA	KIF27	CGTATAGGATCGGAAGAT	KIFC2	GGCACCACTGACGTTTTAT
KIF13B	GGATGATGCTGACCGAGAG	KIF27	GGACCTTACATCCGAGAA	KIFC2	CGCCCTAATACCGTGACT
KIF14	CATAACAGCACTTATGTT	KIF2A	GTGTTTACTTTCCACGAA	KIFC3	CGAGAACCAGGCAATTAAT
KIF14	CATCCCGATGAACAATA	KIF2A	GATCGGATTACGTGGAA	KIFC3	CAGCTCCGGACAGGTTAT
KIF14	CGCTCTCATTCCGTTTTCA	KIF2A	GAACCTGACTGGATCCAA	KIFC3	CCACCTGTTAAGTATGTCA
KIF15	GGCTATTGCTCGACTAGAA	KIF2B	GAAAGAAGATTGAACTGGA	KIF16B	CCTTCGCTATCAAATAGA
KIF15	CCTACGATAACTTACAAGA	KIF2B	CACAATGGGTGAGCCCTT	KIF16B	GGCCTAGATAACATCTCT
KIF15	GGAAATGTAGGTCATCA	KIF2B	GGCAATCAAAATCCGAAA	KIF16B	CTGCCAACTTAGGAGAA
KIF18A	GCAGCTACTAGACAATGGA	KIF2C	CAACGACCAATGGGTTAA	Myo6	CTTCGGATACAATCAACA
KIF18A	TTTGTAAGGACACAATA	KIF2C	GTGACGTTCTCAGAGATCT	Myo6	GTATGAGCACTGTTAA
KIF18A	GACACATATAACTCTTA	KIF2C	GCCAATATAAGCAGGTGA	Myo6	CAGCCTAACAATTGAACCT
KIF18B	CCTATGAGGATATACAA	KIF3A	GTGCGACCAATGAAACGA	Myo5a	GCAAACTCGATCGGAGAAA
KIF18B	AGATCTTTGTGAAGCAGCA	KIF3A	CGTATCGGAATCTAAACT	Myo5a	GATGCTAAAGGATCCGGAT
KIF18B	TGACCACCATGGAACGTGA	KIF3A	GTGGTGCACCAATATGA	Myo5a	GTTTGCCTCTCGAGATCA
KIF19	GCAATGACATGGAATATGA	KIF3B	GGATACAAGAGACCACTGA	Myo5b	GTGTCTTTATACGAACAA
KIF19	CAAAGTGTATCCCGTAA	KIF3B	GGTCAGGCGATCTTACTTA	Myo5b	GGTATCGGGTGTGATGAA
KIF19	CGGGAAGTCATACCTCT	KIF3B	GGGCATCTTACTAGAGAT	Myo5b	CCTGCATACACTCTACA
KIF1A	CAGGATGACCGACCTTCT	KIF3C	ATACAGGCTGAAAATATA	NMHC-IIa	GGTAAATTCTTCGTATCA
KIF1A	GACCGGACCTTCAACGAT	KIF3C	GGAAATTTCTCATGACCAA	NMHC-IIa	CCTCAATTCGGGATCCT
KIF1A	GTCAATCAGGATACGTCAT	KIF3C	CCACGCTAAAGTCCGAAA	NMHC-IIa	CTGCTCGCAAGAACTAGA
KIF1B	GGGCTAAACATTTCCGTTGT	KIF4A	CTAATGTGCTCAGACGTAA	NMHC-IIb	GATCAAAGTTGGCCGAGAT
KIF1B	GCAACGCTGTATCAATGA	KIF4A	CCCAAACTTTCCGTATTA	NMHC-IIc	CCGCTCTGAGTCTAACT
KIF1B	CTGGATCTAATGCGAGAGA	KIF4A	CCTTCGCTATGCTGACAGA	NMHC-IIc	GTGGCTAATACCCGTACA
KIF20A	CGGCAATCCTTACGTGAAA	KIF4B	GAAGTCTAGAAATCGGAAGT	NMHC-IIc	CTGCATCGTCCCAATCAT
KIF20A	CTTCAATCAGACCGTCT	KIF4B	CAAGCGGTTATCATCTAT	Myo10	CTCGAGGTTTGATCGGAT
KIF20A	GCATCATCATATGACGAAA	KIF4B	GGTTATCATCTATCATAT	Myo10	GATCAACTCTTCGACGT
KIF21A	CACGCACTGTGAATACAGA	KIF5A	GGACACCAGCGAAAACGGA	Myo10	GTTACCCGACTCTACACGAA
KIF21A	CCGCGAACATAGATTACAT	KIF5A	GCTGGTACGTGACAATGCA	TM1	AGCACATTGCTGAAGATGCT
KIF21A	GCAAAATCATACGTCGAAA	KIF5A	GAGACCAATAACGAATGCA	TM2	ACTGAGGAGCCGAGAGAG
KIF21B	GACGCTCACTGCTAAGTTC	KIF5B	GGTTATGCAAGACAGACGA	TM3	AAGCTGAGGAAAGCGGAGA
KIF21B	CCCTCGTTGAGATCAAGA	KIF5B	GGAATATGAATGCTTAGT	TM4	ATCAAGCTTCTGTCTGACAA
KIF21B	CTCACTATGACGGTATCGA	KIF5B	GCCTATGCAATGATCGT		

Table 1 | Sequences of the shRNAs used in this study.



# 8

## General discussion

Petra van Bergeijk<sup>1</sup>

---

<sup>1</sup> Division of Cell Biology, Faculty of Science, Utrecht University, Utrecht, The Netherlands.

# General discussion

Molecular motors control the transport of a diverse set of cargoes and can modify the cytoskeleton. The aim of this thesis was to illuminate how the interplay between different motor types determines cargo transport and distribution, and how motor proteins contribute to the maintenance of cell compartmentalization and polarity in neurons. The acquired insights on cargo positioning by molecular motors were deployed to develop a tool to control organelle localization with spatiotemporal precision using blue light, which enables to study spatially defined organelle functions. In this final chapter, I will summarize and discuss the main findings and provide recommendations for further research.

## The interplay between actin and microtubule-based motors

Characteristics of individual motor proteins such as direction, speed, stall force, bound cargoes and preferred tracks have extensively been studied. However, to prevent excessive accumulation at sites where either the plus or minus ends of cytoskeletal tracks terminate, individual cargoes often attach to multiple motors of various classes to ensure their proper distribution. Therefore, the final cargo distribution depends on the overall microtubule (MT) and actin organization as well as the interplay between the motors attached. In chapter 3 we show that on cargoes that contain myosin and kinesin motors, Myosin-V is able to stall kinesin-driven organelle movements and can drive short-range transport towards the cell cortex in COS-7 cells.

### Tools to study motor interactions

When using peroxisome motility to probe motor protein activity, one has to take into account that endogenous motors bound to peroxisomes can also contribute to peroxisome motility or anchoring [1]. Therefore the use of an exogenous particle that is not coupled to any motor protein would be beneficial. Quantum dots, which are very bright and photostable nanocrystal fluorophores, would be a good alternative. They can be internalized using electroporation [2] and functionalized to allow binding to motor proteins [3]. Similarly to the peroxisome based trafficking assay, drug or light-induced based protein heterodimerization could be used to inducibly recruit motor proteins, which would allow studying the interplay between Myosin-V and kinesin motors. To exclude the interference of any endogenous motor when analyzing the interaction between myosin and kinesin motors, it is also possible to directly couple

Myosin-V to kinesin without binding to a cargo vesicle. For example, the direct coupling of Myosin-V and kinesin-2 KIF17 changed the final distribution of KIF17 to a typical Myosin-V distribution in which KIF17 got redistributed to the cell cortex (Figure 1). Interestingly, also the enrichment of Myosin-V in cortical cell regions appeared enhanced upon binding to KIF17.

### The interplay between kinesin and Myosin-V in polarized neuronal transport

In neurons, the interplay between myosin and kinesin motors is especially interesting at the axon initial segment (AIS), which is a specialized structure at the beginning of the axon. The AIS is believed to function as a selective sieve that can halt the entry of somatodendritic cargo [4,5]. Myosin-VI and Myosin-Va have been suggested to promote the directional trafficking into and away from the axon, respectively, due to predominant orientation of actin with its plus-end facing towards the cell body [6-8]. In chapter 4 we show that Myosin-V can block the transport of kinesin-driven cargoes into the axon, but does not reverse transport back to the cell soma. This demonstrates that actin structures at the AIS can mediate a Myosin-V based selective barrier. However, our data suggests there is no clear actin polarity since we observe cargo anchoring, but not reversal upon Myosin-V recruitment. This is consistent with EM data that could not detect any systematic actin directionality within the AIS [9], and the more recent identification of actin patches along the axon and the AIS [10]. Moreover, recent work showed the localization of the dynein regulator NDEL1 at the AIS in mature neurons. It was proposed that NDEL controls dynein activity at the AIS and facilitates the reversal of somatodendritic cargoes in the proximal axon [11]. Together these data imply that myosin-mediated anchoring along with dynein-mediated reversal prevents the entry of somatodendritic cargoes into the distal axon.

Up to date, the AIS has been considered to be the main site where cargo exclusion

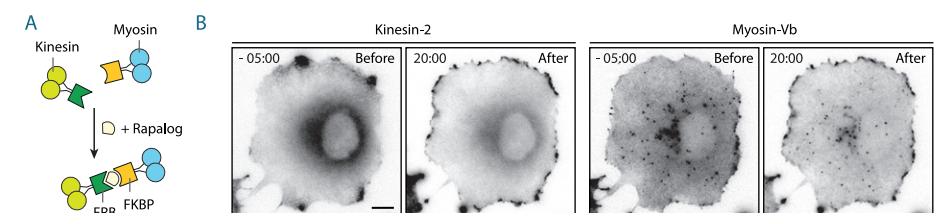


**Figure 1 | Direct coupling of kinesin and myosin motors drives KIF17 towards the cell edge.**

(A) Assay: the addition of rapalog couples Myosin-Vb(1–1090) fused to mRFP and FKBP (MYO-FKBP) to KIF17(1–547) fused to GFP and FRB (KIF-FRB). (B) KIF-FRB (left) and MYO-FKBP (right) distribution in a COS-7 cell before (left) and after (right) the addition of rapalog. Scale bar, 10  $\mu$ m.

from the axon occurs. Deviating from this view it was found that somatodendritic cargoes are redirected away from the axon already at a more proximal region, even in the absence of an AIS in Ankyrin-G depleted neurons. The proximal region where cargo redirection occurred was named the pre-axonal exclusion zone (PAEZ) [12]. The selectivity was based on the preferential binding of kinesin-1 KIF5 to acetylated MTs in the PAEZ, since binding of KIF5 to somatodendritic cargo could steer these cargoes into the axon. How MT acetylation becomes enriched at the PAEZ has to be further investigated. Thus, it seems likely that the entry of somatodendritic cargo into the axon is prevented in three ways; 1) kinesin-based sorting in the PAEZ, 2) myosin-based anchoring at the AIS and 3) dynein-based reversal at the AIS.

In our trafficking assay, constitutive active Myosin-V was sufficient to anchor cargo at the AIS. The fact that coupling to KIF5 could steer somatodendritic cargo into the axon [12] implies that either endogenous myosin levels are too low, or that attached myosins are in an inactive state, resulting in the passage of KIF5 coupled somatodendritic cargoes. A question thus remains how kinesin and Myosin-V activities are regulated at the AIS on cargoes that simultaneously have KIF5 and Myosin-V motors attached. Interestingly, tropomyosins (TMs) are able to modulate myosin processivity as well as the binding of myosins to actin filaments by binding in the actin helix groove [13–15]. For example, the ability of Myosin-Ic to initiate or terminate kinesin-1 driven vesicle transport at engineered MT-actin intersections *in vitro* was shown to be suppressed by the presence of TM2 [16]. Therefore, TMs might be involved in the regulation of myosins at the AIS. In chapter 7 we identified TM2 and TM3, which are different isoforms of the same  $\alpha$ TM gene, as being required for AIS maintenance in hippocampal neurons. In addition, various tropomyosins were found to be involved in the regulation of neurite formation and branching in B35 neuroblastoma cells and rat cortical neurons [15,17,18]. For these reasons it would be interesting to determine the localization of TM2 and TM3 in hippocampal neurons, and to investigate whether the depletion of TM2 or TM3 would affect Myosin-V-induced anchoring or KIF5-mediated passage at the AIS.

#### Interplay between other types of motors

The recruitment of motor proteins to peroxisomes has been used to study if motor proteins would target the axon, dendrites or both [19]. However, some motor proteins might have a more prominent function within these compartments such as the distal part of the axon or dendrites. The successive recruitment of two different motor types now allows for testing this hypothesis. For example, dynein could be recruited to steer peroxisomes into the dendrite, followed by the recruitment of a kinesin to study its effect in the distal dendrite. In addition, the interplay between myosin and dynein, and dynein and kinesin would be interesting to study as well.

## Optogenetic control of organelle transport and positioning

Molecular motors ensure the proper spatial and temporal arrangement of cargoes and organelles, which is important for cell function and survival. Despite the importance of local positioning, the exact connection between subcellular localization and organelle function remains largely unknown. This is due to lack of tools that specifically interfere with the position of a single organelle type with spatiotemporal precision. In chapter 5 we describe a method to optically control intracellular transport by using light-sensitive heterodimerization to recruit specific motor proteins to selected cargoes. We used this system to halt or stimulate axon outgrowth by pulling on recycling endosomes, and showed that mitochondria dynamics can be altered by the recruitment of extra motors or docking factors.

#### Expanding the organelle positioning toolbox

To further expand the organelle-repositioning toolbox, it would be useful to target other membranous organelles including lysosomes [20], synaptic vesicles and multivesicular bodies. Larger organelles such as the nucleus, endoplasmic reticulum (ER), and Golgi might be more difficult to relocate but this remains to be tested. In addition, other motors and anchors than used in this thesis could be coupled to get different organelle motility and redistribution dynamics. Instead of using over-expression constructs, endogenous organelle-targeting proteins can now be tagged with the heterodimerizing components using the recently developed CRISPR-Cas system [21]. This would equalize the expression among cells and would prevent the aggregation and aberrant organelle morphology that was sometimes observed in highly overexpressing cells.

#### The use of Phytochromes to couple motors to cargoes

Both the Cryptochrome and TULIP system, which were used in this thesis to couple motors to organelles, are activated by blue light and passively deactivate over time under dark conditions [22,23]. The deactivation occurs on a scale of many seconds whereas some cellular events might require more persistent organelle relocations. To sustain motor recruitment, continuous illumination could be applied, however, this can harm the cells due to the production of reactive oxygen species (ROS). To solve this issue, the use of a non-reversible photocaged dimerization system has been used to maintain spatially-defined motor recruitment to organelles and thus organelle positioning [24]. Nevertheless, to manipulate organelle positioning for a specified period of time, a system that would allow light-induced motor recruitment as well as the ability to control motor release would be preferred. The light-induced interaction between PhytochromeB (PhyB) and phytochrome interaction factor 6 (PIF6) is initiated by red light (650 nm) and can be deactivated by exposure to far red light (>750 nm)

[25]. The Phy/Pif heterodimerization system would thus be a promising tool to reposition organelles with both short-lived and long-lived redistribution dynamics, to study cellular processes that occur on a second and hour/day scale respectively, without the need for continuous illumination.

Another reason for using PhyB is that during many optogenetic experiments, specified cellular events have to be monitored both before and after light activation. Therefore, the wavelength used for activation cannot be used for imaging purposes, unless simultaneous deactivation takes place. For this reason, the imaging of blue and green fluorescent proteins is not compatible with the use of Cryptochrome and LOV-based proteins. In contrast, assuming PhyB deactivation by >750 nm light would overrule PhyB activation induced by >650 nm light, imaging of blue, green, red and far-red fluorescent proteins would be compatible with PhyB mediated optogenetic manipulations. Thus, using the PhyB based heterodimerization system in concert with 750 nm light, might allow the imaging of multiple types of proteins before and after light-induced manipulations.

The use of PhyB in animal cells has one major drawback. The allosteric transition of light sensitive proteins is triggered by the photoisomerization of a chromophore cofactor. Whereas the Cryptochrome and LOV chromophore flavin is endogenously present in all eukaryotic cells, this is not the case for Phytochromobilin, which is the chromophore needed for the allosteric transition in PhyB. In cell culture, the addition of exogenous Phycocyanobilin (PCB) can substitute Phytochromobilin, however, the purification of PCB is laborious and the half-life time in cell culture medium is only one hour [26,27]. Besides adding exogenous PCB, multi-factor metabolic engineering by means of enzyme overexpression or knockdown could be used to affect the formation and degradation of PCB. This strategy was shown to result in concentrations up to 2  $\mu$ M intracellular PCB, which was sufficient to induce the red light response in the PhyB protein [27]. Instead of increasing the PCB supply, bacteriophytochromes could be used as an alternative. In contrast to plant PhyB, the near-infrared sensitive bacteriophytochromes utilize Biliverdin as their chromophore, which is endogenously present in most mammalian cells [28]. However, the conformational change upon exposure to near-infrared light does naturally not lead to protein binding [29]. Therefore, protein engineering would be needed to induce protein heterodimerization consequent to the allosteric transition in the bacteriophytochrome. If succeeded, near-infrared-induced protein heterodimerization could actively be induced and stopped, without the need to apply any metabolic manipulation or to add any exogenous compound. All in all, when sufficient chromophore levels can be maintained, Phytochromes are promising tools to redistribute organelles for a defined period of time and to perform simultaneous multicolor imaging.

### Overcoming protein fusion incompatibilities

The light-induced interaction between motors and organelles requires creating fusion constructs with the components of the light-sensitive heterodimerization system. However, not all fusions will lead to functional heterodimerization because sterical hindrance will impair the occurrence of conformational changes, and thereby prevent binding to its binding partner. For this reason, LOVpep is only compatible with C-terminal fusions whereas the Cryptochrome is limited to N-terminal fusions. This prohibits for example the direct coupling of LOVpep to RAB GTPases such as RAB11, since both proteins are incompatible with N-terminal fusions. Recently, a new LOV domain based heterodimerization system was engineered, grounded on the interaction between *Escherichia coli* (*E. coli*) SsrA and SspB. 7 residues of the SsrA peptide were added to the end of the LOV  $\alpha$  helix and upon exposure to blue light, SsrA could bind SspB [30]. Importantly, both N- and C-terminal fusions of LOV/SsrA could induce binding to SspB, which now allows the direct fusion of LOV/SsrA to proteins such as RAB11. Thus, the light-induced interaction between SsrA and SspB can now be used to directly recruit motors to RAB GTPase marked vesicles *in vitro* and *in vivo*, without requiring the rapalog heterodimerization system.

### Motor activation upon recruitment to organelles

In the developed organelle relocation assay, constitutive active motors lacking their cargo binding and motor inhibiting tail were used to transport organelles. In other words, motors continuously run along the cytoskeleton but only carry cargo upon exposure to blue light. In cells with a polarized cytoskeleton such as neurons, motors used to steer specified cargoes into the axon might get depleted from the cell body and the proximal axon prior to illumination. Therefore, the ability to activate motor proteins only upon cargo recruitment would perhaps lead to more efficient cargo transport, due to more motors being available for cargo binding. In full-length motor proteins, motor dimerization induced by the coiled-coils in the motor stalk, is needed for processive walking [31,32]. Replacing the dimerizing coils with light-inducible homodimerization modules would keep the motor inactive prior to the experiment, but activate them upon exposure to blue light. The Vivid photoreceptor derived from *Neurospora Crassa* could possibly be used to accomplish this, since it forms a homodimer in response to blue light [33]. In fact, the blue-light-induced dimerization of monomeric kinesin-3 KIF1A fused to Vivid (KIF-VIVID) resulted in the redistribution of KIF-VIVID from the cytoplasm to the MTs. In addition, KIF-VIVID accumulated at the cell periphery upon blue-light-illumination in COS-7 cells, indicating that KIF1A motors become processive only after exposure to blue light (Figure 2). Importantly, KIF-VIVID motors could still induce efficient cargo transport upon dimerization (Figure 2).

Whether Vivid-mediated homodimerization of inactive monomers can increase the efficiency of light-induced cargo transport into structures with a clear cytoskeletal polarization such as axons remains to be tested.

**Optogenetic control of motor speed and direction**

By recruiting motor proteins to the organelle of interest, cargo transport is either turned ON or OFF. Consequently, the dynamics with which cargo motility can be altered is limited by the speed and direction of existing motors. A tool to modify these motor properties would increase the freedom of cargo movements, since it would allow for slowing-down, speeding-up and switching directions of cargo transport. Through the incorporation of a LOV domain in the lever arm of myosin and kinesin-14 family

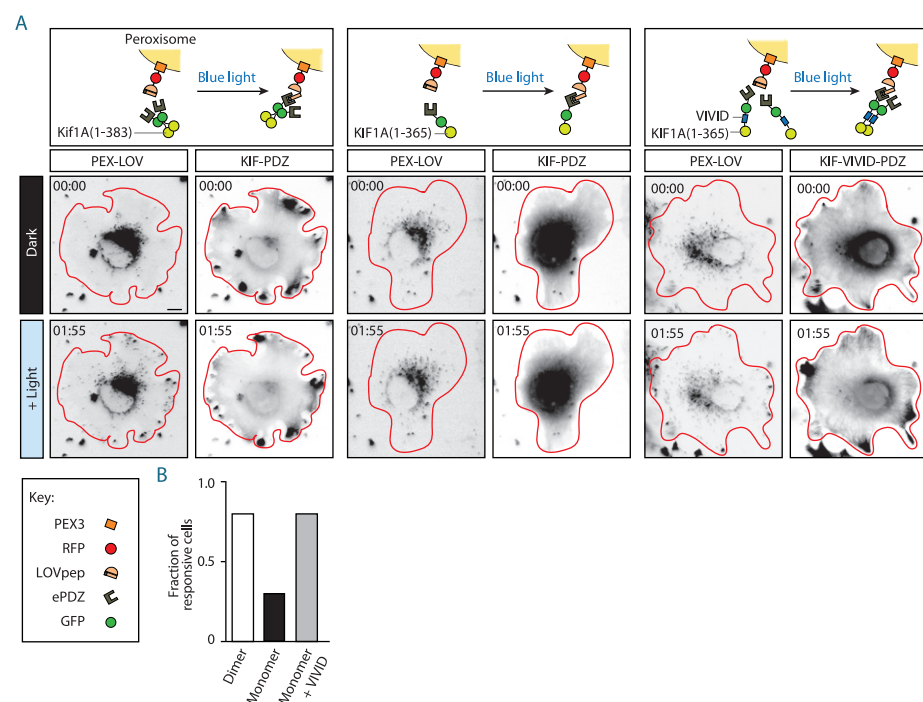


**Figure 2 | KIF1A monomers that have been dimerized by using a light-sensitive homodimerization domain are processive and can perform cargo transport.**

**A)** Peroxisome and KIF1A distributions before and during blue-light-illumination in COS-7 cells transfected with PEX3-RFP-LOVpep and KIF1A(1–383)-GFP-ePDZb1 (left panel), KIF1A(1–365)-GFP-ePDZb1 (middle panel) or KIF1A(1–365)-VIVID-GFP-ePDZb1 (right panel). Red lines indicate cell outlines. Scale bar represents 10 μm. **B)** Fraction of cells that show a redistribution of peroxisomes from the center to the periphery of the cell upon exposure to blue light.

members, motor speed and direction could be photocontrolled *in vitro* [34]. Applying this tool in living cells together with Phytochrome-based motor-cargo attachments would allow the orthogonal control over motor recruitment and motor speed and directionality in living cells, which would further increase the spatiotemporal control of cargo transport and positioning.

**Optogenetic control of organelle transport *in vivo***

The importance of organelle positioning in basal events such as growth, signaling and polarization can be studied in two-dimensional cell culture systems. Nevertheless, we anticipate that two-dimensional systems will underestimate the importance of organelle positioning in multicellular and three-dimensional systems. For example, to study the role of local organelle functioning in asymmetric cell division, stem cell maintenance, cell migration and cell-cell interactions, it would be useful to be able to control organelle position in three dimensional or *in vivo* systems. To facilitate organelle-positioning studies within individual cells of a multicellular organism, we extended the developed light-induced trafficking assay to the *in vivo* model *C. elegans*, as described in chapter 6. We demonstrated that recruitment of either kinesin or dynein is sufficient to selectively target the axon or dendrite of the PQR neuron, respectively. These findings highlight the traffic rules that govern polarized sorting and can be further exploited to alter organelle distributions in a controlled manner.

**Future applications**

Future research using our developed organelle-repositioning assay could be used to unravel spatially defined organelle functions and the mechanisms that control positioning. For example, the role of apically localized mitochondria in cancer epithelial cells could be studied. Whereas mitochondria are uniformly distributed in epithelial cells under normal conditions, an enrichment of mitochondria at the apical site of epithelial cancer cells has been observed. The anterior localization of mitochondria correlates with faster and more directed migration [35], however, the exact role of mitochondria at the apical site is unknown. Remarkably, the asymmetric mitochondria distribution is not observed during spontaneous migration but does occur during chemotaxis or during migration in confined spaces [35]. This suggests that mitochondria are not needed for migration per se and suggest a role for mitochondria besides providing ATP. One hypothesis is that mitochondria buffer Ca<sup>2+</sup> that enters the cell at the leading edge, and thereby maintain the sensitivity to chemical attractant cues [35]. Our organelle-repositioning tool could be used to relocate mitochondria in these and other migrating cells and study the effects on signaling and local Ca<sup>2+</sup> and ATP concentrations.

Another example in which our organelle-repositioning tool would be useful is to

study why and how lysosomes at the cell surface, rather than lysosomes in the cell center, stimulate cell migration and motility. Although lysosomes are most well known for degrading intracellular proteins and membranes, the observation that lysosomes can accumulate at the cell cortex suggests that lysosomes possess non-canonical functions that are limited to the cell surface. In fact, it has recently been suggested that lysosomes can secrete toxic copper species in hepatocytes to maintain copper homeostasis [36], and can secrete adhesion molecules and signaling scaffolds to promote cell spreading and migration [37]. The exact role lysosomes play in these cellular events is likely to be revealed through the controlled relocation of these organelles, and other non-canonical lysosome functions might be discovered. We foresee that our developed tool will considerably contribute to the discovery of novel and spatially-defined organelle functions in many different cell types and model systems in the near future.

### The role of microtubule depolymerizers in neuronal polarization

A plethora of specialized molecular motors can modify the cytoskeleton, and conduct the transport of many different cargoes to maintain cell compartmentalization and polarity. However, exactly which motor proteins play a role in neuronal axon formation and polarization is unknown. In chapter 7 we find that microtubule-depolymerizing kinesins are involved in axon formation. We focused our study on kinesin-8 KIF19 and demonstrate it is localized to axon and dendrite tips and is required for AIS maintenance, neuronal polarity and axon outgrowth, but not axon initiation.

In chapter 7 we discussed possible mechanisms by which KIF19 could be involved in neuronal polarity and the maintenance of axons and AIS structures. In addition, it is interesting to speculate that MT depolymerization is a general mechanism required for these processes. To allow the direct assessment of microtubule shrinkage on axon outgrowth, we developed a tool to induce microtubule depolymerization in living cells through chemically-induced dimerization of KIF19. Although we could induce MT depolymerization in 40% of the treated cells, it would be favorable to have higher response rates. Because full-length MCAK is known to be a more potent MT depolymerizer compared to full-length KIF19, we suggest using MCAK as the platform for induced MT depolymerization in future experiments. However, it is questionable whether MCAK dimerization will increase MT depolymerization rates [38,39] and therefore MCAK uncaging might be more successful than MCAK dimerization. To restrict MT depolymerization to specified areas such as the growth cone, efforts should be made to induce MT-depolymerization using light.

Remarkably, although the depletion of kinesin-13 KIF2A, kinesin-2 KIF3C and KIF19 all affect AIS maintenance and neuronal polarization, the exact phenotype is

different for each of the knockdowns. For example, Trim46 and Tau appeared in multiple neurites upon depletion of KIF19 but remained unaffected upon silencing KIF3C or KIF2A. Moreover, Ankyrin-G and Neurofascin localizations were affected in KIF19 and KIF3C depleted neurons, but not in KIF2A depleted neurons. These differences indicate that if defective MT depolymerization would be the underlying cause, each knockdown might affect MT dynamics at a different time point during development, at a different location, or at a different level. It would therefore be interesting to study KIF2A and KIF3C in more detail as well, and to determine if they show any similarities that could reveal a common mechanism by which they affect neuronal polarization.

Neuronal polarization has extensively been studied and several extrinsic and intrinsic signaling pathways have been described to act on neuronal symmetry breaking and axon formation. Interestingly, these signaling cascades appear to converge on the regulation of the cytoskeleton [40,41]. Besides investigating the downstream effects of motor protein knockdown, it would be interesting to see how KIF19, KIF3C and KIF2A are regulated during neuronal polarization. For KIF2A for example, it has been shown that phosphorylation determines how KIF2A affects MT dynamics [42,43]. Future research should focus on how MT depolymerization affects axon formation and neuronal polarization, as well as on how signaling cascades during neuronal development regulate MT depolymerizers.

### Concluding remarks

Together, dozens of different motor proteins accomplish intracellular transport and arrange the cytoskeleton to geometrically organize the cell, which is indispensable for cell survival. In this thesis, we have described how the interplay between kinesin and myosin motors contributes to the transport and distribution of a single cargo, and how this affects cargo transport into the axon of cultured hippocampal neurons. In addition, we found that a subset of motor proteins is essential for axon formation and neuronal polarization, but the exact mechanism remains to be studied. The acquired insights on cargo transport by molecular motors were deployed to hijack motors to control organelle localization using optogenetics. With this tool available, the exact relation between organelle position and function can now, for the first time, be investigated.

To thoroughly explore local organelle functioning, techniques that have recently been optimized for single-cell analysis, including single-cell transcriptomics and proteomics, should be further optimized towards a single-organelle resolution. Moreover, it would be interesting to apply our developed organelle trafficking assay in diseased cells differentiated from patient-derived induced pluripotent stem (iPS) cells. This will most likely yield new insights into the role of organelle positioning and

molecular motors in both healthy and diseased conditions, and will contribute to a better understanding of pathological processes. All in all, further illuminating and manipulating molecular motors at work will undoubtedly reveal new organelle functions, and will open new avenues for studying the versatile and spatiotemporal tasks of motor proteins.

## References

1. Dietrich, D. et al. (2013) Identification of the kinesin KIFC3 as a new player for positioning of peroxisomes and other organelles in mammalian cells. *Biochim. Biophys. Acta* **1833**, 3013–3024
2. Sun, C. et al. (2014) Intracellular tracking of single native molecules with electroporation-delivered quantum dots. *Anal. Chem.* **86**, 11403–11409
3. Courty, S. et al. (2006) Tracking individual kinesin motors in living cells using single quantum-dot imaging. *Nano Lett.* **6**, 1491–1495
4. Winckler, B. et al. (1999) A diffusion barrier maintains distribution of membrane proteins in polarized neurons. *Nature* **397**, 698–701
5. Song, A.-H. et al. (2009) A selective filter for cytoplasmic transport at the axon initial segment. *Cell* **136**, 1148–1160
6. Lewis, T.L. et al. (2009) Myosin-dependent targeting of transmembrane proteins to neuronal dendrites. *Nat. Neurosci.* **12**, 568–576
7. Lewis, T.L. et al. (2011) A role for myosin VI in the localization of axonal proteins. *PLoS Biol.* **9**, e1001021
8. Watanabe, K. et al. (2012) Networks of polarized actin filaments in the axon initial segment provide a mechanism for sorting axonal and dendritic proteins. *Cell Rep* **2**, 1546–1553
9. Jones, S.L. et al. (2014) Axon initial segment cytoskeleton comprises a multiprotein submembranous coat containing sparse actin filaments. *J. Cell Biol.* **205**, 67–81
10. Ganguly, A. et al. (2015) A dynamic formin-dependent deep F-actin network in axons. *J. Cell Biol.* **210**, 401–417
11. Kuijpers, M. et al. (2016) Dynein regulator NDEL1 controls polarized cargo transport at the axon initial segment. *Neuron* **89**, 461–471
12. Fariás, G.G. et al. (2015) Sorting of dendritic and axonal vesicles at the pre-axonal exclusion zone. *Cell Rep* DOI: 10.1016/j.celrep.2015.09.074
13. Gunning, P.W. et al. (2005) Tropomyosin isoforms: divining rods for actin cytoskeleton function. *Trends Cell Biol.* **15**, 333–341
14. Hodges, A.R. et al. (2012) Tropomyosin is essential for processive movement of a class V myosin from budding yeast. *Curr. Biol.* **22**, 1410–1416
15. Gunning, P.W. et al. (2015) Tropomyosin - master regulator of actin filament function in the cytoskeleton. *J. Cell. Sci.* **128**, 2965–2974
16. McIntosh, B.B. et al. (2015) Control of the initiation and termination of kinesin-1-driven transport by myosin-Ic and nonmuscle tropomyosin. *Curr. Biol.* **25**, 523–529
17. Schevzov, G. et al. (2005) Specific features of neuronal size and shape are regulated by tropomyosin isoforms. *Mol. Biol. Cell* **16**, 3425–3437
18. Curthoys, N.M. et al. (2014) Tropomyosins induce neuritogenesis and determine neurite branching patterns in B35 neuroblastoma cells. *Mol. Cell. Neurosci.* **58**, 11–21
19. Lipka, J. et al. (2016) Microtubule-binding protein doublecortin-like kinase 1 (DCLK1) guides kinesin-3-mediated cargo transport to dendrites. *The EMBO Journal* DOI: 10.15252/embj.201592929
20. Duan, L. et al. (2015) Optogenetic control of molecular motors and organelle distributions in cells. *Chem. Biol.* **22**, 671–682
21. Cong, L. et al. (2013) Multiplex genome engineering using CRISPR/Cas systems. *Science* **339**, 819–823

22. Kennedy, M.J. et al. (2010) Rapid blue-light-mediated induction of protein interactions in living cells. *Nat. Methods* **7**, 973–975
23. Strickland, D. et al. (2012) TULIPs: tunable, light-controlled interacting protein tags for cell biology. *Nat. Methods* **9**, 379–384
24. Ballister, E.R. et al. (2015) Optogenetic control of organelle transport using a photocaged chemical inducer of dimerization. *Curr. Biol.* **25**, R407–8
25. Levsikaya, A. et al. (2009) Spatiotemporal control of cell signalling using a light-switchable protein interaction. *Nature* **461**, 997–1001
26. Müller, K. et al. (2013) A red/far-red light-responsive bi-stable toggle switch to control gene expression in mammalian cells. *Nucleic Acids Res.* DOI: 10.1093/nar/gkt002
27. Müller, K. et al. (2013) Synthesis of phycocyanobilin in mammalian cells. *Chem. Commun. (Camb.)* **49**, 8970–8972
28. Piatkevich, K.D. et al. (2013) Engineering of bacterial phytochromes for near-infrared imaging, sensing, and light-control in mammals. *Chem Soc Rev* DOI: 10.1039/c3cs35458j
29. Ryu, M.-H. et al. (2014) Engineering adenylate cyclases regulated by near-infrared window light. *Proc. Natl. Acad. Sci. U.S.A.* **111**, 10167–10172
30. Guntas, G. et al. (2015) Engineering an improved light-induced dimer (iLID) for controlling the localization and activity of signaling proteins. *Proc. Natl. Acad. Sci. U.S.A.* **112**, 112–117
31. Hirokawa, N. et al. (2009) The mechanisms of kinesin motor motility: lessons from the monomeric motor KIF1A. *Nat. Rev. Mol. Cell Biol.* **10**, 877–884
32. Tomishige, M. et al. (2002) Conversion of Unc104/KIF1A kinesin into a processive motor after dimerization. *Science* **297**, 2263–2267
33. Nihongaki, Y. et al. (2014) Genetically engineered photoinducible homodimerization system with improved dimer-forming efficiency. *ACS Chem. Biol.* **9**, 617–621
34. Nakamura, M. et al. (2014) Remote control of myosin and kinesin motors using light-activated gearshifting. *Nat Nanotechnol* **9**, 693–697
35. Desai, S.P. et al. (2013) Mitochondrial localization and the persistent migration of epithelial cancer cells. *Biophys. J.* **104**, 2077–2088
36. Polishchuk, E.V. et al. (2014) Wilson disease protein ATP7B utilizes lysosomal exocytosis to maintain copper homeostasis. *Dev. Cell* **29**, 686–700
37. Pu, J. et al. (2015) BORC, a multisubunit complex that regulates lysosome positioning. *Dev. Cell* **33**, 176–188
38. Ems-McClung, S.C. et al. (2007) The interplay of the N- and C-terminal domains of MCAK control microtubule depolymerization activity and spindle assembly. *Mol. Biol. Cell* **18**, 282–294
39. Cooper, J.R. et al. (2010) Catalysis of the microtubule on-rate is the major parameter regulating the depolymerase activity of MCAK. *Nat. Struct. Mol. Biol.* **17**, 77–82
40. Tahirovic, S. and Bradke, F. (2009) Neuronal polarity. *Cold Spring Harb Perspect Biol* **1**, a001644
41. Barnes, A.P. and Polleux, F. (2009) Establishment of axon-dendrite polarity in developing neurons. *Annual review of neuroscience* **32**, 347–381
42. Ogawa, T. and Hirokawa, N. (2015) Microtubule destabilizer KIF2A undergoes distinct site-specific phosphorylation cascades that differentially affect neuronal morphogenesis. *Cell Rep* **12**, 1774–1788
43. Watanabe, T. et al. (2015) TTBK2 with EB1/3 regulates microtubule dynamics in migrating cells through KIF2A phosphorylation. *J. Cell Biol.* **210**, 737–751





# Addendum



Summary

Nederlandse samenvatting

Curriculum vitae

List of publications

Acknowledgements

---

## Summary: Illuminating molecular motors at work

Cells constitute all living things on earth and are the smallest biological units that can grow, replicate and respond to stimuli. In order to do so, eukaryotic cells have confined many cellular tasks including DNA storage, energy production and protein degradation to specialized membranous compartments called organelles. In recent years evidence has accumulated that organelles accomplish (non-canonical) functions that depend on the proper spatial arrangements. In other words, the subcellular localization of organelles can be exploited to orchestrate cellular events including cell signaling, polarization, and outgrowth. It is therefore not surprising that the localization of most, if not all, organelles is tightly controlled and can be adjusted in case of changing conditions and demands. Moreover, aberrant organelle distributions have been associated with various diseases such as microvillus inclusions disease, Huntington's disease, Wilson disease and cancer. Despite the importance of local positioning, the precise connection between subcellular localization and organelle function is often not fully understood. This is due to lack of tools to specifically interfere with organelle positioning (**chapter 2**). Therefore, we aimed to develop a tool to manipulate organelle positioning with spatiotemporal precision. In order to do so, a good understanding of how organelles are being transported and positioned is essential.

Organelles are being transported and positioned by molecular motors that walk along a network of motor tracks, called the cytoskeleton. Kinesin motors accomplish fast and long-range organelle transport by walking along microtubules, whereas slow and short-range transport is mediated by myosin motors that walk along the actin cytoskeleton. In fact, a single cargo often travels along both microtubule and actin filaments but how microtubule and actin-based motors contribute to the final motility and distribution of these cargoes is largely unknown. We illuminated the interplay between kinesin and myosin motors and found that on intracellular cargoes that contain both motor types, Myosin-V is able to stall fast kinesin-driven organelle movements and can drive slow and short-range transport towards the plasma membrane in COS-7 cells (**chapter 3**).

Proper organelle transport and positioning is particularly important in polarized and spatially extended cells including neurons. Neurons are the cells from the brain that receive, integrate and transmit signals, which is critical for learning and memory. They receive information via multiple tapering processes called dendrites whereas a single long and thin outgrowth called the axon accomplishes signal transmission.

A specialized set of proteins and organelles, which greatly varies between the axon and dendrites, is essential for both domains to function properly. Polarized transport underlies these differences and a specialized structure at the beginning of the axon, the axon initial segment (AIS) functions as a sorting station; dendritic cargoes cannot pass this point. Although the AIS is an actin-rich structure, the exact role of myosin motors at the AIS remains controversial. Consistent with our findings in chapter 3 we show that the recruitment of Myosin-V to kinesin-propelled cargoes in cultured hippocampal neurons is sufficient to stall kinesin-driven cargo entry into the axon. However, in contrast to previous reports we find that Myosin-V does not cause cargo reversals at the AIS. These data enlighten that Myosin-V prevents dendritic cargo from entering the axon by cargo tethering rather than cargo reversal (**chapter 4**).

Besides contributing to polarized transport in matured neurons, there are ample suggestions that motor proteins also play a role in the maintenance and formation of neuronal polarity. However, the involvement of motor protein family members in axon formation has not systematically been tested. We performed a motor protein knockdown screen in cultured hippocampal neurons and found that microtubule-depolymerizing kinesins are essential for axon formation and neuronal polarization. Although the exact mechanism remains to be studied, our developed tool to induce microtubule depolymerization may be helpful to answer how microtubule depolymerization affects axon maintenance or axon formation (**chapter 7**).

To study local organelle functions, the acquired insights on cargo positioning by molecular motors were subsequently deployed to control the localization of organelles with spatiotemporal precision. More specifically, molecular motors with known speed and direction were manipulated in two-dimensional cell cultures to bind an organelle of interest, only in the presence of blue light. In other words, targeted blue-light illumination could be used to trigger selective organelle translocations. Because two-dimensional systems will most likely underestimate the importance of organelle positioning, we extended the developed light-induced transport assay to manipulate organelle positions within individual cells of a living *Caenorhabditis elegans* roundworm. Using the organelle-repositioning tool we showed that the addition of recycling endosomes into the axonal growth cone stimulated axon outgrowth in cultured hippocampal neurons. This data shows that basal cellular processes are dependent on and can be manipulated by changing organelle distributions. Thus, with this tool available the exact relations between organelle position and function can now be investigated (**chapter 5 and 6**).

All in all, this thesis enlightened us on how kinesin and myosin motors work together to affect the final cargo distribution, and a tool was developed to control organelle transport and positioning in living cells using blue light. Further illuminating and hijacking molecular motors at work will unquestionably increase our knowledge

on local organelle functions and reveal spatiotemporal tasks of motor proteins in both healthy and diseased conditions.

## Samenvatting: Het belichten van moleculaire motoren in functie

Cellen zijn de fundamentele bouwstenen van al het leven op aarde en zijn de kleinste biologische eenheden die kunnen groeien, vermenigvuldigen en reageren op signalen van buitenaf. Om dit te bewerkstelligen worden vele taken in de cel – zoals het opslaan van DNA, de productie van energie en de afbraak van eiwitten – uitsluitend uitgevoerd in gespecialiseerde compartimenten welke gezamenlijk de organellen worden genoemd. De afgelopen jaren is duidelijk geworden dat een aantal organelfuncties afhankelijk is van de juiste positionering van deze organellen. Het is daarom niet verrassend dat de positie van de meeste organellen goed wordt gecontroleerd en kan worden bijgestuurd indien nodig. Een afwijkende lokalisatie van organellen in de cel is dan ook geassocieerd met ziekten zoals kanker, de ziekte van Huntington, de ziekte van Wilson en de microvilli inclusie ziekte. Ondanks het belang van organel positionering is de precieze relatie tussen de lokalisatie en de functie van een organel vaak niet duidelijk omdat er simpelweg geen goede onderzoeksmethoden beschikbaar zijn (**hoofdstuk 2**). Om die reden hebben we getracht een methode te ontwikkelen waarmee de positie van organellen in plaats en tijd gemanipuleerd kan worden. Een goede kennis van de manier waarop organellen normaliter gepositioneerd worden is hiervoor echter onmisbaar.

Organellen worden getransporteerd en gepositioneerd door moleculaire motoren die over een netwerk van wegen in de cel (het cytoskelet) heen lopen. Kinesine motoren verzorgen het snelle en langeafstand transport door zich langs het zogenoemde microtubulusnetwerk te bewegen, terwijl myosine motoren voornamelijk betrokken zijn bij het langzame en korteafstand transport dat over het actine cytoskelet plaats vindt. In werkelijkheid beweegt een transportblaasje of organel zich vaak over zowel microtubuli als actine, maar hoe microtubulus- en actine gebaseerde moleculaire motoren bijdragen aan de uiteindelijke beweeglijkheid en positionering van deze transportblaasjes is niet bekend. In dit proefschrift belichten we het samenspel van kinesine en myosine motoren en concluderen dat op blaasjes die beide type motoren bevatten, myosine in staat is om de kinesine-gedreven cargo-bewegingen te stoppen. Tevens laten we zien dat myosine de transportblaasjes over korte afstanden richting de buitenste regionen van de cel kan transporteren (**hoofdstuk 3**).

De juiste organelpositionering is extra belangrijk in gepolariseerde (asymmetrische) en uitgestrekte cellen zoals de zenuwcellen in onze hersenen. Deze cellen ontvangen, integreren en geven informatie door, wat essentieel is voor leren en het geheugen. Zo ontvangen hersencellen signalen via vele uitlopers die dendrieten worden genoemd terwijl één enkele dunne en lange uitloper – het axon – zorgt voor het doorgeven van signalen naar andere hersencellen. Voor beide domeinen is een gespecialiseerde set van eiwitten en organellen, welke enorm varieert tussen het axon en de dendrieten, essentieel om goed te kunnen functioneren. Gepolariseerd transport zorgt voor deze inhoudsverschillen en een karakteristieke structuur aan het begin van het axon, het axon initieel segment (AIS), fungeert als een sorteerstation; transportblaasjes bestemd voor de dendrieten kunnen dit punt normaliter niet passeren. Alhoewel het AIS een actine-rijke structuur is, is de exacte rol van myosine motoren op deze plek controversieel. Consistent met onze bevindingen in hoofdstuk 3 vinden we dat de rekrutering van myosine naar kinesine-gedreven blaasjes in gekweekte hersencellen voldoende is om deze blaasjes te verankeren in het AIS. In contrast met eerder gerapporteerd onderzoek zien we geen transport terug richting het cellichaam. Deze resultaten brengen aan het licht dat dendritische blaasjes het axon niet inkomen doordat myosine deze verankert in het AIS, maar dat een ander mechanisme verantwoordelijk is voor het transport terug richting de dendrieten **(hoofdstuk 4)**.

Naast het bijdragen aan gepolariseerd transport in volwassen hersencellen zijn er aanwijzingen dat moleculaire motoren ook betrokken zijn bij de totstandkoming van de axon-dendriet polariteit. Echter, de betrokkenheid van motoren in axonformatie is nooit systematisch getest. Door de motoren één voor één uit te zetten laten we zien dat moleculaire motoren die de microtubulus afbreken (depolymeriseren), essentieel zijn voor axonformatie en hersencelpolarisatie. Alhoewel het exacte mechanisme onopgelost blijft, geeft het gebruik van de door ons ontwikkelde methode om microtubulus-depolymerisatie te initiëren, in de toekomst wellicht antwoord op de vraag hoe microtubulus depolymerisatie bijdraagt aan axonformatie **(hoofdstuk 7)**.

De verkregen inzichten in het functioneren van moleculaire motoren hebben we vervolgens gebruikt om de lokalisatie van organellen te manipuleren. Motoren met een bepaalde snelheid en richting werden omgebouwd zodat deze de gewenste organellen konden binden en transporteren, puur en alleen in de aanwezigheid van blauw licht. Met andere woorden, blauwe laserstralen kunnen nu gebruikt worden om organellen heel specifiek in ruimte en tijd te sturen. Omdat in gekweekte cellen het belang van organel positioning waarschijnlijk onderschat wordt, hebben we de organel-transportmethode verder ontwikkeld zodat nu ook organellen in levende *Caenorhabditis elegans* wormen gestuurd kunnen worden. We hebben laten zien dat de geforceerde verrijking van specifieke blaasjes in het axon uiteinde van gekweekte

hersencellen het axon sneller kan laten uitgroeien. Dit resultaat geeft aan dat basale cellulaire processen afhankelijk zijn van, en gemanipuleerd kunnen worden door, het veranderen van organel lokalisaties. Met deze methode kunnen we nu voor het eerst de exacte relatie tussen organelpositie en functie aan het licht brengen **(hoofdstuk 5 en 6)**.

Samenvattend, dit proefschrift heeft het samenspel tussen kinesine en myosine motoren verder belicht. Daarnaast hebben we een methode ontwikkeld waarmee de positie van organellen, met behulp van blauw laserlicht, in levende cellen gestuurd kan worden. Het verder belichten en voor het karretje spannen van moleculaire motoren in functie zal onze kennis van lokale organelfuncties en van de taken van moleculaire motoren verder vergroten in zowel gezonde als pathogene condities.

## Curriculum vitae

Petra van Bergeijk was born on the 25<sup>th</sup> of December 1986 in Lelystad, The Netherlands and received her VWO-diploma (Nassau Veluwe College, Harderwijk) in 2005. Petra continued her education at the University of Groningen where she studied Life Science & Technology and specialized herself in Molecular and Medical Cell Biology. In 2008 she received her bachelor's degree *cum laude* and started the research master Medical and Pharmaceutical Drug Innovation at the same University. As part of the master's program, Petra performed a research internship in the group of prof. dr. Ellen Nollen (University Medical Center Groningen), and the group of prof. dr. Tin Tin Su (University of Colorado at Boulder, USA). Upon obtaining her master's degree *cum laude* in 2010, Petra worked for one year in the lab of prof. dr. René Ketting (Hubrecht Institute, Utrecht). In 2011 she started her PhD in the group of prof. dr. Casper Hoogenraad and dr. Lukas Kapitein at the department of Cell Biology at Utrecht University, of which the results are described in this thesis.

## List of publications

Light-controlled intracellular transport in *Caenorhabditis elegans*.

M. Harterink\*, **P. van Bergeijk**\*, C. Allier, B. de Haan, S. van den Heuvel, C.C. Hoogenraad & L.C. Kapitein.

*Current Biology* (2016); 4, 153-154

Right time, right place: Probing the functions of organelle positioning.

**P. van Bergeijk**, C.C. Hoogenraad & L.C. Kapitein.

*Trends in Cell Biology* (2016); 26, 121-134

Optogenetic control of organelle transport and positioning.

**P. van Bergeijk**\*, M. Adrian\*, C.C. Hoogenraad & L.C. Kapitein.

*Nature* (2015); 518, 111-114

PID-1 is a novel factor that operates during 21U-RNA biogenesis in *Caenorhabditis elegans*.

B.F.M. de Albuquerque, M.J. Luteijn, R.J. Cordeiro Rodrigues, **P. van Bergeijk**, S. Waaijers, L.J.T. Kaaij, H. Klein, M. Boxem & R.F. Ketting.

*Genes & Development* (2014); 28, 683-688

Myosin-V opposes microtubule-based cargo transport and drives directional motility on cortical actin.

L.C. Kapitein, **P. van Bergeijk**, J. Lipka, N. Keijzer, P.S. Wulf, E.A. Katrukha, A. Akhmanova, & C.C. Hoogenraad.

*Current Biology* (2013); 23, 828-834

Extremely stable Piwi-induced gene silencing in *Caenorhabditis elegans*.

M.J. Luteijn\*, **P. van Bergeijk**\*, L.J.T. Kaaij, M. Vasconcelos Almeida, E.F. Roovers, E. Berezikov & R.F. Ketting.

*The EMBO Journal* (2012); 31, 3422-3430

Genome-wide expression analysis identifies a modulator of ionizing radiation-induced p53-independent apoptosis in *Drosophila melanogaster*.

**P. van Bergeijk**, J. Heimiller, L. Uyetake & T.T. Su.

*PLoS ONE* (2012); 7, e36539

Identification of MOAG-4/SERF as a regulator of age-related proteotoxicity.

T.J.van Ham, M.A. Holmberg, A.T. van der Goot, E. Teuling, M. Garcia-Arencibia, H-E Kim, D. Du, K.L. Thijssen, M. Wiersma, R. Burggraaff, **P. van Bergeijk**, J. van Rheenen, G.J. van Veluw, R.M.W. Hofstra, D.C. Rubinsztein & E.A.A. Nollen.

*Cell* (2010); 142, 601-612

Myosin-V opposes kinesin-driven cargo entry into the axon.

A.F.J. Janssen, R.P. Tas, **P. van Bergeijk**, R. Oost, C.C. Hoogenraad & L.C. Kapitein.

*Manuscript in preparation*

\* Equal contribution

# Acknowledgements

Dankzij veel mensen heb ik mijn PhD als een geweldige tijd ervaren en dit proefschrift had niet tot stand kunnen komen zonder de hulp van vele anderen. Allereerst wil ik mijn promotor Casper Hoogenraad en copromotor Lukas Kapitein bedanken. Ik ben heel blij dat ik vier jaar geleden de overstap naar de afdeling Cel Biologie gemaakt heb. Het is een fantastische plek om te werken en het is mooi om te zien hoe jullie allebei met een andere aanpak en achtergrond zo'n goed team vormen.

Lukas, vanaf het eerste sollicitatiegesprek heb jij mij weten te enthousiasmeren en motiveren voor het werk wat je doet. Een paar maanden later begon ik aan een gaaf maar risicovol project en ik denk dat we allebei niet hadden durven dromen dat het project zo goed terecht zou komen. Dit is mede gelukt dankzij een goede begeleiding en samenwerking en het feit dat je me hebt laten inzien dat ik bepaalde kansen voor 200% moet aangrijpen. Ook heb ik veel geleerd van de manier waarop jij je werk weet op te schrijven en te presenteren, en de vele sessies waarin we met figuren en tekst geschoven hebben (soms letterlijk met papier, een schaar en prittstift) heb ik dan ook als zeer waardevol ervaren. Het is mooi om te zien hoe het lab inmiddels flink is gegroeid en ik heb er alle vertrouwen in dat we nog veel van je gaan horen. Dankjewel voor alles!

Casper, het is indrukwekkend om te zien hoe jij zoveel mensen tegelijk kunt aansturen en alles in goede banen kunt laten leiden. Het aantal meetings wat jij op een dag hebt is indrukwekkend. Toch was je er altijd als ik je nodig had voor feedback, om iets te regelen of voor andere dingen die voor mij belangrijk waren. Ik heb veel van je geleerd en wil je bedanken voor alle meetings, feedback en fijne begeleiding!

Ook wil ik graag de leden van mijn promotiecommissie bedanken. Sander, naast het beoordelen van dit proefschrift wil ik je ook enorm bedanken voor je gastvrijheid in het wormenlab en al je input, welke onmisbaar zijn geweest voor hoofdstuk 6 van dit proefschrift. Anna, niet alleen bedankt voor het doorlezen van mijn proefschrift, ook bedankt voor je feedback en het delen van al je kennis tijdens de gezamenlijke werkbesprekingen. Ook de andere leden van mijn promotiecommissie, Sven van IJendoorn, Rik Korswagen, Maarten Merckx en Marca Wauben, bedankt voor het doorlezen en beoordelen van mijn proefschrift.

My paranympths Marina en Max, first of all, thank you for actually being my paranympth. Marina, your optimistic attitude, cheerfulness (including a lot of giggles) and help-

fulness made you a very pleasant colleague to work with. Thank you for all the good times including running, camping and playing laser tag. It was also great visiting you and your newly set-up lab in Hamburg and I'm sure your lab will produce some great science. Good luck with your life as a PI and I hope we keep in touch!

Max, during 1.5 years we have intensively worked together and chapter 5 would not have been published as it is without all your hard work. Thanks for being such a nice person to work with and for all the after work fun. I'm very happy you introduced me to the wonderful world of paragliding! Good luck with finishing your PhD and I think you should aim for a postdoc somewhere in the mountains ;). Keep me updated!

I would like to thank the rest of the Kapitein lab for the Monday afternoon discussion and our refreshing (or freezing cold) early morning swims at lab outings and conferences. Bas, your help with crashed or unusual behaving microscopes has been very valuable. I'm happy you joined the lab and thanks to you I did not leave the Netherlands without having visited a dance party. Eugene, thanks for always being helpful and sharing analysis methods and ImageJ plugins. You are always full of project ideas or things we should do outside the lab, and I enjoyed discussing these things over lunch or during conferences. Anne and Roderick, I am very happy you continued the myosin anchoring/stoichiometry work and good luck with the rest of your PhD. Anaël, thanks for your legendary and hilarious performances during various lab parties. Wilco and Harold, thanks for the nice chats and advices, and I wish you good luck with your projects and grant applications.

I also would like to thank my (former) roommates of N503. Joanna, it was very special to witness your wedding in Poland and to sail the Beagle Channel in Patagonia together last Christmas. Also many thanks for sharing all your shRNA constructs. Marta, thanks for your help with rab11, your advice on what to visit in Lisbon and for all the good chats! Dieudonné, I hope you will have a good time in Odijk and thanks for your openhearted conversations. Robert, thank you for all your help with statistics and putting forward interesting non-scientific topics to discuss in the office. Elena, thanks for teaching me neuron electroporations and for trying to catch some sun during lunch.

To the other members of Cell Biology: Martin, it was during a coffee break at the Hubrecht Institute when we figured out we applied to the same lab. We started on the same day and although we initially worked on different projects, I'm very happy we joined efforts in order to develop light-controlled transport in the worms. Thank you for all your input, help, advice (worm related and unrelated), and for the good times at borrels, parties and retreats! Phebe, you are the driving force behind many borrels and

barbeques. Many thanks for organizing these social activities and for keeping the lab running. Bart, pipetting at the bench was more fun with your wordplay jokes and your comments on the DJ and music on the radio. Cátia, like Bart, also your knowledge about movies and radio songs is extraordinary. Thank you for your movie advices and for sharing your screening data. Phil, thanks for allowing me to use your constructs and I wish you all the best in Switzerland. Laura, thanks for your help on Kif3C and wish you all the best for your future. Sam and Kah Wai, within the timespan of a month the three of us will defend our thesis and luckily I can peek at your defenses before it will be my turn! It was fun having you around and good luck with your after defense life. Marijn, Karin, Feline, Amélie, Gabi, Margriet, Robin, Dennis, René, Sybren, Yujie and Pan, thank you for all the good times and good luck in the future. Marleen and Josta, I want to thank both of you for organizing so many lab activities and for all the good chats and times during these four years. Riccardo, thank you for all your mass spec help. Hai Yin, it's good to have you back in the lab! I wish you the best of luck with your further rehabilitation. Mariella, thanks for sharing your experiences on finishing a PhD and I hope you like the new job. Lena and Inês, you have both been very helpful in the lab. Thank you for answering all my questions! Esther, when I arrived in the lab it was you who familiarized me with cloning and many other techniques in the lab. Thank you for being so helpful and I wish you all the strength and energy for the future. Corette, thank you for your insights on the different Boston neighborhoods. Fons, enjoy your retirement!

To the members of the Developmental Biology department: Sander, Mike, Selma, Thijs, João, Jana, Aniek, Suzanne, Suzan, Vincent, Ruben, Lars and Juliane thank you all for the good atmosphere in the worm lab, your help with worm injections and CRISPR, and for always having so many useful worm strains growing. Without your support the project would have moved forward much slower!

I also would like to thank my students, Loek, Roos, Calixte and Stephan. It was a pleasure working with you and I truly learned so much from supervising each of you. Thank you for all the great work and I wish you all a happy and successful future.

The members of the Akhmanova lab: Ilya, Kai, Ben, Ruddi, Maud, Ankit, Ruddi, Qingyang, Jingchao, Chao, Renu, Hari, Carol and Andrea, thank you all for your input on the Friday meetings and for creating a good atmosphere in the lab. Helma, thanks for all the good chats and your company and best of luck with finishing your PhD. Ivar and Amol, let me know when you are going to run the marathon! Amol, I admire your enthusiasm to learn new things. It was so much fun teaching you ice-skating and to see you practicing the paragliding takeoff literally all day and night long.

To the members of the Molecular oncology group: Paul, Sabrina, Bram, Dušan, Sofia, Purvi, Raimond, Marta, Jarno and Rachid, thank you for your input during the lunch meetings and good luck to you all. Paul, thanks for the nice chats during lunchtime and I might see you on rollerblades or ice-skates again.

I would also like to thank some of my previous supervisors. Ellen and Annemieke, thank you both for making my introduction to science such a good experience. Tin Tin, it is probably in your lab where I learned to independently design and set-up experiments. Thank you for all the freedom you gave me and for making my trip to Colorado unforgettable. René, thank you for the great time I had in your lab. It was a very difficult decision to leave the piRNA field and I'm happy to see you are doing so well in Germany.

Ook wil ik graag mijn vrienden van buiten het lab bedanken. Mijn studiegenootjes van LS&T, Aukje, Marjon, Tryanda, Else, Petra en Simone, bedankt voor de gezellige etentjes, lunches en spelletjes avonden. Vincent, straks woon je eindelijk weer in de buurt. Marieke, ik ben blij dat ook jij je PhD in Utrecht bent gaan doen. Je was altijd wel te porren voor nieuwe dingen zoals een tennis cursus, wakeboarden of paragliden en ook de lunches tussen het werken door had ik niet willen missen.

Corinna, ik herinner me nog als wij elkaar leerden kennen tijdens de MPDI master. Ik weet dat wanneer ik een eerlijk advies of mening nodig heb ik je zelfs midden in de nacht wakker kan bellen. Dank daarvoor! Ik hoop dat we onze jaarlijkse city-trip traditie nog lang zullen voortzetten, alhoewel Istanbul toch echt even moet wachten tot na Cambridge in zowel de UK als de US!

Maartje, alhoewel we al een tijdje niet meer samen op het lab staan vind ik het fijn dat we elkaar nog steeds spreken. Nu ik heel veel nieuwe collega's heb leren kennen durf ik toch wel te beweren dat jij een gave hebt om gesprekken in het lab op de meest, laten we zegen, gevarieerde onderwerpen uit te laten komen. Bedankt ook voor de gezellige lunchwandelingen door de botanische tuinen.

Al mijn schaats en skeeler maatjes en trainers van de afgelopen 4 jaar: bedankt voor de heerlijke sportuurtjes en jullie vergeten me niet te bellen als de Elfstedentocht wordt uitgeschreven hè?

Ton & Maaïke, we hadden ons geen betere burens kunnen wensen. Bedankt voor alle fijne etentjes, wijze adviezen en jullie luisterend oor.

Als laatste wil ik mijn familie en schoonfamilie bedanken. Kees & Nel, bedankt voor het fijne tweede "thuis-thuis", de altijd leuke kampeervakanties en de vele ritjes in het rode blikje richting het treinstation. Oma Annie, ik denk dat u de enige bent die mijn wetenschappelijk artikel daadwerkelijk gelezen heeft toen ik met de papieren versie

kwam aanzetten. Ik waardeer het enorm dat u altijd interesse heeft in ons reilen en zeilen. Marlies & Bart, snel weer eens fietsen in de Limburgse heuvels of Franse Alpen? Paul, jouw frisse blik is onmisbaar geweest voor de fantastische vormgeving van dit boekje. Enorm bedankt voor al je werk en geduld!

Pap & Mam, bedankt voor het fijne thuis en alle steun en kansen die jullie mij hebben gegeven. Niet alleen op het gebied van studie en werk, maar ook de mogelijkheid om zoveel te sporten zijn onbetaalbaar geweest. Anita & Sander, Marinda & Rob, ik vind het altijd fijn om bij jullie op de boerderij langs te komen en op de kids te passen. Als ze straks wat groter zijn moeten we weer eens een weekje gaan skiën!

Lieve Jan, jouw flexibiliteit, zorgzaamheid, en ondersteuning zijn voor mij onmisbaar geweest de afgelopen jaren. Je flauwe grapjes, constante stroom aan plannetjes en nieuwe ideeën (alhoewel doodvermoeiend ;)), maakt dat het met jou nooit saai is en ik kijk ontzettend uit naar ons volgende avontuur in Boston!

Petra

